

An der Fakultät II - Mathematik und Natur-
wissenschaften der TU Berlin eingereichte Dissertation
Berlin 2024

Fluctuations and exciton dynamics in molecular semiconductors

by Alexander Dietrich Neef

 TECHNISCHE
UNIVERSITÄT
BERLIN

FRITZ-HABER-INSTITUT
MAX-PLANCK-GESELLSCHAFT



The cover shows an artist's impression of the transition from the singlet to the bitriplet exciton in a pentacene crystal. © TU Berlin (Artist: Jo Jung-woong of [CUBE 3D graphic](#))

This work was carried out between November 2018 and December 2023 at the Department of Physical Chemistry (headed by Martin Wolf) of the Fritz Haber Institute of the Max Planck Society located in Berlin Dahlem. It was supervised by Ralph Ernstorfer, head of the *Structural and Electronic Surface Dynamics* group at the institute.

[Fluctuations and exciton dynamics in molecular semiconductors](#) © 2024 by Alexander Dietrich Neef is licensed under [CC BY 4.0](#). To view a copy of this license, visit <http://creativecommons.org/licenses/by/4.0/>

Based on a L^AT_EX template originally created by Mathias Legrand (legrand.mathias@gmail.com) with modifications by Vel (vel@latextemplates.com)

Accepted version, March 2024

Fluctuations and exciton dynamics in molecular semiconductors

vorgelegt von

M. Sc.

Alexander Dietrich Neef

ORCID: 0000-0002-2375-5970

an der Fakultät II – Mathematik und Naturwissenschaften
der Technischen Universität Berlin
zur Erlangung des akademischen Grades

Doktor der Naturwissenschaften

- Dr. rer. nat. -

genehmigte Dissertation

Promotionsausschuss:

Vorsitzender: Prof. Dr. Andreas Knorr

Gutachter: Prof. Dr. Ralph Ernstorfer

Gutachter: Prof. Dr. Kirill Bolotin

Tag der wissenschaftlichen Aussprache: 26. Februar 2024

Berlin 2024

Declaration of authorship

I, M. Sc. Alexander Dietrich Neef, declare to the Technical University Berlin that I have completed the submitted dissertation independently and without the use of sources and aids other than those indicated. The present thesis is free of plagiarism. I have marked as such all statements that are taken literally or in content from other writings. This dissertation has not been submitted in the same or similar form in any previous doctoral procedure.

I agree to have my thesis examined by a plagiarism examination software.

Signature:

Date:

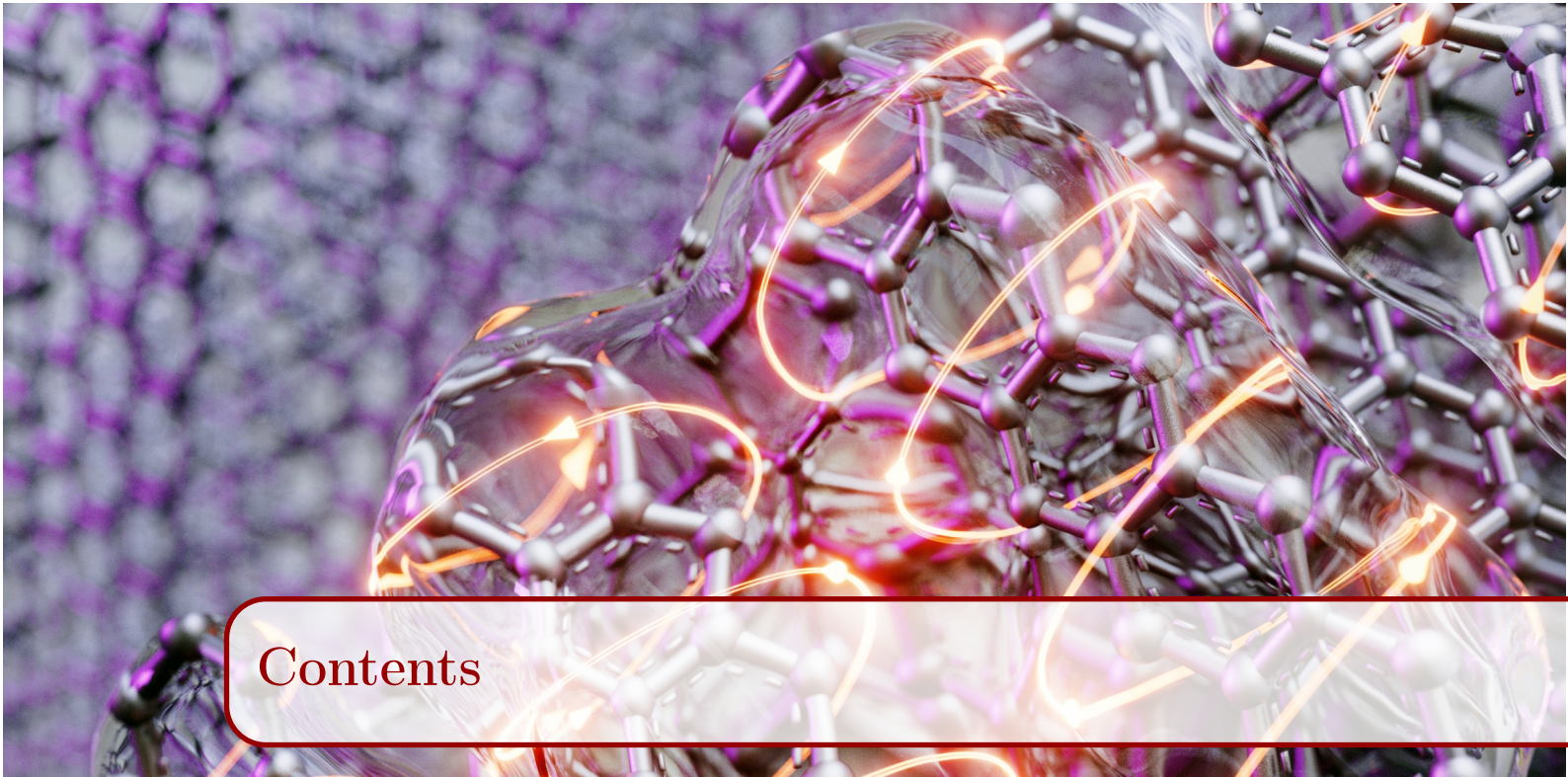
Ask courageous questions. Do not be satisfied with superficial answers. Be open to wonder and at the same time subject all claims to knowledge, without exception, to intense skeptical scrutiny. Be aware of human fallibility. Cherish your species and your planet.

Carl Sagan

To my friends.

To my mum for unconditional love.

And to my dad, who would have been proud.

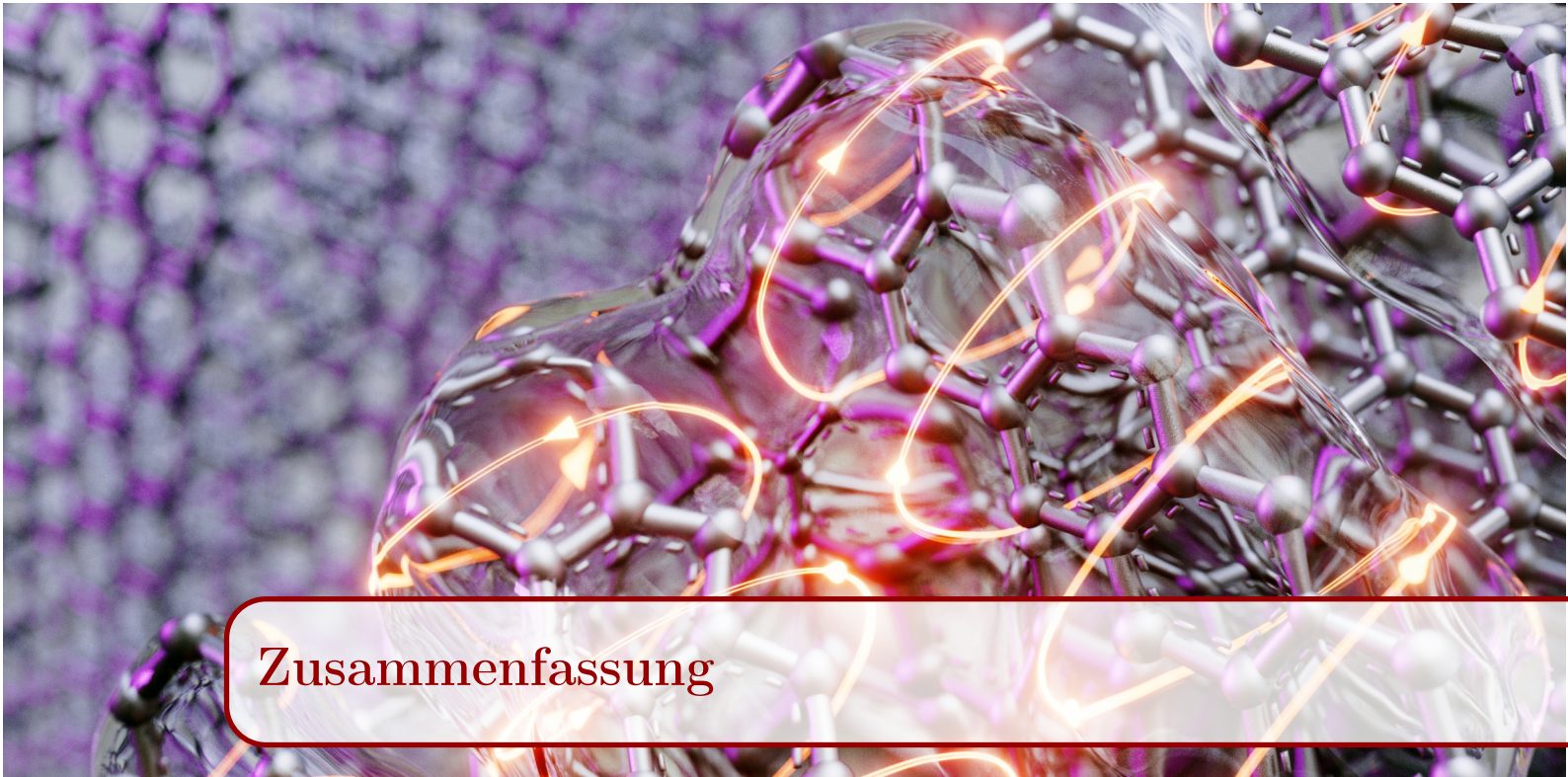


Contents

Contents	iii
Zusammenfassung	v
Abstract	vii
Acknowledgements	ix
Scientific record	xi
1 Introduction	1
2 Physics of molecular semiconductors	7
2.1 The physical regime of molecular semiconductors	8
2.2 Properties of the constituting molecules	10
2.3 Crystal structure and electronic states	13
2.4 Electron-phonon coupling in the crystal	16
2.5 Limitations of band theory	18
2.6 Localization and disorder	19
2.7 Excitons in crystalline molecular semiconductors	21
2.8 Singlet exciton fission	26
2.8.1 Introduction	26
2.8.2 Electronic states in the dimer model	27
2.8.3 Mechanisms of the primary step	30
2.8.4 The secondary step	32
2.8.5 Experimental results	33

3	Introduction to (tr)ARPES	35
3.1	Brief history	35
3.2	Photoemission kinematics	37
3.3	Quantum mechanical treatment	38
3.3.1	The one-electron matrix element	39
3.3.2	Single-particle band structure	40
3.3.3	Multiparticle states: Satellites and electron correlation	41
3.3.4	Vibrational satellites and electron-phonon coupling	42
3.4	Time-resolved ARPES	42
3.5	Brief description of the experimental setup	43
4	Electronic structure and fluctuations of molecular semiconductors	47
4.1	Introduction	47
4.2	ARPES on molecular semiconductors	49
4.3	Investigated materials	51
4.4	Structure of the data	54
4.5	Tight-binding model of molecular semiconductors	54
4.6	Relating the valence band structure to the crystal structure	56
4.6.1	Structure of lower-lying bands in pentacene	58
4.6.2	The band structure of rubrene	59
4.6.3	The band structure of picene	59
4.7	An excursion: π -topology and structure of the frontier orbital	60
4.8	Effective mass at the valence band maximum	63
4.9	Localization properties	64
4.10	Nonlocal electron-phonon coupling and structure of the frontier orbital	66
4.11	Discussion	68
4.12	Conclusions and outlook	69
5	Momentum maps of molecular semiconductors at equilibrium	71
5.1	Anatomy of momentum maps	72
5.2	Momentum maps of similar states in different materials	74
5.3	Molecular orbitals with different symmetries	75
5.4	Momentum maps at different crystal momenta	76
5.5	Band tail states and localization	77
5.6	Momentum maps and band structure	78
5.7	Discussion	78
6	Orbital-resolved observation of singlet exciton fission	81
6.1	Introduction	81
6.2	Experimental setup: pentacene	82

6.3	Results	83
6.3.1	Momentum maps	83
6.3.2	Photoemission transitions	85
6.3.3	Projecting to the orbital character	86
6.3.4	Evolution at longer delays	89
6.4	Discussion	92
6.5	Conclusion	94
7	Different pathways of endothermic singlet exciton fission	95
7.1	Introduction	95
7.2	Singlet exciton fission in tetracene single crystals.	97
7.2.1	Experiment and Results	98
7.2.2	Discussion	100
7.3	Singlet exciton fission in rubrene single crystals	102
7.3.1	Experiment and Results	103
7.3.2	Dynamics in the valence states	105
7.3.3	Discussion	105
7.4	Conclusion	106
8	Summary and outlook	109
8.1	Summary	109
8.2	Conclusions	111
8.3	Outlook and future work	111
	Supplement	115
	Data availability and code usage	119
	Bibliography	121



Zusammenfassung

Diese Arbeit beschreibt experimentelle Untersuchungen der fluktuationsdominierten elektronischen Struktur von molekularen Halbleitern und der Exzitonendynamik in denselben Materialien. Die in dieser Arbeit verwendete Methode ist die zeit- und winkelaufgelöste Photoemissionsspektroskopie.

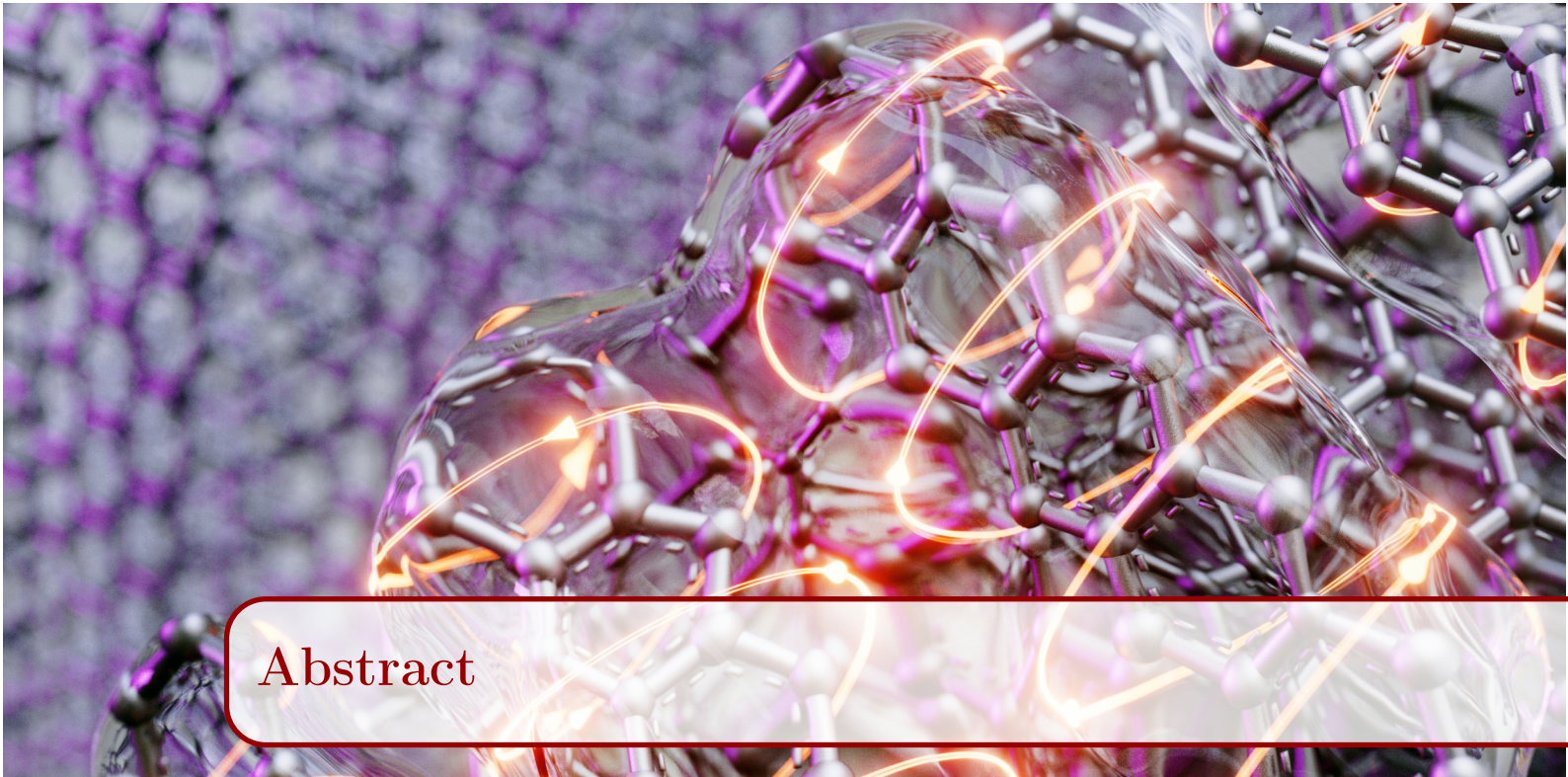
Im ersten Teil wird die elektronische Struktur von molekularen Halbleitern im Gleichgewichtszustand betrachtet. Dort wird gezeigt, dass die experimentelle Bandstruktur mehrerer repräsentativer Molekülkristalle mit einem gemeinsamen Tight-Binding-Modell beschrieben werden kann und es wird analysiert, wie sowohl die Kristallstruktur als auch die π -Topologie die elektronische Struktur beeinflussen. Mithilfe dieser konsistenten Beschreibung der elektronischen Zustände wird diskutiert, wie Fluktuationen auf verschiedene Materialien wirken und wie sie die Ladungstransporteigenschaften beeinflussen. Diese Überlegungen führen zu nicht-trivialen Konstruktionsregeln für zukünftige Materialien mit hoher Ladungsträgermobilität, die unabhängig in Ladungstransportexperimenten verifiziert wurden.

Das folgende Kapitel befasst sich mit der räumlichen Struktur der elektronischen Zustände, die im Impulsraum erfasst werden. Durch Anwendung des zuvor etablierten Tight-Binding-Modells wird eine enge Verbindung zwischen der Anatomie der im Impulsraum aufgenommenen Bilder, d.h. Schnitte bei konstanter Energie durch die dreidimensionale Photoemissionsintensität, der elektronischen Struktur und der Beschreibung der Elektronen im Realraum als Bloch-Zustände hergestellt. Es wird auch diskutiert, ob Eigenschaften, die durch Fluktuationen entstehen, in den Impulsraumbildern sichtbar sind. Vor allem aber liefert dieser Teil die Grundlage für die Interpretation von den im Impulsraum aufgenommenen Bildern von Grund- und angeregten Zuständen.

Im zweiten Teil wird die Exzitonendynamik in denselben Molekülkristallen analysiert, die im vorherigen Teil dargestellt wurden. Für Pentacen-Einkristalle haben wir die ersten im Impulsraum aufgenommenen Bilder von Singulett- und Triplett-Exzitonen erhalten. Diese zeigen den vorhergesagten, aber nie experimentell beobachteten, ähnlichen Orbitalcharakter und die unterschiedlichen Lokalisierungseigenschaften der beiden Exzitonarten, und die

Bilder ermöglichen es, die Singulett-Exzitonenspaltung in noch nie dagewesenem Detail zu untersuchen. Frühere experimentelle Ergebnisse deuteten auf eine sofortige, kohärente Anregung eines Bitriplett-Zwischenzustands hin. Mit Hilfe der Exziton-Impulsraumbilder konnten wir die Dynamik auf den Orbitalcharakter der zugrunde liegenden Zustände projizieren und so nachweisen, dass Bitriplett-Zustände nicht unmittelbar angeregt werden, sondern durch einen ladungstransfervermittelten Übergang vom photoangeregten Singulett-Exziton entstehen. Damit ist der durch Ladungstransfer vermittelte Mechanismus des ersten Schritts der Singulett-Exzitonenspaltung nachgewiesen.

Das letzte Kapitel beschreibt die beobachtete Exzitonendynamik in Rubren- und Tetracen-Einkristallen, in denen die Singulett-Exzitonenspaltung endotherm ist. Die Messungen zeigen, dass die im Impulsraum aufgenommenen Bilder in Tetracen denen des strukturellen Cousins Pentacen sehr ähnlich sind. Die Dynamik unterscheidet sich jedoch erheblich. Wie zeigen, dass ein Schlüssel zum Verständnis der Singulett-Exzitonenspaltung in der relativen Energie und der Kopplungsstärke der Ladungstransferzustände liegt. In Tetracen stabilisieren die Ladungstransferzustände den Bitriplett-Zustand; dies erleichtert die ultraschnelle Erzeugung des Bitriplett-Exzitons, verlangsamt aber seine Aufspaltung in zwei unabhängige Triplett-Exzitonen, die in 6 pSekunden erfolgt. Schließlich wird gezeigt, dass die Spaltung von Singulett-Exzitonen in Rubren aufgrund der hochsymmetrischen Kristallstruktur, die eine Kopplung zwischen Bitriplett- und Ladungstransferzuständen verhindert, einen anderen Weg nimmt. Daher wird das gespaltene Bitriplett-Exziton direkt aus dem Singulett erzeugt, ohne die Beteiligung von Ladungstransferzuständen. Abschließend werden die möglichen Mechanismen eines ultraschnellen, aber energetisch steil ansteigenden Prozesses erörtert, der die Notwendigkeit von Theorien unterstreicht, die sowohl Fluktuationen als auch die Exzitonendynamik behandeln können.



Abstract

This work describes experimental studies of the fluctuation-dominated electronic structure of molecular semiconductors and of the exciton dynamics in the same materials. The method employed in this thesis is time- and angle-resolved photoemission spectroscopy.

In the first part, the electronic structure of molecular semiconductors at equilibrium is considered. We show that the experimental band structure of several representative molecular crystals can be described with a common tight-binding model and analyze how both the crystal structure and the π -topology impact the electronic structure. With this consistent description of the electronic states, it is discussed how fluctuations act on different materials and how they impact charge transport properties. These deliberations lead to non-trivial design rules for future materials with high charge mobilities that have been independently verified in charge transport experiments.

The subsequent chapter concerns the spatial structure of the electronic states captured in momentum space. By applying the previously established tight-binding model, a strong connection between the anatomy of momentum maps, i.e., constant-energy cuts through the photoemission intensity, the electronic structure, and the real space description of electrons as Bloch states is built up. It is also discussed whether properties arising from fluctuations are visible in these maps. Most importantly, this part provides the basis for interpreting momentum maps of ground and excited states.

In the second part, we analyzed the exciton dynamics in some of the same compounds that staged in the previous part. For pentacene single crystals, we obtained the first momentum maps of singlet and triplet excitons. These demonstrate the predicted, but never observed, similar orbital character and different localization properties of the two states and the images allow to study singlet exciton fission in unprecedented detail. Previous experimental results pointed to an instantaneous, coherent excitation of an intermediate bitriplet state. Using the exciton momentum maps, the dynamics could be projected to the orbital character of the underlying states and which proves that bitriplet states are not instantaneously excited, but rather created by a charge-transfer mediated transition from

the photoexcited singlet exciton. That establishes the charge-transfer mediated mechanism of the primary step of singlet exciton fission.

The last chapter describes the observed exciton dynamics in rubrene and tetracene single crystals, where singlet exciton fission is endothermic. We find that the momentum maps in tetracene are highly similar to those of the structural cousin pentacene. However, the dynamics differ substantially. We demonstrate that one key to understanding singlet exciton fission lies in the relative energy and the coupling strength of the charge-transfer states. In tetracene, the charge-transfer states stabilize the bitriplet state; that facilitates the ultrafast < 200 fs creation of the bitriplet exciton but slows down its separation into two independent triplet excitons which occurs in 6 ps. Lastly, it is shown that singlet exciton fission in rubrene takes a different path due to the highly symmetric crystal structure which prohibits a coupling between bitriplet and charge-transfer states. Hence, the separated bitriplet exciton is directly created from the singlet without the involvement of charge-transfer states. We conclude by discussing the possible mechanisms of an ultrafast, but energetically steeply uphill, process, which highlights the need for theories that are able to treat both fluctuations and exciton dynamics.



Acknowledgements

Ah, time flies; you look at the calendar and realize you have spent a good five years counting electrons. The work that I did would not have been possible without quite a number of people whom I want to thank here.

Ralph, thank you for giving me the opportunity to work with an amazing team of scientists and a truly cutting-edge technique. Thank you also for the trust you put in me in providing the freedom to pursue my own research goals and become an independent researcher. You won me over by driving me to the train station in that old family caravan to still catch the train after a first meeting at the institute. I really enjoyed the last minute thrill before the DPG post-deadline session and the creativity we put into selling and telling the singlet fission story.

Laurenz, on an uncountable number of occasions I was impressed by your intricate knowledge about every small part of the trARPES setup. That is absolutely crucial to make the experiments work, especially in the myriad situations where something unexpected goes wrong.

Tommaso, how could I ever forget fishing in vacuum together after another dropped sample? Science would not be as much fun without the joy and humour that should go along with it and that you embody for me.

Sam, thank you for initiating me to the lab and guiding me on the first steps. A lot of the work I did was a continuation of your initial experiments and ideas. In science, it really is true that you stand on the shoulders of your peers.

Shuo, without your magic hands with the laser, my work would not have been possible, thank you for lending a magic hand from time to time.

Hélène, thank you for your calm and profound scientific advice and ideas. I believe you will have a great future at the FU.

I thank Patrick for building up the pipeline to convert the momentum microscope data to workable data sets.

To the cool kids, Marie, Ivana, Reza and Stefano, I can't wait to dance together again.

I am indebted to Martin Wolf for providing the superior infrastructure necessary to conduct cutting-edge measurements and for fostering a diverse and family-friendly environment.

This is to my flat mates, Johannes, Tali, Makan, Nora and Rick, for the best community I could think of and for an endless pool of ideas and laughter, especially at the backdrop of a pandemic. No matter where I end up next, the Nolle memories won't ever leave me.

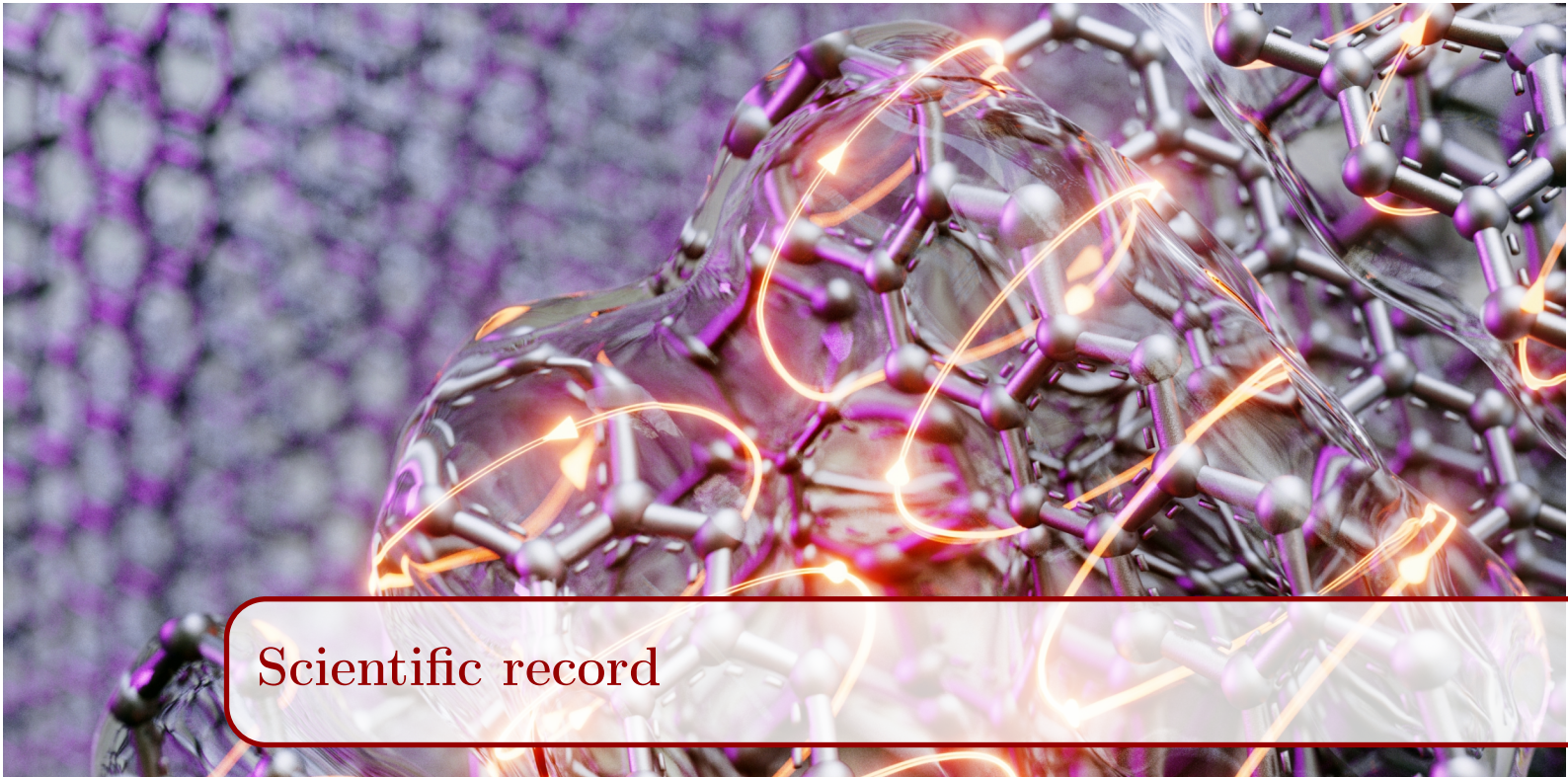
To my collaborators in Würzburg, Sebastian Hammer and Jens Pflaum, who not only provided world class single crystals but also great input in discussing the publications.

To the rest of topfloor scientists, I really enjoyed the open and collaborative atmosphere.

To the PC staff, thank you for being there whenever support was needed (especially with my accident!) and all the work that you are doing in the background.

To my late Mensa group, Dory, Richarda, Double Max and Michael for fun and great discussions at lunch.

To the members of the sustainability group, especially Sina and Ines, I thoroughly enjoyed campaigning for a more sustainable institute with you. We have achieved quite something and even more is to be done. May the bees thrive and the solar panels glow in the sun.



Scientific record

Publications in peer-reviewed journals

*Papers relevant to the content of this thesis are marked with with an *.*

S. Beaulieu, J. Schusser, S. Dong, M. Schüler, T. Pincelli, M. Dendzik, J. Maklar, **A. Neef**, H. Ebert, K. Hricovini, M. Wolf, J. Braun, L. Rettig, J. Minár, and R. Ernstorfer, “Revealing Hidden Orbital Pseudospin Texture with Time-Reversal Dichroism in Photoelectron Angular Distributions”, *Phys. Rev. Lett.* **125**, 216404 (2020).

D. Peller, C. Roelcke, L. Z. Kastner, T. Buchner, **A. Neef**, J. Hayes, F. Bonafé, D. Sidler, M. Ruggenthaler, A. Rubio, R. Huber, and J. Repp, “Quantitative sampling of atomic-scale electromagnetic waveforms”, *Nat. Photonics* **15**, 143–147 (2021).

- This work has been featured in a News and Views article by Jun Takeda and Ikufumi Katayama: [Waveform sampling on an atomic scale](#)

S. Beaulieu, M. Schüler, J. Schusser, S. Dong, T. Pincelli, J. Maklar, **A. Neef**, F. Reinert, M. Wolf, L. Rettig, J. Minár, and R. Ernstorfer, “Unveiling the orbital texture of 1T-TiTe₂ using intrinsic linear dichroism in multidimensional photoemission spectroscopy”, *npj Quantum Mater.* **6**, 1–11 (2021).

J. Maklar, R. Stühler, M. Dendzik, T. Pincelli, S. Dong, S. Beaulieu, **A. Neef**, G. Li, M. Wolf, R. Ernstorfer, R. Claessen, and L. Rettig, “Ultrafast Momentum-Resolved Hot Electron Dynamics in the Two-Dimensional Topological Insulator Bismuthene”, *Nano Lett.* **22**, 5420–5426 (2022).

***A. Neef**, S. Beaulieu, S. Hammer, S. Dong, J. Maklar, T. Pincelli, R. P. Xian, M. Wolf, L. Rettig, J. Pflaum, and R. Ernstorfer, “Orbital-resolved observation of singlet fission”, *Nature* **616**, 275–279 (2023).

- This work has been featured in a News and Views article by Andrew J. Musser and Hannah Stern: [Elusive excited states identified from cutting-edge molecular movies](#)

***A. Neef**, M. Rossi, M. Wolf, R. Ernstorfer, and H. Seiler, "On the Role of Nuclear Motion in Singlet Exciton Fission: The Case of Single-Crystal Pentacene", *Phys. Status Solidi A* **n/a**, 2300304 (2023).

S. Dong, S. Beaulieu, M. Selig, P. Rosenzweig, D. Christiansen, T. Pincelli, M. Dendzik, J. D. Ziegler, J. Maklar, R. P. Xian, **A. Neef**, A. Mohammed, A. Schulz, M. Stadler, M. Jetter, P. Michler, T. Taniguchi, K. Watanabe, H. Takagi, U. Starke, A. Chernikov, M. Wolf, H. Nakamura, A. Knorr, L. Rettig, and R. Ernstorfer, "Observation of ultrafast interfacial Meitner-Auger energy transfer in a Van der Waals heterostructure", *Nat. Commun.* **14**, 1–8 (2023).

***A. Neef**, S. Beaulieu, S. Hammer, S. Dong, T. Pincelli, A. Krueger, M. Wolf, L. Rettig, J. Pflaum and R. Ernstorfer, "How to cool electronic disorder in molecular semiconductors", *Under review at Adv. Mat.* (2023).

Contributions at scientific conferences

DPG-Frühjahrstagung des Fachverbandes Oberflächenphysik, Virtual event, 01.03. - 04.03.2021, Poster: "Observing Singlet Fission in Time-Energy-Momentum Space"

International Conference on Photochemistry, Virtual event, 19.07. - 23.07.2021, Poster: "Observing Singlet Fission in Time-Energy-Momentum Space"

734. WE-Heraeus-Seminar "Photoemission Tomography: Applications and Future Developments", Bad Honnef am Rhein (Germany), 24.10 - 27.10.2021, Poster: "Orbital-resolved observation of singlet fission"

- This contribution was awarded with the Best Poster Prize.

Winter School on Ultrafast Processes in Condensed Matter, Winklmoosalm (Germany), 13.03 - 18.03.2022, Talk: "Orbital-resolved observation of singlet fission"

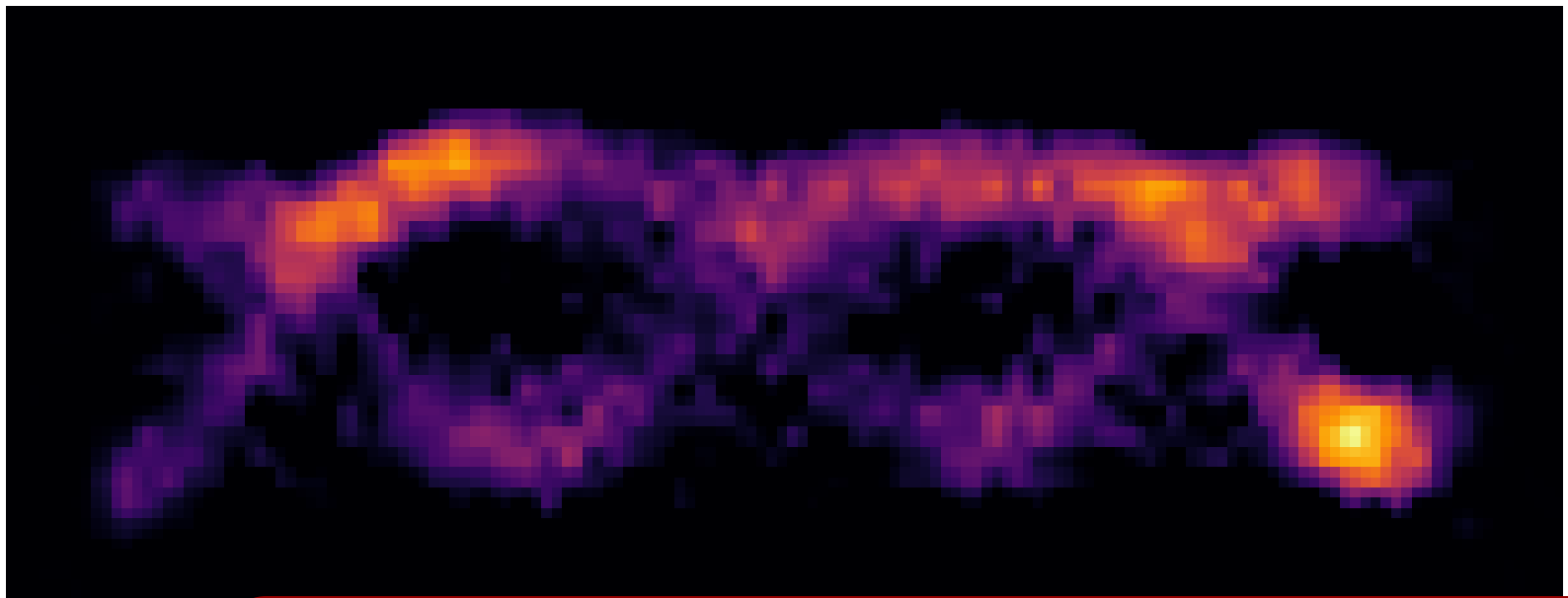
International Conference on Molecular Ultrafast Science and Technology, Grindelwald (Switzerland), 07.06. - 10.06.2022, Talk: "Orbital-resolved observation of singlet fission"

Electronic Processes in Organic Materials Gordon Research School and Conference, Lucca (Italy), 25.06. - 01.07.2022, Poster: "Orbital-resolved Observation of Singlet Fission"

- This contribution was awarded with the Best Poster Prize.

Published research data

***A. Neef**, S. Beaulieu, S. Hammer, S. Dong, J. Maklar, T. Pincelli, R. P. Xian, M. Wolf, L. Rettig, J. Pflaum, and R. Ernstorfer, "Orbital-resolved observation of Singlet Fission" [Data set]. [Zenodo](#) (2023).



1. Introduction

It's very easy to answer many of these fundamental [...] questions: you just look at the thing!

There's plenty of room at the bottom
Richard P. Feynman

Any young student of science will inevitably stumble upon a marvelous equation. Born out of the mind of a man who, far out in the Swiss mountains, was pondering how the newest scientific findings about the microscopic world could be built into a common theoretical framework. In this time of crisis for science, no model existed that could explain the intricate quantization rules found in the elements or the series of lines observed in atomic spectra. Therefore, it is no wonder that these years, in the early 1920s, were full of new ideas, one of which our pondering man caught on: de Broglie's revolutionary idea that particles, and specifically electrons, can be seen as waves of matter. Building on that notion, he realized that quantization rules are a natural outcome of the wave viewpoint. The electron waves could be understood as strings stretched between the ends of an atom, and the number of nodes in the resulting standing wave as a quantum number. In his own words, the breakthrough was to realize that *the atom, in reality, is merely the diffraction phenomenon of an electron wave captured as it were by the nucleus of the atom* [1]. His insight led him to postulate the Schrödinger equation $H\Psi = E\Psi$, with the Hamiltonian H and the electron wave function Ψ . It was published in a series of four articles, all titled *Quantization as an eigenvalue problem* in 1926 [2]. Only seven years later, Erwin Schrödinger was awarded the Nobel Prize for his contribution to the development of quantum mechanics.

His equation was so successful because it solved the puzzle of the atomic spectra and provided an intuitive explanation of the quantization rules found in the periodic table. The agreement between new theoretical predictions and spectroscopic observations, apparent in the transition energies between two states, was remarkable. The energy eigenvalues that allow us to calculate the transition energies are, however, only one result of the solution

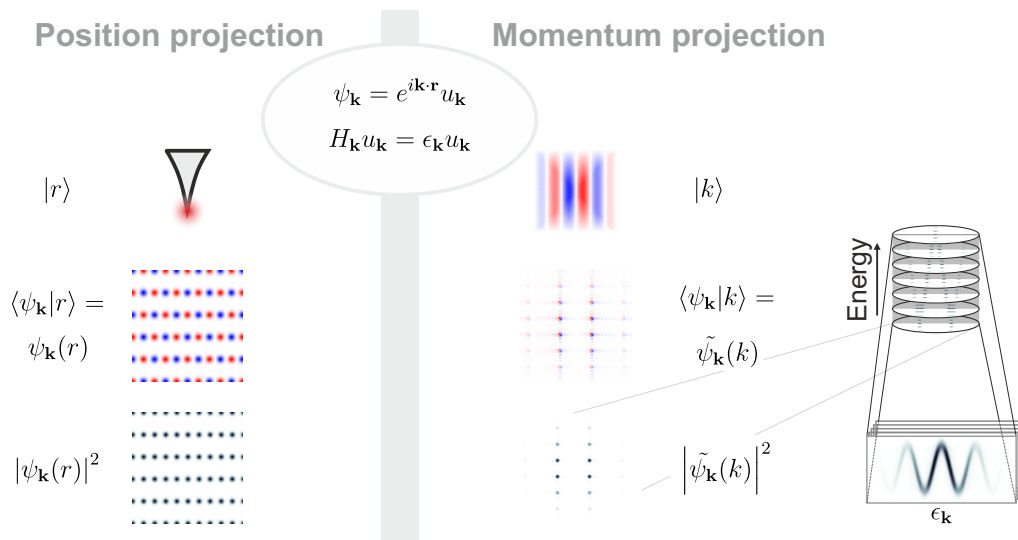


Figure 1.1. Imaging one-electron wave functions with position and momentum probes. In the solid state, electronic states can be cast as Bloch waves. The corresponding Schrödinger equation acts on the periodic function $u_{\mathbf{k}}$, whose energy eigenvalues are the function $\epsilon_{\mathbf{k}}$, commonly known as the band structure. Projecting Bloch waves onto position or momentum states yields its real and reciprocal space forms, respectively. Position projection can be achieved with a δ -like point probe that scans the surface, e.g., in a scanning tunneling microscope. The measured quantity is the absolute square of the projection. Momentum projection, on the other hand, is possible with plane-wave states, that is, with free electrons. One technique that can achieve momentum projection is angle-resolved photoemission spectroscopy. Again, the observable is the absolute square of $\langle\psi_{\mathbf{k}}|k\rangle$. By recording $|\langle\psi_{\mathbf{k}}|k\rangle|^2$ at different kinetic energies, one obtains the band structure $\epsilon_{\mathbf{k}}$, here shown as a slice through the image stack. Thus, momentum projection offers simultaneous access to the spatial structure of one-electron states and their energy eigenvalues.

of the eigenvalue problem, that is, the Schrödinger equation — the other result is the eigenfunction, or wave function, itself. In the early days of quantum mechanics and a prolonged period following it, the concept of a wave function proved extremely helpful in solving a vast array of problems in physics and chemistry. However, it could not be observed in its own right and thus remained a mysterious object.

Orbitals and images.

Today, a chemist learning quantum mechanics encounters the Schrödinger equation but, most likely, quickly works within a powerful approximation. One learns to speak the language of one-electron molecular orbitals laid out by Mulliken and others [3]. The orbitals, especially those close to the Fermi level known as frontier orbitals, dictate the path of chemical reactions [4] and are extremely useful for chemical analysis — and, most importantly, they allow us to visualize the "housing arrangement" of electrons [3].

Given the ability to visualize the orbitals in calculations and see them in science classrooms, one is intrigued to wonder whether such images can be obtained with an experimental technique instead. That dream is already a reality: today, scientists can routinely capture images of orbitals with, e.g., scanning tunneling microscopy.

How is it possible to do a "microscopy" of orbitals? The fundamental principle behind any observation lies in projecting the orbital to a suitable basis state (see Fig. 1.1). Different basis states either allow a projection to the position or the momentum of the orbital. Scanning tunneling microscopy, on the one hand, works by projecting to the position with the "position state" $|r\rangle$ of an idealized δ -like tip. On the other hand, momentum projection

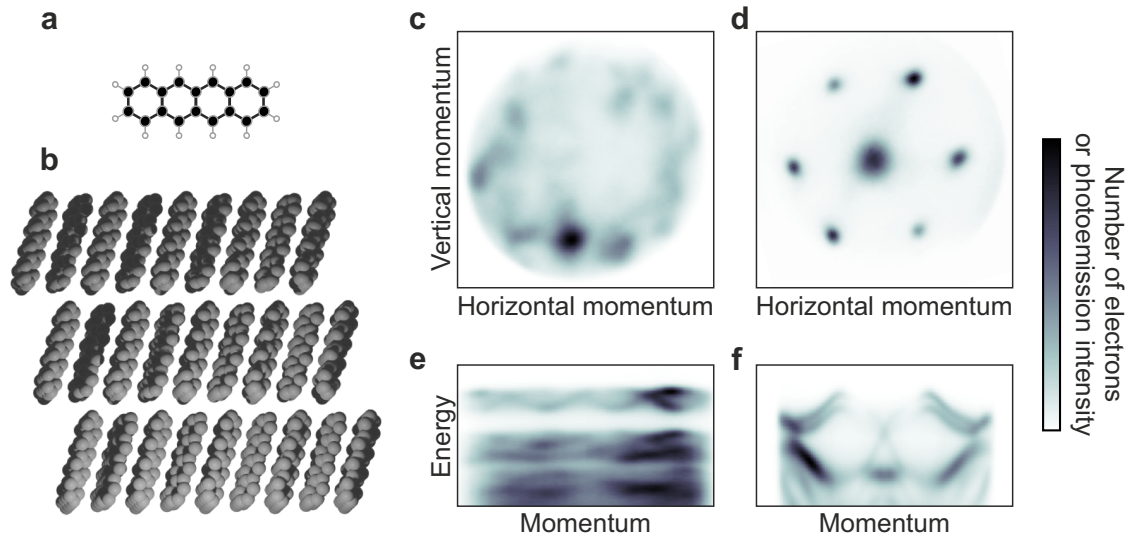


Figure 1.2. Structure of a molecular semiconductor and momentum images of electronic states of a molecular and a conventional semiconductor at equilibrium. **a**, Molecular structure of tetracene, a typical molecular semiconductor, and **b**, the layered arrangement of the molecules in its crystal structure. **c**, Constant-energy cut, or *momentum map*, through the three-dimensional photoemission intensity at the valence band maximum of a pentacene single crystal and **d**, of bulk WSe₂. **e**, Momentum slice through the photoemission intensity of pentacene and **f**, of bulk WSe₂ highlighting the electronic bands. The energy and momentum scales are the same in all images. Data of bulk WSe₂ taken by Shuo Dong (unpublished).

is achieved by angle-resolved photoemission spectroscopy; here, an idealized plane-wave "momentum state" $|k\rangle$ of a free photoelectron serves as the basis state. The observable in both cases is the absolute square of the orbital, and the phase of the wave function is therefore lost in the measurement. Going one step back, each of these methods *counts electrons* which have a certain probability of ending up in a given position or momentum state — in line with Born's statistical interpretation of the wave function.

Eigenvalues and the band structure.

In the above, we were concerned with an eigenstate at a single energy. We can gain even more information when browsing the energy of our basis state, which effectively corresponds to measuring orbitals at different energy levels. When a stack of these images are gathered in momentum space, the data contains the material's band structure $\epsilon_{\mathbf{k}}$ which can be obtained by slicing through it along certain high-symmetry paths. These energy stacks are naturally recorded with angle-resolved photoemission spectroscopy, and so is the band structure. This technique hence "images the Schrödinger equation": it provides simultaneous information about the eigenvalues and eigenstates that result from solving the Schrödinger equation for a material. However, there are some limitations. One primary requirement is that each electron count must originate from a system in the same condition and be independent of each other. The system has to regenerate before the next successful projection, which is the case for many solid-state systems. In chapter 3, I introduce the fundamental concepts underlying angle-resolved photoemission spectroscopy.

The materials at the focus of this work are molecular semiconductors, which are certain types of organic molecules that form well-structured crystals (Fig. 1.2a and b). To appreciate the variety of the electron "houses", or orbitals, arising from the particular structure of a molecular and a conventional semiconductor, momentum images taken for two representatives of those materials are shown in Fig. 1.2. Note the disordered versus ordered

appearance, which is rooted in the unique features of these materials. A general description of the electronic structure of molecular semiconductors will be given in chapter 2.

Disorder and localization.

The band structure theory of solids is based on one fundamental assumption: the atomic structure of the materials appears the same when moving by a unit vector of the crystal, a property known as translational invariance. When impurities are mixed into the crystal or its constituents subject to random displacements, this assumption breaks down, and band structure theory ceases to be appropriate. Anderson realized that disorder might lead to a localization of the eigenstates [5]. His work was concerned with amorphous systems such as alloys and expanded on by Mott, who analyzed the transport properties of non-crystalline materials [6]. Anderson emphasized in his Nobel lecture that *a random system is to be treated not as just a dirty regular one, but in a fundamentally different way* [7]. Recently, localization concepts have been introduced to molecular semiconductors where the disorder stems from thermal fluctuations of the molecules. These concepts play an essential role in understanding charge transport properties [8]. In chapter 4, the origin of the disorder in molecular semiconductors is discussed, and how future materials might be made resilient to disorder. Following this analysis, I discuss whether the eigenstates' localization is visible in the orbitals' momentum images in chapter 5.

Beyond orbitals.

Orbitals are *one-electron* wave functions and, therefore, inherently lack a description of the correlation present in real systems. Imagine two correlated electrons; the energy of the first strongly depends on its relative position to the second electron. Projecting the first electron to a plane wave might "catch" it when it is close or far away from the second one. That influences the energy of the outgoing plane wave and, therefore, the recorded momentum images — a direct feature of electron correlation that goes beyond the orbital picture.

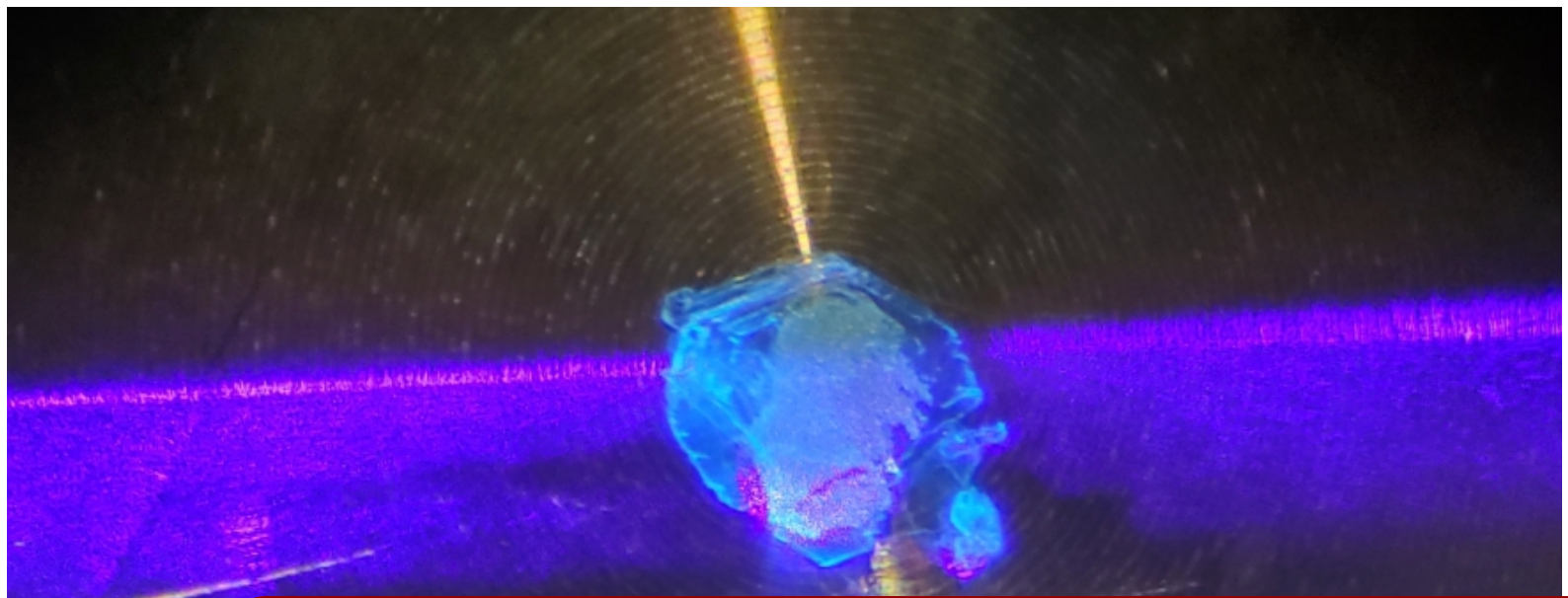
Going out of equilibrium.

The electron correlation might be an inherent feature of the equilibrium state of a system, but it can also be created in non-equilibrium states of weakly-correlated materials. An exciton presents a widely-known example of a correlated non-equilibrium state. In general, non-equilibrium states are more challenging to observe experimentally since they only exist for short periods, and to treat theoretically. However, it is possible to image non-equilibrium states today by exploiting the stroboscopic principle in pump-probe experiments. The non-equilibrium state is launched by a trigger (pump), and some delay time afterward, a camera with an extremely short shutter time (probe) images the state — one thus obtains a snapshot. Even in everyday experiences, such snapshots provide new insights, such as the picture of the stunning coronet created when a drop of milk splashes [9]. By varying the delay time, one obtains a slow-motion picture of the process. In time- and angle-resolved photoemission spectroscopy, the momentum images are combined with the stroboscopic principle, and thus, slow-motion momentum movies of electron dynamics can be obtained.

Splitting an exciton.

In chapters 6 and 7, I used time- and angle-resolved photoemission spectroscopy to image the excitons in molecular semiconductor single crystals and to study their dynamics. These systems feature a pronounced energy gap between the lowest singlet and triplet excitons, a gap large enough to transition from one singlet exciton to two triplet excitons in a process known as singlet exciton fission. Due to the carrier multiplication intrinsic to exciton fission, it has been proposed as a means to circumvent the maximum efficiency limit of silicon photovoltaics [10, 11]. Despite extensive research, the mechanism of singlet exciton

fission remains heavily debated, especially regarding the involvement of the so-called charge-transfer states and nuclear motion. With the help of momentum images of the excitons, some of these questions are resolved for exothermic in chapter 6 and for endothermic singlet exciton fission in chapter 7. From the combined results and the underlying theoretical understanding, a consistent picture of singlet exciton fission emerges in the end.

A photograph of a small, irregularly shaped crystal of a molecular semiconductor. The crystal is illuminated from above by a bright yellow laser beam, which creates a vertical streak of light. The crystal itself glows with a blue and purple luminescence. The background is dark, with some faint horizontal lines of light, possibly from a microscope or other experimental setup.

2. Physics of molecular semiconductors

This chapter introduces the basic electronic and optoelectronic properties of crystalline molecular semiconductors. We start by describing the physical regime of molecular semiconductors on the basis of a few transparent effective parameters. Then, we work our way through the electronic structure of the constituent molecules and how electrons couple to the electric field and vibrations. Equipped with that knowledge, we investigate the properties that arise when packing the molecules into a crystal. We show that the crystalline order is heavily perturbed in molecular semiconductors due to the large fluctuations of the molecules and discuss how the ensuing disorder changes the electronic states. By conducting numerical simulations, we show how the disorder induces localization. Then, we describe the excitons of crystalline molecular semiconductors and how they can interconvert through singlet exciton fission.

In contrast to most conventional semiconductors, molecular semiconductors are fragile and soft materials with low melting points. They do, however, have similarities justifying the common name: they are intrinsically bad conductors and have band gaps around 1 to 3 eV. Charge transport can be activated by different means, e.g., by overcoming the band gap with visible light thus inducing photoconductivity [12] or by doping the material. A major difference, however, is that charge carriers find it much harder to move through molecular semiconductors than through conventional semiconductors. This leads to much smaller charge carrier mobilities ($1 \text{ V cm}^{-2} \text{ s}^{-1}$ in typical molecular semiconductors vs. $1000 \text{ V cm}^{-2} \text{ s}^{-1}$ in purified crystalline semiconductors). A part of this discrepancy comes from the highly purified and defect-free composition of conventional semiconductors with impurity levels below 10^{-10} compared to much higher levels around 10^{-4} in molecular semiconductors [13], thus increasing the chance of a carrier to scatter on a defect. Not only extrinsic disorder but also intrinsic disorder is present in molecular semiconductors, which arises from the motion of molecules in the soft lattice. As electronic disorder leads to the localization of carriers [5], the electronic states in molecular semiconductors behave much differently than the Bloch states of crystalline inorganic materials. Taken together, the

properties of molecular semiconductors are so different that, according to Troisi *et al.*, *the analogy with standard semiconductor physics is of limited use* [14].

Light is strongly absorbed in molecular semiconductors. The strong light-matter interaction enables much thinner active layers for light-emitting or photovoltaic devices since the absorption coefficient in these materials ($\alpha \sim 1 \times 10^5 \text{ cm}^{-1}$) is much higher than for example in the indirect semiconductor silicon ($\alpha \sim 1 \times 10^3 \text{ cm}^{-1}$) and similar to monolayers of transition metal dichalcogenides. The strong absorption has been a driver for adopting organic materials in light-emitting diodes (OLED), which today dominate smartphone displays [15]. A unique feature of molecular semiconductors is their low-lying triplet excited states. These provide undesirable decay channels and are thus detrimental to the performance of OLEDs. However, they also allow for unique processes such as converting optically excited singlet states into two triplet states, known as singlet exciton fission [16].

2.1 The physical regime of molecular semiconductors at room temperature

Molecular semiconductors are characterized by a periodic arrangement of aromatic molecules held together by weak intermolecular forces. The adhesion is granted by several interactions with the strongest being the van-der-Waals dispersion interaction. There is furthermore the quadrupole-quadrupole interaction, whose strength depends sensitively on the intermolecular arrangement. Due to the sensitivity to the relative position, it is often the quadrupole-quadrupole interaction that determines the geometry of a molecular packing — despite the isotropic dispersion force often contributing a greater overall attraction [17]. The proximity of the molecules in a crystal packing leads to electronic overlap between their orbitals. Due to the small intermolecular interactions, the crystals inherit many properties from their building blocks. The separation of *intra-* and *intermolecular* forces into different regimes that can be treated separately is a prominent feature of the physics of molecular semiconductors. This approximation dramatically reduces the complexity both for the electron and nuclear degrees of freedom. It allows treating molecular orbitals as being unperturbed by neighboring molecules. It is well justified by the much more substantial overlap between *p*-orbitals of neighboring carbon atoms within a molecule than between the *p*-orbitals of carbon atoms on different molecules. This order of magnitude difference is quantified by the transfer integral. For two *p_z*-orbitals on different sites *A* and *B* it takes the form [18]

$$t = \langle p_z^A | H | p_z^B \rangle = \langle p_z^A | \frac{\nabla^2}{2} - \sum_i \frac{Z_i}{r_i} | p_z^B \rangle,$$

where the one-electron Hamiltonian *H* accounts for the kinetic energy of the electron and its attraction to the nuclei with index *i*. The carbon-carbon π -bond transfer integral t_{cc} is $\approx 2.7 \text{ eV}$, whereas the intermolecular transfer integral is $\approx 0.1 \text{ eV}$ [19].

Furthermore, we may divide the vibrations into intra- and intermolecular parts, where the latter are called phonons¹. In the context of lattice dynamics, this is known as the *rigid-body approximation* [20, 21]. It finds its justification in the much stronger restoring forces within the molecules and thus also the larger energies of intramolecular vibrations $\hbar\omega \sim 100 \text{ meV}$. The phonons are then treated as translations and rotations of rigid molecules and are found at much lower energies $\hbar\omega \sim 10 \text{ meV}$.

Electronic transitions, either by charge injection or an optical transition, are accompanied by a response of the nuclei. This magnitude of this electron-phonon coupling is

¹This is true for rigid molecules like pentacene. However, in molecules with flexible side groups such as rubrene, intra- and intermolecular motion are mixed in some phonons.

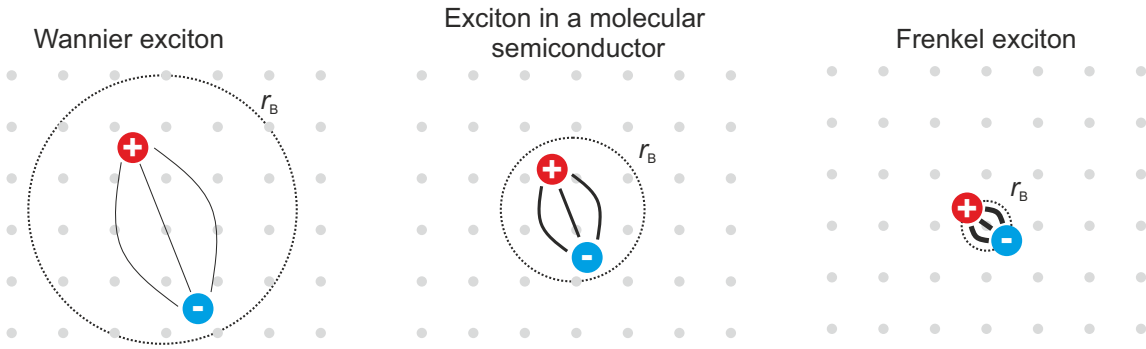


Figure 2.1. Types of excitons. In Wannier excitons (found, e.g., in gallium arsenide), electrons and holes are far apart from each other and weakly bound to each other. They have a large Bohr radius r_B . If electrons and holes are strongly bound and localized to a single or very few sites, the corresponding exciton is called a Frenkel exciton (found, e.g., in sodium chloride). Excitons in molecular semiconductors are in between these two extreme cases.

commonly quantified by the reorganization energy λ . In line with the separation between intra- and intermolecular phonons, we can distinguish electron-phonon coupling arising from intramolecular motion, called Holstein or local coupling, and the coupling arising from intermolecular motion, referred to as Peierls or non-local coupling. The local coupling is directly apparent in the vibrational satellites in photoemission or optical spectra. To differentiate the reorganization upon these two different electronic transitions, one distinguishes the *hole reorganization energy* appropriate for photoemission and *exciton reorganization energy* appropriate for optical transitions.

Electronic states of crystalline materials are described within the band theory of solids. In the *tight-binding approximation*, the molecules contribute molecular orbitals that overlap with neighboring orbitals to form extended states with well-defined momenta. This description relies on one fundamental assumption: the system is invariant to translations. It has limitations for molecular semiconductors because of large thermal fluctuations of the constituent molecules. At room temperature (RT, $T = 298$ K), the thermal energy $k_B T = 26$ meV is sufficient to significantly populate the phonons, and the molecules correspondingly fluctuate substantially around their equilibrium positions. Since the intermolecular transfer integrals strongly depend on the relative arrangement of two molecules, the position fluctuations translate into fluctuations of the transfer integrals. The distribution of the transfer integrals can be parametrized by a Gaussian distribution with the standard deviation σ_t . At RT, the latter is of the same order of magnitude as the transfer integrals themselves [22], thus breaking the translational invariance. To obtain a more complete description of the localized electrons in molecular semiconductors, a treatment of the electronic disorder is necessary.

The states created by the absorption of photons across the optical band gap are referred to as excitons. They are commonly introduced as the weakly bound and delocalized Wannier and the firmly bound and localized Frenkel excitons. In molecular semiconductors, the excitons are between those extreme cases (see Fig. 2.1). They retain a sizeable intramolecular character but also spread out among several molecules due to the involvement of *charge-transfer* exciton states. The size of the exciton depends on its spin state due to the strong intramolecular electron-hole exchange interaction which stabilizes intramolecular triplet over singlet excitons. Hence, singlet excitons are generally more delocalized than triplet excitons. An intriguing process in which both exciton species play a role is *singlet exciton fission*. Here, a singlet exciton with energy E_S splits into two triplet excitons with roughly

Symbol	Magnitude	Description
t	100 meV	Intermolecular transfer integral
λ_h	50 meV	Intramolecular hole reorganization energy [20]
σ_t	50 meV	Standard deviation of the transfer integrals at RT
$\hbar\omega$	130 meV	Vibrational energy of the intramolecular C-C ring-breathing mode
$k_B T$	26 meV	Thermal energy at RT
λ_{ex}	100 meV	Intramolecular exciton reorganisation energy [23]

Table 2.1. Parameters that define the physical regime of crystalline molecular semiconductors at room temperature.

half the energy $2E_T \lesssim E_S$. The process involves a multiexcitonic state, the bitriplet exciton, that serves as an intermediate on the route to independent triplet excitons.

The physical regime of molecular semiconductors is thus characterized by several parameters of the same order of magnitude (see table 2.1). To understand the physics, it is instructive to start from the bottom up and thus with the properties of individual molecules.

2.2 Properties of the constituting molecules

The molecules considered in this work are benzenoid hydrocarbons, made up entirely of carbon and hydrogen atoms. The carbon atoms are arranged in a planar hexagonal lattice akin to the familiar structures of benzene and graphene (Fig. 2.2a). For a description of their electronic states, we consider only the interaction between nearest neighbors, quantified by the transfer integral $t_{cc} \approx 2.7 \text{ eV}$ [19]. A general and important property of hexagonal lattices is their bipartite nature. The carbon atoms in a hexagonal lattice can be arranged into two sets (A and B) that occupy alternating sites. These sets only have connections to the other set, and there are no AA - or BB -connections. The simplest tight-binding Hamiltonian of benzenoid hydrocarbons neglects differences in diagonal on-site energies ϵ_i and electron-electron interactions and is thus [19]

$$H = -t_{cc} \sum_{\langle i,j \rangle} [c_i^\dagger c_j + \text{h.c.}], \quad (2.1)$$

where the sum is over the set of all nearest neighbors $\langle i, j \rangle$ and c^\dagger and c are the creation and annihilation operators, respectively. The energy eigenvalues resulting from diagonalization then span a range of $6t_{cc} \sim 15 \text{ eV}$. The electronic levels are only half filled since each carbon atom only contributes a single π -electron. As consequence of the bipartite lattice, the levels exhibit electron-hole symmetry, that is, for each bonding and occupied state with energy $-\varepsilon$, there is a corresponding antibonding and unoccupied state with energy ε (Fig. 2.2b).

The eigenvectors ϕ are linear combinations of p_z -orbitals centered on the atomic positions \mathbf{R}_i of the two sets A and B

$$\phi(\mathbf{r}) = \sum_i [c_i^A p_z(\mathbf{r} - \mathbf{R}_i^A) + c_i^B p_z(\mathbf{r} - \mathbf{R}_i^B)], \quad (2.2)$$

where the coefficients c_i are obtained by the diagonalization of the Hamiltonian in equation 2.1. Furthermore, the eigenvectors of states related by electron-hole symmetry can be obtained from each other by changing the sign of the coefficients of one set of atoms. The reader is referred to [19] for an illuminating discussion.

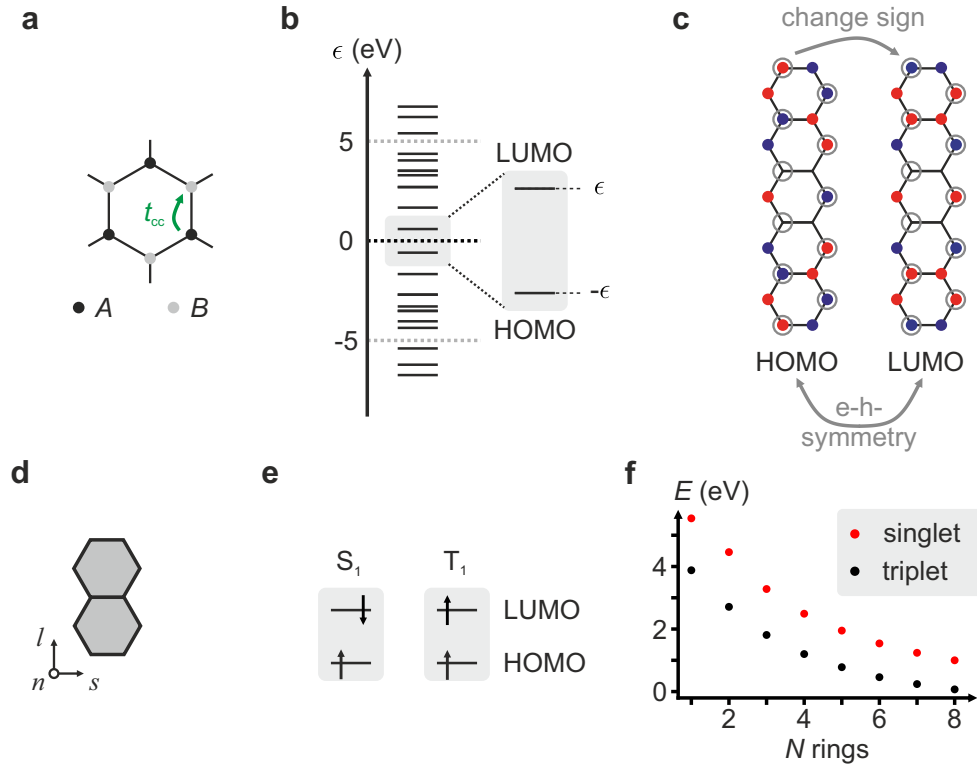


Figure 2.2. Hexagonal lattice, electronic structure of benzenoid hydrocarbons and electronic transitions. **a**, Benzenoid hydrocarbons form hexagonal lattices and can be divided into two alternating sets of atoms A and B . **b**, Energy spectrum of pentacene, a representative MSC exhibiting electron-hole symmetry. **c**, The frontier orbitals of pentacene are related by e-h-symmetry. Hydrogen atoms are not shown for clarity. **d**, Electron configurations of singlet (S_1) and triplet excitons (T_1). **e**, Dependence of the exciton energy on the number of rings in the polyacenes (pentacene is $N = 5$). Data from [24] obtained with UB3LYP/6-31G* for the triplets and TDDFT for the singlets.

We are most interested in the energy levels that separate occupied and unoccupied states since these determine the electrical and optical properties. The most relevant orbitals are the highest-lying molecular orbital (HOMO) and the lowest-lying unoccupied molecular orbital (LUMO), termed frontier orbitals. These orbitals are related by electron-hole symmetry and can be generated from each other by the sign-change rule stated above (Fig. 2.2c). Commonly, the benzenoid hydrocarbons used for MSCs have HOMO-LUMO gaps ranging from the near-infrared to the upper end of the visible spectrum (1–3 eV).

The electronic dipole transition rate w between two states is proportional to the absolute square of the matrix element between initial states $|i\rangle$ and final states $|f\rangle$ [25]

$$w_{fi} \propto \left| \langle i | \hat{p} \cdot \hat{E} | f \rangle \right|^2, \quad (2.3)$$

where \hat{p} is the dipole operator and \hat{E} the electric field vector. Since the dipole operator $\hat{p} = e\hat{R}$ with the separation between two opposite charges \hat{R} is odd, the two states connected by the transition must be odd for a dipole-allowed transition. In benzenoid hydrocarbons, the HOMO and LUMO are of different symmetry due to electron-hole symmetry, and the corresponding transition is therefore always dipole-allowed.

At this point, it is helpful to define a molecular coordinate system, as shown in Fig. 2.2d. The molecules discussed in this work have clearly distinguishable normal (n), short (s),

and long (l) axes. Acenes, that is, benzenoid hydrocarbons that consist of linearly fused hexagons, are at the core of this work and have a transition dipole moment along s for the lowest excitonic transition, that is, the HOMO-LUMO transition.

The resulting excitons are of the Frenkel type, confined to a single molecule, and are firmly bound (~ 1 eV) compared to free electron-hole pairs. As we will see in section 2.7, these localized states are essential for describing excitons in crystalline molecular semiconductors. In benzenoid hydrocarbons, the exchange interaction can significantly stabilize triplet excitons over singlet excitons. Their electronic configurations are shown in Fig. 2.2e.

In the acenes, both excitons decrease in energy for a larger number of rings [24] in line with a diminishing band gap, and the splitting between the two also dips from 2 eV for two rings to 1 eV for seven rings (Fig. 2.2f). The reason for the latter is a diminishing exchange integral that separates singlet from triplet states [18]. In general, electron-electron interactions are smaller in systems with delocalized electrons. They scale as $1/N$, where N is the number of sites over which the state is delocalized. The inherently greater mean distance between two electrons in delocalized states is the origin of the weaker interaction. The large exchange splitting allows for a peculiar situation in some acenes. In tetracene (four rings) and pentacene (five rings), the triplet exciton has roughly half the energy of the singlet exciton. When going to even larger acenes, the trend shows that the triplet exciton will be at negative energies for a certain number of rings and thus be the ground state. Recent studies confirm a substantial ground state triplet character for acenes with more than six rings [26].

Upon an electronic transition, the molecules relax from their initial geometry in the ground electronic state towards a new geometry. This process is accompanied by the release of the *reorganization energy* λ into vibrational modes of the molecules. The coupling between electrons and nuclei manifests itself as vibronic progressions that accompany electronic transitions in optical or photoemission spectroscopy. When an electronic transition is triggered, the molecule finds itself in a new potential energy surface (Fig. 2.3a). In the simplest scenario, a single mode $\hbar\omega_i$ dominates the relaxation to the potential minimum. Signatures of the excitation of this mode are visible as vibronic progressions (see Fig. 2.3b), that are given by a Poisson distribution [27]

$$I_n = \frac{S_i^n}{n!} e^{-S_i}, \quad (2.4)$$

where I_n is the intensity of the n th peak and S_i the Huang-Rhys factor. The Huang-Rhys factor and the reorganization energy are related by

$$S_i = \frac{\lambda_i}{\hbar\omega_i}$$

The response of the nuclei is mainly within the carbon backbone and therefore a C-C stretching mode at $\hbar\omega \approx 170$ meV dominates the vibronic coupling in benzenoid hydrocarbons (Fig. 2.3c) and in graphene (Fig. 2.3d) [28, 29].

Generally, benzenoid hydrocarbons have small reorganization energies ($\lambda \sim 100$ meV) relative to most molecules because of the rigidity of their backbone [20]. The reorganization energy decreases even further with increasing number of π -electrons as $1/N_\pi$ [27, 30] (Fig. 2.3e). More delocalized electrons lead to a smaller perturbation of the nuclei, which we can see directly by formulating the electron-phonon coupling differently. The Huang-Rhys factor defined above can be thought of as the number of phonons associated with the reorganization. It is related to other formulations of the electron-phonon coupling [20]

$$S_i = \frac{\lambda_i}{\hbar\omega_i} = g_i^2 = \frac{(\partial\epsilon_{\text{HF}}/\partial Q_i)^2}{2M_i\hbar\omega_i^3}, \quad (2.5)$$

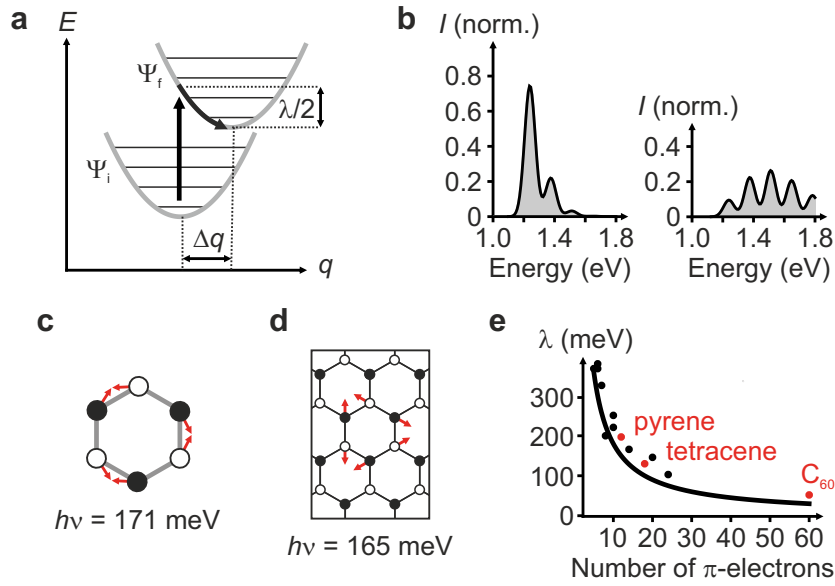


Figure 2.3. Vibronic coupling in molecules. **a**, Electronic transition between two states. In a semiclassical picture, the nuclei move down the parabolic potential of the final state. In the full quantum mechanical picture, the transition excites vibrational quanta. The so-called normal coordinate q is commonly used in chemistry literature to denote a generalized displacement from equilibrium. **b**, Simulated absorption spectrum of an electronic transition with the same vibrational frequency ($\hbar\nu = 170$ meV) but different reorganization energies (up: $\lambda = 100$ meV, down: $\lambda = 800$ meV). The upper curve is typical for electronic transitions in BHs. **c**, C-C stretching mode in benzene [31]. **d**, The A'_1 phonon mode at K in graphene [32, 33] also known as ring-breathing mode. The displacement vectors are only shown for six atoms for clarity. **e**, Dependence of the reorganization energy on the number of π -electrons. The data points show LDA calculations for several molecules, and the solid line is a $1/N_\pi$ fit. Data taken from [30].

where g_i is the dimensionless electron-phonon coupling, ϵ_{HF} is the Hartree-Fock energy, Q_i is a normalized coordinate, and M_i is the reduced mass. Importantly, for an individual mode i , $\lambda_i \propto (\partial\epsilon_{\text{HF}}/\partial Q_i)^2$ from which we get the total reorganization energy by summing over all modes. The total reorganization energy can be brought to a slightly different form by invoking the Einstein approximation. We replace the nuclear modes i with a single mode with an average frequency $\sum_i \hbar\omega_i/N_i$, where N_i is the number of modes. The reorganization energy is now $\lambda = \sum_\alpha \lambda_\alpha \propto (\partial\epsilon_{\text{HF}}/\partial u_\alpha)^2$, with the displacement u of an individual atom α [30]. If the states are delocalized over N atoms, each atom will only feel a fractional charge e/N and each individual term λ_α will vary as $1/N^2$. By summing over all N atoms, we are left with $\lambda \propto 1/N$. In systems with delocalized electrons, such as graphene or graphite, the reorganization energies are hence much smaller, $\lambda \sim 3$ meV [29], than typical values of ~ 100 meV in finite molecules.

2.3 Crystal structure and electronic states

Benzenoid hydrocarbons attract each other by the van-der-Waals or dispersion interaction and can condense into a crystalline state, a *molecular crystal*. In general, crystals of nonpolar molecules, like the benzenoid hydrocarbons, will adopt the densest possible packing, thus maximizing attractive van-der-Waals and quadropole-quadropole interactions. The quadropole of these molecules is visualized in Fig. 2.4a. Often, the quadropole-quadropole attraction is apparent in the crystal structure, e.g., as stable slipped parallel dimers or a T-like arrangement (the hydrogen atoms on the edge of one molecule lie on the π -electrons

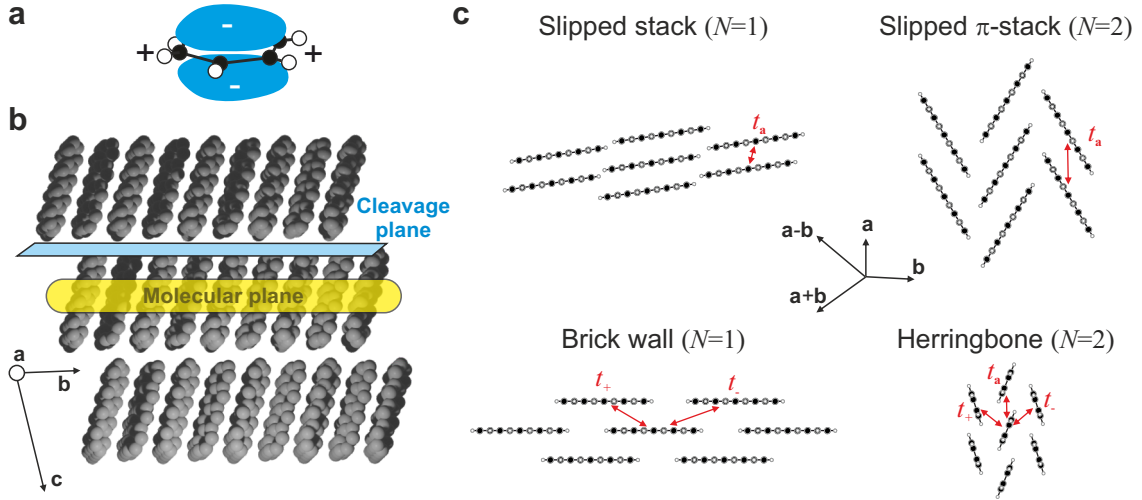


Figure 2.4. Crystal structure and nearest neighbors. **a**, Visualization of the electric quadrupole of a benzene molecule. The π -electron cloud is negatively charged and the hydrogen atoms positively. **b**, Crystal structure of tetracene (herringbone packing), highlighting the layered structure with well-defined cleavage and molecular planes. Crystal structure data from [35]. **c**, Common packing motifs in crystalline molecular semiconductors. In the slipped stack, slipped π -stack, and the brick wall, the short molecular axis s is normal to the cleavage plane. In the herringbone packing, the long axis l is roughly normal to the cleavage plane. The packings differ in the number of molecules per unit cell N and the number of nearest neighbors with which each molecule overlaps strongly. The latter leads to anisotropic interactions and different numbers of large transfer integrals t . Adapted from [34].

at the face of its neighbor) [17]. Due to the weak cohesive forces, molecular crystals break easily, and the force constants for intermolecular motion are small, thus leading to large displacements of the molecules. The crystal structures are generally categorized by a low triclinic and sometimes orthorhombic symmetry of their unit cell. They are determined by the three unit vectors (in ascending length) \mathbf{a} , \mathbf{b} and \mathbf{c} . Commonly, the crystals adopt layered structures, allowing for a natural cleavage plane (Fig. 2.4b) — usually the \mathbf{ab} -plane. The occurring crystal structures can be categorized into different *packing motifs*. The most prominent are the slipped stack, the slipped π -stack, the brick wall, and the herringbone packing (Fig. 2.4c) [34]. In each of these, the molecules have six nearest neighbors within the cleavage plane, separated by roughly 4 Å. This short distance allows for $\pi\pi$ -overlap between the molecular orbitals of nearest neighbors, whereas the overlap with other neighbors is negligible. Following the preceding discussion on the separation between intra- and intermolecular electronic states, we can adopt a purely intermolecular model to describe the electronic states in molecular semiconductors. This general tight-binding model is based on a distorted triangular lattice and includes the interactions with the two neighbors along $\frac{\mathbf{a}+\mathbf{b}}{2}$, the two along $\frac{\mathbf{a}-\mathbf{b}}{2}$, and the two along \mathbf{a} . These pairs of neighbors are equivalent due to inversion symmetry. We denote the three transfer integrals occurring due to molecular overlap as t_+ , t_- , and $t_{\mathbf{a}}$, respectively (see Fig. 2.5). We consider the case of a single molecular orbital and write the Hamiltonian in the basis of this orbital as

$$H_{\mathbf{k}} = \sum_i c_i^\dagger c_i (\epsilon + 2t_{\mathbf{a}} \cos \mathbf{k} \cdot \mathbf{a}) + \sum_{\langle i,j \rangle} [c_i^\dagger c_j + \text{h.c.}] t_{ij} e^{i\mathbf{k} \cdot \delta_{ij}}, \quad (2.6)$$

where ϵ is the on-site energy, the first sum runs over all inequivalent molecules in the unit cell, and the second sum runs over all nearest neighbors, separated by the vector δ_{ij} . Note that compared to the intercarbon transfer integrals of p_z -orbitals, the intermolecular

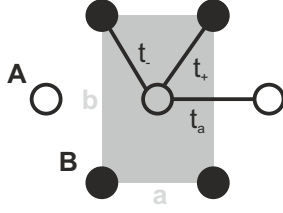


Figure 2.5. Tight-binding model for molecular semiconductors. Simplified model of a molecular semiconductor with two molecules per unit cell (**A**, **B**) and six nearest neighbors.

transfer integrals are smaller by a factor of 30. We can denote the Hamiltonian for the common case of two inequivalent molecules per unit cell, each supplying one molecular orbital ϕ_A and ϕ_B :

$$H_{\mathbf{k}} = \begin{pmatrix} h_0 & h_1 \\ h_1 & h_0 \end{pmatrix} \quad (2.7)$$

$$= \begin{pmatrix} \epsilon + 2t_a \cos \mathbf{k} \cdot \mathbf{a} & 2(t_+ \cos \mathbf{k} \cdot \frac{\mathbf{a}+\mathbf{b}}{2} + t_- \cos \mathbf{k} \cdot \frac{\mathbf{a}-\mathbf{b}}{2}) \\ 2(t_+ \cos \mathbf{k} \cdot \frac{\mathbf{a}+\mathbf{b}}{2} + t_- \cos \mathbf{k} \cdot \frac{\mathbf{a}-\mathbf{b}}{2}) & \epsilon + 2t_a \cos \mathbf{k} \cdot \mathbf{a} \end{pmatrix}. \quad (2.8)$$

Diagonalizing this Hamiltonian yields the two electronic band branches

$$\varepsilon_{\pm}(\mathbf{k}) = \epsilon + 2t_a \cos \mathbf{k} \cdot \mathbf{a} \pm 2 \left(t_+ \cos \mathbf{k} \cdot \frac{\mathbf{a} + \mathbf{b}}{2} + t_- \cos \mathbf{k} \cdot \frac{\mathbf{a} - \mathbf{b}}{2} \right). \quad (2.9)$$

A crucial property of this TB model is the dependence of the transfer integrals on the relative position of neighboring molecules. Thus, different band structures emerge for different relative positions, caused, e.g., by thermal displacements and slightly different crystal structures. From the packing motifs in Fig. 2.4c, it is clear that the transfer integrals vary significantly for different neighboring pairs — that is, the overlap is much larger for certain nearest neighbors than for others. In the slipped stack and the slipped π -stack, the interaction along \mathbf{a} is much stronger than along the other two directions, leading to an almost one-dimensional band structure. The number of strongly interacting neighbors grows in the brick wall packing to four and in the herringbone packing to six.

By diagonalizing equation 2.8, we get the infinitely extended Bloch orbitals $\psi_{\mathbf{k}}(\mathbf{r})$ of the perfect crystal. We have to reconsider our description of the periodic system briefly. The form of the Hamiltonian 2.8 separates intra- and intercell degrees of freedom. It only depends parametrically on the crystal momentum \mathbf{k} . Two different terms then modulate the coefficients of the molecular orbitals ϕ_A and ϕ_B . The intra-cell degree of freedom is captured by the Wannier function, in which the molecular orbitals are combined to yield $w_{\mathbf{k}} = c_A^{\mathbf{k}}\phi_A + c_B^{\mathbf{k}}\phi_B$, with the coefficients $c_A^{\mathbf{k}}$ and $c_B^{\mathbf{k}}$ that depend on the crystal momentum \mathbf{k} . The coefficients are obtained by diagonalizing the Hamiltonian in eq. 2.8. The intercell degree of freedom involves the combination of Wannier functions in different unit cells situated on the lattice sites \mathbf{R}_n . The coefficients are given by a plane wave $e^{i\mathbf{k}\cdot\mathbf{R}_n}$. A Bloch orbital of the crystal is then written as

$$\psi_{\mathbf{k}}(\mathbf{r}) = \frac{1}{\sqrt{N}} \sum_n e^{i\mathbf{k}\cdot\mathbf{R}_n} w_{\mathbf{k}}(\mathbf{r} - \mathbf{R}_n) = \frac{1}{\sqrt{N}} \sum_n e^{i\mathbf{k}\cdot\mathbf{R}_n} \left[c_A^{\mathbf{k}}\phi_A(\mathbf{r} - \mathbf{R}_n) + c_B^{\mathbf{k}}\phi_B(\mathbf{r} - \mathbf{R}_n) \right]. \quad (2.10)$$

In chapter 4, we will analyze the electronic states in more detail.

For a molecular crystal with two molecules per unit cell (such those that form a slipped π -stack or a herringbone packing), twelve phonon branches originate from the six degrees of

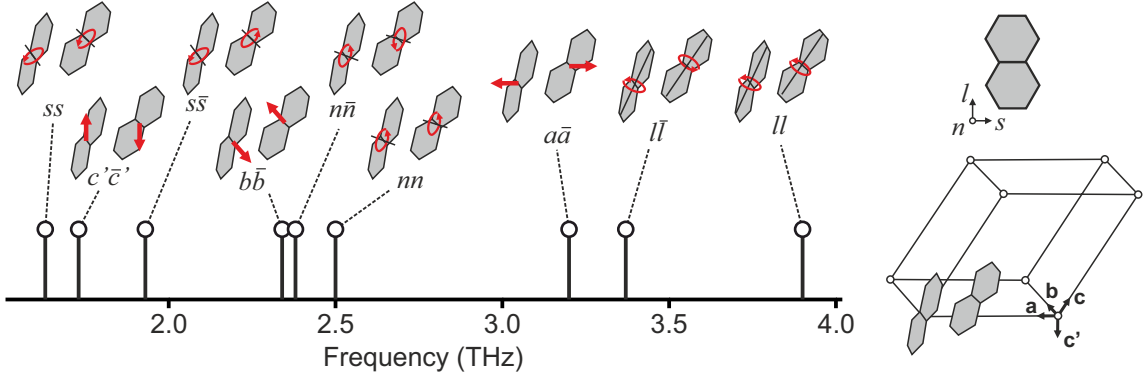


Figure 2.6. Phonons in molecular semiconductors. Displacement vectors and frequencies for the nine optical phonons in crystalline naphthalene at the Γ -point. Six phonons involve translational motions, while the remaining three are translational displacements. The indices for each phonon denote the crystal axes (a, b, c') and the molecular axes (n, l, s). A bar on one axis (e.g., $a\bar{a}$) indicates out-of-phase motion. Adapted from [36].

freedom of each molecule. Of these twelve, six branches involve translational motion, and the other six involve rotational motion. The motions associated with these phonons are depicted in Fig. 2.6, sorted by ascending frequencies at the Γ -point. Due to the weak van-der-Waals forces, the phonon frequencies are small compared to intramolecular vibrations and lie in the range 1 to 4 THz [36]. The translational motions occur along the crystal axes \mathbf{a} , \mathbf{b} , and along $\mathbf{c}' = \mathbf{a} \times \mathbf{b}$. They are either in-phase, leading to acoustic branches, or out-of-phase, leading to optical branches. With the molecular axes introduced previously, we can categorize the rotational motions. The axes of rotation pass through the center of mass and align with the normal axis n , the short axis s , and the long axis l [36]. Again, we distinguish in-phase and out-of-phase motion, yielding the six rotational branches. The thermal energy $k_B T = 26$ meV at room temperature is larger than the highest phonon frequencies ($4 \text{ THz} \approx 15$ meV) and the phonons therefore highly populated. The corresponding motions are substantial, as we can quickly evaluate by invoking the thermal populations of a classical harmonic oscillator (an approximation that is valid in the high-temperature limit $k_B T \gg \hbar\omega$). We get for the standard deviation σ_r of the motion along a specific direction r [37]:

$$\sigma_r = \sqrt{\frac{2k_B T}{M\omega^2}}. \quad (2.11)$$

At room temperature, with the mass of a tetracene molecule $M = 228$ Da and the frequency $f = 1$ THz, we get for the displacement $\sigma_r = 0.23$ Å which agrees well with experimentally measured values [38].

2.4 Electron-phonon coupling in the crystal

In molecular semiconductors, we face two different electron-phonon coupling mechanisms¹: (1) intramolecular vibrations that couple to the on-site energy ϵ , called Holstein, diagonal or local coupling, and (2) intermolecular vibrations that couple to the transfer integrals t , called Peierls, off-diagonal or non-local coupling. Before we discuss these two mechanisms, we recapture some general properties of the treatment of phonons.

Due to the generally small displacements of the atoms or molecules with respect to the bonding dimensions, we adopt the harmonic approximation and neglect non-linear

¹Note that we use the term electron-phonon coupling as a synonym for vibronic coupling.

or anharmonic coupling [39]. Furthermore, we exploit that electrons have much smaller masses and, therefore, much higher velocities than the nuclei ($m_p \approx 10^4 m_e$). We can then separate the electronic (\mathbf{r}) and nuclear (\mathbf{R}) degrees of freedom by factorizing the total wave function [40]

$$\Psi_{\text{total}}(\mathbf{r}, \mathbf{R}) = \Psi_{\text{el}}(\mathbf{r})\Psi_{\text{nuc}}(\mathbf{R}).$$

For any instantaneous nuclear configuration, the electrons are in their ground state, and the electronic Schrödinger equation only depends parametrically on the nuclear coordinates

$$H_{\text{el}}^{\mathbf{R}}(\mathbf{r})\Psi_{\text{el}}(\mathbf{r}) = E_{\text{el}}^{\mathbf{R}}\Psi_{\text{el}}(\mathbf{r}). \quad (2.12)$$

That is the Born-Oppenheimer or adiabatic approximation. Solving equation 2.12 for different nuclear configurations then yields potential energy surfaces $E_{\text{el}}(\mathbf{R})$ on which the nuclei move [40]. As long as the gap between two electronic states is large compared with the frequency of excited phonons in the system $\Delta E \gg \hbar\omega$, the adiabatic approximation can be employed [41]. We will discuss some possible breakdowns of the adiabatic approximation in the context of singlet exciton fission.

An expression for Holstein coupling has already been given in equation 2.5, which we derive here with the approximations above for a single vibrational mode. We have an electronic ground state $|0\rangle$ whose minimum is located at $Q = 0$ and its potential energy surface is $\epsilon_0(Q) = \frac{M\omega^2}{2}Q^2$ (compare Fig. 2.3b). The minimum of the excited state $|1\rangle$ is displaced by ΔQ . Its potential energy surface is $\epsilon_1(Q) = \frac{M\omega^2}{2}(Q + \Delta Q)^2 + \Delta\epsilon$, where we have also assumed that the normal modes of the excited state are the same as for the ground state and $\Delta\epsilon$ is the energy difference at the potential minima. We can now determine the Holstein reorganization energy upon a vertical transition (Franck-Condon principle) from $|0\rangle$ to $|1\rangle$ as

$$\lambda_{\text{H}} = \epsilon_1(0) - \epsilon_1(-\Delta Q) = \frac{M\omega^2\Delta Q^2}{2} = \frac{(\partial\epsilon/\partial Q)_{Q=0}^2}{2M\omega^2}.$$

We then get the dimensionless Holstein electron-phonon coupling

$$g_{\text{H}} = \sqrt{\frac{\lambda_{\text{H}}}{\hbar\omega}} = \frac{(\partial\epsilon/\partial Q)_{Q=0}}{\sqrt{2M\hbar\omega^3}}.$$

Similarly, we can derive the electron-phonon coupling for a Peierls mechanism where the on-site energy is replaced by the transfer integral t and the intramolecular coordinate Q by the intermolecular coordinate \mathbf{R} [20]

$$g_{\text{P}} = \sqrt{\frac{\lambda_{\text{P}}}{\hbar\omega}} = \frac{(\partial t/\partial \mathbf{R})_{\mathbf{R}=0}}{\sqrt{2M\hbar\omega^3}}. \quad (2.13)$$

These expressions emphasize the similarity of the two mechanisms. However, intramolecular vibrations are roughly ten times faster than phonons and are not substantially populated at room temperature.

From equation 2.13, we deduce that the derivative of the transfer integral with respect to a molecular displacement at the equilibrium position is the quantity that determines the strength of Peierls coupling. How, then, do the transfer integrals depend on the intermolecular displacement? We will discuss this for a cofacial alignment of two tetracene molecules, see Fig. 2.7. The transfer integral connecting the molecular orbitals ϕ_A and ϕ_B is then given by

$$t(\mathbf{R}) = \int d\mathbf{r}\phi_A(\mathbf{r} - \mathbf{R})h\phi_B(\mathbf{r}), \quad (2.14)$$

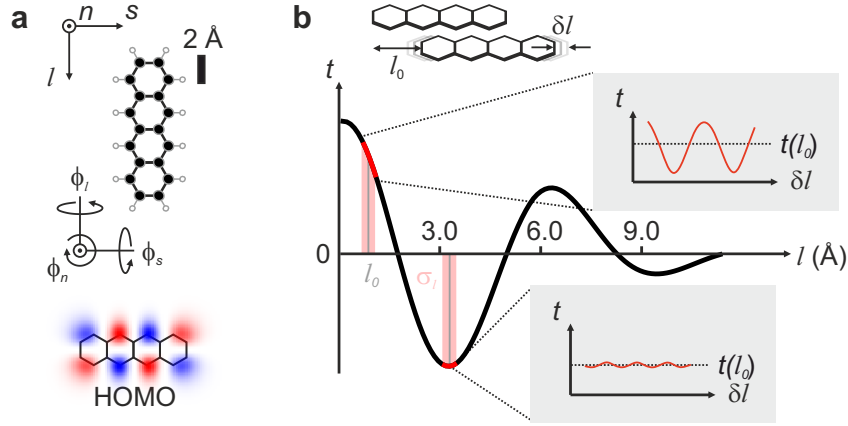


Figure 2.7. Mechanism of transfer integral fluctuations. **a**, Molecular structure of tetracene, a typical molecular semiconductor with normal (n), long (l) and short (s) axis and the corresponding rotations ϕ_i . **b**, Schematic dependence of the transfer integral t on the long-axis displacement l for the tetracene HOMO. Thermal movement δl leads to fluctuations of the transfer integral. The magnitude of the transfer integral fluctuations depend on the derivative $\partial t/\partial l$ at the equilibrium position l_0 and the magnitude of the position fluctuations σ_l .

where h is the one-particle Hamiltonian [18]. In Fig. 2.7b, we show the dependence of the transfer integral of the HOMO in a face-on tetracene dimer on an intermolecular displacement along the long molecular axis l . When comparing the $t(l)$ curve with the structure of the molecular orbital, it is apparent that its nodal structure determines the shape of the curve (i.e., there are as many nodes in the transfer integral curve as in the molecular orbital). Consequently, the derivative of the transfer integral curve $\partial t/\partial l$, shown in Fig. 2.7c, has large values at the zero crossings and vanishes at the extremal points. Therefore, apart from determining magnitude and sign of the transfer integrals, the equilibrium offset between two molecules also fixes the strength of electron-phonon coupling.

With the value for the standard deviation of the long axis displacement at room temperature $\sigma_r = 0.23 \text{ \AA}$ determined from equation 2.11, we can get a rough estimate of how much the transfer integrals themselves fluctuate. Since the thermal displacements are still small compared to the length of a molecule, we can retain only the linear term in the dependence of the transfer integral on the displacement [8]. This yields

$$\sigma_t = \sigma_r \left| \left(\frac{\partial t}{\partial r} \right)_{r=r_0} \right|.$$

We take the two exemplary positions: (1) no displacement, i.e., $l = 0 \text{ \AA}$ and (2) a displacement just up to the zero crossing, i.e., $l \approx 1.5 \text{ \AA}$. In case (1), $\sigma_t = 0 \text{ meV}$ and $t = 200 \text{ meV}$, whereas in case (2), $\sigma_t = 50 \text{ meV}$ and $t = 0 \text{ meV}$. The comparison of these values highlights the range of values that the dimensionless electronic disorder $\sigma = \frac{\sigma_t}{t}$ can take. In case (1), $\sigma = 0$, and in case (2) $\sigma = \infty$, indicating that essentially any value for the electronic disorder is achievable for different relative positions of the molecules in the crystal.

2.5 Limitations of band theory

In the most prominent crystalline molecular semiconductors, the electronic disorder at room temperature is $\sigma = 0.3 - 0.5$ [34]. The electronic disorder manifests not in a periodic modulation of the transfer integrals but leads to random distributions of their values. The

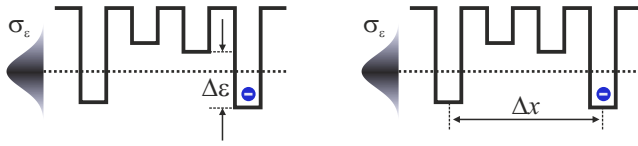


Figure 2.8. Origin of localization for disordered on-site energies ϵ . Nearby sites have different energies, and sites with degenerate energy are far apart.

electronic disorder in molecular semiconductors is large enough to break the assumption of translational invariance [22]. Applying band theory to describe both the electronic states and the coupling to phonons is, therefore, of dubious validity. While some insights might be gained from the dispersion relation, describing the electrons as being completely delocalized is certainly an oversimplification. Many simulations [22, 42–44] and experiments [45–47] have shown that the electrons are localized to a finite number of molecules. We, therefore, need to include electronic disorder and, hence, localization in the description of the physics of molecular semiconductors.

2.6 Localization and disorder

The crystalline, i.e., perfectly periodic, state is an idealization: real systems feature at least some degree of disorder. Nonetheless, for various systems, describing deviations from periodicity as mere perturbations of the crystalline state proves incredibly powerful [48]. The perturbation acts as a source of scattering, which restricts the movements of particles to within a mean free path. Anderson showed in 1958 that such a description becomes invalid at large enough strengths of the electronic disorder [5]. The electrons are then not infinitely extended but relatively localized, and one has to include a *localization length* L to describe their wave functions. We hence introduce an envelope F_{env} function, here centered at the origin, to the Bloch orbitals in equation 2.10:

$$\psi_{\mathbf{k}}(\mathbf{r}) = \sum_n e^{i\mathbf{k}\cdot\mathbf{R}_n} w_{\mathbf{k}}(\mathbf{r} - \mathbf{R}_n) F_{\text{env}}(\mathbf{R}_n). \quad (2.15)$$

Anderson used an exponential form of the envelope function $F_{\text{env}}(\mathbf{R}) = e^{-\frac{|\mathbf{R}|}{L}}$ [48], but other forms may be used as well.

The original idea of localization was developed for disordered semiconductors or alloys, where a random occupation of the sites by different atoms leads to a disorder of the on-site energies ϵ . This disorder can be quantified by its distribution, which we consider Gaussian with a standard deviation σ_ϵ . We briefly discuss the origin of localization, following [48]. If an electron is on a single site, the surrounding sites have different energies due to random fluctuations. The mixing between these sites is inversely proportional to their energy difference $\frac{1}{\Delta\epsilon}$ and will thus be small for large disorder, see Fig. 2.8. At the same time, there might be states of degenerate energy, but these will be far away for a large enough disorder, and hence, the overlap and mixing between the degenerate sites is small. Because the mixing with nearby sites is small, the electron is localized. In the extreme case of large disorder, every particle is localized — leading to the fundamental result that transport in the system becomes impossible.

A model that considers static disorder of ϵ is appropriate to describe disordered conventional semiconductors, but the situation is quite different in crystalline molecular semiconductors. Here, thermal fluctuations of the molecules are the leading cause of disorder, and it is the transfer integrals that are affected by nuclear motion. If we consider the system at a given moment in time, the situation will appear rather different sometime later (say 10 ps, so several oscillation periods of the phonons). The disorder is, therefore, dynamic.

It is instructive to do a brief check on which magnitude of disorder is necessary to induce localization. We investigate a real space realization¹ of the tight-binding Hamiltonian (see eq. 2.6), but set the transfer integrals to the value t for all nearest neighbors. To introduce disorder, each transfer integral is modulated by the term δt_{ij} and the Hamiltonian then is:

$$H = \sum_{\langle i,j \rangle} [c_i^\dagger c_j + \text{h.c.}] (t + \delta t_{ij}) \quad (2.16)$$

$$P(\delta t) = \frac{1}{\sigma\sqrt{2\pi}} \exp\left(\frac{-\delta t^2}{2\sigma^2}\right), \quad (2.17)$$

With this model, we get merely static disorder or, rather, a snapshot of the system at a given time. Eigenstates resulting from a representative implementation of this model are shown in Fig. 2.9. With low disorder, the states are essentially delocalized over the whole system, but as the fluctuations approach the value of the transfer integrals themselves, localization effects become prominent. To adequately describe the influence of dynamic disorder, we must include time-dependent fluctuations. Troisi and Orlandi developed a paradigmatic model featuring the essential physics [22]. They worked with a 1D chain, where disorder changes the transversal offset of neighboring molecules and, by Peierls coupling, the transfer integrals. A single vibrational mode with frequency ω dictates the evolution of the offsets. In the model, Holstein coupling is completely neglected — an appropriate approximation for common molecular semiconductors where $t > \lambda/2$, the critical value at which a particle does not localize anymore as a small polaron [44].

At zero temperature, there are no fluctuations, the states are delocalized over the entire crystal, and the density of states features a van-Hove singularity at the band extrema (see Fig. 2.10). Higher degrees of disorder and, therefore, higher temperatures wash out the singularities and shift the band maximum to slightly higher values. Beyond the band extrema, *tail states* emerge from large fluctuations. In the band center, the states are extended over many molecules, but the tail states are localized to very few molecules. Consequently, localized and delocalized states are *simultaneously* present in crystalline molecular semiconductors at room temperature.

Now, we investigate the consequences of dynamic disorder, which we can easily understand based on the static model. Initially, the particle is delocalized over a small number of sites. The temporal evolution of the transfer integrals changes the energy landscape so that the particle may move to a new location at a certain point and then stay localized until the transient landscape once again allows it to move to another location.

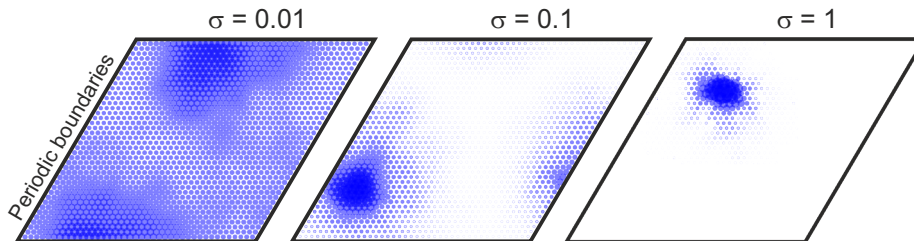


Figure 2.9. Disorder and localization of eigenstates. Highest electronic states of a triangular lattice (40×40 sites) with disorder in the transfer integrals. From left to right, the electronic disorder increases (weak, intermediate, strong), and the states correspondingly localize. More information on the used disorder model is given in the main text. The figure is based on simulations carried out by myself.

¹It must be in real space because a description in reciprocal space is not possible anymore. The translational symmetry is broken.

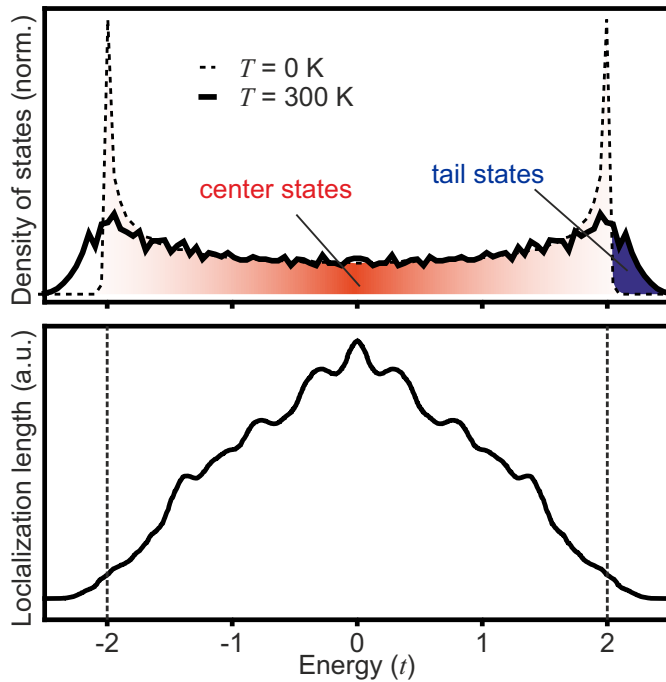


Figure 2.10. Properties of a disordered chain. Density of states and localization lengths of a 1D chain (compare eq. 2.16) for different degrees of disorder corresponding to different temperatures. At zero temperature, the DOS features a van-Hove singularity at the band extrema, which is washed out by disorder. Furthermore, new states emerge beyond the band extrema, which are highly localized compared to the delocalized states in the band center. Results from a simulation with 5000 sites, inspired by [8].

The motivation for this model was to understand charge transport in the original physical regime of crystalline molecular semiconductors, where $t \approx \sigma_t$. From the model, one then straightforwardly obtains that diffusion diminishes with decreasing vibrational frequency ω . In the limiting case of $\omega \rightarrow 0$, the particle remains localized at its initial position, and diffusion vanishes — just the case of static disorder.

Fratini *et al.* [8] built on Troisi’s Peierls coupling model to derive a new theory of transport in crystalline molecular semiconductors, *transient localization* theory. Based on the observation of localization and delocalization in the 1D model, they derived an analytic expression for the charge mobility μ by invoking the relaxation time approximation [8]:

$$\mu = \frac{e}{k_B T} \frac{L^2}{2\tau}.$$

Here L is the localization length, and $\tau \approx 1$ ps is the time scale of intermolecular vibrations. This expression reconciles discrepancies observed in the charge transport properties of crystalline molecular semiconductors, such as the band-like temperature dependence of the mobility [49] and the presence of localized states. We will elaborate on transient localization theory in chapter 4.

2.7 Excitons in crystalline molecular semiconductors

As we have seen, the equilibrium electronic states of crystalline molecular semiconductors can be understood as a linear combination of overlapping molecular orbitals. We now address how the interaction between molecules changes the *excited* states and, therefore, their optical properties. Before we discuss the excitons in detail, we clarify the terminology. The previous sections concerned purely single-particle interactions, and it was therefore sufficient to work in the basis of single-particle wave functions, i.e., molecular orbitals, because the total wave function Ψ in the absence of electron-electron interaction can be denoted as a single Slater determinant Φ . That, in turn, allows for a factorization of the total wave function into individual molecular orbitals ϕ . The excitonic states analyzed in

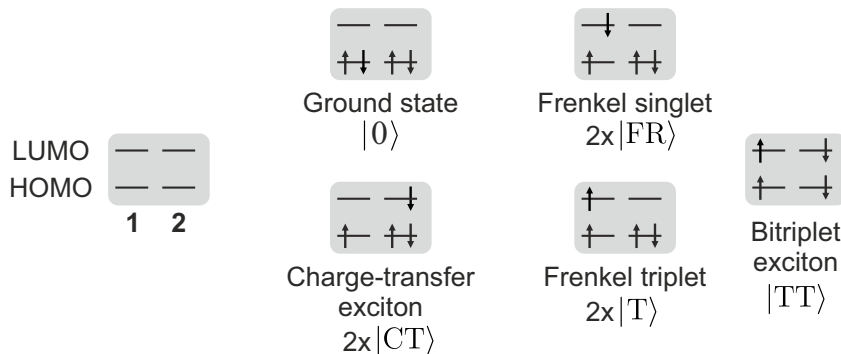


Figure 2.11. Electron configurations of diabatic exciton states. Lowest relevant diabatic exciton states or electron configurations in a molecular dimer. Note that there are two inversion-symmetric configurations each for |FR>, |T> and |CT> and that the actual |FR> and |CT> states are combinations of these configurations to yield overall singlets.

this section feature significant electron-electron interaction, and the total wave function will, therefore, be a linear combination of Slater determinants or electron configurations, and factorization is no longer possible. The Slater determinants can include single, double, and higher excitations, and we can hence write the total wave function as [18]

$$\Psi = c^{(0)}\Phi^{(0)} + \sum_i c_i^{(1)}\Phi_i^{(1)} + \sum_j c_j^{(2)}\Phi_j^{(2)} + \dots, \quad (2.18)$$

where $\Phi^{(0)}$ is the ground state, $\Phi_i^{(1)}$ is a single excitation and $\Phi_j^{(2)}$ is a double excitation. The electron-electron interaction determines the coefficients. In practice, not every electron configuration is relevant, and one truncates the configuration basis by physical arguments.

To describe the lowest electronic excitations in crystalline molecular semiconductors, three different states with well-defined characters form an appropriate basis which we call the diabatic basis [23]. It is sufficient to denote these states for a molecular dimer with molecules 1 and 2; more complicated arrangements can be deduced from the dimeric states. We additionally make the approximation that the frontier orbitals, i.e., HOMO and LUMO, are a reasonably sound basis for one-electron states. This approximation is justified by the rather large (> 1 eV) separation of the other molecular orbitals in benzenoid hydrocarbons (compare Fig. 2.2). In this dimer basis, there are two diabatic states with local single excitations, which can be either on molecule 1 or molecule 2, the Frenkel singlet exciton |FR> and the Frenkel triplet exciton |T> (see Fig. 2.11). The excitation can also be delocalized over the two molecules with a hole on one molecule and the electron on the other and vice versa; these states are the two charge-transfer excitons |CT>. We consider the charge-transfer excitons because they are close in energy to |FR> and might mix. There is, furthermore, the energetically close doubly-excited state |TT> consisting of two triplet excitations that we include here for completeness. However, we will only discuss them in the next section. Of all these states, only the singlet Frenkel exciton can couple to light since it is a local excitation, i.e., electron and hole are located on the same molecule, and the ground state to Frenkel transition is spin-allowed. The other states have negligible transition dipole moments [23].

The Hartree-Fock energies of the diabatic excited states with respect to the ground state can be evaluated directly [50]. From configuration interaction, we get:

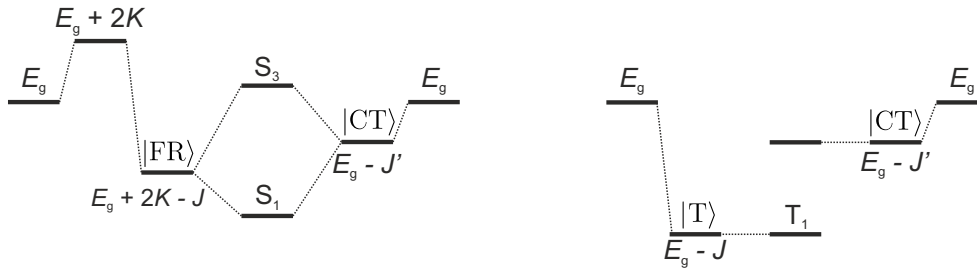


Figure 2.12. Configuration interaction diagram for the singlet and triplet excitons in acene systems. In the singlet manifold, the electron-hole exchange interaction K destabilizes the Frenkel exciton, bringing them to energetic proximity with CT states. The triplet Frenkel exciton does not mix with CT states, which are energetically too far away. Adapted from ref. [50].

$$E_{\text{FR}} = E_g + J - 2K \quad (2.19)$$

$$E_{\text{T}} = E_g + J \quad (2.20)$$

$$E_{\text{CT}} = E_g + J', \quad (2.21)$$

where $E_g = \epsilon_{\text{LUMO}} - \epsilon_{\text{HOMO}}$ is the bare band gap, J is the attractive intramolecular electron-hole Coulomb interaction, K is the repulsive intramolecular electron-hole exchange interaction and J' is the intermolecular electron-hole Coulomb attraction. As we have already seen in section 2.2, the triplet energies fall below the singlet energies due to the missing repulsive exchange interaction K (see Fig. 2.12). Note that in the expression for the $|\text{CT}\rangle$ energy, the intermolecular exchange interaction has been neglected since it is much smaller. It falls off faster with distance than the Coulomb attraction J' , which explains why, in the absence of spin-orbit coupling, there is no splitting between singlet and triplet excitons in conventional semiconductors with their large-radius Wannier excitons [51].

Due to electron-electron interaction, the diabatic states (or electron configurations) mix and thus form excitonic states. These are obtained by diagonalizing the Hamiltonian

$$H = \sum_i |i\rangle E_i \langle i| + \sum_{i \neq j} |i\rangle V_{ij} \langle j|, \quad (2.22)$$

with the states $|i\rangle$ of the diabatic basis, their respective energies E_i , and couplings V_{ij} . Its diagonalization yields the coefficients of each configuration and the resulting eigenstates define the excitonic basis. The $|\text{CT}\rangle$ state can energetically be close to the $|\text{FR}\rangle$ state in acene systems, since here $J - 2K \approx J'$, which allows for mixing between these configurations [52]. Such a mixing is greatly reduced for the triplet configuration, which is much lower in energy. It is common to sort the bright singlet excitonic states by their energy so that the lowest-lying bright exciton is labeled S_1 and the next highest S_2 . The same procedure is applied to the triplet states, yielding T_i .

Before we address the consequences of the state mixing, we recapitulate the hierarchy of electronic interactions discussed thus far (Fig. 2.13). We started with the single-particle states of benzenoid hydrocarbons, which are molecular orbitals ϕ formed by linear combinations of carbon p_z -orbitals. Adjacent molecular orbitals overlap in the tightly-packed crystal, and the resulting Bloch orbitals $\psi_{\mathbf{k}}$ are linear combinations of the molecular orbitals ϕ . The spectrum of the Bloch orbitals is given by the single-particle band structure $\epsilon_{\mathbf{k}}$. An anti-symmetric product of single-particle states forms Slater determinants, which may

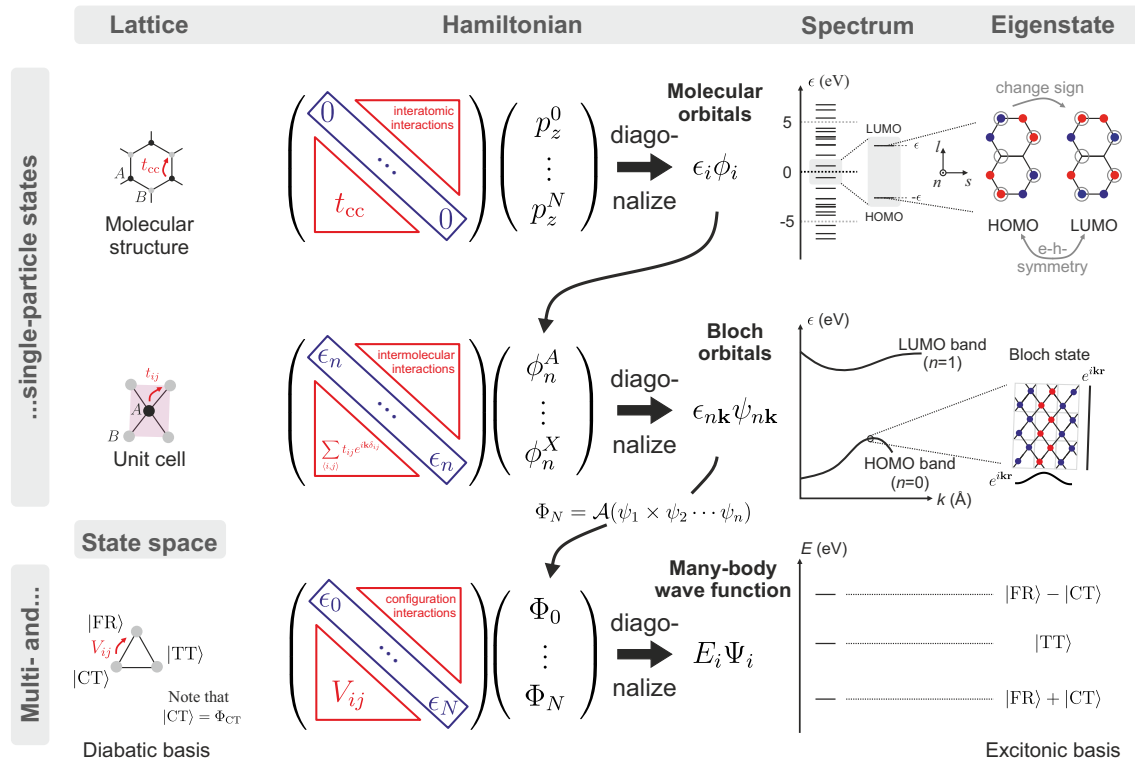


Figure 2.13. Hierarchy of electronic states and interactions in molecular semiconductors. The molecular orbitals ϕ are determined by the bipartite molecular structure. Overlap between these orbitals then leads to the formation of extended Bloch orbitals $\psi_{\mathbf{k}}$ and the emergence of a band structure. With the basis of single-particle states, we can construct multi-particle Slater determinants Φ . The coupling between Slater determinants (or diabatic states) yields the many-body exciton wave function Ψ .

couple to each other. The physically observable excitonic states are then linear combinations of the Slater determinants, where the mixing between different configurations is determined by their relative energies and the coupling between them.

We get the desired couplings by inspecting the possible pathways between the diabatic states. Firstly, in purely carbon-based systems, spin-orbit coupling is weak, and the interaction between states of different spins can hence safely be neglected. Secondly, we can separate the remaining interactions into two categories: one-electron couplings for $\langle \text{CT} | V | \text{FR} \rangle$ and $\langle \text{CT} | V | \text{TT} \rangle$, and two-electron couplings for $\langle \text{TT} | V | \text{FR} \rangle$ and $\langle \text{FR} | V | \text{FR} \rangle$ (see Fig. 2.14).

To specify the one-electron couplings in the molecular dimer, we now distinguish between the two $|\text{FR}\rangle$ states as $|10\rangle$ and $|01\rangle$ and between the two $|\text{CT}\rangle$ states as $|+-\rangle$ and $|-+\rangle$. The one-electron couplings are then [53]:

$$\begin{aligned}
 \langle +- | V | 10 \rangle &= t_{\text{LL}} & \langle -+ | V | 10 \rangle &= -t_{\text{HH}} \\
 \langle +- | V | \text{TT} \rangle &= \sqrt{3/2} t_{\text{LH}} & \langle -+ | V | \text{TT} \rangle &= \sqrt{3/2} t_{\text{HL}} \\
 \langle +- | V | 01 \rangle &= -t_{\text{HH}} & \langle -+ | V | 01 \rangle &= -t_{\text{LL}},
 \end{aligned} \tag{2.23}$$

with the transfer integrals t_{HH} , t_{LL} , t_{HL} , and t_{LH} that connect different orbitals, where the index H stands for HOMO and L for LUMO. The one-electron couplings depend on the overlap between molecular orbitals located on different molecules (compare equation 2.14)

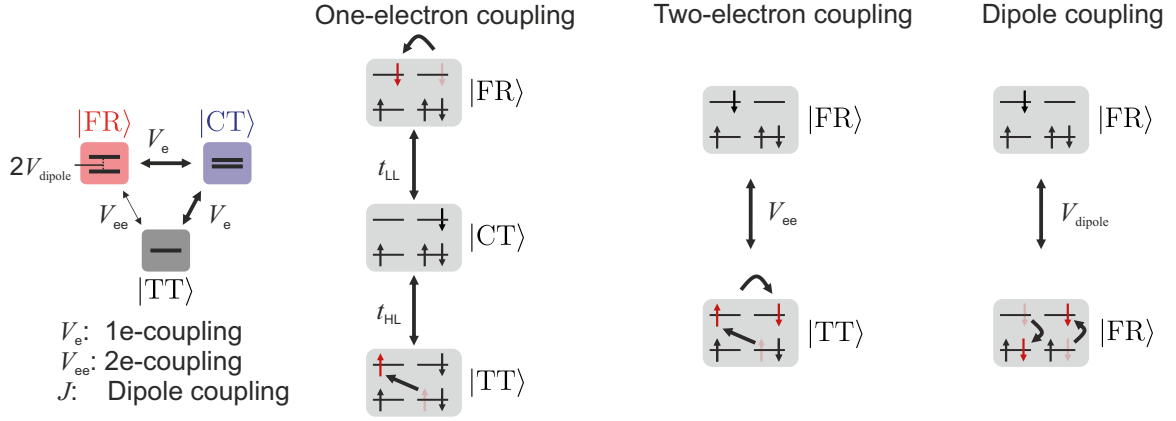


Figure 2.14. Electronic coupling of the diabatic states. The couplings can be divided into one-electron couplings V_e , two-electron couplings V_{ee} , and the dipole coupling V_{dipole} .

and are on the order of ~ 100 meV. They can, in principle, be obtained by the off-diagonal terms of the Fock operator (see [23]) or, as done in chapter 4, by the dimer splitting method.

The dipole two-electron coupling $V_{\text{dipole}} = \langle 10|V|01\rangle$ is determined by the transition dipole from HOMO to LUMO and depends on the relative orientation of the two molecules. With the two dipole moments $\boldsymbol{\mu}_1$ and $\boldsymbol{\mu}_2$ of molecule 1 and 2, respectively, the coupling is [54]

$$V_{\text{dipole}} = \frac{\boldsymbol{\mu}_1 \cdot \boldsymbol{\mu}_2 - 3(\boldsymbol{\mu}_1 \cdot \hat{R})(\boldsymbol{\mu}_2 \cdot \hat{R})}{4\pi\epsilon R^3},$$

where R is the center-of-mass distance and $\hat{R} = \mathbf{R}/R$. The value of V_{dipole} varies between positive and negative values, depending on the relative orientation, and is on the order of ~ 10 meV for common molecular semiconductors.

We briefly investigate the dipole coupling for two molecules in a herringbone-like arrangement and a dipole moment along s (for a more detailed discussion, see [55]). The coordinate system is given by the s - and n -axis of one molecule, and we neglect the l -dimension. The dipole moment of molecule 1 is $\boldsymbol{\mu}_1 = \begin{pmatrix} \mu \\ 0 \end{pmatrix}$. Molecule 2 is separated by $\mathbf{R} = \begin{pmatrix} 0 \\ R \end{pmatrix}$ and its dipole moment is rotated by the angle θ : $\boldsymbol{\mu}_2 = \mathbf{M}_\theta \begin{pmatrix} \mu \\ 0 \end{pmatrix}$, where \mathbf{M}_θ is the 2D rotation matrix. The two combined dipole moments of the molecules point in the orthogonal directions $\boldsymbol{\mu}_+ = \boldsymbol{\mu}_1 + \boldsymbol{\mu}_2 \parallel \mathbf{a}$ and $\boldsymbol{\mu}_- = \boldsymbol{\mu}_1 - \boldsymbol{\mu}_2 \parallel \mathbf{b}$. These are roughly parallel to the lattice vectors in the molecular plane of the unit cell. In typical herringbone packings, $\theta \approx 50^\circ$ and the couplings along the two directions are: $V_{\text{dipole}}^+ > 0$ and $V_{\text{dipole}}^- < 0$ (compare Fig. 2.15a).

The splitting between the corresponding excitons along the two lattice vectors is observable in optical spectroscopy and known as Davydov splitting ΔD . For the present case, the dipole couplings suggest that the lowest-bright exciton S_1 is polarized along \mathbf{b} and S_2 polarized along \mathbf{a} with $\Delta D \approx 20$ meV. That is in direct contradiction to the observed absorption spectra of crystalline acenes such as tetracene. Here S_1 is polarized along \mathbf{a} and ≈ 80 meV below the \mathbf{b} -polarized S_2 . Thus, the splitting is considerably larger and of the opposite sign. Yamagata *et al.* reconciled the observations with the underlying theory by including the mixing between almost degenerate Frenkel and charge-transfer excitons [55], as apparent from the Hamiltonian in equation 2.22. The energy of the excitons is then corrected in a perturbative treatment by [52]:

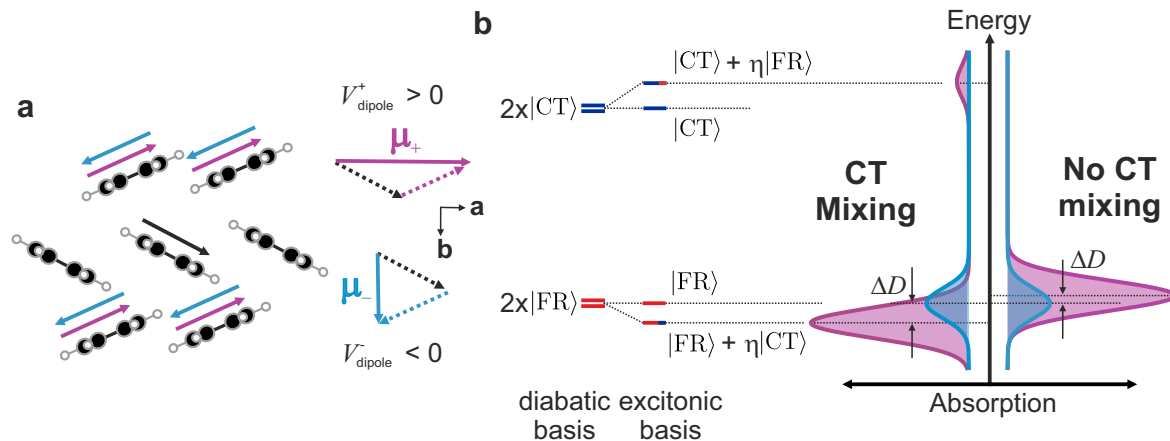


Figure 2.15. Lowest optical excitations in molecular semiconductors. **a**, Alignment of the dipole moments μ in a herringbone packing, leading to the emergence of the two combined states μ_+ and μ_- . **b**, Energy levels in the diabatic and excitonic basis and absorption spectrum for a system that mixes Frenkel and charge-transfer states and a system without mixing. Note that the mixing also causes new visible peaks in the spectrum.

$$\Delta E^\pm \propto -\frac{(t_{\text{HH}} \pm t_{\text{LL}})^2}{|E_{\text{FR}} - E_{\text{CT}}|}.$$

If the transfer integrals of HOMO and LUMO are of the same sign — as in the case of tetracene — the μ_+ -state is downshifted by ≈ 100 meV below the μ_- -state, in agreement with observation. The lowest-bright excitons of crystalline acenes thus feature large mixing between Frenkel and charge-transfer excitons (Fig. 2.15b).

2.8 Singlet exciton fission

2.8.1 Introduction

An exciton rarely shares its energy with another to produce two stable excitons. Commonly, this exciton multiplication must compete with the highly efficient electron-phonon scattering. A process that — in the long run — leads to the thermalization of the exciton energy. In conventional semiconductors, creating new charge carriers by another highly excited or hot charge carrier is called impulsive ionization. It is either immediately outpaced by electron-phonon scattering [56] or the new carriers that were produced by it quickly thermalize with the lattice, i.e., they are not in stable states. The situation is improved in quantum dots where spatial confinement relaxes the strict momentum conservation and enhances electron-electron interactions [57]. However, the overall efficiency of carrier multiplication remains low due to competing scattering channels. In molecular semiconductors, the spatial confinement of charge carriers is even larger, thus further intensifying electron-electron interactions. As we have seen, the correspondingly large exchange interaction may bring the lowest bright singlet exciton into energetic proximity with two triplet excitons - opening up a unique and efficient electron-electron scattering channel: *singlet exciton fission*.

Overall, singlet exciton fission converts a singlet exciton into two triplet excitons, captured in the simple reaction scheme $S_1 \rightarrow T_1 + T_1$. The efficiency reaches the theoretical limit 200% in crystalline acenes — every initial excitation is converted to two triplet excitons. The critical difference between singlet exciton fission and impact ionization is that in the former, the excitons are not "hot". After optical excitation, they are located at the bottom

of the conduction band, and no further scattering within the band is possible due to a lack of available singlet electronic states at lower energies. There are, however, triplet states at lower energies which can be accessed by singlet exciton fission. Singlet exciton fission can outcompete electron-phonon coupling because it is a spin-allowed process, obliterating the need for a spin flip. New intermediate states characterize this process, which we will briefly discuss.

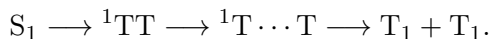
The bitriplet exciton.

The earliest observations of singlet exciton fission were made in the 1960s and led to the formulation of the single-step reaction scheme $S_1 \rightarrow T_1 + T_1$ [58]. Soon, it was noted that two triplet excitons in spatial proximity, such as those formed directly after the decay of the singlet exciton, may interact and form a new state: the bitriplet exciton (or correlated triplet pair) 1TT [59, 60]. It comprises two correlated electron-hole pairs situated on neighboring molecules that form an overall spin singlet. Due to its doubly-excited nature, the bitriplet exciton poses a challenge to computations, and it is furthermore difficult to observe since it is spectroscopically dark. Properly understanding singlet exciton fission requires knowledge of the structure and dynamics of the bitriplet exciton.

The separated bitriplet exciton.

As the two triplet excitons diffuse apart, proximity effects, i.e., interactions between them via orbital overlap, become negligible. Nonetheless, the spins of the two excitons remain correlated since the triplet hopping that drives diffusion does not act on the spin [61]. At this stage, we must, therefore, treat the excitation as a single state — in contrast to two independent triplet excitons. These properties, i.e., spin correlation and the absence of proximity effects, define the separated bitriplet exciton ${}^1T \cdots T$.

Scholes included the two states in a more detailed reaction scheme [61]:



This scheme underpins the current understanding of singlet exciton fission in crystalline materials. In the primary step (SF1), the singlet exciton is converted into the bitriplet exciton. After its emergence, the individual triplet excitations diffuse away from each other while maintaining spin coherence; this defines the secondary step (SF2) and leads to the formation of the separated bitriplet exciton. Lastly, the spin coherence is lost, and two independent triplets are formed.

Even with this scheme, however, the key questions remain unanswered. (1) What is the structure of the bitriplet excitons? (2) What mechanism drives the transition, and which parameters control it? To answer them, we reduce the complexity of the process by describing it in a molecular dimer. Furthermore, we first neglect the role of electron-phonon coupling and discuss it later in this section.

2.8.2 Electronic states in the dimer model

This analysis and the simulations contained in this subsection are my own work. The dimer model was already introduced in the context of the exciton states of molecular semiconductors (see section 2.7) and included two Frenkel and two charge-transfer states. These are states with a well-defined electronic character that form part of the diabatic basis. In addition to these four states, we now include the diabatic bitriplet exciton TT . We refer here to the bitriplet and spin singlet configuration of this doubly excited state. There are 15 more eigenstates of the \hat{S}^2 -operator contained in one quintet level, three triplet levels, and one singlet level. The other singlet state, which can be categorized as a bisinglet state, is too high in energy to mix with the bitriplet state, while the other states belong to different

spin manifolds [61]. Additionally, we denote TT as a single spin configuration instead of the \hat{S}^2 -eigenstate to simplify the notation. The excitation energy of TT corresponds to two individual triplet excitations by construction.

Electronic couplings of the diabatic states.

The electronic couplings have already been defined in eq. 2.23 and depend on the one-electron couplings t_{HH} between HOMO and HOMO, t_{LL} LUMO and LUMO, and t_{HL} HOMO and LUMO as shown in Fig. 2.14. The sign of the couplings depends on the alignment of the molecules in the dimer under investigation. Here, the signs are set to those found in molecular dimers in a pentacene crystal, a representative singlet exciton fission system, and the magnitude of all couplings is $t = 0.1 \text{ eV}$, similar to the value obtained by computations [53]. The topology of the configurations and their interactions is shown in Fig. 2.16a as a graph.

The dimer model is of great use since it allows an intuitive understanding of how a few well-defined parameters of the molecular system influence singlet exciton fission. In the graph representation, SF1 is equivalent to the pathway from one of the two Frenkel states to the bitriplet. We now focus on the pathway starting from $|01\rangle$. The direct pathway is forbidden since we have set the two-electron couplings to zero. The remaining two indirect paths each cross a $|CT\rangle$ state. Because of the different signs of $\langle +-|V|TT\rangle$ and $\langle -+|V|TT\rangle$, the two pathways destructively interfere. With the chosen coupling parameters, this makes a direct mixing of Frenkel and bitriplet states impossible.

Diagonalization and excitonic states.

We obtain the excitonic states, that is, the eigenstates of the configuration interaction Hamiltonian defined by Fig. 2.16a, by diagonalization. The five diabatic states lead to five eigenstates, which we label as follows. There are three bright excitons, i.e., excitons with Frenkel characters, which are sorted by energy and labeled S_1 , S_2 , and S_3 . Note that S_2 is the anti-symmetric Frenkel state $|10\rangle - |01\rangle$ which does not mix with CT states. The remaining two excitons are dark and are mixtures of $|CT\rangle$ and $|TT\rangle$.

We can immediately extract quantities of physical significance from the exciton energies. The offset between the two lowest bright excitons, S_1 and S_2 , is the Davydov splitting ΔD . Its magnitude increases with the amount of mixing between $|FR\rangle$ and $|CT\rangle$ states and the coupling between them. The energy difference between the diabatic $|TT\rangle$ and S_1 is the singlet exciton fission energy ΔE_{ST} . Apart from the obvious dependence of this energy on the offset between $|FR\rangle$ and $|TT\rangle$, it also depends on the energy of $|CT\rangle$ due to the presence of these states in S_1 . Lastly, we can extract an energy difference that is related to SF2: the offset between the diabatic $|TT\rangle$ and the excitonic 1TT that defines the biexciton binding energy E_{BX} . It measures the energy difference between the adiabatic 1TT and ${}^1T \cdots T$. Its magnitude depends on the amount of mixing between $|CT\rangle$ and $|TT\rangle$ — if these are close in energy, the biexciton binding energy can be sizable.

Scenarios.

The excitonic states are shown in Fig. 2.16b-d for different scenarios. In all of them, the $|CT\rangle$ energy is scanned, and the eigenvalues of the excitons are plotted along the vertical axis while the state character is indicated by the color code and the thickness of the lines. We now analyze a scenario that is akin to the energetic alignment of the diabatic states found in tetracene ($E_{\text{FR}} = 2.4 \text{ eV}$ and $E_{\text{TT}} = 2.5 \text{ eV}$). For very low $|CT\rangle$ energies, shown in the right of Fig. 2.16b, the mixing between the states is small, and the energies of the diabatic states are close to the excitonic states. As we increase the $|CT\rangle$ energy, the states mix, and two avoided crossings become visible. The first avoided crossing occurs between

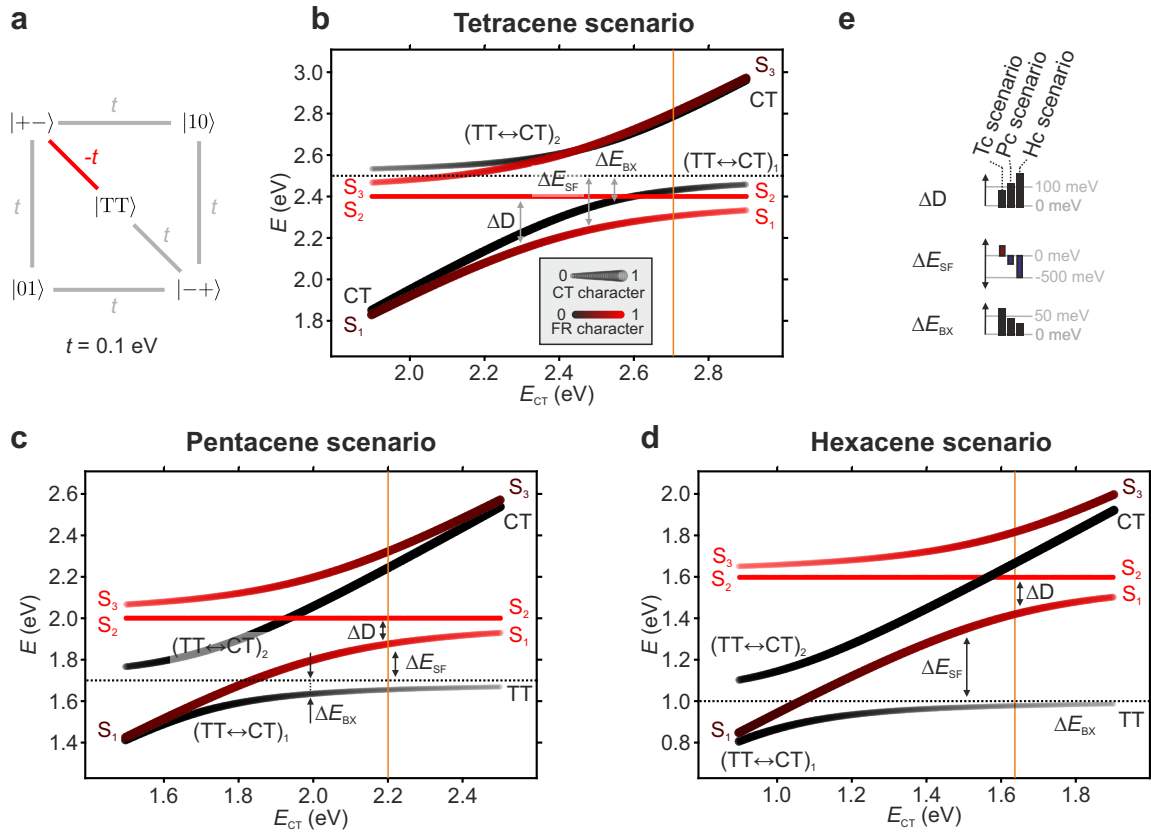


Figure 2.16. Properties of the SF dimer model. **a**, Graph representation of the model. **b**, The energy of the excitonic states for the tetracene scenario for varying CT energies. The states are labeled by their character. The width of the lines represents the CT character, while the color represents the brightness or FR character. Some important energy differences, as defined in the main text, are indicated: the Davydov splitting ΔD , the singlet exciton fission energy ΔE_{SF} , and the biexciton binding energy ΔE_{BX} . The orange line depicts the CT energy, which reproduces the Davydov splitting in the crystal. The diabatic bitriplet and Frenkel energies are: $E_{FR} = 2.4$ eV and $E_{TT} = 2.5$ eV. **c** and **d**, The same for the pentacene scenario with the diabatic energies $E_{FR} = 2.0$ eV and $E_{TT} = 1.7$ eV and the hexacene scenario with $E_{FR} = 1.6$ eV and $E_{TT} = 1.0$ eV, respectively. **e**, Trends of important energies in for the three scenarios.

the S_1 and S_3 excitons at an energy where $E_{CT} = E_{FR}$. Also, the $|CT\rangle$ and $|TT\rangle$ may hybridize, leading to another avoided crossing between the dark exciton branches. As we reach $|CT\rangle$ energies larger than those of the other two diabatic states, the mixing between the states is reduced again. To set an approximate value for the $|CT\rangle$ energy, we can match the experimental ΔD from the crystal to the ΔD that emerges from our model. The experimental splitting is $\Delta D = 80$ meV [55] and we get $E_{CT} = 2.7$ eV. The singlet exciton fission and biexciton binding energies are then $\Delta E_{SF} = 200$ meV and $\Delta E_{BX} = 70$ meV, respectively.

We now investigate two other scenarios, the pentacene and hexacene scenarios, for which the bitriplet energy is reduced by 0.8 eV and 1.5 eV, respectively, compared to the tetracene scenario. In comparing these scenarios, a trend of the ΔE_{BX} , ΔE_{SF} , and ΔD energies becomes apparent (Fig. 2.16e). The Davydov shift increases in the oligoacene series, in line with an increasing delocalization and charge-transfer character of S_1 [55, 62]. In the larger acenes, $|FR\rangle$ and $|CT\rangle$ come into energetic proximity. Correspondingly, the energy of $|CT\rangle$ decreases faster with increasing acene size than $|FR\rangle$ [50].

Another well-known trend reproduced in the dimer model is the increasing exothermicity of SF. In tetracene, SF is substantially endothermic. The overall process becomes exothermic in pentacene and strongly exothermic in hexacene. These vastly different energetics determine the dynamics of SF and require a more specific treatment of the phonon bath that supplies or absorbs energy.

Intriguingly, the biexciton becomes less strongly bound in the larger acenes. The diabatic bitriplet drops quickly in energy, and the offset between it and the charge-transfer states becomes larger for the larger acenes. In tetracene, the biexciton is bound by > 50 meV due to a large $|CT\rangle$ character. Hexacene, in contrast, features a weakly bound 1TT . These energetics have interesting consequences for the mechanism of SF. The endothermicity inherent to tetracene is shared among the two first steps and includes overcoming a sizeable bitriplet binding energy.

Constructive interference.

The preceding discussion built on the sign of the couplings observed in acene dimers in the crystal, yielding a specific sign combination such that the overall SF1 pathways destructively interfere. However, there might be systems in which interference is constructive. Here, the excitonic states will be mixtures of all three diabatic species instead of mixtures between just two diabatic states. Thus, the lowest-bright singlet exciton might have an intrinsic and substantial $|TT\rangle$ character. Furthermore, the couplings in our model are generically set to the value 100 meV. In the actual dimers, individual values differ slightly, and the destructive interference is imperfect. Consequently, the lowest-bright singlet excitons in the acenes may have (marginal) $|TT\rangle$ character.

2.8.3 Mechanisms of the primary step

We wish to understand qualitatively how the optically prepared S_1 transitions to 1TT . It is helpful to distinguish two dynamics regimes that depend on the energetic position of the $|CT\rangle$ states. The first occurs when the energy offset of these states to the diabatic Frenkel and bitriplet states is significantly larger than the coupling between them. In this so-called superexchange regime, the mixing between the states is small, and a perturbative treatment is appropriate. The other regime encompasses degenerate diabatic states and, hence, strong physical mixing in the excitonic states. The scenarios discussed above belong to this regime. However, it is nonetheless insightful to discuss the superexchange regime.

Superexchange.

When the mixing of $|CT\rangle$ into S_1 is not too large, the coupling corresponding to SF1 can be evaluated perturbatively [53]. It is given by

$$\begin{aligned} \langle FR|\hat{V}_{el}|TT\rangle &\approx \langle FR^{(0)}|\hat{H}_{el}|TT^{(0)}\rangle - 2\frac{V_{10,+}V_{+,-,TT} + V_{10,-}V_{-,+,TT}}{(E_{CT} - E_{TT}) + (E_{CT} - E_{FR})} \\ &= V^{(0)} - 2\sqrt{\frac{3}{2}}\frac{t_{LL}t_{LH} - t_{HH}t_{HL}}{(E_{CT} - E_{TT}) + (E_{CT} - E_{FR})}, \end{aligned}$$

where $X^{(0)}$ signifies pure states (zeroth order mixing). The coupling is, therefore, the sum of a direct transition involving a two-electron integral and of two terms that involve the product of two one-electron integrals. The two-electron integral is of the order of ~ 1 meV and hence significantly smaller than the second term in the equation (~ 100 meV). It can therefore safely be neglected. With Marcus theory, the coupling yields the following rate

for SF1 [53]:

$$k_{\text{SF1}} \approx \frac{2\pi}{\sqrt{4\pi\hbar^2\lambda k_{\text{B}}T}} \frac{|V_{\text{I0,+}}V_{+, \text{TT}} + V_{\text{I0,-}}V_{-, \text{TT}}|^2}{(E_{\text{CT}} - E_{\text{TT}})^2} e^{-\frac{(E_{\text{FR}} - E_{\text{TT}} + \lambda)^2}{4\lambda k_{\text{B}}T}},$$

where λ is the reorganization energy associated with SF1. Within the perturbative approximation, the rate depends to the fourth order on the transfer integrals $k_{\text{SF1}} \propto t^4$. There is furthermore a weak power-law dependence on $E_{\text{CT}} - E_{\text{TT}}$ and a dominant exponential dependence on $E_{\text{FR}} - E_{\text{TT}}$. We can expect the rate to be negligible for large energy offsets between $|\text{FR}\rangle$ and $|\text{TT}\rangle$. Without a strong role for the phonon bath, systems with too large endo- or exothermicity thus do not undergo singlet exciton fission, in line with intuitive expectation.

However, the perturbative treatment completely neglects the energy shifts expected when the diabatic states strongly mix and hence yields poor results for the crystalline acenes. In the literature, the SF1 mechanism described here is called the charge-transfer mediated mechanism since the dominant coupling stems from one-electron couplings to charge-transfer states.

Physical mixing.

In the crystalline acenes, the excitonic states are mixtures of the diabatic states prohibiting a perturbative treatment of the electronic coupling. We can, nonetheless, make some statements about the effective coupling between S_1 and ^1TT . Since the direct $\langle \text{FR} | \hat{V}_{\text{el}} | \text{TT} \rangle$ coupling is weak compared to the mediated coupling, the $|\text{CT}\rangle$ character of S_1 determines the overall coupling strength [50]. Coming back to the acene series, we notice that the SF1 coupling increases when going from tetracene to hexacene, which might, however, be compensated by a larger mixing of $|\text{CT}\rangle$ into ^1TT .

Electron-phonon coupling.

Apart from the electronic coupling, we must consider the coupling to the phonons. Two major reasons make this necessary. (1) The coherences between the two excitonic states must be removed for successful population transfer, and (2) unmatched energy must be supplied or absorbed by the phonons. The phonons and vibrations yield a density of states at each phonon frequency. At ~ 100 meV we find the fastest vibrations which are intramolecular C-C stretching modes¹. It is *a priori* unclear and computationally expensive to quantify how strongly each vibrational mode is coupled to the electronic transition. However, we can immediately make some general remarks. The SF1 rate depends on the availability of strongly coupled phonons at the energy mismatch [53, 63]. The e-ph coupling strength in the SF1 transition is parametrized as in section 2.2 by the reorganization energy λ . If only a single vibrational mode is involved in the transition, the rate depends linearly on λ . Furthermore, endothermic SF1 must absorb energy from thermally populated phonons, and increased temperatures should be beneficial. Lastly, strongly exothermic SF1, as in hexacene, presents an energy mismatch that is too large to be overcome by a single vibrational quantum. In this energetically steeply downhill step, the SF1 rate should decrease since the excitation of more than one vibrational quantum is less likely [50]. This regime is known as the inverted Marcus regime.

Nuclear coherence and conical intersections.

We briefly discuss the possible back-action of nuclear modes on the electronic transition in SF1. Several measurements have observed nuclear coherences following SF1 [64, 65], and

¹There are even faster C-H vibrations at 300 meV, but these local vibrations are weakly coupled to electronic transitions within the delocalized π -network.

it has been suggested that these play a crucial role in a conical intersection mechanism. Here, specific nuclear coordinates lead to a degeneracy of electronic states, making a rapid transition between them possible. The simplest model of a conical intersection can be constructed from just two vibrational modes. These are (1) the tuning mode with coordinate Q_t and (2) the coupling mode with coordinate Q_c . The tuning mode changes the energy offset between two states with e-ph coupling strength κ and the coupling mode the electronic coupling with e-ph coupling strength Λ [66], leading to the following Hamiltonian

$$H = \begin{pmatrix} \Delta E - \kappa Q_t & \Lambda Q_c \\ \Lambda Q_c & 0 \end{pmatrix}.$$

The critical point is that two nuclear modes act in synergy to facilitate population transfer and that the transfer rate *depends on the position of the nuclei*, $k_{\text{SF}}(Q)$. The conical intersection mechanism contrasts the previously discussed coupling to a phonon bath, where the nuclear positions do not act back on the rate. In the presence of a conical intersection, we expect to see a modulation of the transfer rate with the phonon frequencies of the tuning or coupling modes.

From the dimer model to an extended system.

In the previous sections, we have restricted SF to a molecular dimer. In an extended system, two fundamental differences should change the dynamics. Firstly, the energies of the diabatic states change with respect to each other, and secondly, the density of these states changes. The first point can be easily incorporated into the presented model, but the second merits in-depth consideration. A simple point illustrates the issue. The dimer model hosts five low-energy singlet states, of which two are |FR>, two are |CT>, and one is |TT). In a heptamer, again taken from the herringbone structure of the acenes, the relative number of states changes significantly. There are now 46 diabatic states: 7 |FR), 26 |CT), and 13 |TT). Crucially, the ratio $\frac{N_{\text{FR}}}{N_{\text{TT}}}$ changes from 2 to 0.5. For even larger clusters, this ratio will further decrease. Eventually, it will saturate because we must truncate the diabatic states to nearest neighbor states — to which the bitriplet excitons are confined. Due to the increased density of states (DOS) of biexcitonic states in extended systems, the SF1 transition rate is expected to increase. This increase can be interpreted as an entropic driving force [67]. Teichen *et al.* derived the general rule that the SF1 rate increases with a higher degree of delocalization in the singlet exciton due to the increasing number of localized bitriplet states sampled by a delocalized S_1 [68].

2.8.4 The secondary step

After the primary step, the bitriplet exciton has formed. In a molecular dimer, this state cannot transition to the separated bitriplet exciton since there are no molecules to which a lone triplet exciton could diffuse. In an extended system, however, the secondary step becomes possible via a hopping transfer of one constituent triplet exciton to neighboring molecules [69]. This step involves overcoming the biexciton binding energy and depends on the rate of triplet hopping in the system. The latter is commonly referred to as the rate of Dexter energy transfer, and it involves a simultaneous transfer of the electron and the hole from one site to the next. As such it depends on the transfer integrals t_{HH} and t_{LL} [70]. Their values are quite similar amongst the crystalline acenes, and we thus expect the SF2 rate to be dominated not by the coupling, but by differences in the biexciton binding energy. The large value in tetracene should inhibit bitriplet separation, whereas a much faster rate is expected for the weakly bound bitriplet excitons in pentacene or hexacene.

2.8.5 Experimental results

We have thus far discussed the theoretical background of singlet exciton fission in the solid state. The advances in understanding the mechanism have built on experimental results using ultrafast methods, which we briefly summarize here. For more extensive reviews, the reader is referred to the works by Smith and Michl for work done before 2010 [16], by Miyata *et al.* for more recent studies [71] and by Musser and Clark for bitriplet excitons [72].

Transient absorption spectroscopy.

Most studies on singlet exciton fission have used transient absorption spectroscopy and assigned spectral features to the states participating in singlet exciton fission. The earliest studies focused on tetracene, in which two triplet excitons are energetically above the singlet exciton, and pentacene, in which the situation is reversed. Due to the lack of knowledge about the origin of spectral signals, an ambiguity prevailed in assigning the time scale of SF1 in tetracene. Whereas some studies claimed an ultrafast < 300 fs decay of the singlet exciton [73], others observed longer time constants of 10 to 90 ps [74, 75]. Similar issues were present in the interpretation of transient absorption data in pentacene. Most authors agreed on an ultrafast decay of the singlet exciton (~ 100 fs), but there has been no consensus on another time scale ~ 1 ps [76–79]. Pensack *et al.* found spectroscopic differences in the near-infrared between the bitriplet exciton and the separated bitriplet exciton and extracted a ≈ 2 ps time scale for SF2 in a pentacene derivative [80].

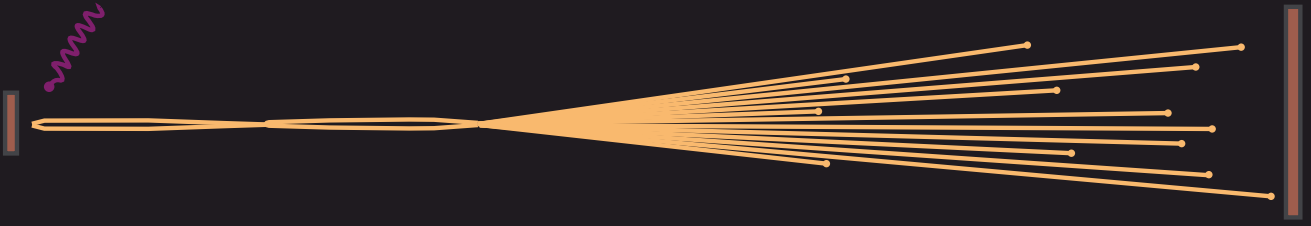
Two-photon photoemission spectroscopy.

Two-photon photoemission spectroscopy (2PPE) was employed to obtain new insights on singlet exciton fission in tetracene, pentacene, and hexacene. The first work focused on pentacene and confirmed the ultrafast decay of the singlet exciton in ~ 100 fs [81]. Additionally, the authors found an instantaneously populated signal at lower energies, which relaxes within ~ 500 fs. In a similar experiment, the same authors found a 6 ps decay of the singlet exciton in tetracene and also observed an instantaneous signal at lower energies [67].

Other techniques.

Two studies employed photoluminescence spectroscopy to find signatures of the bitriplet exciton in tetracene and pentacene [82, 83]. These authors established that the otherwise dark bitriplet exciton can luminesce via a Herzberg-Teller mechanism [84] and does not form independent triplet excitons at low temperatures in pentacene due to an energetic barrier. In the Herzberg-Teller mechanism, an otherwise forbidden coupling is activated by a vibrational mode that breaks the symmetry of the system. Using two-dimensional electronic spectroscopy, Musser *et al.* observed a transfer of vibrational coherence from the photoexcited singlet exciton to the triplet excitons in a pentacene derivative [64]. Coherence transfer was also found in similar studies on rubrene [85] and pentacene [65, 86].

While some time scales, such as the decay of the singlet exciton in pentacene, were quickly established in the field, others, such as the same decay in tetracene, remain debated. The central issue none of the above studies addressed is the ambiguity in assigning spectroscopic signals. The mentioned techniques do not provide information about the nature of the participating states apart from the alignment of transition dipoles. This work fills this major gap by investigating singlet exciton fission with time- and angle-resolved photoemission spectroscopy, which provides information about the states in momentum space. The next chapter discusses the working principle of this cutting-edge technique.



3. Introduction to (tr)ARPES

In this chapter, the principles of time- and angle-resolved photoemission spectroscopy — the experimental method used in this thesis — are introduced. It starts with a brief history of photoemission, which dates back to 1887 and works its way to state-of-the-art instrumentation. Then, we describe the photoemission process with Fermi’s Golden Rule by using the well-established three-step model and thereby show how the electronic structure relates to the photoemission signal. We further introduce the plane-wave approximation, which allows us to view the photoemission signal as a Fourier transform of the initial wave function. Often, electronic states are multiparticle states, and we describe how the corresponding correlation manifests itself as satellite peaks in the photoemission signal. Finally, we discuss some aspects of time-resolved ARPES and briefly introduce the experimental setup.

Photons with sufficient energy may release electrons from their bound states. The resulting photoelectrons escape from their origin while carrying information about it with them. When the electrons are collected in a detector that measures their energy and momentum, the ensuing signal supplies detailed information about the electronic structure of a material. *Relating photoelectron properties to the electronic structure of materials* is the essence of photoemission spectroscopy. However, the history of photoemission started on quite a different note.

3.1 Brief history

The first observation of the photoelectric effect — that is, the electrical discharging of an object by short-wavelength light — was made by Hertz in 1887 (Fig. 3.1a). At first a curiosity, the photoelectric effect quickly supplied crucial information for discovering the electron and the photon. Just ten years after Hertz, J. J. Thomson postulated the existence of electrons and then showed that cathode rays created either by field emission or radiation are the same phenomenon [93], both consist of electrons. Shortly after, Einstein explained the photoelectric effect by quantizing light into photons. He could then show why the kinetic energy of liberated electrons only depends on the light’s frequency and

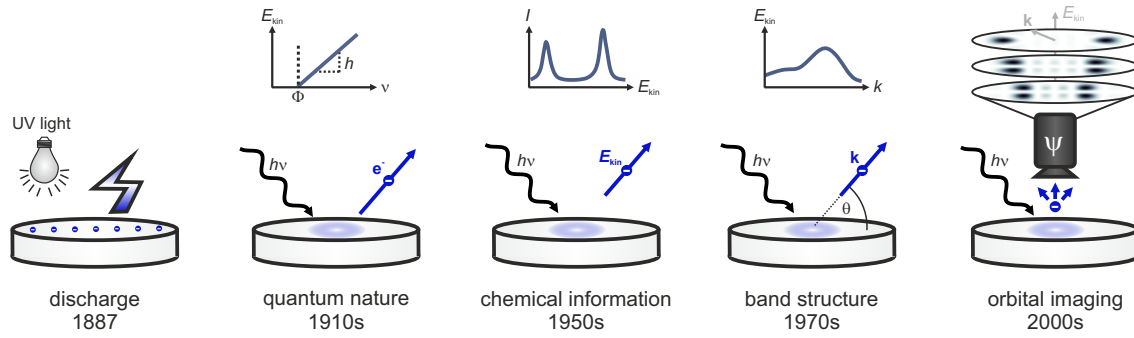


Figure 3.1. Evolution of photoelectron techniques. **a**, The first observation of the photoelectric effect by Hertz [87]. **b**, Millikan used photoemission to test the quantum nature of photons [88]. **c**, Photoemission with X-rays (also called electron spectroscopy for chemical analysis, or ESCA) was invented by Siegbahn to study the chemical composition of compounds [89]. **d**, Angle-resolved photoelectron spectroscopy matured as a technique to obtain band structures of solids [90]. **e**, Today, new detectors allow faster and multidimensional acquisition of photoelectron data [91, 92]. Imaging of molecular and Bloch orbitals is possible.

not on its intensity [94]. In an attempt to disprove Einstein's $E = h\nu$ by photoelectron experiments, Millikan instead put the quantum theory on a firm foundation and obtained accurate values for Planck's h (Fig. 3.1b). This achievement marked the end of the first generation of photoelectron experiments that extracted general information about matter based on a coarse approximation of the kinetic energy of photoelectrons.

A few decades later, in the 1950s, Siegbahn realized that photoelectron experiments could be developed into a spectroscopic method supplying information about the chemical composition of materials [89]. This insight was the birth of photoemission spectroscopy, which quickly overcame the initial difficulties related to the strong interactions of electrons with matter, which makes the method extraordinarily surface-sensitive and requires sophisticated vacuum methods. Advances in instrumentation, a mature theory of the solid state, and the ability to grow single crystals brought photoelectron spectroscopy to a new level. Siegbahn developed the use of X-rays to study the chemical environment of atoms into a technique routinely used for chemical analysis (Fig. 3.1c). As the technique matured, it went beyond using X-rays to study the atomic environment to many implementations, ranging from bulk-sensitive hard X-ray photoelectron spectroscopy to photoelectron diffraction and photoelectron microscopy. Among these, the study of the angular distribution of electrons photoemitted from a solid (angle-resolved photoemission spectroscopy - ARPES) became "the method of choice to study the electron dispersion curves of solids" [95] (Fig. 3.1c). It allowed the determination of the band structure of metals [90], the detection of the small superconducting gap in high-temperature superconductors [96], and the observation of Dirac fermions in graphene [97].

Then, advances in photoelectron detectors made it possible to routinely measure the whole photoemission hemisphere (Fig. 3.1d). Modern detectors provide more than just spectroscopic information by imaging electrons in a two-dimensional momentum space, thus giving direct access to spatial information. The data sets obtained by these new detectors are three-dimensional — they provide the photoelectron intensity $I(k_x, k_y, E)$ as a function of the in-plane momenta and the kinetic energy. Cutting through such a data set at constant energy gives *momentum maps*.

Today, ever more dimensions are being added to the photoelectron spectroscopy arsenal. Pump-probe techniques make it possible to record the dynamics of photoexcited states in a stroboscopic fashion. The resulting data sets consist of 3D snapshots of the electronic

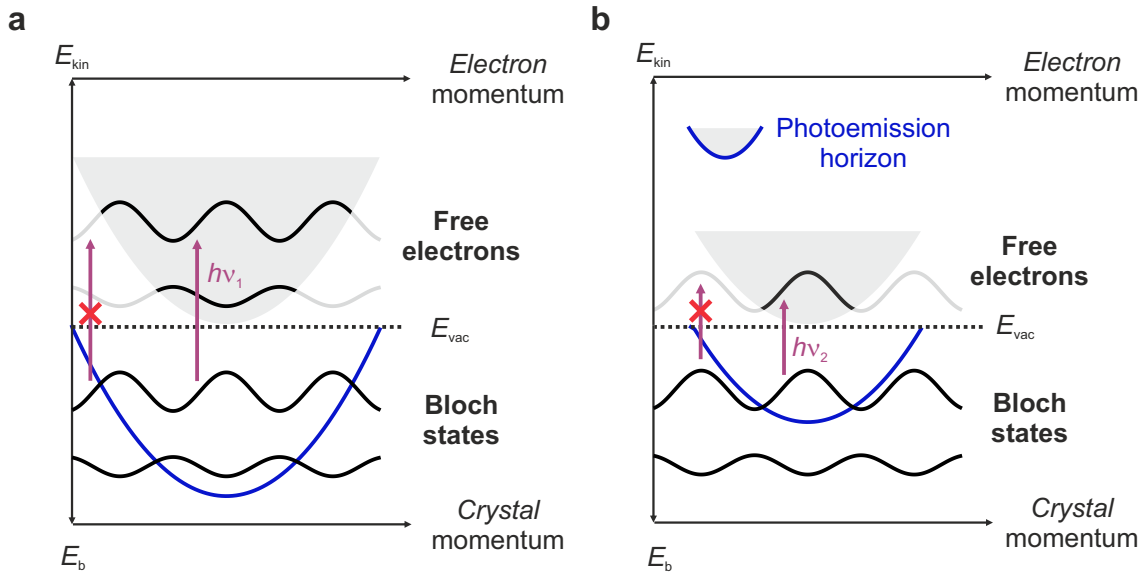


Figure 3.2. Photoemission kinematics with two different photon energies. **a**, A photon with energy $h\nu_1$ ejects an electron from a Bloch state into a free electron state. **b**, The same diagram with a smaller photon energy $h\nu_2$.

structure at different time delays Δt and are thus four-dimensional, $I(k_x, k_y, E, \Delta t)$. This technique is called time-resolved and angle-resolved photoelectron spectroscopy (trARPES) and is the method used in this thesis. High dimensionality is not restricted to the time delay in a pump-probe experiment; any continuously scanned variable, such as pump polarization, sample position, or temperature, can be recorded. The resulting data set is multidimensional and a function of many variables $I(k_x, k_y, E, \Delta t, \theta, \sigma, x, y, \dots)$.

3.2 Photoemission kinematics

The impinging photons define the limits of the kinetic energies and momenta of the outgoing photoelectrons. Quite generally, a photoemission experiment involves the excitation of an electron with a photon of energy $h\nu$, the subsequent escape of the photoelectron, and its detection. Depending on the binding energy E_B of the electron, it leaves the material with a kinetic energy $E_{\text{kin}} = h\nu - E_B - E_I$. Here, E_I is the ionization energy of the material, which for an extensive range of materials is ~ 5 eV. Because the kinetic energy must be greater than zero, only states with $E_B < h\nu - E_I$ can be accessed; higher photon energies allow measuring more firmly bound states with a larger E_B .

The velocity of the released electron has two in-plane components and one out-of-plane component. During photoemission, in-plane momentum is conserved and a Bloch state with in-plane crystal momentum \mathbf{k}_{\parallel} is converted to a free electron with in-plane momentum \mathbf{p}_{\parallel} (see Fig. 3.2). The maximum free electron momentum attainable for a given photon energy $p_{\text{max}} = \sqrt{2E_{\text{kin}}m}$ defines the photoemission horizon. For a typical photon energy $h\nu = 20$ eV, the maximum momentum is $\frac{p}{\hbar} \approx 2 \text{ \AA}^{-1}$ — large enough to fully sample the Brillouin zone of most materials. Smaller photon energies only probe a fraction of the Brillouin zone. The photon energy thus defines the range of probed binding energies and the radius of the photoemission horizon. The photon energy also determines the cross section of the photoemission transition — generally, at low kinetic energies, the cross-section is enhanced for states with low angular momentum (electrons in s - or p -orbitals) and at

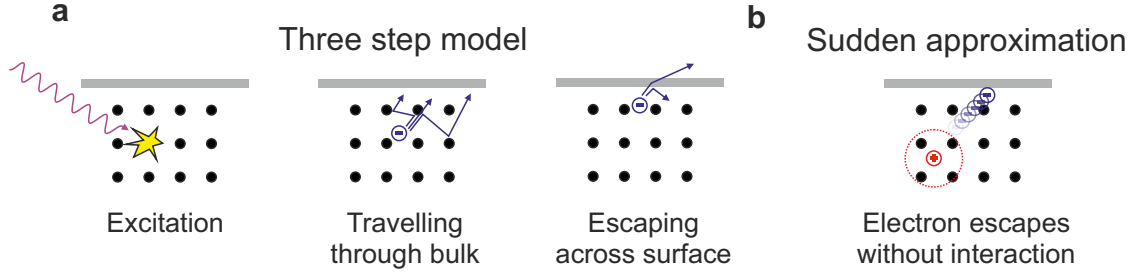


Figure 3.3. Approximations in the theoretical treatment of photoemission. **a**, The three-step model separates the photoemission process into three steps. The photoexcitation (1) is followed by the already independent photoelectron traveling through the bulk and scattering on the lattice (2) and the escape of the photoelectron at the surface (3). **b**, In the sudden approximation, any interaction of the photohole with the photoelectron is neglected.

high kinetic energies, the cross-section with states of high angular momentum (electrons in d -orbitals) is enhanced [95].

3.3 Quantum mechanical treatment

To relate the recorded photoelectron momenta and energies to the electronic structure, we describe the interaction of the photon's electric field with the material's electronic states in a perturbative regime. The final states $|f\rangle$ can be approximated by a continuum of free electron states. We may employ Fermi's golden rule to derive the transition rate from a bound initial state $|i\rangle$ to a free final state $|f\rangle$ with kinetic energy E_{kin} :

$$w_{fi} = \frac{2\pi}{\hbar} \left| \langle f | \hat{H}' | i \rangle \right|^2 \delta(h\nu - E_I - E_B - E_{\text{kin}}). \quad (3.1)$$

Here, the δ -function ensures energy conservation. The perturbation H' of the electron with momentum \mathbf{p} with the electric field with vector potential \mathbf{A} in the dipole approximation is given by $\hat{H}' = -\frac{e}{mc} \mathbf{A} \cdot \mathbf{p}$ [98]. While the photoemission process is, in principle, a single coherent process influenced by scattering and interference effects, it is a reasonable approximation to separate the process into three steps (see Fig. 3.3a). The first step is the photoexcitation of the bound electron. Then, the liberated electron travels through the bulk and may scatter on the atoms it passes. Finally, it escapes through the surface, where it may refract and scatter. This approximation has been routinely and successfully used and is known as the *three step model*, and allows writing the total photoemission intensity a product of the individual steps [99].

To proceed, we need to define the initial and final states. If the photoelectron is fast, we may assume it does not have enough time to interact with the positive charge left behind (see Fig. 3.3). Then, we can write the final state as a product of a free electron $\varphi_{\mathbf{k}}^f$ and a $(N-1)$ -electron state Ψ_{N-1}^f . Such an approximation (called *sudden approximation*) is appropriate for photons with energies > 15 eV ejecting electrons near the Fermi energy [98]. The initial state $|i\rangle = \Psi_N^i$, on the other hand, may be a weighted sum of different Slater determinants $\Psi_N^i = \sum_j c_j \Phi_N^j$ and must hence be written as a sum of terms, one for each determinant. Each term consists of a product of a one-electron orbital with a corresponding $(N-1)$ -electron state. We can then write the interaction term in eq. 3.1 as

$$\langle f_{\mathbf{k}} | \hat{H}' | i_{\mathbf{k}} \rangle = \sum_j c_j \langle \varphi_{\mathbf{k}}^f | \hat{H}' | \psi_{\mathbf{k}}^j \rangle \langle \Psi_{N-1}^f | \Phi_{N-1}^j \rangle = \sum_j c_j M_{fj} S_{fj}. \quad (3.2)$$

We are now left with two separate terms. The first term M_{fj} is the one-electron matrix element that describes the interaction of the electric field with a one-electron Bloch state $\psi_{\mathbf{k}}^j$. The second term S_{fj} accounts for the overlap of the impulsively ionized system with different cationic $(N-1)$ -electron states. In the following, the matrix element will first be discussed, and then the overlap term.

3.3.1 The one-electron matrix element

A straightforward description of the final electron state is treating it as a free electron and therefore as a single plane-wave component $e^{i\mathbf{p}\cdot\mathbf{r}/\hbar}$ [99, 100]. The power of this simplification is the reduction of the matrix element to a Fourier transform of the initial Bloch orbital modulated by a polarization-dependent term [101]. We remind ourselves of the form of the Bloch orbital in eq. 2.10 [39]. Instead of writing it as a sum of Wannier orbitals centered on different lattice sites, we may recast it as a convolution of a Dirac comb with the plane-wave modulated Wannier function

$$\psi_{\mathbf{k}}(\mathbf{r}) = \frac{1}{\sqrt{N}} \sum_n e^{i\mathbf{k}\cdot\mathbf{R}_n} w_{\mathbf{k}}(\mathbf{r} - \mathbf{R}_n) = \frac{1}{\sqrt{N}} \mathbb{M}_{\text{UC}}(\mathbf{r}) * w_{\mathbf{k}}(\mathbf{r}) e^{i\mathbf{k}\cdot\mathbf{r}}.$$

Here $\mathbb{M}_{\text{UC}}(\mathbf{r})$ is a Dirac comb with the periodicity of the unit cell, and $\frac{1}{\sqrt{N}}$ is a normalization factor. In the plane-wave approximation, we can use this formulation to write the matrix element as a Fourier transform of the Bloch orbital

$$M_{fj}(\mathbf{p}/\hbar) \propto \langle \mathbf{p}/\hbar | \psi_{\mathbf{k}}^j \rangle = \mathbb{M}_{\text{BZ}}(\mathbf{p}/\hbar - \mathbf{k}) \tilde{w}_{\mathbf{k}}^j(\mathbf{p}/\hbar).$$

$\mathbb{M}_{\text{BZ}}(\mathbf{p}/\hbar - \mathbf{k})$ is a Dirac comb with the periodicity of the Brillouin zone shifted by the crystal momentum \mathbf{k} , and we have included the index j to stress that the matrix element varies for different Slater determinants in the initial state. The matrix element is hence proportional to a product of δ -functions at all equivalent \mathbf{k} -points of the initial state and the Fourier transform of the associated Wannier function. For completeness, we note that we can equivalently perform the Fourier transform on a localized Bloch orbital as defined in eq. 2.15. This yields

$$M_{fj}(\mathbf{p}/\hbar) \propto \left(\mathbb{M}_{\text{BZ}}(\mathbf{p}/\hbar - \mathbf{k}) * \hat{F}_{\text{env}}(\mathbf{p}/\hbar) \right) \tilde{w}_{\mathbf{k}}^j(\mathbf{p}/\hbar).$$

In contrast to the infinitely narrow δ -functions of the Bloch orbitals, the peaks at each \mathbf{k} -point have now acquired a finite width proportional to the width of the Fourier-transformed envelope function. An insightful analogy to the matrix element and, correspondingly, the photoemission intensity is a slit interference experiment, as shown in Fig. 3.4. If we investigate a state localized to a single site, the photoemission intensity is proportional to the absolute square of the Fourier transform of the corresponding orbital. In the analogy, we replace the site with a single slit on which a plane-wave is impinging. The transmitted intensity on the detector is proportional to the Fourier transform of the slit function. A delocalized state, on the other hand, consists of many sites coherently emitting electrons over a localization length L , in close analogy to a plane-wave passing through multiple slits that mutually interfere.

The simple Fourier correspondence of the wave function and the photoemission signal is the hallmark of the plane-wave approximation. The analysis was so far carried out in two dimensions, however, and we have completely neglected the dependence of the photoemission intensity on the out-of-plane momentum. Naturally, the orbital will have a specific shape normal to the plane. Instead of evaluating just the in-plane orbital structure, the entire

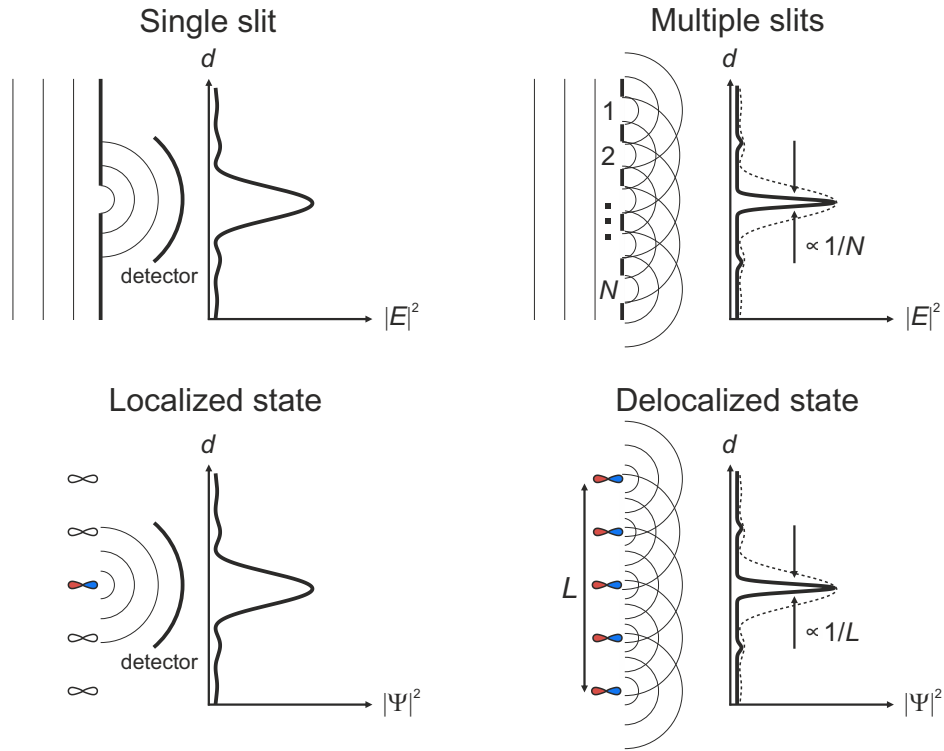


Figure 3.4. Photoemission as a slit interference experiment. In the plane-wave approximation, the matrix element of the photoemission transition can be seen as a Fourier transform of the one-electron Bloch state the photoelectron originated from. Photoemission from a localized state is then related to a plane wave passing through a single slit. A delocalized state emits coherent electron waves from different sites and can be understood as a plane wave passing through multiple slits that mutually interfere.

three-dimensional shape has to be taken into account. The corresponding three-dimensional Fourier transform must then be evaluated on a hemisphere with the radius of the PE horizon. Furthermore, there are limitations of assuming the final state is a single plane-wave component. This approximation applies to materials made of light atoms and to normal emission from π -orbitals [101, 102], as realized for photoemission from flat-lying benzenoid hydrocarbons. For more complex materials and a more complete picture, it might be necessary to include more plane-wave components in the description of the final state or to employ a full one-step and many-body description of the photoemission process [99].

The polarization of the impinging light leads to a modulation of the matrix element that is given by [101]

$$M_{fj}(\mathbf{p}/\hbar) \propto \mathbf{A} \cdot \mathbf{p}/\hbar,$$

making apparent the intuitive suppression of photoemission intensity if the electric field is normal to the momentum of the photoelectron.

In chapter 5, the structure of momentum maps, constant energy cuts through the photoemission intensity, will be discussed in more detail.

3.3.2 Single-particle band structure

Without electron correlation, the initial wave function can be represented by a single Slater determinant for each value of \mathbf{k} . The overlap term in S_{fj} is then unity for a single configuration, and the photoemission intensity features a single peak at the single-particle

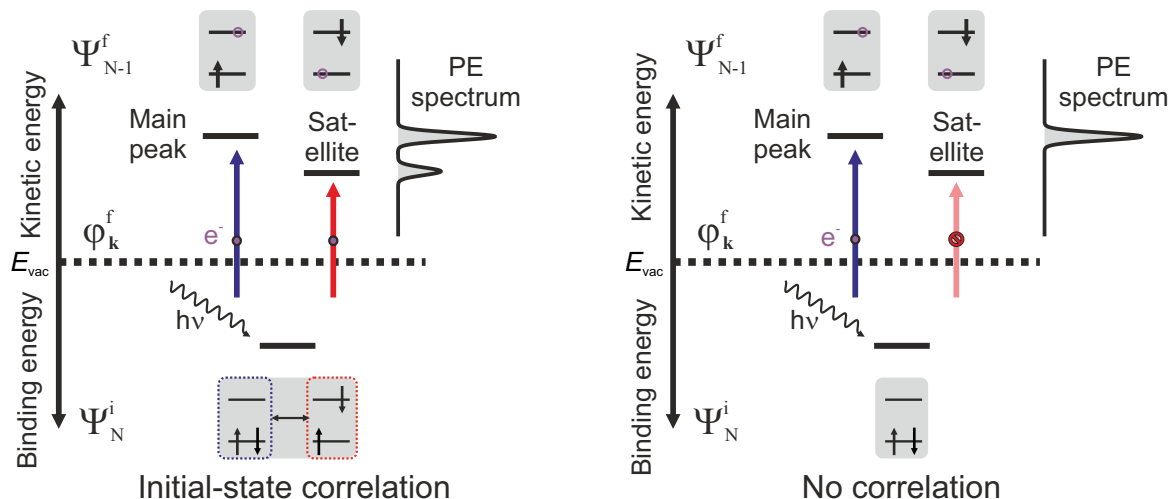


Figure 3.5. Satellite peak due to initial-state correlation. The combination of two Slater determinants in the initial state allows for the emergence of a satellite below the main peak. The corresponding transition would be forbidden without the admixture of the excited configuration.

band energy $\epsilon_{\mathbf{k}} = h\nu - E_{kin} - E_f$. Sampling the whole Brillouin zone of a material then yields the single-particle band structure.

3.3.3 Multiparticle states: Satellites and electron correlation

Molecules and solids are many-electron systems. Ripping out an electron from this system must lead to a response of the remaining electrons. The response manifests in the population of excited cationic states in the system, which leads to a lower kinetic energy of the outgoing electron. In the photoemission spectrum, these excitations are visible as *satellite* lines that accompany the main single-particle line, and their relative strength is determined by the overlap of the initial- and final-state wave functions. Many electronic states show correlation, either in the ground or an excited state, and the wave function cannot be factorized into one-electron orbitals anymore and instead has to be denoted as a combination of Slater determinants. This correlated initial state might overlap with many cationic final states and cause the emergence of satellite lines. On the other hand, the ionization of a state without correlation, a single-particle state, might overlap with several cationic states that do show correlation and hence must be denoted as a combination of Slater determinants — again causing satellite lines. Here, we focus on the description of satellites due to initial-state electron correlation and neglect final-state correlation, for which we refer the reader to the works of Siegbahn [103] and Huefner [95].

Consider an N -electron state that is a combination of two N -electron Slater determinants, (1) the ground state configuration and (2) the first excited configuration, as shown in Fig. 3.5. The incident light can rip out an electron from either of the two configurations. For the blue ground state configuration, removal from the lowest-lying level is possible, leaving a hole in this level behind in the $(N-1)$ -electron final state. The red excited configuration can transition to the same final state if an electron is removed from the highest-lying level. However, a second transition is possible when an electron is ejected from the lowest-lying level. Now, the remaining electron is in the highest-lying level, and the excited $(N-1)$ -electron state left behind has more energy. Correspondingly, the photoemission process populated an excited cationic state and ripped out a photoelectron with less kinetic energy that accounts for the emergence of a new peak — the satellite peak.

In real systems, the description of the wave function becomes much more complex, and the correlation might take on different forms. In conclusion, initial-state correlation leads to the emergence of satellite peaks in the photoemission spectrum that would not be expected for a single electron configuration.

3.3.4 Vibrational satellites and electron-phonon coupling

Like any electronic transition, the photoemission transition obeys the Franck-Condon principle. Upon ionization, the system finds itself in a new potential energy surface, and the transition may excite vibrational quanta. The relative intensities of the vibrational satellites accompanying the main 0–0 transition are given by the overlap of the nuclear wave functions before and after ionization. The intensities of the peaks are usually well-reproduced by the Poisson progression introduced in eq. 2.4 and parametrized by the Huang-Rhys factor. The difference here, however, is that the transition is from a neutral initial to a cationic final state. As in the case of the HOMO-LUMO transition, the vibrational substructure of the spectrum can be used to determine the reorganization energy associated with creating a hole. The photoemission spectrum, therefore, provides information about the electron-phonon coupling in the system.

3.4 Time-resolved ARPES

The above discussion has been limited to states in equilibrium, where ARPES has provided detailed information and novel insights, specifically into many-body states. With the progress made in laser technology after the 1960s, it became possible to do time-resolved photoemission experiments to study non-equilibrium states using pump-probe techniques [104]. In these experiments, a pump pulse excites the system, and a short-wavelength probe pulse probes the system after a time delay Δt . The technique matured to two-photon photoemission spectroscopy (2PPE) [105]. While offering access to femtosecond time resolution and providing valuable insights into hot-electron or surface state dynamics, 2PPE lacked the momentum resolution of static ARPES. With the advent of high-harmonic generation (HHG), which made pulsed extreme-ultraviolet (XUV) sources possible, the door opened to table-top ARPES experiments with femtosecond time resolution. In time-resolved ARPES (trARPES), the photoemission intensity also depends on the pump-probe delay: $I(\mathbf{k}, E_{\text{kin}}, \Delta t)$.

In standard HHG setups, a laser provides ultrashort light pulses that are split between a pump and a probe line. In the probe line, the pulses are guided into a vacuum chamber in which they are focused onto a stream of rare gas atoms. The strong electric fields due to the tightly focussed and ultrashort pulse (on the order of the field strength between valence electrons and nuclei ($\sim 1 \text{ V \AA}^{-1}$)) lead to the ionization of the atoms, which release bursts of XUV radiation upon recombination with the accelerated electron. While the process is a single coherent event, it can be simplified into three steps: ionization, acceleration, and recombination [106]. At each wave crest of the oscillating field, electrons escape into the vacuum in the presence of the strong field. They accelerate in the slope of the pulse and, as the pulse field changes sign, return to the cationic atom, where they recombine and release their energy as a burst of XUV radiation. The spectrum of this radiation consists of only odd harmonics of the driving frequency, and the beam has to consequently be frequency-filtered to obtain the monochromatic XUV radiation required for photoemission.

The frequency of the pump pulse defines which non-equilibrium process is launched in the studied system. Correspondingly, a large variety of experimental schemes exist for the pump line, depending on the process under investigation. In the pump lines, non-linear optics

(most commonly second harmonic generation, optical rectification or optical parametric amplification) is exploited to obtain wavelengths from the THz- to the VIS-regime. Such a wide variety of excitation conditions makes investigating many physical processes possible. Some examples include the dynamics and characterization of bright and dark excitons [107], the observation of structural [108] or electronic phase transitions [109], observing currents driven by lightwaves [110] and a band-resolved analysis of electron-phonon coupling [29, 111, 112].

A fundamental limit to the processes observable by trARPES is set by the time- and energy resolution (Δt and ΔE , respectively) determined by the bandwidth of the light pulses. There is a trade-off between high time resolution, which requires large bandwidths, and high energy resolution, calling for a narrow bandwidth [113]. State-of-the-art HHG-based trARPES setups operate in two different regimes: a high time-resolution regime where $\Delta t \approx 50$ fs and $\Delta E \approx 100$ meV [107, 114] and a high energy-resolution regime where $\Delta t \approx 200$ fs and $\Delta E \approx 20$ meV [115].

Additional limitations are the interaction of ejected photoelectrons with themselves (probe-induced space charge) and with pump-induced photoelectrons (pump-induced space charge). The former is controlled by the number of photoelectrons N_{em} emitted per probe pulse. For large N_{em} , the photoelectrons interact with each other and experience a shift of their kinetic energy, which leads to a loss of information. For practical purposes, the number of detected electrons per pulse N_{det} is a more helpful measure since it is the quantity that is directly measured by the detector. The threshold value at which a visible shift of the bands sets in depends on the collection efficiency of the detector and the detection scheme itself [114, 116].

If the energy of the pump photons is close to the work function of the sample, multi-photon photoemission becomes likely. Furthermore, sharp features of the sample surface might locally reduce the work function or favor plasmon-enhanced photoemission, additionally amplifying photoemission from the pump. The resulting pump-induced electrons possess a much lower kinetic energy than the probe-induced electrons. On the way from the sample to the detector, the faster probe-induced electrons dynamically interact with the pump-induced electrons. This interaction restricts the photon energies of the pump to typically < 3 eV and the fluences at photon energies > 1 eV. Furthermore, it may lead to artifacts in the signal that have to be carefully accounted for. These effects are most pronounced for detectors that rely on a time-of-flight detection scheme in which the interaction volume of pump- and probe-induced electrons is substantial [114].

3.5 Brief description of the experimental setup

The experimental setup¹ consists of a light source and an ultra-high vacuum (UHV) analysis chamber to which the light source is coupled. The initial mode-locked light pulses are generated in a Yb oscillator, which supplies pulses centered at 1030 nm at a 25 MHz repetition rate and 100 mW power. These pulses are amplified in a fiber amplifier, which increases the power to 10 W at a reduced repetition rate $f_{\text{rep}} = 500$ kHz. At this stage, the beam is split into two arms; one supplies the seed for the next amplification stage while the other arm is split again, where one part is guided to a white light generation setup and the other to the first pump arm. In the next amplification stage, a slab amplifier further increases the power to 200 W. The output is compressed and guided to a BBO crystal in which the second harmonic at 515 nm is generated by a second-order non-linear process.

¹Note that this section describes the experimental setup used at the Fritz Haber Institute up to 2023, at which point it was substantially upgraded.

The output pulses are the pump pulses for a noncolinear optical parametric amplifier (NOPA) [117].

The beam split off after the first amplification stage is first compressed and then focused onto a YAG crystal, in which white light is generated via a third-order non-linear process. The broadband pulses are stretched and guided to a BBO crystal, where they serve as a seed for the OPCPA. In the BBO, the seed and pump pulses are recombined and amplified pulses tunable in a range from 650 nm to 950 nm are generated [118]. The output light has a power of 15 W and the pump-seed delay is set such that the central wavelength is at 800 nm with a bandwidth of $\text{FWHM} = 80 \text{ meV}$. They are compressed in a prism compressor to a pulse duration $< 40 \text{ fs}$ [119]. After the compression, the beam is split into two arms: a second pump arm and the probe arm.

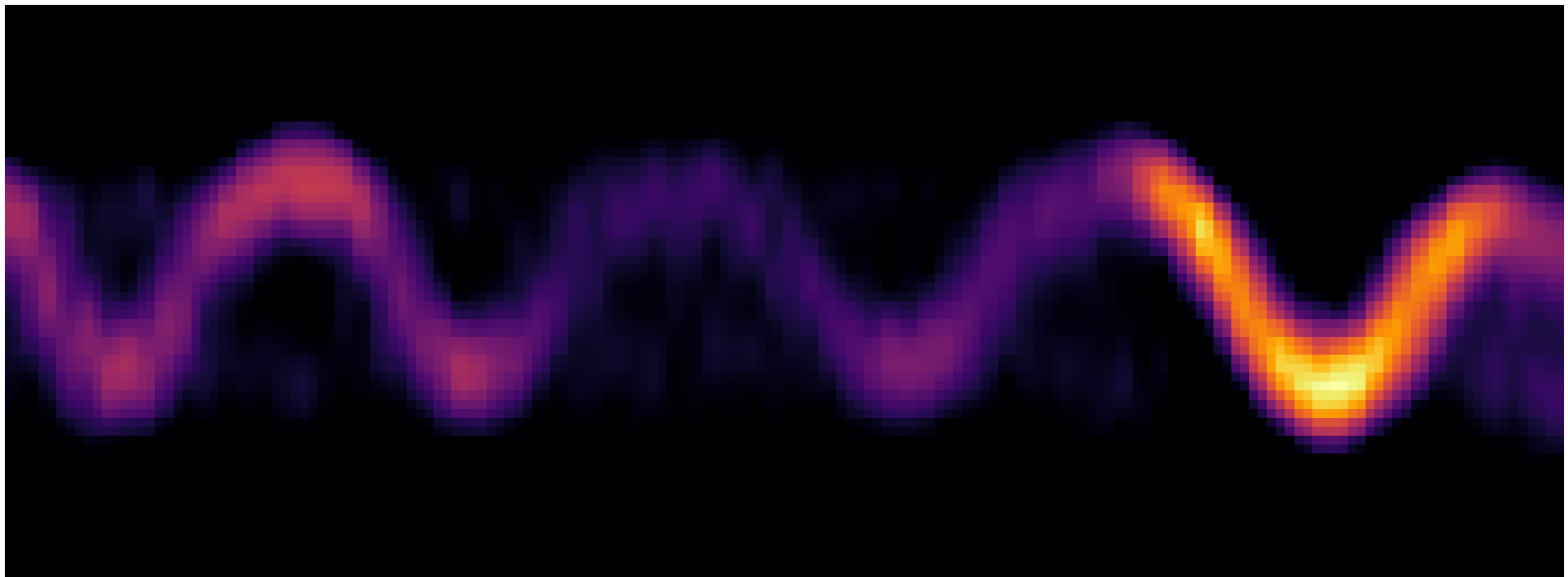
In the probe arm, the pulses are frequency doubled to 400 nm and then coupled into a vacuum chamber which hosts the HHG setup. Here, a gas nozzle supplies a constant stream of Argon atoms onto which the beam is focussed. As described above, the HHG process allows for the generation of odd multiples of the driving pulses' frequency, $E = (2n + 1)\hbar\omega$ with $\hbar\omega = 3.1 \text{ eV}$. It is crucial to separate the fundamental frequency from the high-order harmonics and one high-order harmonic frequency from the other harmonics. Several methods have been implemented in the trARPES setup at the FHI to achieve the former, including a reflection on a silicon wafer at the brewster angle, on which most of the fundamental is absorbed. At the same time, the high-order harmonics are mostly reflected [119], and a holed focussing mirror, which generates a ringed fundamental beam in the far field. An aperture then separates the ringed beam. The latter setup allows a rotation of the polarization, which is forbidden in the Brewster plate configuration. Selection of a single harmonic, which is set to the seventh harmonic at 21.7 eV, is achieved via a combination of a reflection on a multilayer mirror and a transmission through a tin foil, guaranteeing a contrast of 10^{-4} between the 7th and the ninth harmonic. [119]. The energy width of the output XUV pulses ($\text{FWHM} = 110 \text{ meV}$) is slightly larger than the width of the pump pulses.

There is a third pump arm, which is a copy of the high-power NOPA — it combines the 1030 nm split-off arm after the fiber amplifier and the leftover fundamental at 1030 nm from the second harmonic generation stage after the slab amplifier. The former is again used to generate white light to seed the NOPA, and the latter is frequency doubled to supply the pump for the NOPA at 515 nm. After parametric amplification in a BBO, the pulses are guided to a prism compressor, finally yielding pulses that are tunable in a range from 650 nm to 760 nm. The limited tunability compared to the high-power NOPA results from the narrower white light spectrum. The first pump arm is the remaining output of the Yb oscillator at 1030 nm which may be frequency doubled to supply pulses at 2.4 eV and $t_{\text{FWHM}} = 200 \text{ fs}$.

The pump pulses are focussed just before they are coupled into a vacuum chamber, where they rejoin the path of the probe pulses. Both beams are collinearly incident on the sample in the UHV measurement chamber. The spot size of the probe beam on the sample is $130 \mu\text{m}$ (FWHM) [119], and for the pump beam it varies for different photon energies, but is commonly on the order of $200 \mu\text{m}$. The spot sizes for each measurement are given in chapter 6. In the case of molecular semiconductors, the pump pulses serve two purposes: (1) they populate non-equilibrium states, and (2) they generate photocarriers that provide sufficient conductivity to avoid sample charging. The XUV pulses then eject photoelectrons from the excited sample which are collected in a time-of-flight momentum microscope (all details of the detector end station can be found in [114]). First, the photoelectrons travel through an extractor lens, which collects the whole hemisphere of emitted electrons by

applying a large positive voltage. Subsequently, the electrons are subject to an array of electrostatic lenses, which create first a reciprocal image plane and then a Gaussian image plane. It is possible to place contrast and field apertures, respectively, into these image planes, which allows selecting sections of the full reciprocal or real space. After passing through the image planes, the electrons travel through a fieldless time-of-flight drift tube until they reach a delay-line detector, where each electron's arrival time and position are recorded. These parameters are converted into kinetic energy and momentum, respectively, and, finally, the electron point cloud is binned into a 3D histogram, in which the electron counts in each $(E_{\text{kin}}, k_x, k_y)$ -bin correspond to the PE intensity $I(E_{\text{kin}}, k_x, k_y)$ [120].

Having discussed the basics of time- and angle-resolved photoemission spectroscopy, we turn to the electronic structure of single crystals of molecular semiconductors at equilibrium in the next chapter.



4. Electronic structure and fluctuations of molecular semiconductors

Here, the fundamentals of charge transport and their application to crystalline molecular semiconductors are introduced. Due to the inherent fluctuations in these materials, transport is thought to occur in the so-called transient localization regime. We show how ARPES can provide crucial information for understanding charge transport and describe how it is conducted on single crystals of molecular semiconductors. We then introduce the investigated materials and the general structure of an ARPES data set. Based on a simple tight-binding model, we discuss how the observed electronic structure can be understood and how the tight-binding parameters determine the resilience of electronic states to fluctuations. Subsequently, we present the experimental band structures of the highest-lying bands and how they relate to the crystal structure. We find that the structure of the underlying molecular orbitals is crucial to understanding the electronic structure and, hence, investigate the origin of the orbital structure. Then, we extract parameters relevant to charge transport from the presented data: the effective mass and the localization properties of the highest-lying states. The last section introduces how rationally engineered orbitals may reduce the electron-phonon coupling and thereby enhance charge transport in next-generation materials.

The results presented in this chapter are under revision after submission to *Advanced Materials* at the time of writing.

4.1 Introduction

How do electrons move through the dense arrangement of atoms in a solid? This question is fundamental to electronics and has been triumphantly answered for inorganic crystals by solid-state physics in the first half of the 20th century. The first theory of electron conduction was developed by Drude [121], who considered a fixed and periodic arrangement of nuclear cores surrounded by free, unbound electrons in a so-called electron gas. In this picture, the electrons may freely move through the solid until they collide with an impurity or a cation. Shortly after Drude, Bloch was the first to describe electronic states in a periodic potential using the newly developed quotoolkit of quantum mechanics [122]. He

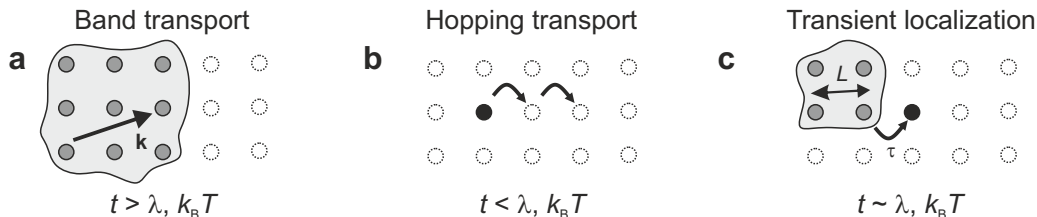


Figure 4.1. Mobility models. **a**, In the band transport model, charge carriers are delocalized over many unit cells and have a well-defined momentum. **b**, The limit of small transfer integrals t is the basis of incoherent hopping transport, where localized charge carriers have to pay the reorganization energy to hop to the next site. **c**, In between those two limits, the transient localization scenario describes transport based on delocalized carriers that localize by large intermolecular vibrations.

suggested that electrons in the solid reside in orbitals that are delocalized over the whole system. His theory was the basis for the band theory of solids, which correctly describes the electronic states in crystalline metals, semiconductors, or insulators. Due to impurities and phonons, the Bloch electrons do not extend over the whole material. They do, however, form wave packets that span many unit cells [39] and therefore have a well-defined *crystal momentum* k . Intriguingly, an electric field present in the material works on the crystal momentum in the same way as it does on the electrons' momentum in free space, giving rise to the semiclassical equations of motion [39]. The effect of the solid is to change the mass of the electron to the *effective mass*, determined by the band structure. Such a description of charge transport is valid if the trap potential for an electron on an atom (quantified by the hole reorganization energy λ_h) is much smaller than the kinetic energy it gains by delocalization (quantified by the transfer integral t). The parameter space of small λ_h and large t marks the regime of band transport (Fig. 4.1a).

Conduction in amorphous systems operates drastically differently from band transport [123]. Due to the disorder, the electrons are localized and trapped and, hence, do not have a well-defined momentum. They must be promoted to an extended excited state to hop to the next trap. This process leads to a complete loss of coherence after the jump, and an activation energy needs to be paid again for the next jump to occur. Such a regime is reached if the trapping energy is larger than the kinetic energy and the thermal energy. Transport occurring in this regime is called *hopping transport* (Fig. 4.1b). A similar description also holds for systems with strong electron-phonon coupling, where the charges are trapped as polarons by the reorganization of surrounding nuclei [124].

Charge transport measurements on molecular semiconductors at room temperature have revealed several inconsistencies between both theories. In high-mobility molecular semiconductors, the mobility decreases with temperature [49, 125, 126], as predicted by the increased scattering on phonons in a band picture. At the same time, the mean free path of carriers in molecular semiconductors is smaller than the lattice spacing. This condition is called the Ioffe-Regel criterion and flags the breakdown of bandlike transport [8]. Thus, neither entirely incoherent hopping nor fully coherent bandlike transport adequately captures transport phenomena in these soft materials. The reason lies at hand: the assumptions of the microscopic states underlying both theories are inappropriate for molecular semiconductors. Here, electrons are coherently delocalized over several molecules, in contrast to the fully localized states in hopping theory and the fully delocalized states of band theory. Furthermore, the disorder that leads to localization is dynamic due to the thermal movement of the molecules. These fluctuations change the interaction between molecules so drastically that the assumption of translational invariance breaks down.

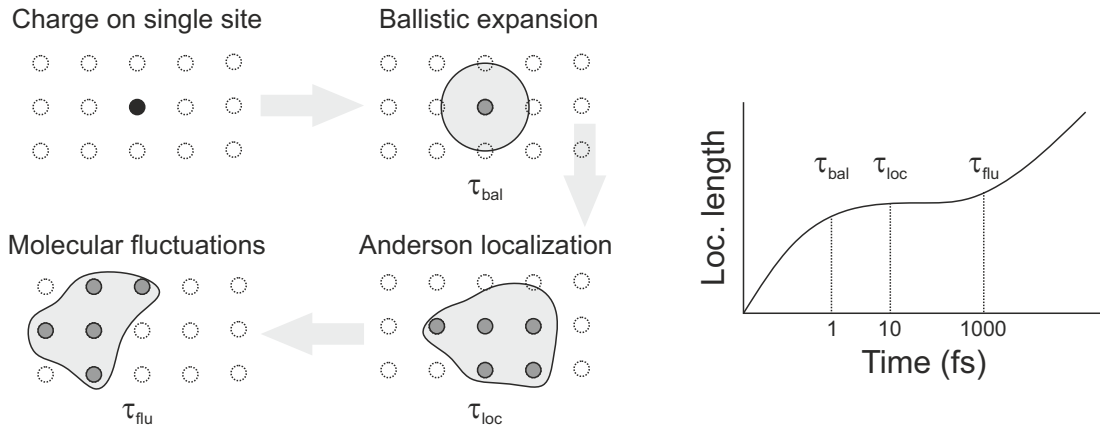


Figure 4.2. Time scales of transient localization. A charge initially localized on a single site expands ballistically over a time scale defined by τ_{bal} . Due to disorder, ballistic expansion is halted, and the charge is confined to a few sites which occurs in a time scale defined by τ_{loc} . Then fluctuations of the molecules kick in, defined by the period of molecular phonons ($\tau_{\text{flu}} \sim 1$ ps). These change the disordered landscape dynamically and allow for the diffusion of the charge. Inspired by [8].

In this original situation, transport is thought to occur as depicted in Fig. 4.2. A charge initially localized to a single site ballistically expands over a time scale τ_{bal} . Due to disorder, it cannot expand indefinitely and remains localized over a time scale τ_{loc} in which its movement is inhibited. Then, molecular fluctuations change the disorder landscape and allow the charge to localize at a different position. The period of the relevant phonons $\tau_{\text{flu}} \sim 1$ ps determines this regime. Since the charges continuously transition between localized and delocalized states defined by the fluctuating molecular lattice, this scenario has been termed *transient localization theory*.

A key ingredient to the theoretical advances has been the observation of electronic bands in molecular semiconductors [127–129]. ARPES measurements have revealed a sizable bandwidth ~ 500 meV in crystals of representative molecules. Since a band structure only forms if the underlying states are sufficiently delocalized, these measurements prove that the states span several molecules. Furthermore, the values for t and λ could be directly determined and compared, confirming that they are of a similar size, $t \approx \lambda$. Recent theoretical work emphasized that not only the magnitude of t determines transport properties, but also the relative sign of t between the three different nearest-neighbor pairs [43], a result linked to the geometrical frustration in a triangular lattice [130, 131] and the correspondingly reduced effective mass at the band edges. The exact values of the three t 's have been obtained for several compounds from ARPES data.

ARPES data, therefore, serves dual purposes in addressing the pressing question of charge transport in molecular semiconductors. (1) It directly contains information about the microscopic parameters to describe transport, specifically the transfer integrals t . (2) It probes the localization properties of states. Point (1) will be addressed in this chapter, and point (2) in the next.

4.2 ARPES on molecular semiconductors

Here, we present a brief overview of ARPES experiments performed on molecular semiconductors; for a more extensive review, the reader is referred to [132]. Performing angle-resolved photoemission spectroscopy on crystalline molecular semiconductors presents several chal-

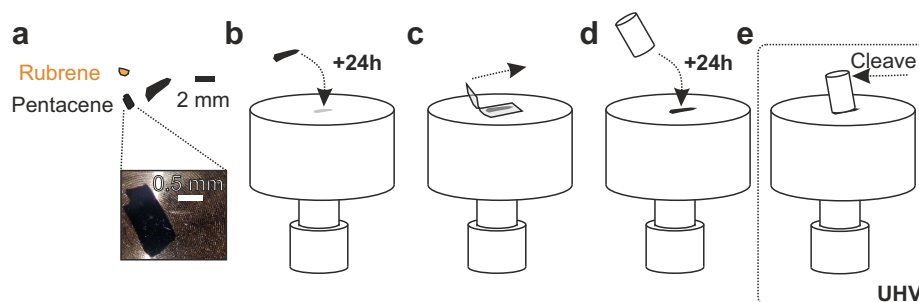


Figure 4.3. Sample preparation. **a**, Typical crystals of rubrene and pentacene used in the experiment (thickness $\sim 100 \mu\text{m}$). The sample preparation consists of several steps. **b**, Gluing the crystal to the sample holder using a minimal amount of conductive glue and waiting 24 h. **c**, Testing the exfoliation properties of the crystal with adhesive tape. **d**, Gluing a ceramic pin to the crystal with minimal glue on the pin. Crucially, the glue from the pin should not touch the sample holder and the pin should be the same size as the crystal. Then waiting for 24 h. **e**, Bringing the sample holder to ultrahigh vacuum and cleaving the pin.

lenges that have been overcome since the first experiments in the 1980's. First, a sample that is crystalline over the XUV spot size (typically $100 \mu\text{m}$) is needed. There have been two ways to achieve this: (1) by deposition of molecules on metal surfaces to form highly oriented thin films [127, 129, 133] and (2) by the growth of single crystals [128], an approach pursued in this work. Secondly, the surface of the sample needs to be free from contamination. That can be achieved by cleaving the sample in ultra-high vacuum, in our case at a pressure $p = 1 \times 10^{-10}$ mbar, which produces a fresh surface that remains clean due to the low pressure. A sketch of the sample preparation is provided in Fig. 4.3. In the two necessary gluing steps, a conductive and UHV-compatible glue is used, which ensures electrical contact with the copper sample holder. The morphology at the surface of the crystals consists of atomically flat staggered terraces with monomolecular step heights [134].

Furthermore, the XUV radiation causes unavoidable and irreversible damage to the molecules in the material that most likely occurs via chemical modifications [132]. This problem can be approached in two ways. One can either maximize the photoelectron detection efficiency by collecting the whole hemisphere of emitted photoelectrons and by avoiding information loss due to space charge effects. Or, one can investigate a larger sample area by working with larger field apertures. That enables higher count rates at constant XUV flux and thus reduces the measurement time and XUV exposure. In effect, the number of sampled molecules is thereby increased. Lastly, a sufficient sample conductivity is a prerequisite to avoid charging the sample by replenishing the missing electrons. Molecular semiconductors have significant band gaps and, therefore, a small number of free carriers that can neutralize the positive charge created by photoemission. However, these carriers can be generated by illumination with photons above the band gap, first pioneered by Sato et al. [135], and the resulting photoconductivity is large enough to prevent charging at room temperature. At lower temperatures, preliminary experiments indicate that sample charging cannot be overcome by creating photocarriers for thick single crystals. Thinner samples or thin crystalline films grown on a substrate might be used to reduce the influence of charging.

The data sets discussed in this thesis were acquired at room temperature using a momentum microscope based on a time-of-flight energy analyzer. In a momentum microscope, a large positive voltage at the objective lens, located close to the sample, draws in the whole hemisphere of emitted photoelectrons. The electrons pass through a lens system, which creates two planes: (1) the image plane, where the position of the outgoing electrons

Molecule	Pentacene	Tetracene	2,2'-ditetracene	Rubrene	Picene
Herringbone angle	52°	55°	54°	62°	59°
Tilt angle	24.8°	22.2°	8.5°	-	15.0°

Table 4.1. Parameters of the crystal structure of the investigated materials. See Fig. 4.4 for sources of the crystal structure data.

is imaged, and (2) the Fourier plane, where the angle is imaged instead. Field apertures with different sizes inserted into the image plane allow selecting different spot sizes on the sample [92]. The lens system can be set to either project a real space image or a momentum space image onto the multichannel plate, which creates the photoemission signal. In this thesis, the data sets were acquired in the momentum mode, which generates a photoemission intensity as a function of kinetic energy E and the two in-plane momentum components k_x and k_y , yielding $I(k_x, k_y, E)$.

4.3 Investigated materials

Five different crystalline molecular semiconductors were considered in this work: pentacene, tetracene, 2,2'-ditetracene (henceforth ditetracene), rubrene, and picene. The first four belong to the class of polyacenes; that is, their core structure consists of linearly fused benzene rings made up only of carbon and hydrogen. Ditetracene is a dimer of two tetracene cores, and rubrene has a tetracene core with four phenyl rings attached to it. The absorption edge of these molecules lies in the visible range with significant oscillator strengths $\alpha \sim 1 \times 10^5 \text{ cm}^{-1}$ at resonant frequencies. In the crystal phase, pentacene, tetracene, ditetracene, and picene grow in a herringbone structure with two molecules per unit cell (Fig. 4.4). The herringbone angles between the two different molecules in the crystal are similar ($\approx 50^\circ$) for all of the investigated materials, but the tilt angles between the long molecular axis and the **ab**-plane increase when going from ditetracene to pentacene (Table 4.1). Rubrene crystallizes in a slipped π -stack structure, in which the molecules align their long axis to the cleavage plane.

Due to the layered structure of the crystals, the nearest neighbors of a molecule all lie in the molecular plane. Each molecule then has six nearest neighbors, of which there are three distinct pairs due to inversion symmetry (see also chapter 2.3). The increasing tilt angle in the herringbone structures increases the offset along the long molecular axis between two neighbors. However, as we will see later, the tilt angle only affects two neighboring pairs.

All crystals were grown in the group of Jens Pflaum at the University of Würzburg using horizontal physical vapour deposition [140], in which the purified material is heated close to its sublimation temperature. A nitrogen flow transports the evaporating molecules towards a cooler region. Here, the oversaturated vapor starts to resublimates and form up to cm-sized single crystals.

The electronic structures of rubrene, tetracene, and pentacene crystals have been studied in great detail theoretically [42, 43, 131, 141–143] and there have also been experimental measurements of the band structures of pentacene and rubrene [127–129, 144]. The experimental band structure measurements were recently summarized by Nakayama *et al.* [132]. However, no published band structure data was available on picene, tetracene and ditetracene at the time of writing.

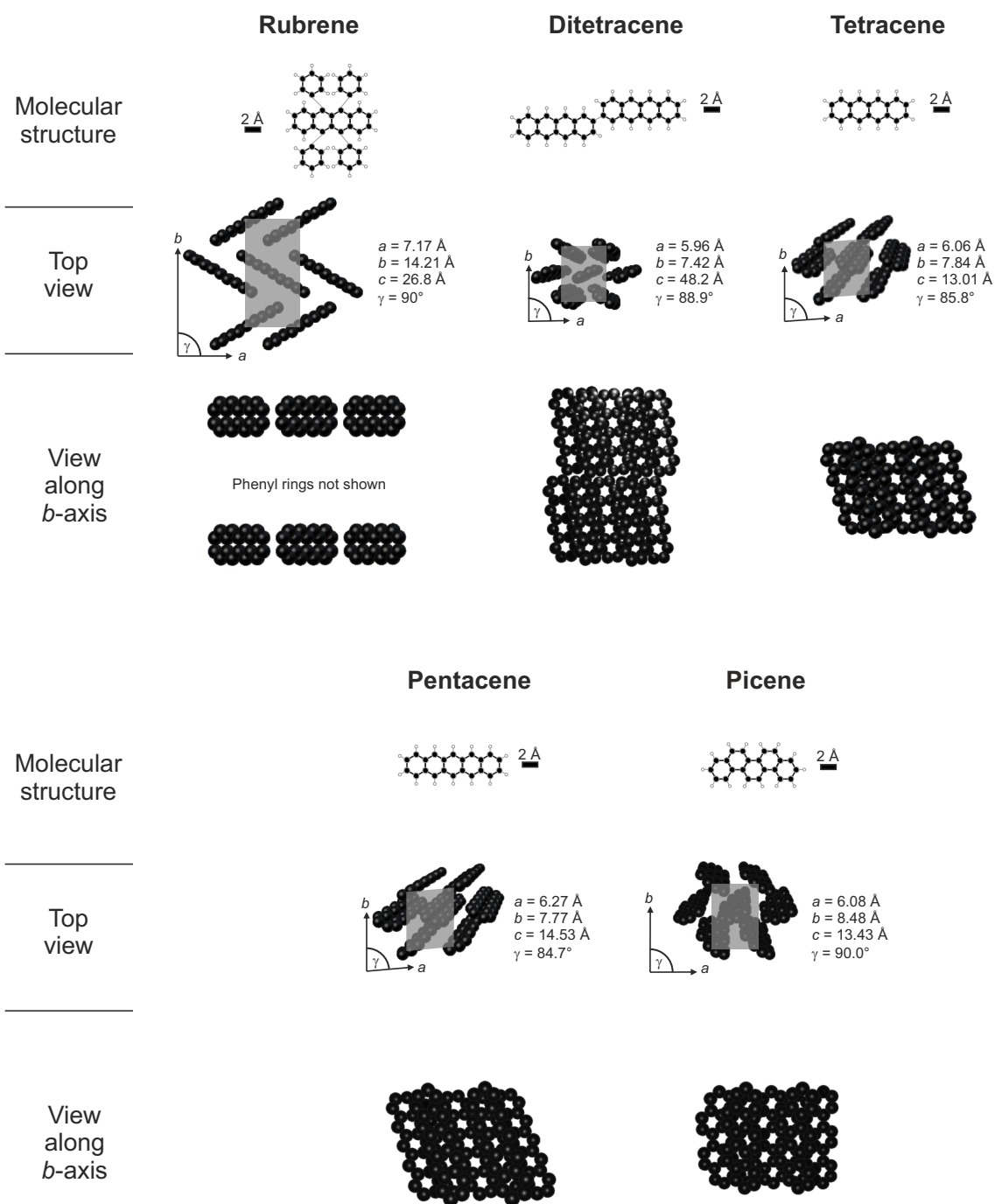


Figure 4.4. Molecular and crystal structure of the investigated materials. In the crystal structure, the hydrogen atoms and phenyl rings of rubrene are omitted for clarity. In the convention used here, the axes are sorted by their length, i.e., *a* is the shortest and *c* the longest axis. Sources of the crystal structures: rubrene [136], ditetracene [137], tetracene [35], pentacene [138], picene [139].

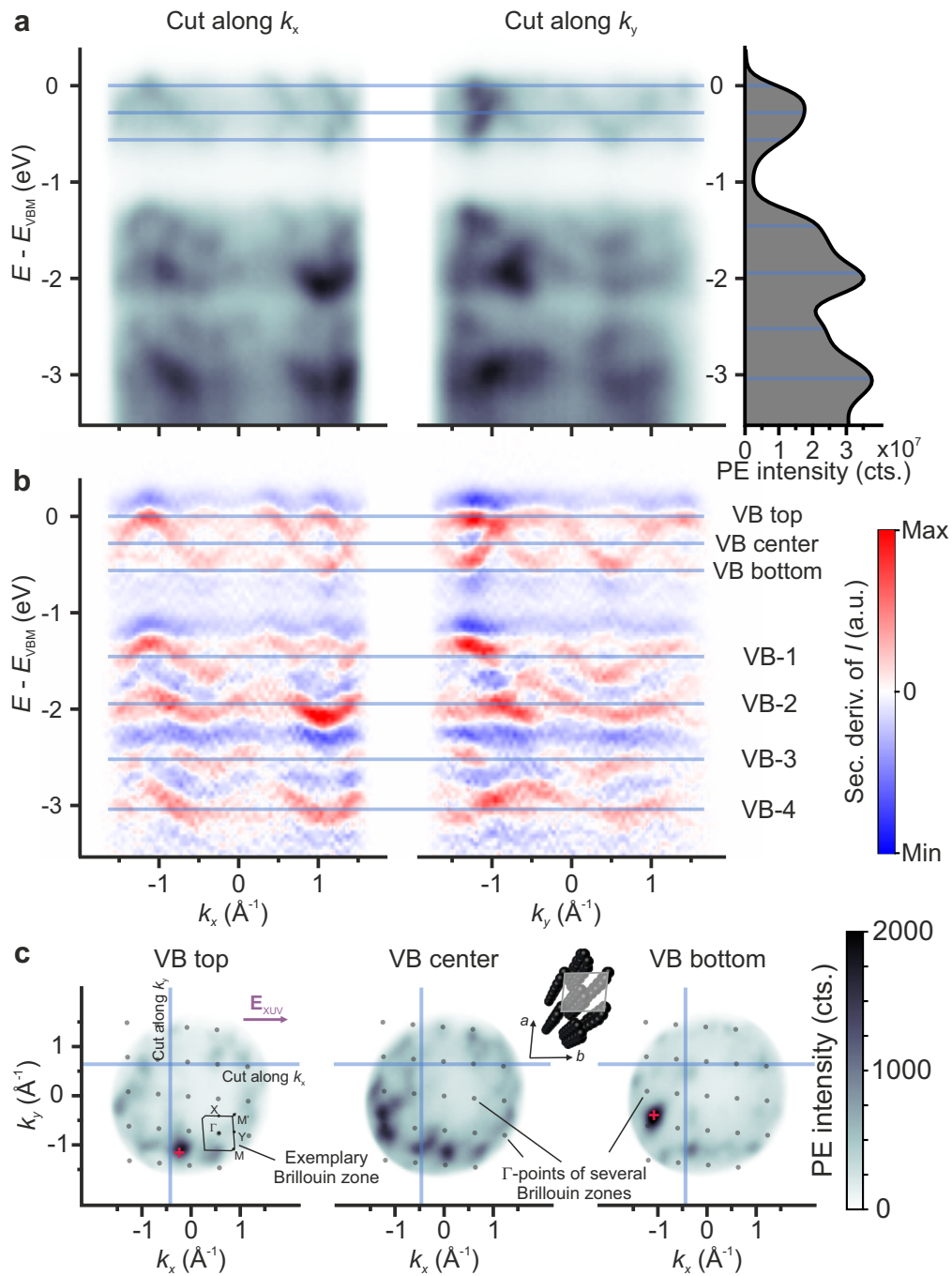


Figure 4.5. Structure of the data: ARPES data of pentacene. **a**, Left: Cuts of the 3D photoemission intensity along two different directions. The color scale is the same as in **c**. Right: Momentum-integrated spectrum. **b**, Same as in **a**, but here, the second derivative of the photoemission intensity with respect to energy is shown. **c**, Constant energy cuts (a.k.a. momentum maps) of the photoemission intensity at energies corresponding to the top, center, and bottom of the VB.

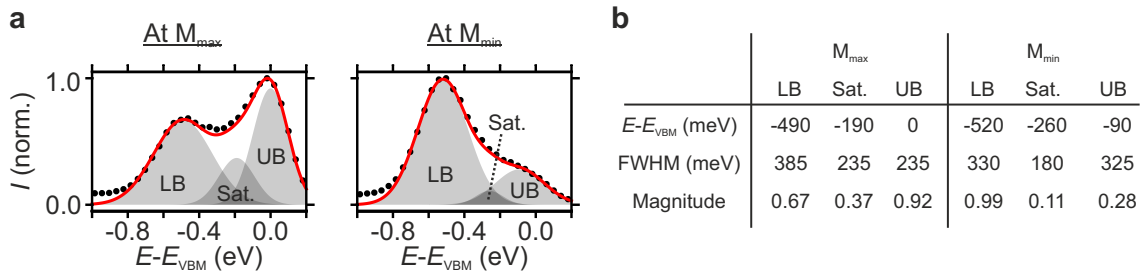


Figure 4.6. EDCs of the valence band of pentacene. **a**, Experimental PE intensity at two points in k -space where the extrema of the band are most pronounced (dotted line). The EDCs were fitted following a procedure in [141] using three Gaussians (red solid line). Two for the two band branches and one for a vibrational satellite of the upper band. The locations of the EDCs are indicated in Fig 4.5c as red crosses. **b**, Parameters of the fitted Gaussians.

4.4 Structure of the data

A representative data set is shown in Fig 4.5. The studied material was a single crystal of pentacene. The bare photoemission intensity $I(E, \mathbf{k})$ is rather blurry, but a faint band structure is visible in the valence band (VB) as the constant momentum cuts along k_x and k_y reveal (Fig. 4.5a). As expected from the two molecules in the unit cell of pentacene, the VB features two branches, as does each of the lower-lying bands. These lie well-separated > 1 eV below and are then spaced by ~ 0.5 eV. Taking the second derivative of the photoemission intensity with respect to energy reveals the bands much more clearly (Fig. 4.5b). The periodicity of the bands is apparent with a period of 0.8 \AA^{-1} along k_x and 1.0 \AA^{-1} along k_y , consistent with the Brillouin zone of pentacene. As the lower-lying bands partially overlap in energy, it is more challenging to distinguish individual branches.

Slicing the data set along constant energy yields the *momentum maps* shown in Fig. 4.5c for the VB top, center, and bottom. In these maps, the different Brillouin zones are hard to disentangle because the photoemission intensity is additionally strongly modulated by the photoemission matrix element, which enhances the intensity in the lower left quadrant. The matrix element is analyzed in more detail in chapter 5. The periodicity of the data is most apparent in the map of the VB bottom, which shows pronounced intensities at the M -points located at the corners of the Brillouin zone where the band extrema are expected.

In Fig. 4.6, energy distribution curves (EDC) at two different M -points are shown. We employed the model used in [141] to fit the EDCs by considering a vibrational satellite of the upper band branch located a vibrational quantum below. The bandwidth W of the VB is given by the maximum separation of the upper and lower branches and amounts to 520 meV, comparable to values in the literature [127, 129]. The full width at half maximum (FWHM) is smaller for the upper branch than for the lower branch. Comparing the width of the upper branch (FWHM = 235 meV) to the width found by Hatch *et al.* (FWHM = 190 meV), we find good agreement [129]. The slightly increased width in our measurement might arise from the worse energy resolution. At lower temperatures, these widths reduce significantly due to a decreased phonon population [145].

4.5 Tight-binding model of molecular semiconductors

In chapter 2.3, we discussed the electronic structure of molecular semiconductors in a tight-binding approximation. We make extensive use of this model to fit the measured band structures. The model is shown again in Fig. 4.7a for convenience and includes three

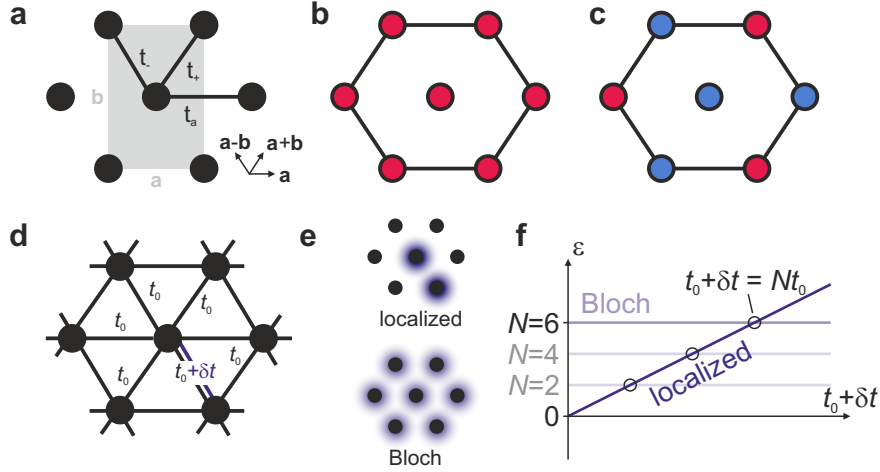


Figure 4.7. Tight-binding model and resilience to disorder. **a**, General tight-binding model of MSCs. **b**, Eigenstate at the band maximum for the case $t_i = t_0$ and **c** for the case $t_i = -t_0$. **d**, Fluctuation model with **e**, two states that highlight the reaction to disorder, the fully localized and the fully delocalized Bloch state. **f**, Energies of the localized and the Bloch state with increasing fluctuation strength. Energies of the Bloch state for lattices with different numbers of neighbors N are also indicated.

different transfer integrals t_a , t_+ , and t_- which connect nearest neighbors. The resulting energy eigenvalues are given by

$$\varepsilon_{\pm}(\mathbf{k}) = \varepsilon + 2t_a \cos \mathbf{k} \cdot \mathbf{a} \pm 2 \left(t_+ \cos \mathbf{k} \cdot \frac{\mathbf{a} + \mathbf{b}}{2} + t_- \cos \mathbf{k} \cdot \frac{\mathbf{a} - \mathbf{b}}{2} \right). \quad (4.1)$$

It has been recognized that most known molecular semiconductors can be well described with this model and that, amongst them, the transfer integrals can take any value in the range $-100 \text{ meV} \lesssim t_i \lesssim 100 \text{ meV}$ [43]. How, then, does a specific combination of transfer integrals affect the electronic properties? We explore this question for two representative cases: (1) all transfer integrals equal t_0 , and (2) all transfer integrals are equal to $-t_0$. In the first case, the band maximum is at Γ with the value $\varepsilon = 6t_0$ and thus counts the number of nearest neighbors N of which there are six in a triangular lattice. If we instead set all transfer integrals to $-t_0$ and determine the band maximum, we find that two of the transfer integrals exactly cancel, and the band maximum at Γ is reduced to $\varepsilon = 2t_0$. This reduction can be understood in terms of the geometrical frustration in triangular lattices [130].

If the first case $t_i = t_0$, the eigenstate at the band maximum consists of all sites having the same coefficient, shown in red in Fig. 4.7b. The second case $t_i = -t_0$ is the so-called frustrated case because the highest lying state would consist of a complete "antiferromagnetic" ordering, in which neighboring sites have alternating coefficients (or colors) — which, however, is impossible in a triangular lattice (Fig. 4.7c). At the Γ -point, the best one can do is to color the sites at the edges of the hexagon alternatingly and is then left to choose which color the central site has. The energy of the state is much smaller than the band maximum of the $t_i = t_0$ case because neighboring pairs with the same color reduce the eigenvalue at the Γ -point, i.e., the band maximum. The effective number of neighbors is thus reduced from 6 to 2.

With this in mind, we turn to an analysis of fluctuations in the transfer integral. The most straightforward situation is depicted in Fig. 4.7d. We imagine an infinite lattice and perturb a single transfer integral by adding the term δt . Then, we investigate the energies

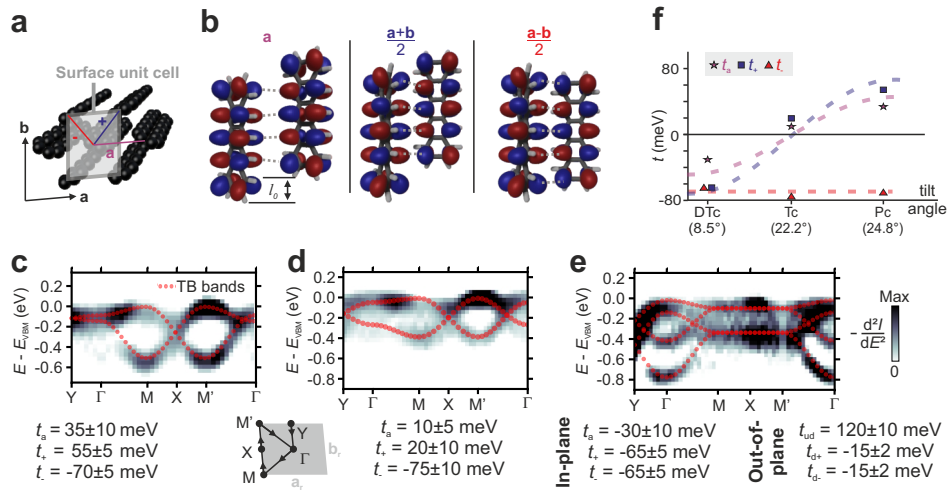


Figure 4.8. Case study — the acenes. **a**, Crystal structure of pentacene. **b**, HOMO overlap of the three different nearest-neighbor pairs in pentacene. **c**, Band structure of pentacene obtained by ARPES. The second derivative along the energy axis of the photoemission intensity is shown along the indicated path in reciprocal space. The red curves are tight-binding fits with the model in Fig. 2a, resulting in the shown values for t_a , t_+ and t_- . In **d** and **e** the same is shown for tetracene and ditetracene, respectively. Since the band structure of ditetracene features four bands, the model was slightly modified (see Methods). Notice that the band maxima is at Γ in ditetracene due to the sign change of t_a and t_+ compared to tetracene. **f**, Schematic dependence of the transfer integrals on the tilt angle in different acenes. The transfer integrals were obtained by tight-binding fits to experimentally measured band structures. The dashed lines should guide the eye. DTc: 2,2'-ditetracene, Tc : tetracene, Pc: pentacene.

of the states shown in Fig. 4.7e, a completely localized state, and a wholly delocalized Bloch state. At which value of δt will the localized state be higher in energy than the Bloch state? As just shown, the energy of the Bloch state is Nt_0 , and the energy of the localized state can be easily calculated to be $t_0 + \delta t$, yielding the critical value for the perturbation $\delta t = (N - 1)t_0$ (see Fig. 4.7f).

Consequently, the number of neighbors determines the critical value at which the localized state becomes higher in energy than the Bloch state. The sign combination of the transfer integrals can dramatically change the number of neighbors and, therefore, the critical value. A lower critical value might also occur in certain crystal packings, where the number of neighbors is reduced to 4 or 2, yielding the correspondingly lower eigenvalues $4t_0$ and $2t_0$ at Γ . We stress again, that the maximum eigenvalue $6t_0$ in a triangular lattice requires a positive product of the transfer integrals, whereas a negative product yields the frustrated system with the maximum eigenvalue $2t_0$.

4.6 Relating the valence band structure to the crystal structure

We now turn to the connection between the band structure and the crystal structure. The crystal structure of pentacene is shown in Fig. 4.8a in which the three distinct neighbors are indicated. To understand how the transfer integrals arise from the crystal structure, we must investigate the constellation of the neighbors for a specific orbital (Fig. 4.8b). The neighbors along \mathbf{a} and $\frac{\mathbf{a}+\mathbf{b}}{2}$ are shifted with respect to each other along the long axis by l_0 , whereas the neighbors along $\frac{\mathbf{a}-\mathbf{b}}{2}$ are barely shifted. Coincidentally, the value of l_0 fits the distance between the orbital lobes of the HOMO such that t_+ and t_- have different signs. Furthermore, all five lobes overlap for the $\frac{\mathbf{a}-\mathbf{b}}{2}$ neighbors, whereas only four do for

	Pentacene VB	VB-1	VB-2	VB-4	Tetracene	Ditetracene	Rubrene	Picene
t_a	35, 18 ^a , 34 ^b , 24 ^c	0, 3 ^c	-10	-10	10, 3 ^b	-30	100, 110 ^d , 125 ^e	75, 70 ^f
t_+	55, 47 ^a , 47 ^b , 43 ^c	0, 7 ^c	-35	-35	20, 7 ^b	-65	5, 0 ^d , 6 ^e	70, 66 ^f
t_-	-70, -56 ^a , -85 ^b , -79 ^c	-80, -80 ^c	40	40	-75, -80 ^b	-65	5, 0 ^d , 6 ^e	70, 54 ^f

Table 4.2. Fit parameters from measurements in this work are shown in black, experimental measurements by other groups in blue and parameters obtained from computations in gray. All values are in meV. References: *a* [129], *b* [55], *c* [146], *d* [128], *e* [147], *f* [148].

the other two. Together with the smaller center-of-mass distance of the $\frac{\mathbf{a}-\mathbf{b}}{2}$ neighbors, this indicates that t_- must be the largest transfer integral in magnitude. It is important to note that the shift l_0 is a consequence of the tilt angle of the molecules and that larger tilt angles lead to more significant shifts along the long axis [138]. Additionally, only two of the three neighbors are affected due to the following rationale. The tilt most occur around an axis in the molecular plane, which in the case of pentacene is the $\frac{\mathbf{a}-\mathbf{b}}{2}$ axis. All neighbors that are connected by this axis are not shifted with respect to each other, but all neighbors in other directions are. The tilt hence only changes the long axis offset of the \mathbf{a} and $\frac{\mathbf{a}+\mathbf{b}}{2}$ dimers.

In the next step, we extract the valence band structure from the measurements on pentacene, tetracene, and ditetracene. The band structure of pentacene is shown in Fig. 4.8c along the indicated path in reciprocal space. The maximum separation of the two band branches occurs at the M -point, as is well-known for pentacene [129]. The curvature of the lower branch is much more pronounced than that of the upper branch. We fitted the bands with the tight-binding model (see eq. 4.1, which yielded the indicated values for the transfer integrals. These values compare favorably with experimental and theoretical values from the literature (see table 4.2).

We repeated the analysis for the valence bands of tetracene, for which we reported the band structure for the first time (Fig. 4.8d). Compared to pentacene, the separation of the band branches is much smaller, and they are symmetric with respect to the band center. Fitting the tight-binding model reveals that the transfer integral t_- is similar to the value in pentacene. However, the other two are much smaller which follows from two factors of the crystal structure that act together to reduce these transfer integrals: (1) the tilt angle is smaller in tetracene than in pentacene, and (2) the distance between orbital lobes is slightly larger. The HOMOs of the tetracene neighbors are then in a position where the orbital lobes of one molecule are located on the nodal planes of the other, thus reducing the overlap.

The valence band of ditetracene is split into four branches since four tetracene cores per unit cell interact. In contrast to the other two materials, the maximum band separation is at the Γ -point in ditetracene. The four branches pair into two bands, offset in energy, that resemble the valence band of pentacene, albeit the two have slightly different separations of the band branches. Modeling the band structure with tight-binding requires a slight modification of the model used before, which is achieved by expanding the dimensionality of the Hamiltonian and adding three new transfer integrals, t_{ud} , t_{d+} and t_{d-} that connect tetracene cores perpendicular to the molecular plane. The details are in the supplementary chapters. The original transfer integrals t_a , t_+ , and t_- can nevertheless be extracted and retain their meaning. The fit reveals that the transfer integrals are now all negative, and the shift of the maximum band separation to Γ arises from the same sign of t_+ and t_- . From the crystal structure, we know that the tilt angle is smaller in ditetracene, leading to a negligible shift between molecular neighbors along \mathbf{a} and $\frac{\mathbf{a}+\mathbf{b}}{2}$. With the orbital structure in mind, the smaller shift displaces the orbitals by a single lobe such that the signs of the

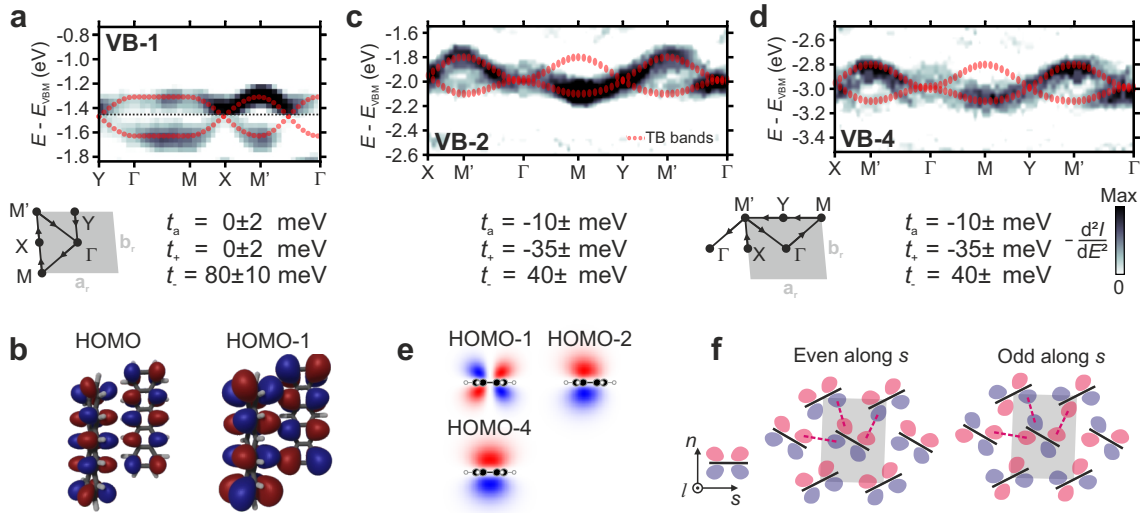


Figure 4.9. Band structure of lower-lying states. **a**, The VB-1 of pentacene along the given path in reciprocal space with extracted tight-binding parameters. Note that the upper and lower branches had to be extracted in different Brillouin zones due to matrix element effects. The colormap shows $-\frac{d^2I}{dE^2}$. **b**, Molecular neighbors along $\frac{\mathbf{a}+\mathbf{b}}{2}$ with HOMO and HOMO-1. **c** and **d**, The VB-2 and VB-4 along a slightly different path than the VB-1. **e**, Molecular orbitals of the above bands highlight the symmetry along the short axis s . **f**, Overlap of molecular orbitals in the molecular plane for two different symmetries of the orbital along s .

overlap and therefore of the transfer integrals along the same directions change compared to pentacene.

Recalling the connection between the long axis offset and the sign and magnitude of the transfer integral discussed in chapter 2, we note a corresponding relation between the tilt angle of the molecules and the transfer integrals. That is shown in Fig. 4.8f, where the transfer integrals of pentacene, tetracene, and ditetracene are plotted. With the increasing tilt angle from ditetracene to pentacene, t_+ and t_- change sign, whereas t_{\pm} does not, and in all cases, the product of the three transfer integrals remains negative. Consequently, the tilt angle does not determine the sign of the transfer integral product. These findings are substantiated by a computational study by Yoshida and Sako of the band structure of different pentacene polymorphs, which only differ in their tilt angles [146]. Despite the different tilt angles, the products of the extracted transfer integrals remain the same throughout all polymorphs.

4.6.1 Structure of lower-lying bands in pentacene

The band structure measurements carried out on pentacene crystals thus far only reported the structure of the valence band. Here, we investigate the structure of the lower-lying bands for the first time. In Fig. 4.9a, the structure of the VB-1 is shown, which features a smaller overall dispersion than the VB. Furthermore, the dispersion is dominated by a single transfer integral along $\frac{\mathbf{a}-\mathbf{b}}{2}$ as the tight-binding fit reveals. The other transfer integrals are negligible, which can be explained by the different distance between orbital lobes in the HOMO-1, which forms the VB-1 for the long axis-shifted dimers along \mathbf{a} and $\frac{\mathbf{a}+\mathbf{b}}{2}$ (Fig. 4.9b). In the HOMO-1, the orbital lobes are spaced slightly further apart from each other than in the HOMO, causing a destructive interference between the orbitals, as already pointed out by Yoshida and Sato [146].

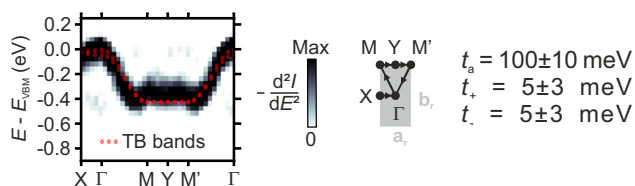


Figure 4.10. Experimental band structure of the valence band of rubrene. Second derivative of the photoemission intensity with respect to energy along the given path in reciprocal space. The tight-binding fit resulted in the shown parameters.

We now focus on the VB-2 and VB-4. These are shown in Fig. 4.9c and d, and both feature the familiar two branches, albeit with a smaller overall band width ~ 200 meV than the higher-lying bands. In contrast to all previous bands, however, the upper branch has a *larger* curvature than the lower branch at the M -points. The tight-binding fit reveals that the transfer integrals are pretty small and, crucially, that each one of them has changed sign compared to those of the higher-lying bands. The reason is the symmetry along the short axis of these orbitals. In the herringbone structure of pentacene, the orbital overlap between molecular neighbors occurs via one of the four "quadrants" that surround the molecule when viewed along the long axis (see Fig. 4.9f). With the chosen phase convention, the overlap integral between all six neighbors for an orbital with odd symmetry along the s -axis is negative. For an orbital that is even along the s -axis, all transfer integrals change sign and are positive.

Consequently, the product of the transfer integrals for orbitals that are even along s is positive. We have therefore found a knob to tune the sign of the product of the transfer integrals. Orbitals that are even along the short axis guarantee a positive transfer integral product in the herringbone structure. Yoshida and Sako came to the same conclusion when comparing computed band structures of the pentacene HOMO (odd along s) and LUMO (even along s) [146].

4.6.2 The band structure of rubrene

Rubrene is the molecular semiconductor with the highest reported mobilities and has not been surpassed in more than two decades [34, 126]. Rubrene crystallizes with two molecules per unit cell in a slipped π -stack packing in which the long axis of the tetracene core lies in the molecular plane. The molecules are arranged so that the dominant orbital overlap is with neighbors along the crystal's \mathbf{a} -axis, and much weaker overlap is present along other directions which makes rubrene a quasi one-dimensional material. Furthermore, the phenyl groups that are attached at the long edge of the tetracene core are known to lock the molecule into position, thus restricting its movement along the long molecular axis [149].

The measured band structure of rubrene is shown in Fig. 4.10. Only one band branch is visible due to the small overlap between the two distinct molecules in the unit cell. A tight-binding fit reveals the dominant transfer integral $t_a = 100$ meV and the two much smaller $t_+ = t_- = 5$ meV. These parameters agree well with values found in the literature (compare table 4.2).

4.6.3 The band structure of picene

Crystalline picene attracted a lot of attention several years ago due to the claimed observation of superconductivity at $T_c = 18$ K when doping it with potassium [150]. Subsequent studies could not reproduce the superconductivity nor observe metallicity in alkali-doped picene [151]. Apart from the interest arising from this refuted claim, picene has been studied as a potential transistor material for organic electronics, mainly due to its air stability arising from a low-lying valence band (ionization potential 5.5 eV [152]) and sizeable optical

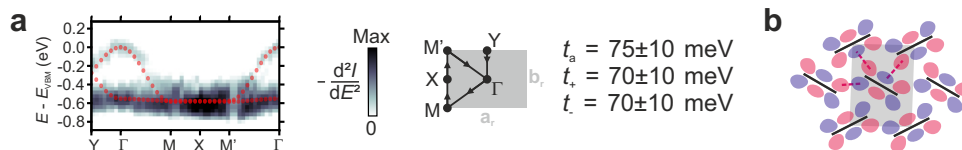


Figure 4.11. Experimental band structure of the valence band of picene. **a**, Second derivative of the photoemission intensity with respect to energy along the given path in reciprocal space along with a tight-binding fit. **b**, Overlap of the HOMOs in crystalline picene at the valence band maximum viewed down the long axis, inspired from [155]. **c**, HOMO of picene.

band gap $E_g = 3.2 \text{ eV}$ [153]. So far, one work has studied the electronic structure of picene with ARPES [154], but the agreement between computational band structures [155] and the experiment could be better. Picene crystallizes in a monoclinic structure and a herringbone packing [156], akin to the packing of the acenes. Due to its larger width along the short axis compared to the acenes, the ratio between the crystal **a**- and **b**-axis is reduced, and the herringbone angle between the two inequivalent molecules in the unit cell slightly larger [157].

The experimental band structure of the valence band is shown in Fig. 4.11a. It features two band branches with a faint upper branch and a clear and almost flat lower branch. The bandwidth extracted as the difference between the upper branch at the Γ -point and the lower branch at the X -point, $W = 680 \pm 50 \text{ meV}$, is comparatively large. Fitting the tight-binding model to the experimental band structure reveals the three transfer integrals $t_a = 75 \pm 10 \text{ meV}$, $t_+ = 70 \pm 10 \text{ meV}$, and $t_- = 70 \pm 10 \text{ meV}$. The fit reproduces the band structure quite well, except for the band splitting at the Y -point, which is missing in the tight-binding bands. The striking part about the valence band of picene is that the lower and upper branches are mirrored compared to, e.g., the valence band of pentacene. In picene, it is the upper branch that has a sizable and negative curvature, whereas in pentacene, it is the lower branch that has a large and positive curvature. The difference is also reflected in the sign of the transfer integrals, which are all positive in picene.

It is instructive to investigate the overlap of the HOMOs in picene, shown in Fig. 4.11b. Picene features three orbital lobes along the short axis and six orbital lobes overall when viewed along the long axis. Each of the lobes overlaps with a lobe of one of the six nearest neighbors, and each overlap is between lobes of different signs. The corresponding transfer integrals are then positive, in agreement with the tight-binding fit. The crucial point here is that, as in the case of the HOMO-2 and HOMO-4 in pentacene (see Fig. 4.9f), the orbital lobes on opposite sides of the short axis have the same sign. Since the orbitals always change sign along the normal axis due to the nature of the p_z -orbital, the transfer integral t_a is then positive. Regarding the other two transfer integrals, we notice that both overlaps occur between an edge lobe and a central lobe, indicating that their sign should be the same. However, we have to check the long axis offset to be sure. Critically, the HOMO of picene (Fig. 4.11c) does not change sign along the long axis. Hence, the 15° -tilt of the molecules with respect to the molecular plane does not lead to a change in sign of the transfer integrals, in contrast to the case of the acenes. Taken together all transfer integrals are positive due to a combination of the orbital symmetry along the short axis and a constant-phase along the long axis.

4.7 An excursion: π -topology and structure of the frontier orbital

As we have seen, the symmetry of the orbital along the short axis determines the sign of the transfer integral product and, consequently, the resilience to fluctuations. It therefore

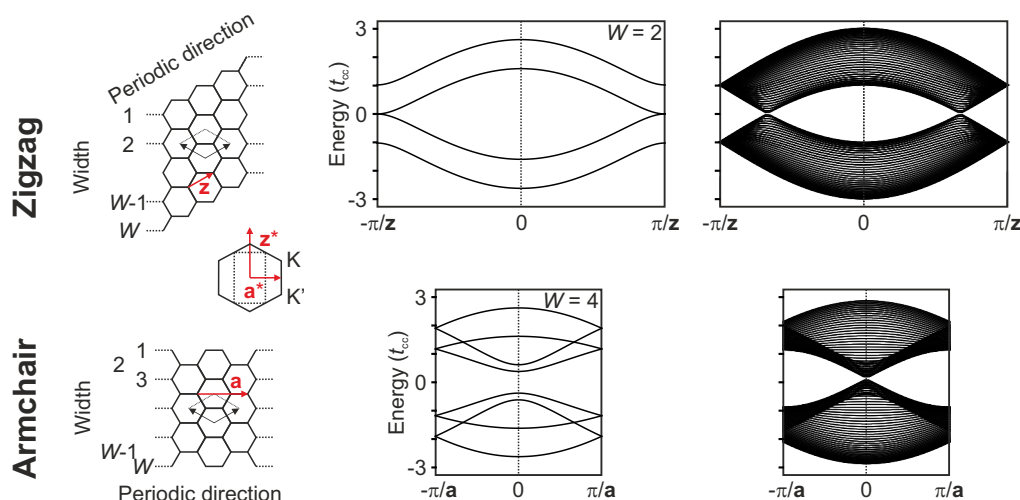


Figure 4.12. Band structure of GNRs derived from graphene. Left: The carbon network of zigzag and armchair GNRs with the lattice vectors \mathbf{z} and \mathbf{a} and the Brillouin zone of graphene. Right: The band structure of the two types of GNRs for specific widths W and the band structure of graphene projected to the respective reciprocal lattice vectors.

seems desirable to control the symmetry and shape of the *frontier orbitals* that govern charge transport. To that end, we investigate the influence of the π -topology of benzenoid hydrocarbons on the shape of the frontier orbitals, building on the already discussed tight-binding model in chapter 2. This section borrows from the well-established theory of graphene nanoribbons (GNR) [158], which are infinite ribbons of sp^2 -hybridized carbon atoms with finite width defined by the number of carbon atoms N and which are thus periodic benzenoid hydrocarbons¹. We begin by discussing the electronic structure of GNRs and then use the insights to derive rules on how to design the π -topology of benzenoid hydrocarbons for desired frontier orbitals.

All graphene nanoribbons can be thought of as cutting out an infinitely long ribbon of graphene with finite width W . The confinement of the electrons resulting from the edges of the fragment modifies the electronic structure. Two types of edges can be distinguished (see Fig. 4.12): armchair edges and zigzag edges. The orientation between these two edges differs by 30° . GNRs are correspondingly classified into zigzag graphene nanoribbons (ZGNR) and armchair graphene nanoribbons (AGNR). Furthermore, they are characterized by their width, that is, the number of carbon atoms in the non-periodic direction. With the band structure of graphene in mind, the band structure of the GNRs can be determined by the projection of the graphene bands onto the reciprocal lattice vectors \mathbf{z}^* and \mathbf{a}^* for ZGNR and AGNR, respectively [158].

For all widths, the ZGNRs are metallic, with two bands crossing $E = 0$ close to the Brillouin zone edge. In the limit of infinite widths, the band structure of graphene is regained. Since the band crossing is located at the Brillouin zone edge, the corresponding Bloch orbitals strongly oscillate between different unit cells. In contrast to the ZGNRs, the character of AGNRs changes periodically with increasing widths - for $W = 3N$ and $W = 3N + 1$, they are semiconducting, and for $W = 3N + 2$ they are metallic. The band extrema are at the Γ -point for all AGNRs which allows, in principle, for Bloch orbitals that exhibit a constant phase along the periodic axis. It will become more apparent in the next section why this is desirable; for now, it suffices to state that it is desirable. The necessary

¹Note that the field of GNRs originates in quite a different context (solid state theory) than benzenoid hydrocarbons (mathematical chemistry) and the two fields have no common nomenclature.

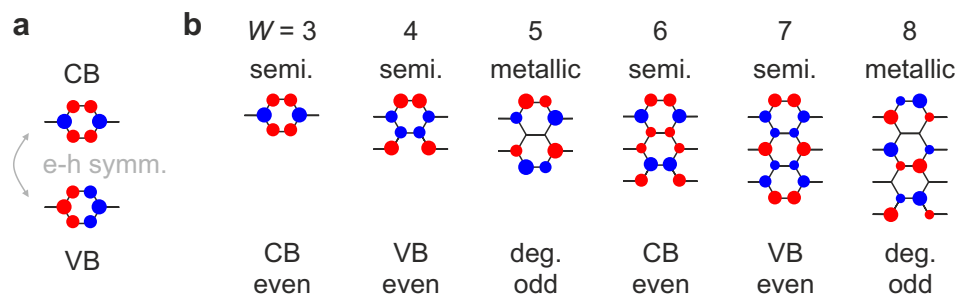


Figure 4.13. Wannier functions of AGNRs. **a**, The Wannier functions at the Γ -point of VB and CB of the $W = 3$ AGNR. The two are connected by electron-hole symmetry. The phase of the CB Wannier function does not change sign along the periodic axis. **b**, Constant phase Wannier functions of AGNRs with different widths. Its position (VB, CB) and symmetry along the short axis are also indicated. The periodicity of the symmetry (even, even, odd for $W = 3N, 3N + 1, 3N + 2$) persists for larger widths. Note that symmetry is used loosely here since it is only well-defined for odd-integer widths.

information to deduce the Bloch orbitals is in the corresponding Wannier functions, from which we want to know whether there is a nodal plane along the periodic axis or not. Without a nodal plane, the Bloch orbitals will feature a constant phase along the ribbon. The Wannier functions of VB and CB at the Γ -point of the $W = 3$ AGNR are shown in Fig. 4.13a. These two are connected by electron-hole symmetry (see section 2.2). Of these, the CB Wannier function does not feature a nodal plane along the periodic axis, whereas the VB does - a necessary consequence of the electron-hole symmetry. Furthermore, both the VB and CB Wannier functions are symmetric with respect to the short axis.

The Bloch orbitals with a constant phase persist in the series of AGNRs with increasing width (Fig. 4.13b). In addition to the periodicity of metallic and semiconducting character, there is another repeating pattern for every $3N$ atoms. The Wannier function without a nodal plane is located at the CB for $W = 3N$, at the VB for $W = 3N + 1$, and at $E = 0$ for $W = 3N + 2$. Additionally, there is a periodicity in the symmetry of the Wannier function along the short axis; the constant phase Wannier functions of semiconducting ribbons are even along s , whereas the corresponding Wannier functions of metallic ribbons are odd.

With these properties in mind, we turn to the frontier orbitals of benzenoid hydrocarbons that can be derived from the infinite GNRs. The density of states (DOS) and frontier orbitals of some benzenoid hydrocarbons (triphenyl, picene, terrylene, peropyrene, pentacene) with similar lengths are shown in Fig. 4.14. With the additional confinement along the long molecular axis, the DOS is localized at quantized energy levels whose distribution resembles the DOS of the parent GNRs shown in grey. Additionally, the molecules cannot be classed into metallic and semiconducting but rather into small and large band gap species, respectively. Apart from these differences, however, the frontier orbitals closely resemble a chain of Wannier functions of the parent GNRs. A chain of three conduction band Wannier orbitals of the $W = 3$ AGNR is similar to the LUMO of triphenyl (Fig. 4.14). Both feature a constant phase along the long (periodic) axis, and both are symmetrical across the short axis. This correspondence holds for the other molecules, with one exception. In the molecules derived from the metallic AGNRs, the ending of the molecules may be either "blunt", like in terrylene or "sharp", as in peropyrene. The ending determines the ordering of the constant phase orbital and its e-h symmetric equivalent - in terrylene the LUMO is the constant phase orbital, and in peropyrene, the HOMO. Furthermore, the symmetry of the constant phase orbitals across the short axis follows the symmetry of the parent GNRs.

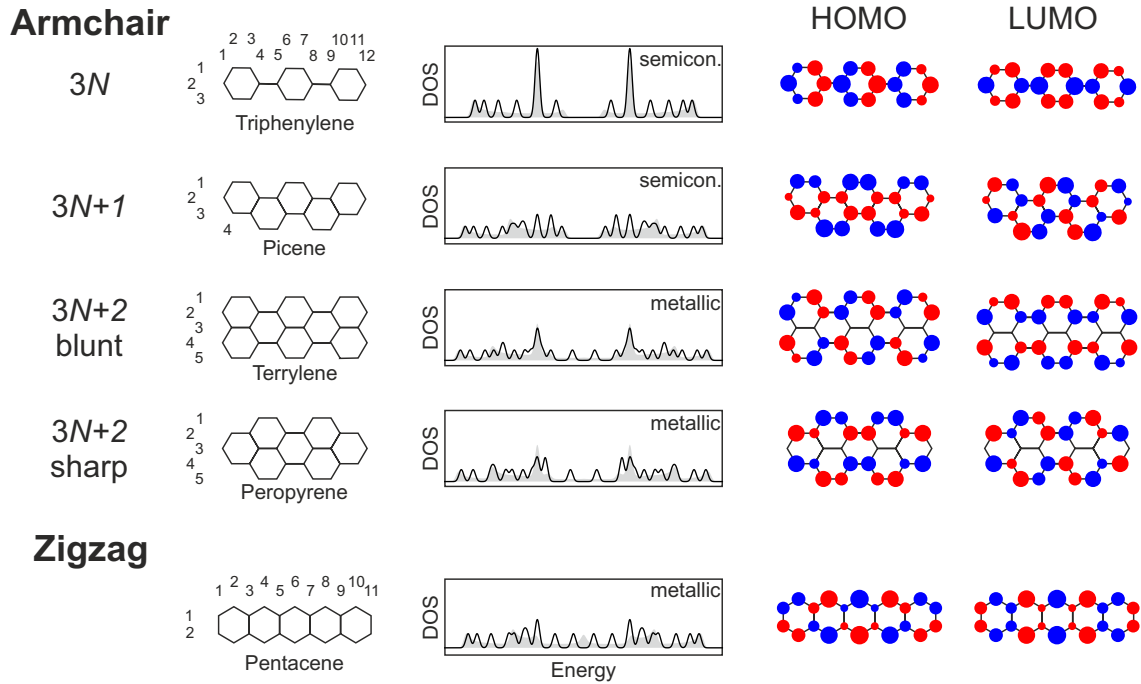


Figure 4.14. Electronic structure and frontier orbitals of AGNRs and ZGNRs with finite length. The left column shows the molecular skeleton and the number of carbon atoms W and L that define the width and the length of the molecule, respectively. In the center, the DOS resulting from the tight-binding model for the molecules (in black) and for their parent GNRs (in grey) is shown, and the right column features the structure of the frontier orbitals.

We have thus elucidated rules that determine how the π -topology of the benzenoid hydrocarbon shapes the frontier orbitals.

4.8 Effective mass at the valence band maximum

The tight-binding fits to the experimental band structures allow to determine the hole effective mass m_h^* for different crystallographic directions by calculating the effective mass tensor for holes [39]

$$[\mathbf{M}^{-1}(\mathbf{k})]_{ij} = -\frac{1}{\hbar^2} \frac{\partial^2 \varepsilon(\mathbf{k})}{\partial k_i \partial k_j}, \quad (4.2)$$

which is essentially the Hessian matrix of the valence band. The resulting minimum effective masses are given in table 4.3. The values agree with those found in the literature for pentacene and rubrene. No data was available for the other materials. The effective masses for rubrene and picene are significantly smaller than for the other materials. In the case of rubrene, the light hole mass arises from the combination of a large transfer integral

	Pentacene	Tetracene	Ditetracene	Rubrene	Picene
$m_h^* (m_0)$ exp.	2.02	2.24	2.11	0.71	0.93
$m_h^* (m_0)$ lit.	2.2 [129]	-	-	0.66 [128]	-

Table 4.3. Minimum effective mass of the holes derived from tight-binding fits to the experimental band structure and corresponding literature values where available.

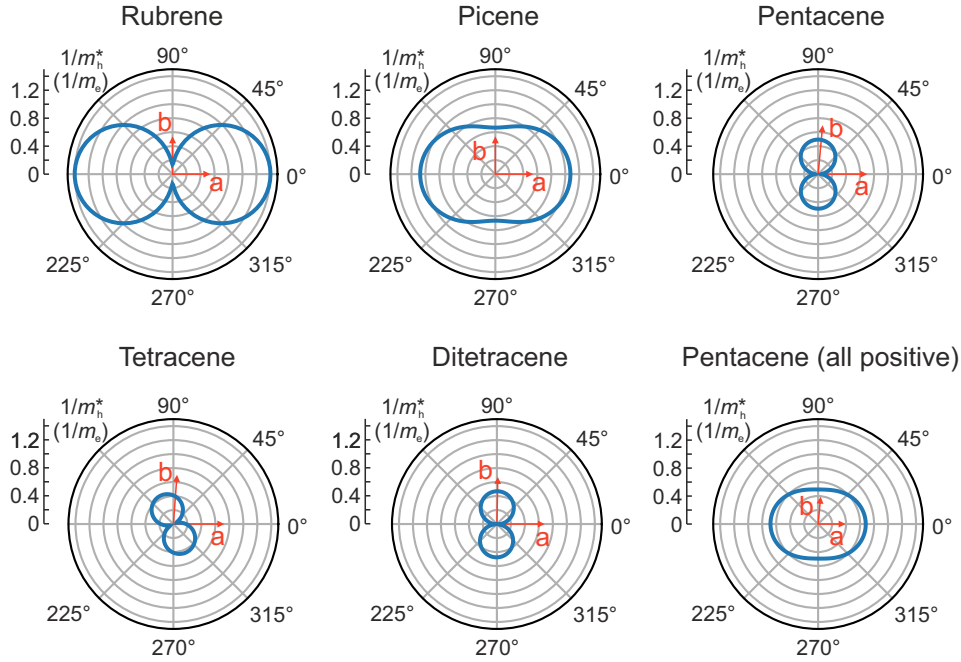


Figure 4.15. Inverse effective mass as a function of in-plane angle. The inverse effective mass calculated via equation 4.2 from the tight-binding fits to experimentally obtained band structures. The directions of the unit cell vectors are indicated in red. In the bottom right panel, m_h^* was calculated for pentacene by setting all transfer integrals to their absolute value.

along \mathbf{a} and a comparatively large unit cell vector \mathbf{a} (which factors in as $m_h^* \propto \frac{1}{|\mathbf{a}|^2}$). In contrast, in picene it is a consequence of quite large transfer integrals and all three of them acting in concert along \mathbf{a} . We also calculated the angular dependence of the effective mass, shown in Fig. 4.15. The effective mass is highly anisotropic in rubrene ($\frac{m_b^*}{m_a^*} = 10$) due to the anisotropy of the transfer integrals, whereas in picene with its isotropic transfer integrals there is no pronounced angular dependence ($\frac{m_b^*}{m_a^*} = 1.6$). The latter is in strong contrast to pentacene, tetracene, and ditetracene, in which the effective mass is highly anisotropic ($\frac{m_b^*}{m_a^*} \approx 0.1$). That might seem surprising given a similar magnitude of the transfer integrals. However, in these three materials the transfer integrals along \mathbf{a} cancel each other and thus flatten the band.

To highlight the effect of the sign combination of the transfer integrals, we investigate the effective mass for the pentacene tight-binding model but set all transfer integrals to their absolute value. The resulting angular dependence of the effective mass shown in Fig. 4.15 reveals that the effective mass is dramatically reduced along the crystalline \mathbf{a} -direction.

4.9 Localization properties

While the effective mass directly correlates with the charge mobility for bandlike states well described by semiclassical theory, this is not necessarily true for molecular semiconductors in a transient localization regime [43, 159]. In transient localization theory, the mobility is proportional to the localization length L_τ of charge states at the onset of molecular fluctuations, $\mu \propto L_\tau^2$ [8]. It is thus essential to get insights into the localization properties of the states in molecular semiconductors. To this end, we carried out simulations on a disorder model already introduced in eq. 2.16. In brief, the model is a TB Hamiltonian on a lattice spanned by 70×70 sites with periodic boundary conditions. The disorder is included

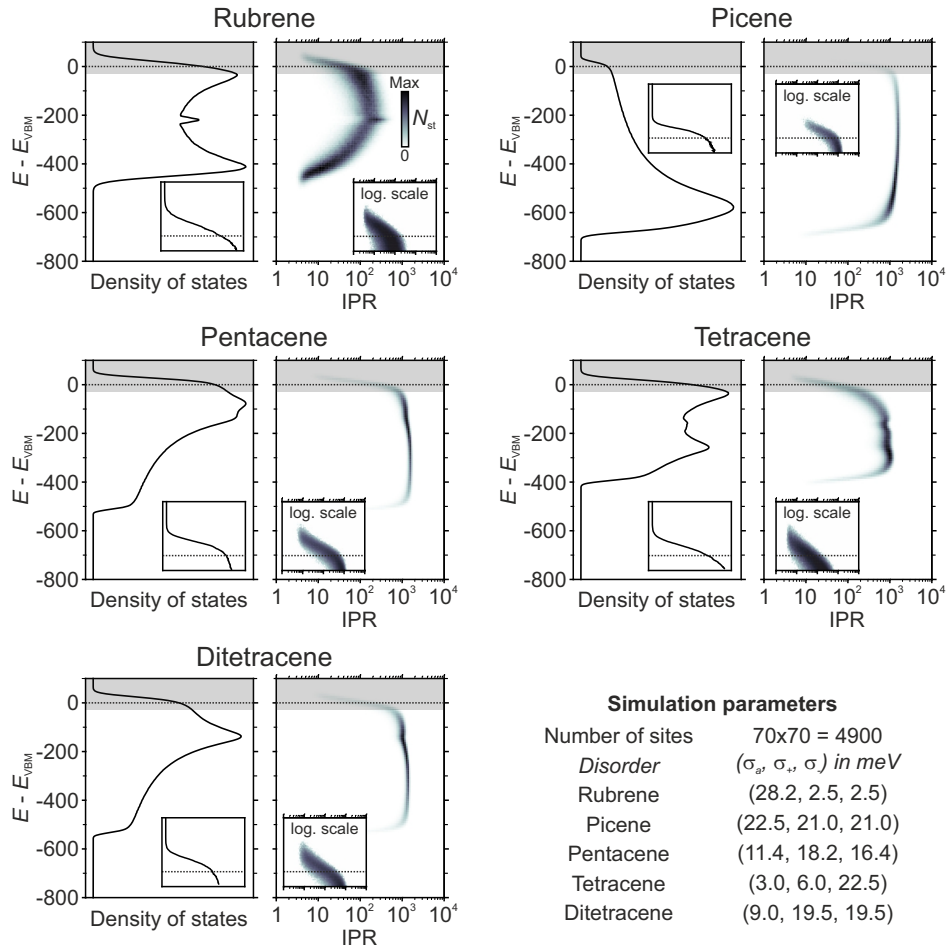


Figure 4.16. Density of states and localization properties of the investigated materials. Each panel shows the results of a disorder simulation with TB parameters from the experimental band structure. The left subfigures show the DOS, and the right subfigures a two-dimensional histogram (counting the number of states N_{st}) of energy and IPR for all eigenstates. The IPR is defined in the main text — it essentially counts the number of sites over which an eigenstate is delocalized. The simulation was carried out with the disorder parameters in the bottom right panel. For pentacene and rubrene, the disorder was taken from the calculations in ref. [43]. For the other materials, it was set to $\frac{\sigma_t}{t} = 0.3$, which is similar to the disorder calculated for pentacene. The most relevant states for transport are around the band maximum, to which the inset zooms in (shaded area). In the inset, the colorscale of the histogram is logarithmic to visualize the localized tail states better. The dashed lines indicate the VBM of the periodic TB model.

in the model by sampling each transfer integral from a Gaussian distribution characterized by the mean value t_a, t_+ , and t_- and standard deviation σ_a, σ_+ , and σ_- . Note that this model does not include disorder in the site energies or local electron-phonon coupling and can, therefore, only provide qualitative yet valuable insights.

This disorder model is fed with the TB parameters extracted from the experimental band structures. The amount of disorder, characterized by $\frac{\sigma_t}{t}$, is taken from calculations at room temperature for the case of rubrene and pentacene [43]. For the other materials, no calculations were available, and the disorder was therefore set to $\frac{\sigma_t}{t} = 0.3$, which is similar to the value calculated for pentacene. The simulation was carried out for 200 different initiations of the disorder landscape for each material. To analyze the results, we calculated

the DOS and the inverse participation ratio (IPR). The IPR is a common measure of localization in disordered systems [160]. For an eigenstate α , it is given by

$$\text{IPR}_\alpha = \frac{1}{\sum_i |a_i^\alpha|^4 / \left(\sum_i |a_i^\alpha|^2\right)^2},$$

where the sum is over all sites i . If the eigenstate is perfectly delocalized, the IPR equals the number of sites N . In contrast, an eigenstate localized to a single site has an IPR of unity. The results are shown in Fig. 4.16.

All materials develop a tail of states that extends beyond the VBM of the periodic TB model (dashed line). The DOS of states in these tails scales with the DOS at the band maximum of the periodic TB model without disorder. In picene, which has a low DOS at the VBM, the tail has a significantly lower DOS — a consequence of the details of the band structure discussed in previous sections.

When inspecting the localization properties, it is striking that the states in the band center are much more delocalized than states at the band edges — a common property of states in a disordered system [48]. Moreover, the states in rubrene and tetracene are generally much more localized than in the other materials. In these two, the IPR ranges between 10^2 to 10^3 , compared to values $> 10^3$ in the other materials. For bands that are close to being one-dimensional, such as those of rubrene and tetracene, an increased tendency toward localization is expected. One of the first results following Anderson’s seminal localization paper was that states in a one-dimensional disordered system are always localized, no matter how small the disorder [161].

Another crucial observation is the difference between the band edges of pentacene and picene. In the simulations of these materials, the disorder is set to similar values, and differences in localization properties are thus dominated by the structure of the valence band. As already mentioned earlier, the bands of pentacene and picene are roughly mirror images of each other with respect to energy. That is visible in both the DOS and the IPR curves. There is a large DOS of highly localized states ($\text{IPR} < 10$) at the band maximum in pentacene that extend up to $E - E_{\text{VBM}} = 50$ meV. By contrast, the tail states in picene are much more delocalized — even the most localized states have an $\text{IPR} > 40$ — and they spread less in energy, the highest-lying states are at $E - E_{\text{VBM}} = 30$ meV. Assuming a similar amount of disorder, we get the result that the highest-lying states are highly localized in pentacene and substantially delocalized in picene, which is mainly caused by the larger resilience to disorder of the states at the VBM in picene, as discussed in section 4.5.

The localization properties paint a contrasting picture to the effective masses obtained in the previous section. There, rubrene featured the smallest effective mass, implying the greatest mobility within semiclassical theory. In the context of transient localization theory, however, the relatively small localization length in rubrene suggests it does not show the greatest mobility. If we neglect extrinsic factors, it is instead picene with its intrinsic resilience to localization that is expected to perform better.

4.10 Nonlocal electron-phonon coupling and structure of the frontier orbital

The disorder of the transfer integrals that is ultimately responsible for the localization physics described above arises from an interplay of the thermal displacement of the molecules and Peierls (non-local) e-ph coupling. To discuss the electronic disorder among the studied materials, first, the thermal displacement is analyzed, and then the Peierls e-ph coupling.

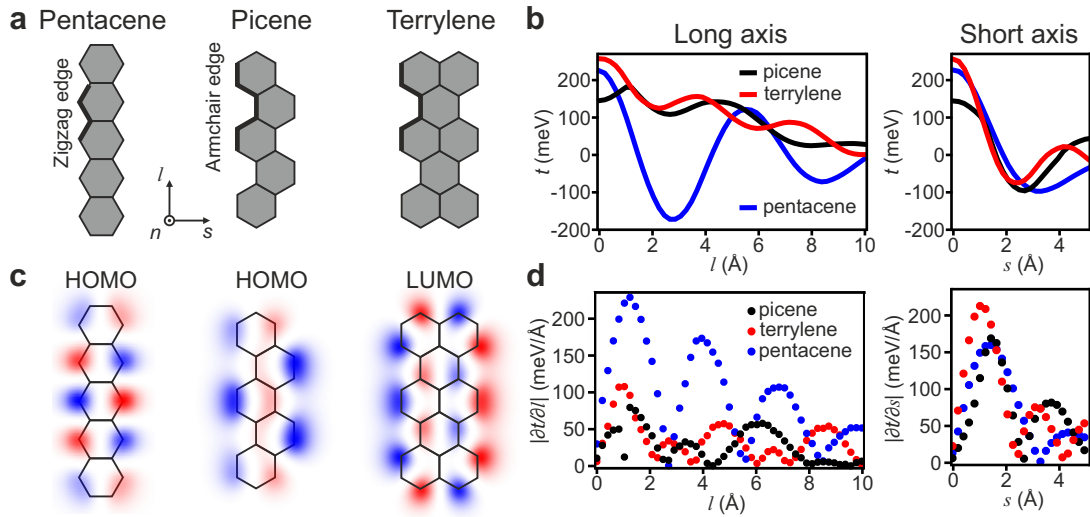


Figure 4.17. Zigzag and armchair benzenoid hydrocarbons and nonlocal electron-phonon coupling. **a**, Molecular structure of the zigzag benzenoid hydrocarbon pentacene and the armchair benzenoid hydrocarbons picene and terrylene. **b**, Dependence of transfer integrals on long and short axis displacement for the pentacene and picene HOMO and the terrylene LUMO. The transfer integrals were obtained by DFT calculations for face-on dimers at a dimer distance $d = 3.74 \text{ \AA}$ along the normal axis found in crystalline rubrene. **c**, Frontier orbitals of the three molecules. **d**, Absolute value of the derivative of the transfer integral along the long and short axis for the pentacene and picene HOMO and the terrylene LUMO. The computations were run with the Quantum Espresso code using the PAW pseudopotential with a plane-wave cutoff at $E_{\text{kin}} = 810 \text{ eV}$.

The phonon modes remain the same throughout the studied herringbone-type and unsubstituted MSCs, with slight changes in the frequencies connected to the different intermolecular interactions and molecular masses or inertia tensors (compare ref. [162] for the acene series and [163] for picene). For longer molecules (e.g., pentacene vs. naphthalene), the phonon frequencies change only slightly except for two modes that strongly shift to lower frequencies: the long-axis sliding motion and the in-phase rotation about the short axis — a consequence of the larger inertia of longer molecules for these two phonon modes. In pentacene, these two modes are already at half the frequency of the next-lowest mode. Hence, the largest amplitude displacements σ_r are along the long axis, because $\sigma_r \propto \omega^{-1}$ in the high temperature limit $k_B T > \hbar\omega$. The phonon spectrum has also been calculated for picene, and it is quite similar to pentacene [163] with low-frequency long-axis motion and modes with other displacements at slightly higher frequencies. Overall, the thermal displacement is thus expected to be quite similar in the herringbone-type materials studied here and is in the range $\sigma_r \sim 0.3 \text{ \AA}$ for long axis displacements and smaller for displacements along the other axes [164].

In the slipped π -stack structure of rubrene, the phonon modes and, correspondingly, the thermal displacement of the molecules are different from molecules forming a herringbone packing. The rubrene molecules have their long axis in the molecular plane, whose movement is restricted due to the presence of nearby molecules. An analysis of the thermal displacement via diffuse scattering in electron microscopy [164] revealed that the displacement along the long molecular axis in rubrene ($\sigma_r = 0.08 \text{ \AA}$) is significantly smaller than in herringbone-type molecular semiconductors ($\sigma_r = 0.30 \text{ \AA}$) [164].

We now turn to the other part of the disorder, the Peierls e-ph coupling. Recalling the discussion in section 2.4, the variation of the transfer integral with the molecular

displacement $|\frac{\partial t}{\partial \mathbf{R}}|$ determines the strength of the e-ph coupling. Two main factors influence $|\frac{\partial t}{\partial \mathbf{R}}|$, (1) the relative position of molecular neighbors and (2) the shape of the molecular orbital. We are first concerned with (1). When discussing the different band structures of the acenes, it became clear that the relative position of the neighboring acenes determines the mean value of the transfer integral. In the same spirit, $|\frac{\partial t}{\partial \mathbf{R}}|$ also depends on the relative position. Recalling the connection between position fluctuations and the electron-phonon coupling, different values of $|\frac{\partial t}{\partial \mathbf{R}}|$ lead to greatly change the amount of disorder. The disorder correspondingly varies significantly amongst t_a , t_+ , and t_- within a single material and the same transfer integral, e.g. t_a , for different materials with similar orbitals (e.g. tetracene and ditetracene). Slight changes in the crystal structure of a material, leading to different relative positions, may have a significant impact on the electronic disorder.

Point (2) concerns the shape of the molecular orbital. Since the transfer integral is effectively a convolution of the orbitals on neighboring molecules, the spatial properties of the orbital determine $|\frac{\partial t}{\partial \mathbf{R}}|$. The question then arises whether the structure of the orbital can be optimized to reduce $|\frac{\partial t}{\partial \mathbf{R}}|$. We intuitively expect that if the orbital is a slowly-varying function of the position, so is the transfer integral. Which in turn leads to small derivatives. To investigate that more closely, we inspect the frontier orbital transfer integrals of the three representative benzenoid hydrocarbons shown in Fig. 4.17a. In Fig. 4.17b, the long and short axis dependence of the transfer integral for face-on dimers of pentacene, picene, and terrylene is shown. While t_{pen}^h oscillates strongly between positive and negative values, t_{pic}^h and t_{ter}^l remain positive and vary much more slowly. We have already shown that benzenoid hydrocarbons with armchair edges feature constant-phase frontier orbitals. The slowly-varying transfer integrals along the long axis in picene and terrylene are a consequence of this specific structure of the orbital, see Fig. 4.17c).

In contrast, a short axis displacement of all three molecules similarly changes the respective transfer integrals. That is per a similar spatial structure of the orbitals along the short axis. Thus, while displacements along the short axis lead to substantial variations in the transfer integrals for all three orbitals, displacements along the long axis lead to only minor changes for the constant-phase orbitals. In Fig. 4.17d, the derivatives of the transfer integrals along the long and short axis are shown. There are specific displacement values for which all derivatives are zero, namely at the extremal points of $t(\mathbf{R})$. However, overall, the derivative is much smaller for the long axis displacement of ϕ_{pic}^h and ϕ_{ter}^l .

4.11 Discussion

Here, we have shown how a wide variety of experimental band structures of molecular semiconductors can be accurately described with the simple TB model in equation 2.9. The transfer integrals for a given band are due to the combination of a particular constellation of neighboring molecules and the structure of the band-forming orbital. Comparing the band structures of pentacene, tetracene, and ditetracene revealed the effect of changing the long-axis offset of neighboring molecules. Due to the nodal structure of the acene HOMO, slight changes in l have dramatic effects on the band structure — from a quasi one-dimensional valence band in tetracene to the two-dimensional valence bands in pentacene and ditetracene. Furthermore, the lower-lying bands in the same materials unveiled the effect of the short-axis symmetry of an orbital on the band structure. In the herringbone packing of the acenes, this symmetry dictates the sign combination of the transfer integrals and, thus, the curvature at the band maximum. In the example of picene, our results reveal how a HOMO of the proper symmetry may lead to a valence band with a much smaller effective hole mass than in the acenes. The physical essence behind the effect of the sign

combination of the transfer integrals lies in the geometrical frustration of a triangular lattice.

Recent computational work emphasized the role of the sign combination: it controls the localization length of states at the VBM and thereby the charge transport properties [165]. Our simulations based on experimentally extracted transfer integrals underline this observation. However, we had to make physically motivated assumptions on the fluctuations of the transfer integrals, a point that should be elaborated on in future studies. A combination of molecular dynamics simulations and electronic structure calculations could obtain the amount of dynamical disorder.

In addition, we have shown how specific π -topologies of benzenoid hydrocarbons lead to frontier orbitals with a constant phase along the long axis. Such orbitals significantly reduce the electron-phonon coupling for long-axis displacements and thus promise to lower the amount of disorder arising from thermal fluctuations of the molecules. To further investigate the effect of such rationally engineered orbitals, the fluctuations of the transfer integrals for actual thermal displacements along all directions in the crystal have to be evaluated.

The idea of engineering the π -topology to obtain frontier orbitals with a constant phase has been pioneered by Okamoto *et al.* [166–168]. In these works, the authors reported that particular sulfur-based molecular semiconductors structurally similar to picene feature the desired frontier orbitals. They, too, noted that such orbital configurations might reduce the coupling to thermal displacements along the long axis. To test the idea, they produced single crystals of these molecules, which featured sizable hole mobilities on the order of $10 \text{ cm}^2 \text{ V}^{-1} \text{ s}^{-1}$ — thus rivaling the record charge mobility in rubrene single crystals. Structural analogs of terrylene (or, more frequently, the smaller perylene) have also been successfully used as building blocks for materials with large electron mobilities in the range of $2 \text{ cm}^2 \text{ V}^{-1} \text{ s}^{-1}$ [169, 170]. Especially perylene diimide derivatives, which commonly assemble in a brickwork packing, have found increasing interest. Although the cited reports do not specifically mention the idea of engineering the π -topology, the favorable structure of the LUMOs might be one cause for the success of perylene analogs. These experiments suggest the validity of the design principle.

4.12 Conclusions and outlook

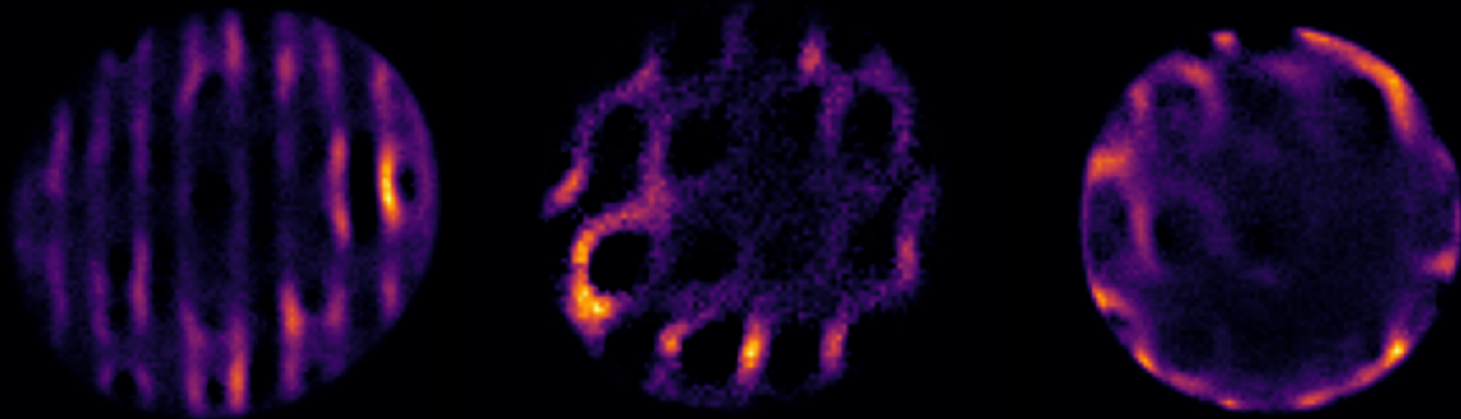
Our work provides a firm basis for understanding the relation between the π -topology of benzenoid hydrocarbons and their crystal and electronic structure. From experimental data, we directly obtained essential parameters for describing charge transport in molecular semiconductors. However, band structure data alone cannot reveal the localization length that goes into the mobility derived from transient localization theory. In chapter 5, we discuss the localization of states visible in momentum maps. We envision that temperature-dependent measurements of the localization length combined with a mobility characterization on the same material will establish the still missing direct connection between wave function properties and charge transport characteristics proposed by transient localization theory.

In the molecular semiconductor community, there is a demand for design rules for high-mobility materials. The principles derived from transient localization theory are (1) a decreased dynamic disorder and (2) isotropic transfer integrals [34]. These generic rules have to be translated into molecular and crystal structures. Surprisingly, few guidelines exist. Our general proposal might open the door to a new generation of materials with rationally designed π -topologies.

Furthermore, the π -core structure can be combined with chemical modifications that change the crystal packing (such as replacing carbon atoms in the core with nitrogen atoms) and with side groups that enhance the solubility. These modifications do not change the

π -topology, and they can hence be optimized independently. An ideal structure would exploit the low electron-phonon coupling along the long axis by reducing thermal displacements along the other directions. This idea corresponds to aligning the transfer integral gradient with the direction of the smallest thermal displacements such that the overall disorder is reduced. Several reports have already pointed out similar strategies [159, 171].

Equipped with extensive knowledge of the band structure of molecular semiconductor single crystals, we discuss the spatial structure of the electronic states recorded in momentum maps in the next chapter.



5. Momentum maps of molecular semiconductors at equilibrium

In this chapter, we first provide a historical overview of the wave function concept in quantum mechanics and how different methods can image one-electron wave functions today. We proceed by showing how constant energy cuts through the photoemission data sets — termed momentum maps — directly relate to the real-space structure of a wave function, which we describe as a localized Bloch orbital. Based on several experimental examples, it is then discussed how different factors to the orbital, that is, the envelope function, the orbital character, or the crystal momentum, manifest themselves in momentum maps. Then, we investigate momentum maps of band tail states and their relation to fluctuations and localization. We conclude this chapter by pointing out the limitations of the analogy between momentum maps and the spatial structure of orbitals.

With the advent of quantum mechanics, scientists were quickly able to calculate with sufficient accuracy the spectra of atoms and molecules. The energies of the transitions measured by experimentalists could be reproduced with Schrödinger's wave equation¹. This agreement was a great leap forward compared to the old quantum theory, which could only explain the spectra of hydrogen [172] and inspired confidence in the freshly proposed laws. In his famous equation, Schrödinger introduced the concept of the wave function as a central pillar to quantum mechanics — although, at the time, nobody was sure what the wave function represented. Born offered the interpretation that the absolute square of the wave function is a measure of the probability of finding the particle in a particular position (or momentum). This interpretation has withstood the test of time as it was used to correctly predict, e.g., the scattering rates of particles. In this interpretation, the wave function itself correspondingly describes the *probability amplitude* of a particle.

The first problems solved by quantum mechanics, such as the structure of the dihydrogen cation published by Burrau in 1927 [173], can nowadays be found as student problems in modern textbooks. They are comparatively easy to solve because they are *single-electron*

¹Actually, the first calculations of the transitions were made using Heisenberg's matrix mechanics, but Schrödinger later showed that both approaches yield the same results.

problems, and any interaction between electrons is absent. Much harder are *many-body* problems that occur for every molecule with more than one electron. Here, a gross but powerful approximation can be made. Instead of treating the system as a complex N -body problem, it can be treated as N single-electron problems, i.e., every electron behaves independently of all the others. That allows us to dissect the complex many-body wave function into an antisymmetric product of single-electron wave functions, or *orbitals*. These orbitals, whose name is derived from Bohr's electron orbits, do not prescribe an electron path but the probability of finding the electron at a particular place. Each orbital is associated with a specific energy, the ionization energy, that quantifies how much energy is needed to remove an electron from this orbital into free space — this is known as Koopman's theorem. Taken together and "according to a picturesque expression once used by Van Vleck, a set of orbitals represents a housing arrangement for electrons" [3].

The energies associated with the orbitals were successfully obtained using photoelectron spectroscopy and closely corresponded to the single-electron interpretation. However, it was much harder to observe the spatial counterparts of the energies. How could one "see" the "houses" of the electrons? With the help of computations, the shape of the orbitals for many chemical compounds became available, and orbitals entered chemistry classrooms. To see the orbitals experimentally, a microscope with extreme resolving power must be used — with wavelengths as small as the size of individual atoms. Many methods working with these small wavelengths, such as X-ray diffraction or electron scattering, are, however, only sensitive to the total electron density and not to the probability amplitude of an individual orbital. An orbital-imaging method must, therefore, offer not only supreme spatial resolution, usually guaranteed by the small wavelength of electrons but also energy resolution. Several methods were successful at imaging orbitals in the 2000s, (1) the HOMO of N_2 was reconstructed using tomographic imaging based on high-harmonic generation [174], (2) the HOMO of pentacene was imaged using scanning tunneling microscopy [175], and (3) the HOMO of again pentacene was reconstructed using ARPES [101].

Conceptually, these methods are similar in that they all use the interaction of a "probe" or final state electron with the orbital or initial state to be imaged. In the case of ARPES, the final state can be approximated as a plane wave, and the initial state of the electron in the solid state system is a Bloch orbital. Each photoelectron is then characterized as a plane wave whose momentum components and kinetic energy are recorded in a detector. The spatial properties of the orbital govern the probability of finding the electron in a particular plane wave state. By measuring the probability distribution of (many) electrons that arrive at the detector with the same kinetic energy, a reciprocal space image of the orbital is formed. These images map the momentum of the photoelectrons and are therefore referred to as *momentum maps*.

5.1 Anatomy of momentum maps

In the case of electrons in molecular semiconductors, we are dealing with states in a crystalline environment that might be localized due to disorder. The disorder arises from the thermal fluctuation of molecules around their equilibrium position and dynamically changes the transfer integrals between nearest neighbors. We hence assume the following form for the localized states of the system (see equation 2.15)

$$\psi_{\mathbf{k}}(\mathbf{r}) = \sum_n e^{i\mathbf{k}\cdot\mathbf{R}_n} F_{\text{env}}(\mathbf{R}_n) w_{\mathbf{k}}(\mathbf{r} - \mathbf{R}_n). \quad (5.1)$$

The states thus maintain phase coherence across different lattice sites, but their amplitudes are suppressed by the envelope function when going away from the origin. The Wannier

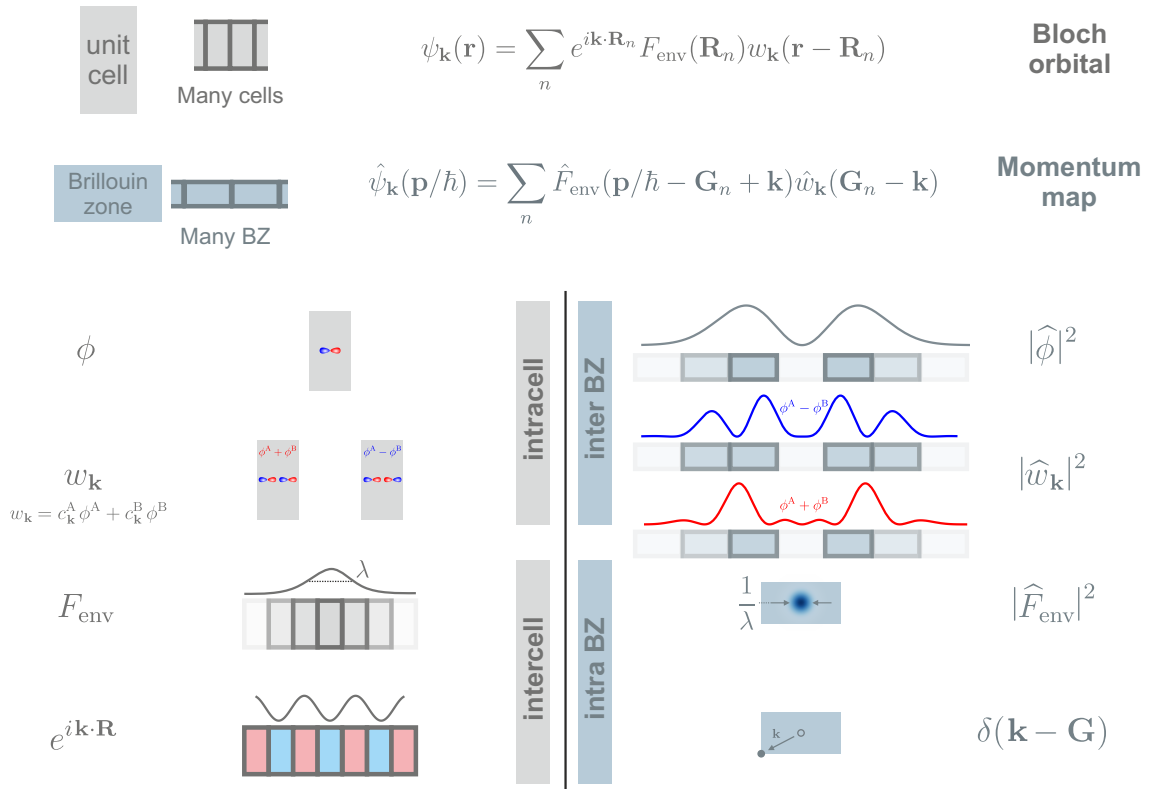


Figure 5.1. Anatomy of momentum maps. The parts that make up a (localized) Bloch orbital in real space are converted into their Fourier-transformed counterparts in reciprocal space. These parts make up the momentum maps. The orbital character ϕ , the Wannier function $w_{\mathbf{K}}$, the envelope function F_{env} , and the plane wave $e^{i\mathbf{K}\cdot\mathbf{R}}$ each lead to different signatures. Whereas the former two modulate the intensity of the momentum maps between different Brillouin zones, the latter two modulate the intensity within a single Brillouin zone.

function $w_{\mathbf{k}}$ is a linear superposition of the orbitals ϕ_i located within one unit cell. In the case of two molecules per unit cell, we have $w_{\mathbf{k}} = c_A^{\mathbf{k}} \phi_A + c_B^{\mathbf{k}} \phi_B$ where the coefficients depend on the crystal momentum \mathbf{k} .

To derive the structure of momentum maps, we work in the plane-wave approximation, which allows us to write the photoemission intensity as a Fourier transform of the initial state. This converts equation 5.1 to

$$\hat{\psi}_{\mathbf{k}}(\mathbf{p}/\hbar) = \sum_n \hat{F}_{\text{env}}(\mathbf{p}/\hbar - \mathbf{G}_n + \mathbf{k}) \hat{w}_{\mathbf{k}}(\mathbf{G}_n - \mathbf{k}),$$

where the sum is over all Brillouin zones spaced by the reciprocal lattice vector \mathbf{G} . Each factor to the localized Bloch orbital produces a distinct signature in a momentum map (see Fig. 5.1). The molecular orbital ϕ leads to a variation of the PE intensity over several Brillouin zones; in the case of the p -orbital shown in the figure, the intensity in the first Brillouin zone is completely suppressed. The linear superposition of two molecular orbitals in a Wannier function also modulates the intensity in different Brillouin zones depending on the coefficient $c_{\mathbf{k}}^i$. In contrast, the envelope function, which determines the amplitude of ψ over different unit cells, modulates the PE intensity within a single Brillouin zone. The width λ of the envelope function quantifies the width of a peak in a momentum map. Finally, the plane wave $e^{i\mathbf{k}\cdot\mathbf{R}_n}$, which determines the phase of ψ in different unit cells, is

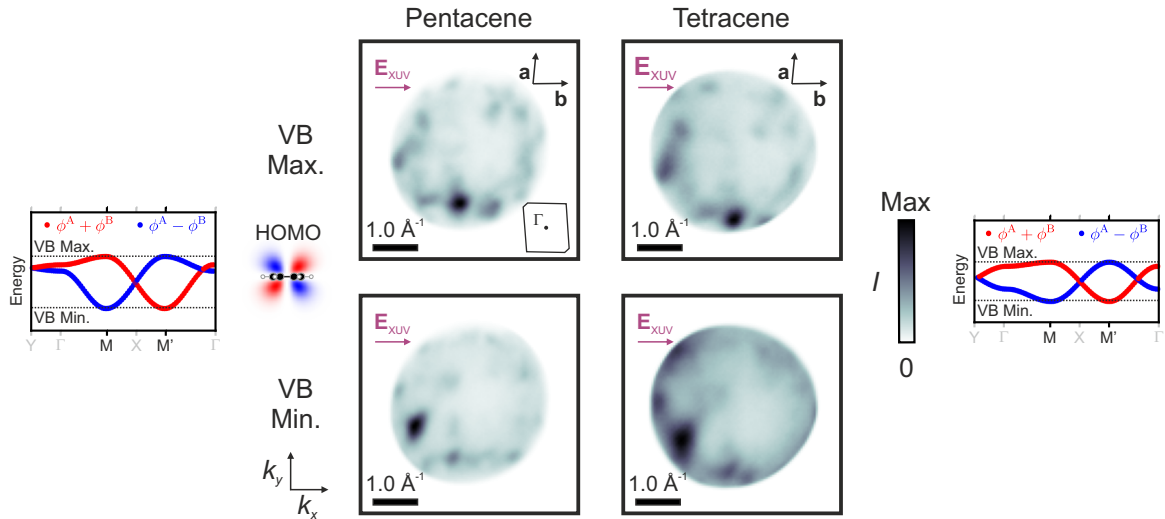


Figure 5.2. Momentum maps of the valence band maximum and minimum of pentacene and tetracene. The momentum maps of pentacene are constant energy cuts at $E - E_{\text{VBM}} = 0.00$ eV and -0.52 eV, respectively. Those of tetracene are at $E - E_{\text{VBM}} = 0.00$ eV and -0.36 eV. The HOMOs of tetracene and pentacene feature the same structure at the surface (the molecule is viewed along the long axis). The polarization of the XUV beam, the orientation of the crystal axes, and the size of a Brillouin zone are indicated. The band diagrams show the position of the momentum maps and the Wannier function character within the respective band. Note that the assignment of the crystal axes is subject to some error in tetracene since the high-symmetry points are not visible. Note, furthermore, that the tetracene data set was mirrored along the vertical axis for ease of comparison which does not change the symmetry of the experiment.

converted to a δ -function in reciprocal space that shifts the PE intensity within a Brillouin zone by the crystal momentum \mathbf{k} .

5.2 Momentum maps of similar states in different materials

Despite the simplicity of the description given above, momentum maps of molecular semiconductors can be challenging to analyze. It is not a priori clear how to associate peaks with certain high-symmetry points. That is exemplified by the momentum map of pentacene at the valence band maximum, shown in Fig. 5.2. It features a multitude of peaks that are not organized in a regular pattern, as one would expect for a crystalline system. The momentum map of the pentacene valence band maximum (VBM) is characteristic of molecular semiconductors, and its apparent disorder is due to a combination of the low symmetry of the pentacene crystal, the localized nature of the electrons, and the asymmetric experimental geometry. Recalling the crystal structure of pentacene, we notice that the molecules are tilted with respect to the cleavage plane, and there are furthermore two molecules in each unit cell rotated by $\approx 50^\circ$ around the long axis.

Tetracene is not only closely related in its molecular structure, leading to a similar shape of the HOMO, but it also features a highly similar crystal structure to pentacene (compare Fig. 4.4). The momentum map of crystalline tetracene at the VBM is shown in Fig. 5.2. Note that the experimental geometry in this measurement is close to the geometry in the pentacene measurement; in both cases, the crystal \mathbf{b} -axis is aligned with the direction of XUV propagation. Furthermore, there is a slightly different and uncorrected artefactual distortion in the two momentum maps intrinsic to measurements with a momentum microscope [120].

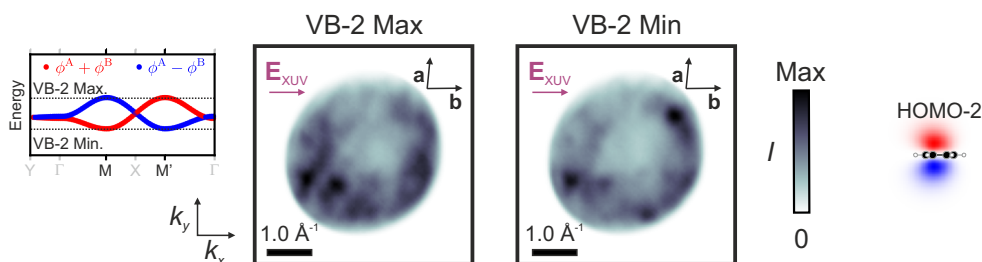


Figure 5.3. Momentum maps of the maximum and minimum of the VB-2 of pentacene. The momentum maps of the VB-2 maximum and minimum are constant energy cuts at $E - E_{\text{VBM}} = -1.81$ eV and $E - E_{\text{VBM}} = -2.13$ eV, respectively. The structure of the HOMO-2 at the surface, which forms the VB-2, is indicated (the molecule is viewed along the long axis). The band diagram shows the position of the momentum maps and the Wannier function character.

The similarity of the two momentum maps is immediately apparent. All peaks visible in the pentacene momentum map can also be seen in the tetracene momentum map.

In the momentum map of the pentacene VB minimum, the periodicity of the signal peaks is more clearly resolved due to the more significant band curvature at the band minimum. Considering only the band structure, one would expect the peaks to be at the M -points for both the VB maximum and minimum. While some of the peaks are at the same position in both momentum maps, others appear in only one of the two, e.g. the most substantial peak in the VB minimum momentum map — a consequence of the different structure of the Bloch orbitals of these states. The Wannier function character is different at these energies, at the band maximum the Wannier function character is symmetric, i.e., it can be denoted as $\phi^A + \phi^B$, at the M -point and anti-symmetric at the M' -point, while it is exactly the other way round at the band minimum. The momentum map at the tetracene VB minimum again appears similar to the one of pentacene, albeit much less pronounced due to a smaller band curvature and likely a larger localization.

In summary, the difference between the momentum maps at the band maximum and minimum is a combination of the band curvature and a symmetric/antisymmetric Wannier function. Between different materials with similar states, the momentum maps are highly similar and differ only slightly due to different band curvatures and different degrees of localization. Having shown the similarity of momentum maps that arise from similar states but from two different materials, we now turn to a state that is constructed from orbitals with a different symmetry at the surface.

5.3 Molecular orbitals with different symmetries

The VB-2 of pentacene is formed by the HOMO-2, which has no nodal plane along the short axis of the molecule and therefore also when viewed normal to the crystal surface. As already discussed in chapter 4, this changes the band structure of the VB-2 compared to bands formed by molecules with one nodal plane — the bands are mirrored along the energy axis. Apart from this change, the momentum map at the minimum and maximum of the VB-2 also looks substantially different (see Fig. 5.3). The overall intensity distribution is highest at the bottom left and top right. Therefore, the symmetry of the orbital in the surface plane strongly modifies the appearance of the momentum map. Due to the different band composition compared to the VB, the Wannier function character is also flipped, i.e., at the band maximum the Wannier function character is now anti-symmetric at the M -point and symmetric at the M' -point.

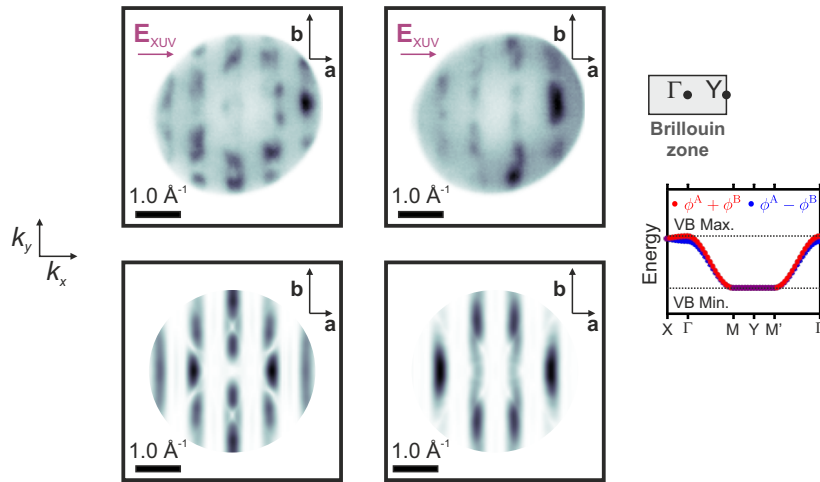


Figure 5.4. Momentum maps of rubrene at the Γ - and the Y -point. The upper row shows the momentum maps at $E - E_{\text{VBM}} = 0.00 \text{ eV}$ and -0.44 eV . The band diagram shows the position of the momentum maps and the Wannier function character. The lower row shows Fourier transforms with an envelope function of the following parameters: $(\sigma_x, \sigma_y) = (9 \text{ \AA}, 3 \text{ \AA})$.

5.4 Momentum maps at different crystal momenta

The effect of the plane wave in a localized Bloch state (eq. 5.1) is to shift the peaks to a different position within the Brillouin zone. That is exemplified by the momentum maps of rubrene at the Γ - and the Y -point of the valence band, shown in Fig. 5.4. Here, the periodic structure of the underlying states is visible in the momentum map as periodic vertical stripes. The symmetry of the experimental geometry is also apparent as a mirror axis along the y -direction — note that the symmetry is present in rubrene (and not, e.g., in pentacene) because the rubrene crystal has a higher symmetry and one molecular axis is aligned with the surface normal.

The stripes in the two momentum maps are evidently localized at two different momenta. In the Γ -point momentum map, five stripes are visible, evenly spaced about $k_x = 0 \text{ \AA}^{-1}$ with one stripe at the center. In the Y -point momentum map, we can discern four stripes evenly spaced about $k_x = 0 \text{ \AA}^{-1}$ and hence no stripe at the center. Assuming the same envelope function at both crystal momenta, the description of the two states differs only by the crystal momentum. Crucially, the Wannier function is the same, and there is, hence, a similar intricate modulation of the PE intensity with the most intense features at the right of the momentum maps.

To test the validity of the plane-wave approximation, we computed localized Bloch orbitals by a tight-binding procedure at the two crystal momenta and their momentum maps created by a Fourier transform of a two-dimensional slice through the orbitals. Since the localization length is not *a priori* known, several values were tried, of which the best fitting was chosen by visual comparison. The results are shown in the lower row of Fig. 5.4. Due to the neglect of the photon polarization in these computed momentum maps, the long-range modulation in the experimental data causing a rising intensity from left to right is missing, compare [99]. Furthermore, some features are clearly not visible in the simulation and require a more sophisticated treatment of the photoemission data. Apart from these differences, the resemblance of experiment and computation is remarkable given the simplicity of the computation and allows to obtain a rough estimate of the localization length of the rubrene states, which is on the order of $\sigma_x = 9 \text{ \AA}$ in the x -direction and $\sigma_y = 3 \text{ \AA}$ in the y -direction (σ is the standard deviation).

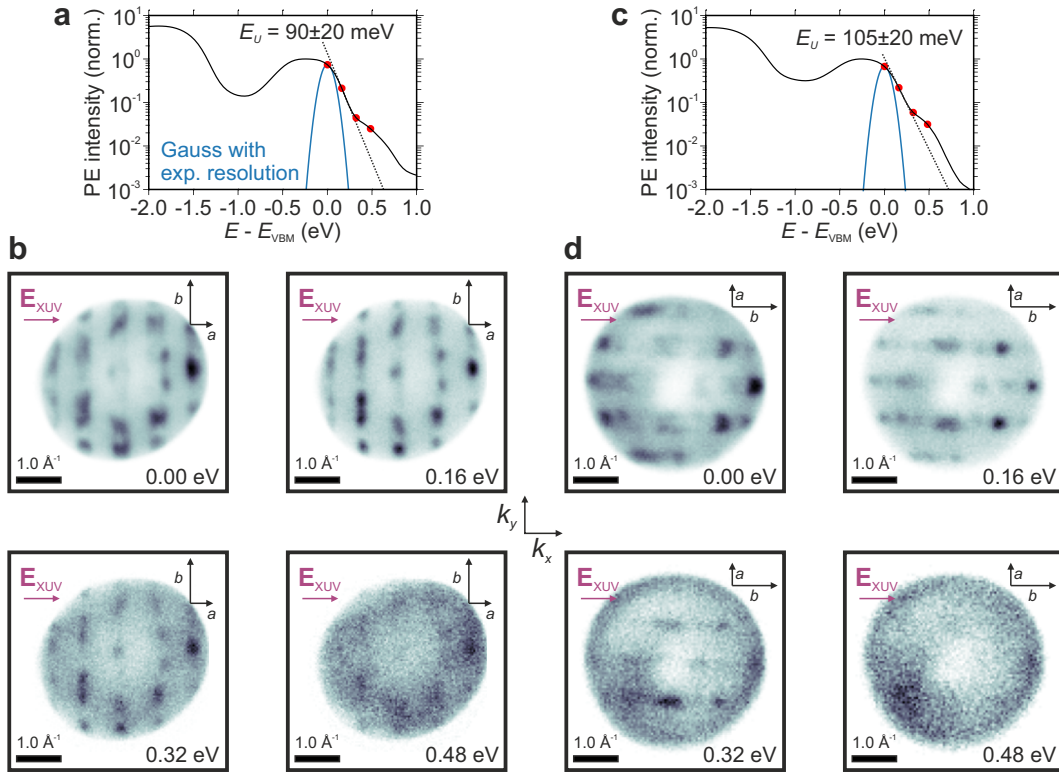


Figure 5.5. Momentum maps of rubrene at and above the valence band maximum. **a**, Logarithmic plot of the momentum-integrated PE intensity of rubrene normalized to the highest intensity in the valence band for a data set with the XUV polarization in parallel to the crystal a -axis. The blue line is a Gaussian with $E_{FWHM} = 150$ meV and indicates the experimental resolution. The dashed line is an exponential fit to the band tail. **b**, Momentum maps of the corresponding data set at the energies indicated by the red dots in **a**. **c**, Same as **a** but for a data set with the XUV polarization in parallel to the crystal b -axis. **d**, Momentum maps of the corresponding data set at the energies indicated by the red dots in **c**.

5.5 Band tail states and localization

States above the edges of a band may arise due to impurities or disorder in a system [6]. The intrinsic dynamic disorder in MSCs is, therefore, also expected to give rise to tail states. Commonly, the DOS of tail states measured with photoemission spectroscopy are fitted with an exponential Urbach tail with a characteristic Urbach energy E_U [176]

$$I = I_0 e^{-\frac{(E-E_{VBM})}{E_U}}, \quad (5.2)$$

with the PE intensity at the VBM I_0 . From different techniques, the Urbach energy is known to be in the range of 50 to 100 meV for single crystals of pentacene and rubrene [177–179]. For rubrene, we expect the localization effects to be most pronounced due to its one-dimensional band structure.

The momentum-integrated PE intensity of rubrene is shown in Fig. 5.5a. There are states beyond the intensity expected from the experimental energy resolution alone. Fitting the tail states with equation 5.2, reveals an Urbach energy $E_U = 90 \pm 20$ meV, in reasonable agreement with literature values. The shoulder at $E - E_{VBM} = 0.4$ eV has been observed in the literature before [179] and cannot be categorized into the disorder-induced band tail. A likely explanation is an oxygen-induced chemical modification of rubrene [180, 181]. A measurement on a 90° -rotated crystal yielded a similar spectrum with a slightly larger

Urbach energy, see Fig. 5.5c. Note that this data set was acquired on a different crystal, causing different impurity levels.

The tail states are much more localized than states within the band. We thus expect to see signs of the localization in the momentum maps shown in Fig. 5.5b&d. In the momentum maps at the VBM, the peaks appear pretty broad, and it is apparent that there is a signal from lower-lying states with different crystal momenta. At slightly higher energies, the peaks become more pronounced, and the signal mainly comes from states at the band maximum. The momentum maps at 0.32 eV should be within the band tail, and the signal is correspondingly smaller. Overall, the momentum map appears similar to the one at lower energies. It is, however, hard to judge whether the corresponding states are more localized. Some of the peaks seem more pronounced, while others blur compared to the momentum map at 0.16 eV. The momentum maps at 0.48 eV are within the defect-induced shoulder. In the Fig. 5.5b, the corresponding momentum map appears similar to the ones at lower energies, but the features are strongly blurred and thus indicate robust localization. In the 90°-rotated data (Fig. 5.5d), there might be signs of localization, although it is difficult to tell whether the signal is artefactual or comes from a localized state.

5.6 Momentum maps and band structure

In molecular semiconductors that crystallize in herringbone packings, there is a remarkable connection between the symmetry of a molecular orbital imprinted in a momentum map and the band structure arising from this molecular orbital. We have already hinted at this connection earlier when discussing the structure of momentum maps from molecular orbitals with different symmetries and in chapter 4 when discussing the band structure of the same. The reasoning is as follows: molecular orbitals with different in-plane symmetries (in-plane refers to the plane in the photoemission geometry) lead to distinctly different momentum maps and simultaneously flip the band structure around the energy axis by a change of the sign of all transfer integrals. These are, therefore, two separate and complementary observable consequences of a different in-plane symmetry of the molecular orbital.

To visually support this argument, the momentum maps and band structures of several bands and their corresponding molecular orbitals are shown in Fig. 5.6 for tetracene and pentacene.

5.7 Discussion

Do momentum maps fully represent orbitals? While they provide detailed information, as was laid out in the previous sections, there are some major caveats.

First, obtaining photoemission data at a single photon energy is equivalent to sampling momentum space on a single spherical slice with radius $k = \sqrt{2m/\hbar^2 E_{\text{kin}}}$. Such a single slice does not provide the complete three-dimensional information. To obtain this information, we must carry out the measurement for different photon energies instead, which correspondingly changes E_{kin} and therefore allows us to sample the entire three-dimensional structure on spherical slices of different radii (compare Fig. 5.7a). These measurements have been carried out for ordered molecular films and allow the complete reconstruction of the real-space orbital. The method has been named orbital tomography [101]. All measurements presented above have been carried out with a single photon energy, and some information is therefore missing. The electronic structure of the studied molecular semiconductors, however, is known to be 2D, with little interaction normal to the surface. Modulation of the PE intensity due to the z -direction hence arises mainly due to the well-known structure of an isolated molecular orbital.

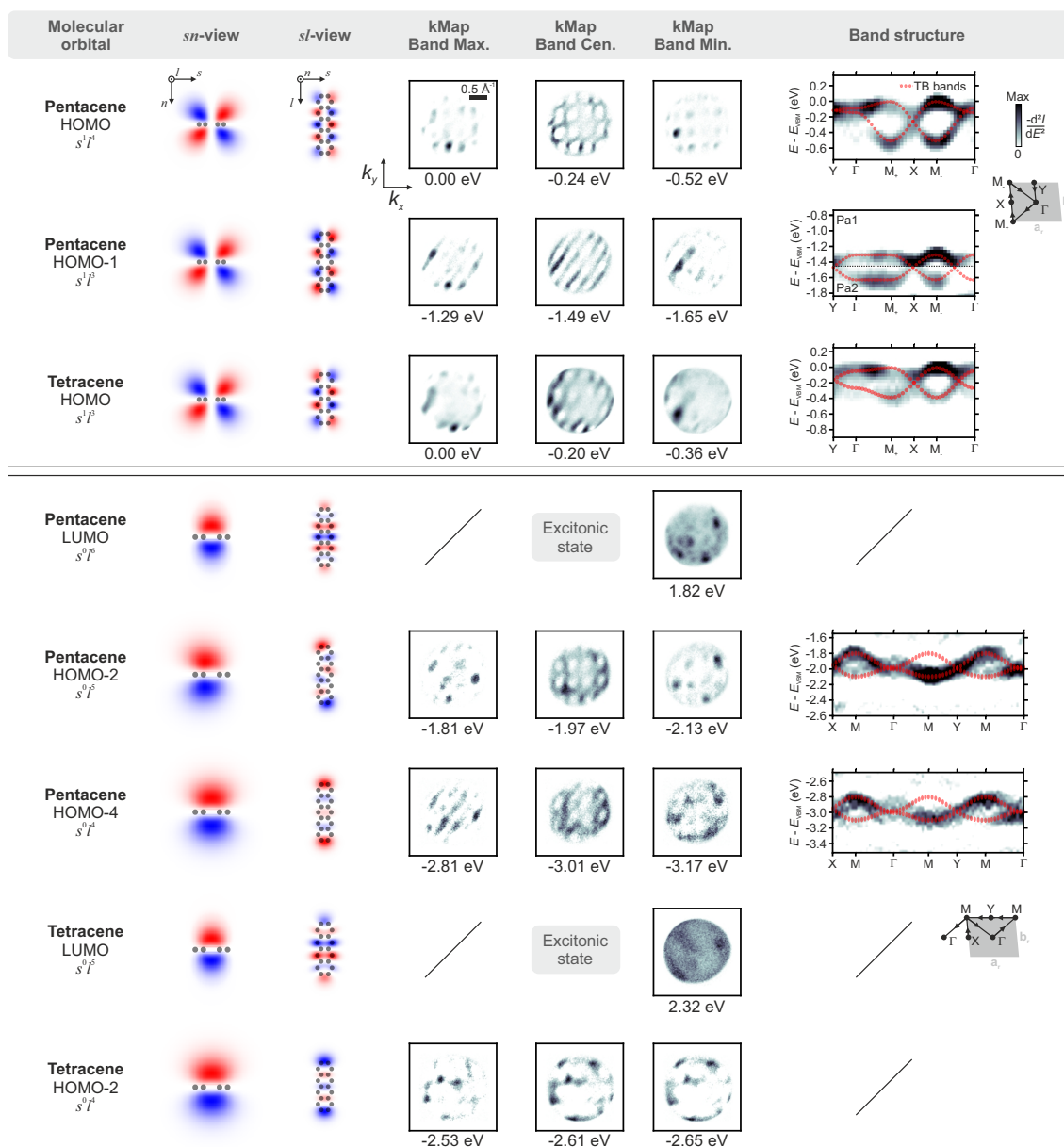


Figure 5.6. Orbital symmetry, momentum maps, and transfer integrals. Each row shows a molecular orbital of pentacene or tetracene, momentum maps arising from the corresponding bands (band maximum, center, and minimum), and the band structure with extracted transfer integrals. The orbitals are sorted by their symmetry along the s -axis. The upper three orbitals are all odd along this axis, whereas the lower five are even. Here, the color shows the second derivative of the photoemission intensity with respect to energy. The modulation of the momentum maps can clearly be grouped according to this orbital symmetry. Furthermore, the signs of the extracted transfer integrals of the two symmetry classes are related by changing the sign of all transfer integrals. Energies are referenced to the valence band maximum.

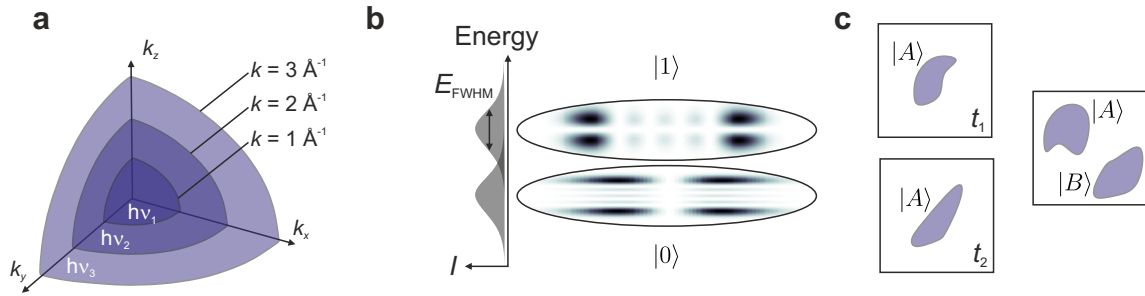


Figure 5.7. Limitations of orbital imaging in ARPES. **a**, With a single photon energy, the photoemission data for a state with binding energy E_B consists of a spherical slice through three-dimensional momentum space. To obtain information about all three dimensions, we can acquire the data with different photon energies. That allows a tomographic reconstruction of the orbital. **b**, Due to the finite energy resolution of the experiment, the signal coming from two distinct states might overlap strongly in energy, and a momentum map, therefore, shows the sum of the signal from two states. **c**, Due to the dynamically changing landscape of a system, the eigenstates change over time. The XUV photons of different pulses, spaced with the inverse repetition rate $1/f_{\text{rep}}$, probe different states. Furthermore, the XUV photons within one pulse eject electrons from a large area, and two states with similar energies but different spatial properties contribute to the signal within a momentum map.

Secondly, photoemission signals from states with slightly different binding energies might overlap due to the limited energy resolution of the measurement. This is schematically shown in Fig. 5.7b. A momentum map is usually the sum of signals from states of different energy — an exception is momentum maps of states isolated in energy, e.g., excitonic states. It is possible to reduce the mixing of the signals with higher energy resolution.

Lastly, the principle of any photoemission experiment only allows us to measure averaged information about the system. Imagine a state $|A\rangle$ at time t_1 from which an electron is removed. This electron is detected with a specific momentum and kinetic energy, providing some information about the state. A single electron does not provide enough information to construct the spatial structure of the state. Therefore, another electron is ejected at time t_2 . Due to the significant dynamical evolution of the system in molecular semiconductors, the state has changed (see Fig. 5.7c). A photoemission data set consists of $> 10^6$ recorded electrons, each probing a slightly different system. It is, therefore, a temporal average of the system and not an instantaneous snapshot. Furthermore, the spot size of the XUV sources generally used is much larger than the dimensions of the probed states. Within the spot area, there might be states with similar energies but different spatial properties that both contribute to the signal. A photoemission data set is, therefore, also a spatial average of the states in the system.

Notwithstanding these limitations, momentum maps provide intricate and new information about all contributing factors to the wave function: the orbital character, the crystal momentum, and the localization length. In the next chapter, we will see how this information can be applied to disentangle the complex dynamics of singlet exciton fission.



6. Orbital-resolved observation of singlet exciton fission

In the previous chapter, we have gained an understanding of the information contained in the momentum maps of molecular semiconductors. Here, we exploit that knowledge to investigate exothermic singlet exciton fission in pentacene single crystals. From the measured momentum maps, we can infer the orbital character of a transition, which makes it possible to dissect the photoemission signal into main peaks and satellites arising from the admixture of charge-transfer states. We show momentum maps of the singlet exciton and, crucially, of the doubly-excited and elusive dark bitriplet exciton for the first time. Momentum maps with well-defined orbital characters are used to project the time-resolved signal to its orbital character, which allows us to disentangle the dynamics of energetically overlapping transitions. We then show that singlet exciton fission proceeds via a charge-transfer mediated mechanism and discuss the exciton dynamics following the primary step.

The results of this chapter have been published in *Nature* [182] and *Phys. Statuts Solidi A* [183].

6.1 Introduction

Few processes can reliably split the energy of an exciton in half to yield two new stable excitons. Singlet exciton fission achieves this feat with efficiencies close to 200 % for the best systems. During singlet exciton fission, a singlet exciton, which is usually optically excited, is converted to two dark triplet excitons. The process is usually ultrafast (~ 1 ps) and outcompetes other decay channels such as fluorescence or intersystem crossing. Direct fluorescence of singlet exciton fission materials is hence efficiently quenched. In the 1960s, this observed lack of fluorescence in tetracene crystals motivated the formulation of a bimolecular decay, or, as it is known today, a singlet exciton fission mechanism [60]. This insight marked the birth of the field. Triplet excitons created by singlet exciton fission can undergo fusion to reform the initial singlet exciton, which may emit photons — a process known as delayed fluorescence. Its yield depends on the spins of the two triplet excitons

and can thereby be controlled by a magnetic field. This magnetic-field dependence was observed shortly after, providing solid evidence for the initial exciton fission [184, 185].

For three decades, the process remained a mere curiosity without the promise of being useful. However, Dexter [186] and later Hanna and Nozik [11] pointed out the potential of singlet exciton fission materials to increase photovoltaic efficiencies. The later paper hit a nerve in the 2000s with a growing demand for renewable energies. Despite a subsequent outbreak of research activity, the detailed mechanism of singlet exciton fission remained unresolved due to the significant challenge of observing the intermediate dark bitriplet excitons.

Singlet exciton fission is generally understood to occur in three sequential steps¹, as depicted in Fig. 6.1a. The bitriplet excitons are the product of the primary step. They are converted to the separated and spin-coherent bitriplet exciton by triplet hopping in the secondary step. In the last step, independent triplet excitons emerge.

The mechanism of the primary step has been a hot topic of debate in the years following Hanna and Nozik’s paper. The field focused on pentacene, where singlet exciton fission is ultrafast, exothermic, and highly efficient. Two distinct mechanisms emerged based on different electronic couplings between the singlet and bitriplet excitons. The so-called *coherent* mechanism was formulated based on the claimed observation of a coherent superposition of Frenkel and bitriplet diabatic states directly after photoexcitation [81]. A strong and direct electronic coupling between these two states was brought forward to explain the instantaneous population of the bitriplet state.

In contrast, in the *charge-transfer mediated* mechanism, the coupling between the excitons is enhanced by charge-transfer states [53]. These serve as a bridge between the diabatic Frenkel and bitriplet excitons, which are only weakly linked by a direct two-electron integral. The overall coupling is a product of two strong one-electron integrals, one between the Frenkel and charge-transfer states and the other between the charge-transfer and bitriplet states.

Another discussion concerned the involvement of nuclear motion. While some emphasized an active role for the nuclei in the form of a conical intersection mechanism [64, 187], others assumed an incoherent bath of nuclei that absorbs excess energy [53, 188].

The difficulties in assigning the mechanisms are based on an assignment problem. Signals coming from different states might overlap in energy, and in the absence of other information, there is an ambiguity. Which part of the signal corresponds to which state? A powerful way to address the challenge is to gather more information on the states. That is where trARPES comes into play. It provides detailed information about each state in the form of momentum maps, which are in a first approximation Fourier transforms of the state’s orbital (see Fig. 6.1b).

6.2 Experimental setup: pentacene

To follow the dynamics of singlet exciton fission in crystalline pentacene, we first prepared single crystals of sufficient size (roughly $1 \times 1 \times 0.1 \text{ mm}^3$). The growth of the crystals is described in chapter 4. The samples were brought to ultra-high vacuum and cleaved to produce fresh and clean surfaces. In the next step, a spot of the crystal surface was sought after, which yielded clear bands under simultaneous XUV and VIS illumination. This search is an essential and tedious task since the cleaving process is stochastic and leaves a complex surface behind, in which only a few excellent spots emerge. The spots are

¹The understanding and current theories of singlet exciton fission have already been discussed in detail in section 2.8.

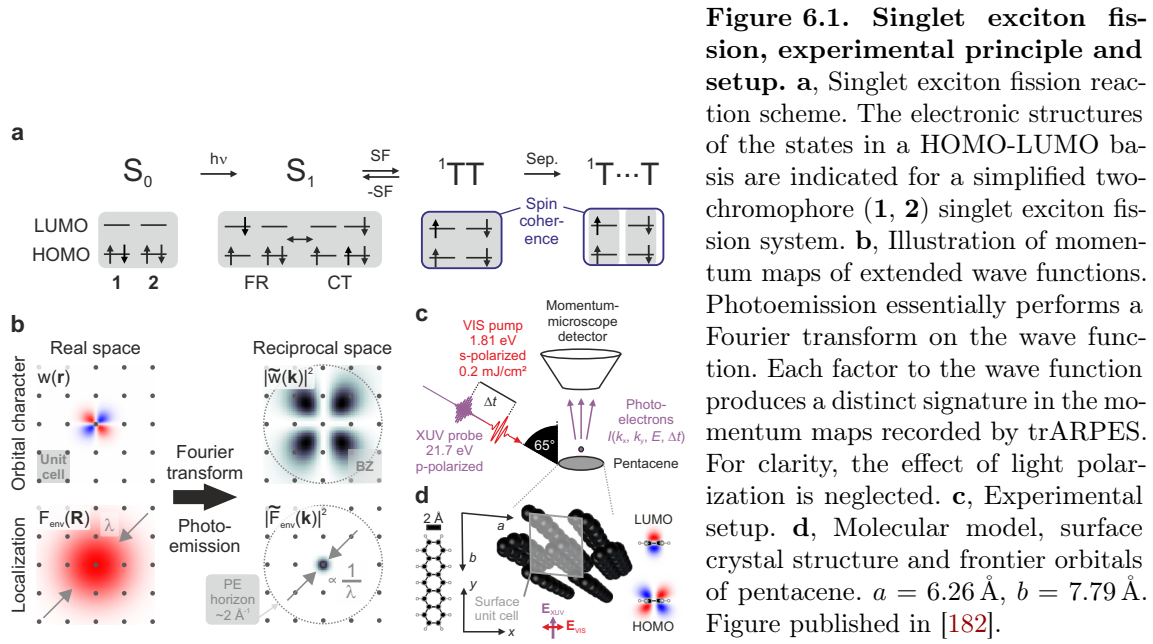


Figure 6.1. Singlet exciton fission, experimental principle and setup. **a**, Singlet exciton fission reaction scheme. The electronic structures of the states in a HOMO-LUMO basis are indicated for a simplified two-chromophore (**1, 2**) singlet exciton fission system. **b**, Illustration of momentum maps of extended wave functions. Photoemission essentially performs a Fourier transform on the wave function. Each factor to the wave function produces a distinct signature in the momentum maps recorded by trARPES. For clarity, the effect of light polarization is neglected. **c**, Experimental setup. **d**, Molecular model, surface crystal structure and frontier orbitals of pentacene. $a = 6.26 \text{ \AA}$, $b = 7.79 \text{ \AA}$. Figure published in [182].

defined by showing a clean momentum-integrated spectrum, a clear band structure, and few photoemission counts due to the pump pulses. Subsequently, the sample was rotated such that the **a**-axis of the crystal aligned with the polarization of the pump pulses. That was achieved by maximizing the counts in the excited states under the same excitation conditions. Sometimes, the rough alignment was achieved by inferring the crystal orientation directly from the ARPES data and rotating it to the desired orientation. The experimental setup and the alignment of the crystal with the impinging beams are shown in Fig. 6.1.

The energy of the pump photons was tuned to the absorption maximum of the lowest bright exciton in pentacene at 1.81 eV. This low photon energy is beneficial for obtaining high-quality trARPES data due to the reduction of pump-induced photoemission that requires ≈ 4 photons for this photon energy. To maximize the signal in the excited states, we sought the largest fluence before the data started deteriorating for various reasons. The limit was usually set by heating the crystals and evaporating the molecules, signs of which were visible as burned spots on the crystal. At the fluence $J = 200 \mu\text{J cm}^{-2}$, the data acquisition was stable, enabling an excitation of roughly 1 in 100 molecules. The pump and probe lines were incident collinearly at an angle of 65° to the surface normal, the probe pulses *p*- and the pump pulses *s*-polarized. The overall system response function had a $\text{FWHM} < 50 \text{ fs}$.

6.3 Results

6.3.1 Momentum maps

The three-dimensional photoemission intensity $I(k_x, k_y, E)$ before excitation is shown in Fig. 6.2a. The dispersing states of the valence band (VB) and valence band-1 (VB-1) are visible. Right after photoexcitation ($\Delta t = 0 \text{ fs}$, a signal labeled S appears at $E - E_{\text{VBM}} = 1.81 \text{ eV}$ (VBM: valence band maximum) which corresponds to the singlet exciton. Simultaneously, the signal X is visible at lower energies ($E - E_{\text{VBM}} = 0.95 \text{ eV}$). These signals have disappeared after the primary step is complete at $\Delta t = 500 \text{ fs}$ and a new signal TT that stems from the bitriplet exciton has emerged at $E - E_{\text{VBM}} = 0.65 \text{ eV}$.

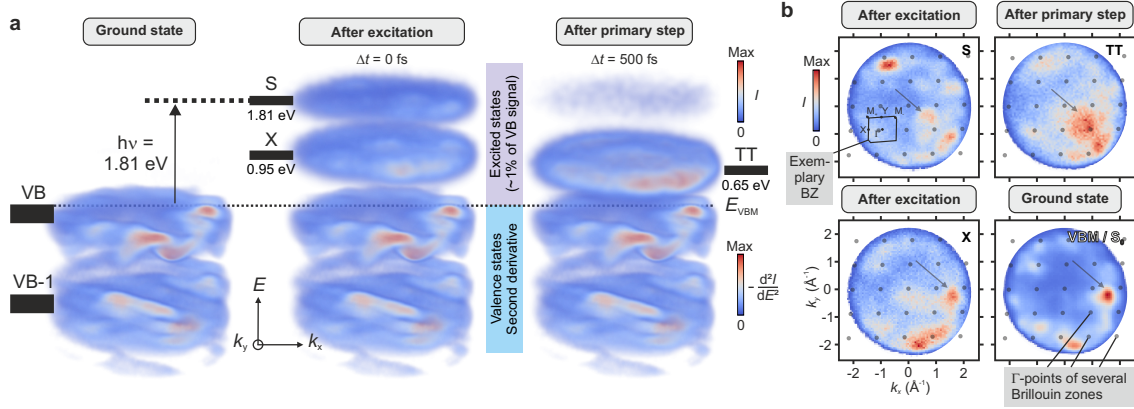


Figure 6.2. Investigating singlet exciton fission with trARPES. **a**, Visualization of the photoemission intensity of pentacene during singlet exciton fission. The energies of the states are referenced to the VBM. **b**, Momentum maps of the singlet exciton, the signal X (a satellite peak of the singlet exciton), the bitriplet, and the ground state at the VBM. The arrows indicate high-intensity features related to the orbital character. For the momentum map of the ground state, the signal is shown at $E - E_{\text{VBM}} = 0.00$ eV, for those of the excited states, the signal was integrated over the following energy and time ranges: S: (1.60 to 2.00 eV | -10 to 140 fs), X: (0.95 to 1.30 eV | -10 to 35 fs), TT: (0.50 to 0.80 eV | 480 to 520 fs). Figure published in [182].

In Fig. 6.2b, the momentum maps corresponding to these signals are shown. Compared to momentum maps of inorganic crystals, these seem somewhat disordered due to the low symmetry of the pentacene crystal and the slanted alignment of the molecules. The momentum map S of the singlet exciton shows several peaks on the right side that are roughly spaced with the size of the Brillouin zone. Furthermore, there is an overall modulation of the photoemission intensity over many Brillouin zones that suppresses the lower left and upper right corners of the map. Lastly, the peaks in the momentum are rather pronounced and easily distinguishable from each other. These three features, the periodicity, the intensity modulation, and the pronounced peaks, arise from the structure of the exciton wave function. A one-electron Bloch orbital in the solid state that is localized can be described as:

$$\psi_{\mathbf{k}}(\mathbf{r}) = \sum_{\mathbf{R}} w_{\mathbf{k}}(\mathbf{r} - \mathbf{R}) F_{\text{env}}(\mathbf{R}) e^{i\mathbf{k} \cdot \mathbf{R}}.$$

Here, we sum over all unit cells spaced by \mathbf{R} . The wave function within the unit cell is made up by the Wannier function $w_{\mathbf{k}}$, which defines the orbital character. The phenomenological envelope function F_{env} describes the localization of the particle, parameterized by the localization length λ . Performing photoemission on this state can be approximated as a Fourier transform (see Fig. 6.1b), and each factor to the Bloch orbital has its equivalent in the corresponding momentum map.

The overall modulation of the map is thus a signature of the lowest-unoccupied molecular orbital (LUMO) character of the electron in the singlet exciton, whereas the cause of the pronounced peaks is a relatively localized Bloch orbital with a considerable localization length λ . In contrast, the momentum map TT of the bitriplet exciton is less defined. The peaks in the momentum map are less pronounced, and there is no periodic pattern. However, the overall intensity modulation of the momentum map is similar, pointing to a similar orbital character of singlet and bitriplet excitons. Indeed, in both states, an electron is located in the LUMO, and a similar orbital character is expected. Apart from the orbital character, the momentum map TT also reveals localization of the bitriplet exciton with respect to the singlet exciton, as apparent in the peak widths shown in Fig. 6.3. This

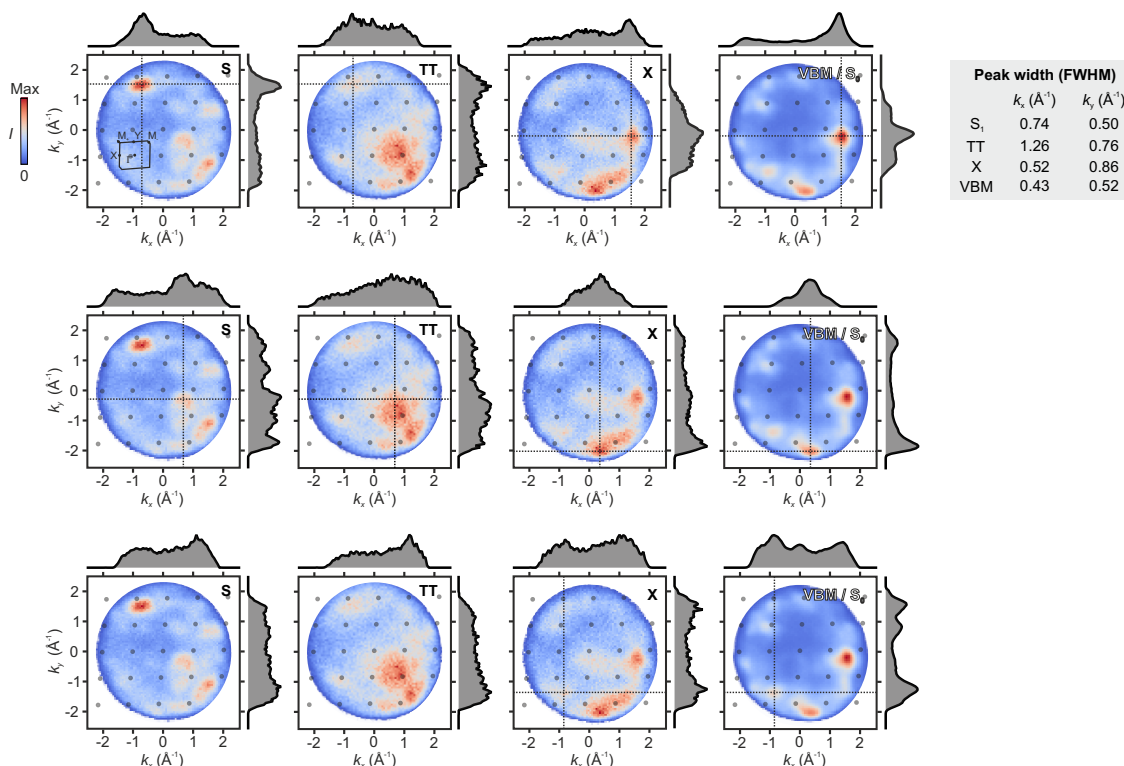


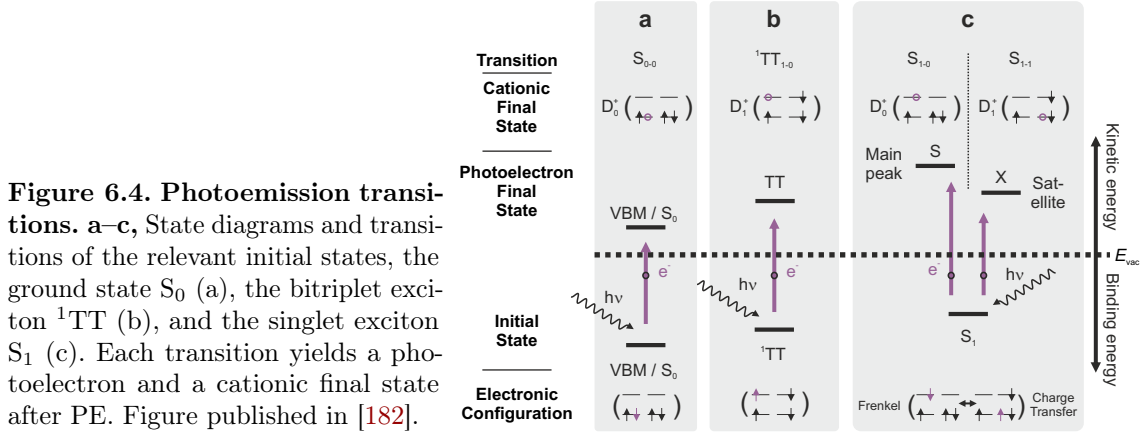
Figure 6.3. Momentum maps and peak widths. Momentum maps S, TT, X, and VBM. The momentum distribution curves (MDC) along the respective cuts in momentum space are shown for each state. The full width at half maximum (FWHM) of the MDCs is evaluated for the indicated peak in the top row. Figure published in [182].

observation agrees well with theoretical predictions of a singlet exciton delocalized over ~ 10 molecules and a triplet exciton localized to a single molecule [189].

The momentum map X of the signal that simultaneously appears with the signal S (also shown in Fig. 6.2b) features an overall intensity modulation very different from S and TT. However, it shows similarly pronounced peaks as S (see Fig. 6.3). Furthermore, X looks strikingly similar to the momentum map of the VBM. Since the VBM is formed by a combination of HOMOs at the M -points, the signal X originates from a state with HOMO character at the same crystal momentum. Compared to the VBM, the peaks of X are slightly broader.

6.3.2 Photoemission transitions

To understand the origin of X, we turn to the possible photoemission transitions of the relevant states, shown in Fig. 6.4. Ejecting an electron from the VBM in the ground state S_0 leaves a hole behind in a HOMO and creates the ground state cation D_0^+ . We label this transition S_{0-0} . From the diabatic bitriplet exciton, two transitions are possible, one from the LUMO and one from the HOMO. The latter transition, labeled ${}^1\text{TT}_{1-1}$, would appear at a kinetic energy similar to the VBM transitions and thus be undetectable on the large background. The first transition, labeled ${}^1\text{TT}_{1-0}$, leaves an excited state of the cation D_1^+ behind and corresponds to the momentum map TT. Lastly, we turn to the transitions of the singlet exciton, a mixture of Frenkel and charge-transfer diabatic states. Transitions are possible from either of the configurations. From the Frenkel state, we can remove an electron from the LUMO and end up with the cation D_0^+ which is the main peak S_{1-0} ,



yielding the signal S. The charge-transfer state also allows for a transition to the ground state cation but additionally opens a path to the excited cation D_1^+ by ejecting an electron from a HOMO and leaving a triplet excitation left behind in the cation. This transition $S_{1,-1}$ should be separated by roughly a triplet energy ($E_T = 0.86$ eV, ref. [190]) from the main peak. The satellite peak corresponds to the momentum map X, which has a HOMO character and is located $E_S - E_X = 1.81$ eV $-$ 0.95 eV $=$ 0.86 eV below the main peak. Thus, the signal X does not arise from a distinct state but rather is a consequence of the charge-transfer character of the optically excited singlet exciton.

6.3.3 Projecting to the orbital character

With the knowledge about the origin of X at hand, we now turn to the dynamics. The momentum-integrated photoemission intensity in Fig. 6.5a shows that the singlet exciton decays throughout 100 fs. Furthermore, there is an apparent relaxation of the signal X over time. Chan *et al.* interpreted this signal as a signature of the bitriplet exciton, which in turn led to them to the conclusion that the optical excitation directly populates a coherent superposition of singlet and bitriplet states [81].

At each pixel ($E, \Delta t$), there is a momentum map (though with a much weaker signal than the integrated maps in Fig. 6.2b), which we can use to disentangle the dynamics by a projection procedure. The idea of projecting the signal to a known basis of momentum maps has been pioneered by Puschnig *et al.*, who used a computationally obtained basis [191]. We extend this idea and use an intrinsic basis defined by two momentum maps with different orbital characters, the momentum maps X with HOMO character and TT with LUMO character, see Fig. 6.5b. The basis was chosen carefully and integrated over an energy and time window that reduces spurious counts from other states.

The projection procedure yields the coefficients $\alpha_{\text{HOMO}}(E, \Delta t)$ and $\alpha_{\text{LUMO}}(E, \Delta t)$ which quantify the orbital character of a given momentum map $I_{E, \Delta t}(\mathbf{k})$. Before the projection, we normalize all momentum maps as $\frac{I}{\int I dk_x dk_y}$ and convolute the 4D PE intensity with a Gaussian ($\sigma_k = 0.05 \text{ \AA}^{-1}$, $\sigma_E = 40$ meV, $\sigma_t = 3$ fs) making the procedure more stable. The coefficients are obtained by a minimization of the error χ^2 :

$$\chi^2 = \int (I(\mathbf{k}) - \alpha_{\text{HOMO}} \mathbf{X}(\mathbf{k}) - \alpha_{\text{LUMO}} \mathbf{TT}(\mathbf{k}))^2 dk_x dk_y,$$

where $\alpha_{\text{HOMO}} + \alpha_{\text{LUMO}} = 1$. Fig. 6.5c&d show the results of the projection. The separation works best for large signals, e.g. below 0.25 eV — the photoemission intensity in the VB is roughly a hundred times greater than for the excited states.

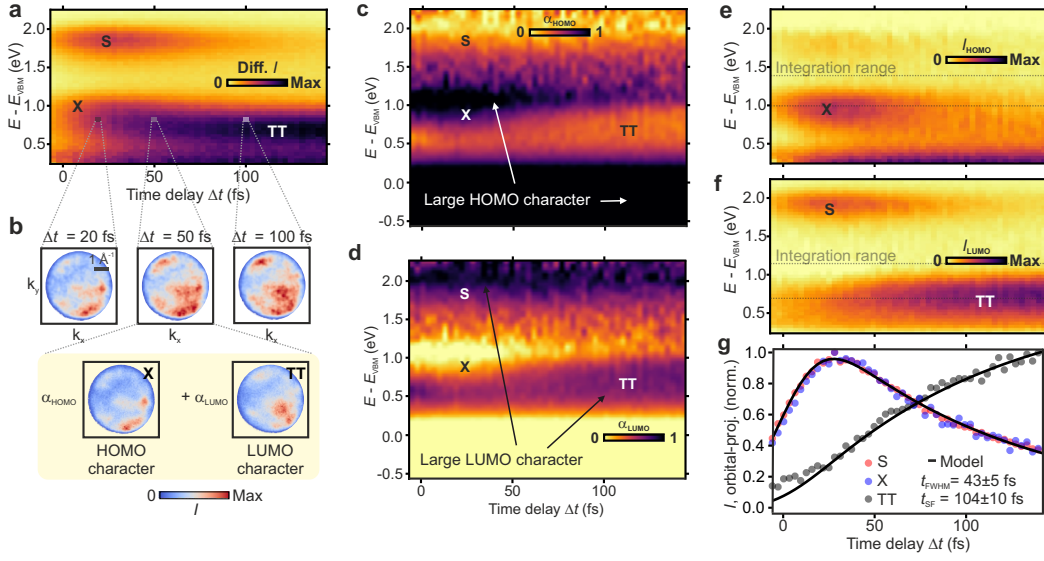


Figure 6.5. Orbital-projected dynamics. **a**, Momentum-integrated dynamics of singlet exciton fission in pentacene, showing the differential PE intensity (equilibrium signal subtracted). **b**, Momentum maps at $E - E_{\text{VBM}}$ and illustration of the decomposition procedure. **c** and **d**, Orbital populations as obtained by the minimization procedure of states with **c**, HOMO and **d**, LUMO character. **e**, The dynamics of states with HOMO and **f**, LUMO character. These images are the product of the PE intensity in **a** with the orbital populations in **c** and **d**, respectively. **g**, Orbital-projected population dynamics of the excited states shown with the model fit. The signal was integrated over the shown energy range in **e** and **f** to reduce spurious counts from lower-lying states. Figure similarly published in [182].

A much clearer picture emerges by taking the product of the coefficients with the time-resolved density of states (DOS). This yields the time-resolved and orbital-projected density of states I_{HOMO} and I_{LUMO}

$$\begin{aligned} I(E, \Delta t) &= I_{\text{HOMO}}(E, \Delta t) + I_{\text{LUMO}}(E, \Delta t) \\ &= [\alpha_{\text{HOMO}}(E, \Delta t) + \alpha_{\text{LUMO}}(E, \Delta t)] \times I(E, \Delta t). \end{aligned}$$

These are shown in Fig. 6.5e&f, respectively. The HOMO-projected DOS mainly features the signal X, whose dynamics resemble those of the singlet exciton. In contrast, the LUMO-projected DOS shows the signals S and TT. The projection separates states based on their orbital character, and the procedure is quite robust. Notice that even though the momentum maps S and TT look quite different, the projection on X and TT still finds that S is similar to TT, a true projection on the orbital character. We emphasize that the main reason for this robustness is the different symmetry of HOMO and LUMO at the surface (compare Fig. 6.1d), leading to very different momentum maps. This observation finds strong evidence when comparing occupied orbitals with larger binding energies in pentacene, which have symmetries akin to HOMO or LUMO and feature correspondingly similar momentum maps (see Fig. 5.6).

After successfully deconvoluting the overlapping X and TT signals, we can extract the kinetics of the signals shown in Fig. 6.5g. The signals S and X feature the same decay dynamics, which is definite proof that they are two different transitions arising from a single state. In contrast, TT builds up with the decay of the singlet exciton. A kinetic model with a single time constant t_{SF} , representative of the primary step, is sufficient to fit the

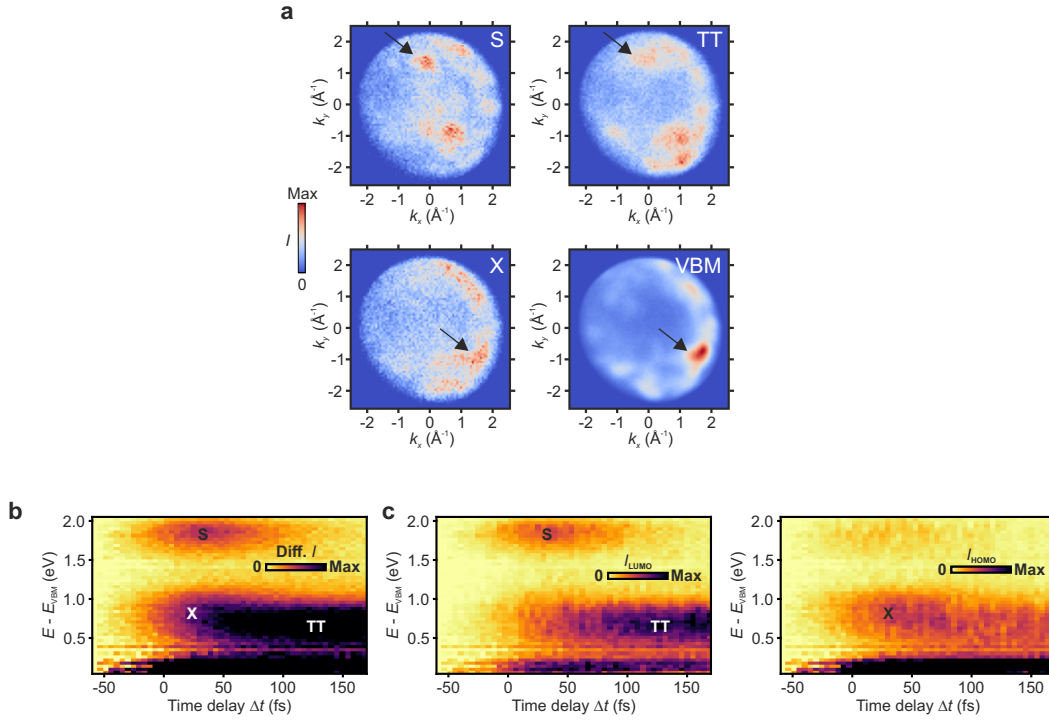


Figure 6.6. Momentum maps and projected dynamics for the crystal rotated 10° about the surface normal. **a**, Momentum maps of the singlet exciton, the triplet exciton, the satellite X, and the valence band maximum. For the momentum map of the ground state, the signal is shown at $E - E_{\text{VBM}} = 0.00$ eV, for those of the excited states, the signal was integrated over the following energy and time ranges: S: (1.60 to 2.00 eV | -10 to 140 fs), X: (0.95 to 1.30 eV | -20 to 60 fs), TT: (0.50 to 0.80 eV | 580 to 620 fs). **b**, Momentum-integrated dynamics, equilibrium signal subtracted. **c**, Orbital-projected dynamics with the maps T for LUMO character and X for HOMO character. Figure published in [182].

dynamics:

$$\begin{aligned} \frac{d[S_1]}{dt} &= -k_{\text{SF}}[S_1] + I_{\text{SRF}} \\ \frac{d[{}^1\text{TT}]}{dt} &= k_{\text{SF}}[S_1], \end{aligned}$$

where $[S_1]$ and $[{}^1\text{TT}]$ are the populations of singlet and bitriplet and $I_{\text{SRF}} = e^{-\frac{t^2}{2\sigma}}$ is the system response function. The resulting time constant $t_{\text{SF}} = 104 \pm 10$ fs agrees well with previous results [76, 81].

To prove the robustness of the projection procedure, we performed it on a 10° -rotated crystal. The corresponding momentum maps, shown in Fig. 6.6a, are similar to the unrotated maps. Notice, however, that they cannot be generated by a mere rotation of the unrotated data set since the angle between the crystal and the XUV polarization is different. The time- and orbital-projected DOS (Fig. 6.6b) again clearly separates the dynamics based on the orbital character.

To further test the validity of the decomposition, we investigated the dynamics of features A and B in the momentum maps that are characteristic of the HOMO or LUMO character, respectively (see Fig. 6.7a). Such an analysis is commonly employed for trARPES data of inorganic semiconductors. The corresponding dynamics also separate the signal by the orbital character (see Fig. 6.7b-d). However, the separation is far less clear than

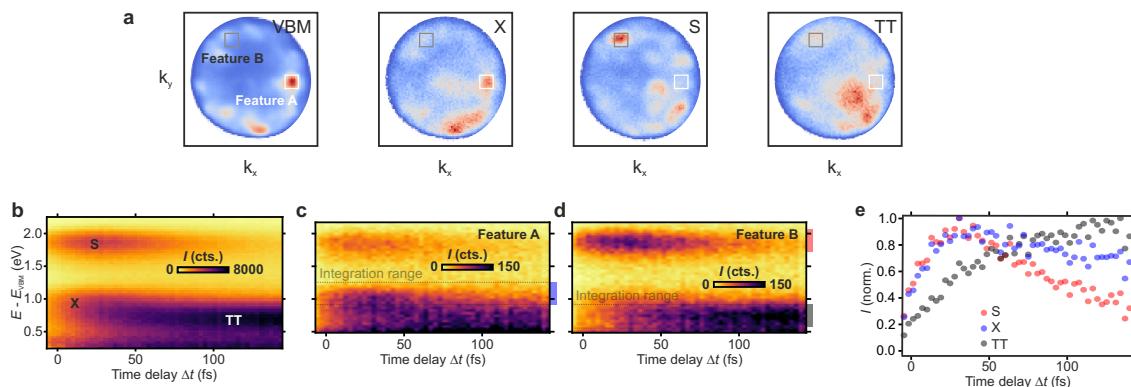


Figure 6.7. Dynamics of HOMO and LUMO features. **a**, Selected features characteristic of HOMO and LUMO characters on the momentum maps of VBM, X, S, and TT (the same as in Fig. 6.2). **b**, Dynamics of signal integrated over all momenta, shown here for comparison. **c** and **d**, Dynamics of signal integrated over the squares around the characteristic features A and B. **e**, Energy-integrated dynamics of S, X, and TT. The signal was integrated over the shown range. Figure published in [182].

after the projection procedure. Fitting a model to the kinetics in Fig. 6.7e would yield different results. This analysis does not work well here because the states in molecular semiconductors are generally too localized, and the corresponding momentum maps are too blurry. Consequently, projecting the dynamics to momentum maps of well-known characters should be preferred when analyzing trARPES data of molecular semiconductors.

Lastly, we checked the statistics of the decomposition to address the question of whether it can be applied to other systems with weaker signals in the excited states. Fig. 6.8 shows the results of the decomposition procedure using the same basis momentum maps applied to data sets acquired with different measurement times. The decomposition quality depends on the number of photoemission counts in the excited states. Here, we choose the integrated counts in the singlet exciton as a reference. At 150 kcts, or after 4 h of measurement time, the projection is of a similar quality as for the full data set with 730 kcts. after 27 h of measurement time. These numbers suggest that the decomposition should work for molecular semiconductors with a lower count rate in the excited state. Assuming a ten-fold smaller count rate, a data set with 150 kcts. could still be acquired in reasonable time (40 h). We again emphasize that the decomposition works well because of the different symmetries of HOMO and LUMO at the surface. If the orbitals have the same symmetry, a decomposition is significantly more challenging.

6.3.4 Evolution at longer delays

If the kinetics of the model with a single time constant perfectly described the observed dynamics, there should be no signal S anymore after ≈ 300 fs. However, the signal shows a biexponential decay at later delays as shown in Fig. 6.9a, and there still is $\approx 25\%$ of the maximum signal. The corresponding second time constant $\tau_2 \approx 600$ fs is only visible in the dynamics of S, but not in the bitriplet signal. Noticeably, there is also a slight relaxation of the energetic position of S by > 50 meV over 150 fs (Fig. 6.9b). The TT signal, on the other hand, shifts slightly up by ≈ 10 meV in the time range from 100 fs to 2000 ps (Fig. 6.9c). Over the corresponding time scale, there is no visible change in the TT momentum map (Fig. 6.9d). The momentum-integrated spectrum, however, does change: at 250 fs delay, the spectrum features a high-energy tail that cannot result from the remaining singlet exciton

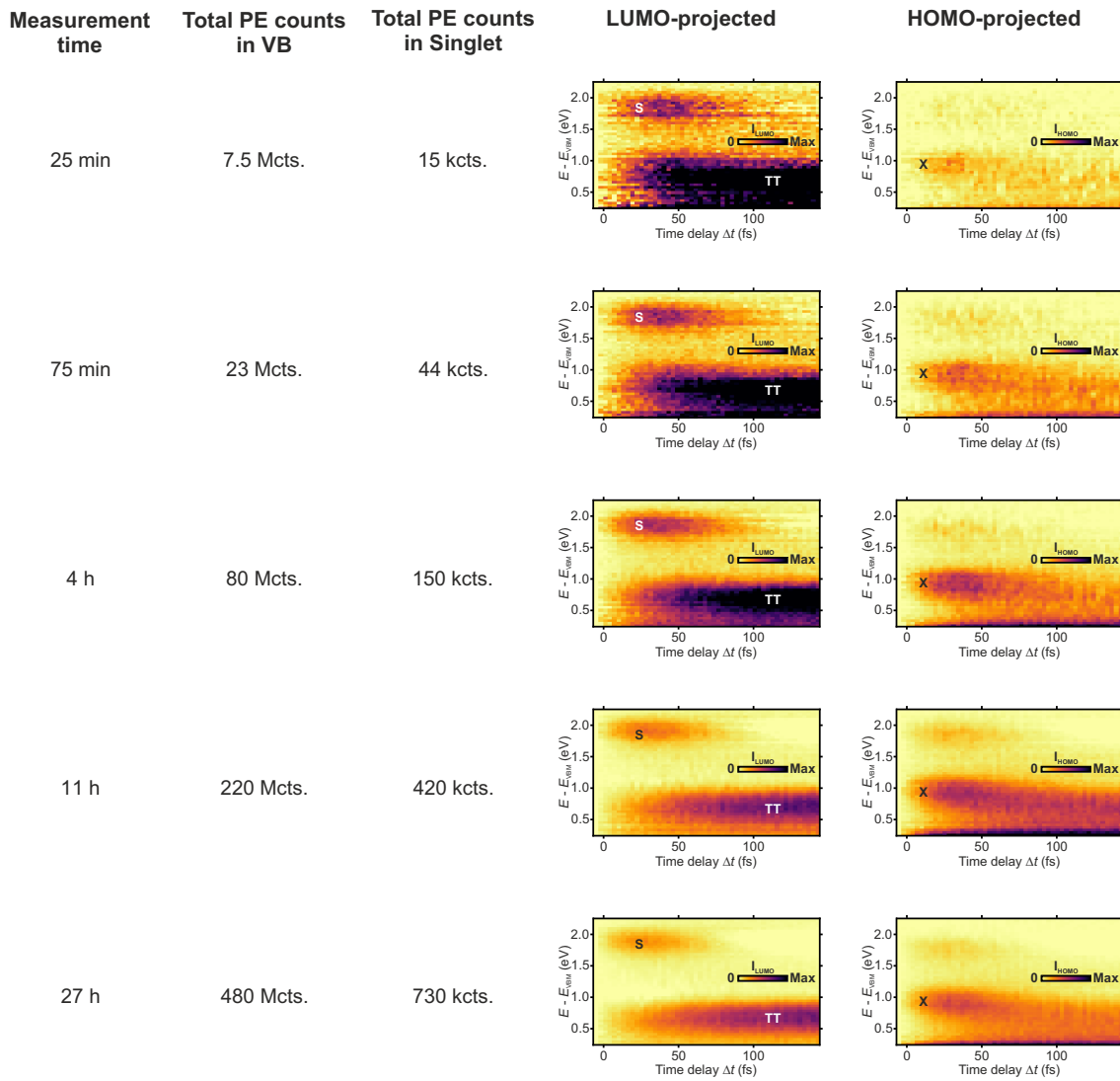


Figure 6.8. Statistics and decomposition. Orbital-projected dynamics for various measurement times and respective total counts in the VB and the singlet exciton. All plots are based on the main data set and normalized to the total count rate in the VB for each row. Figure published in [182].

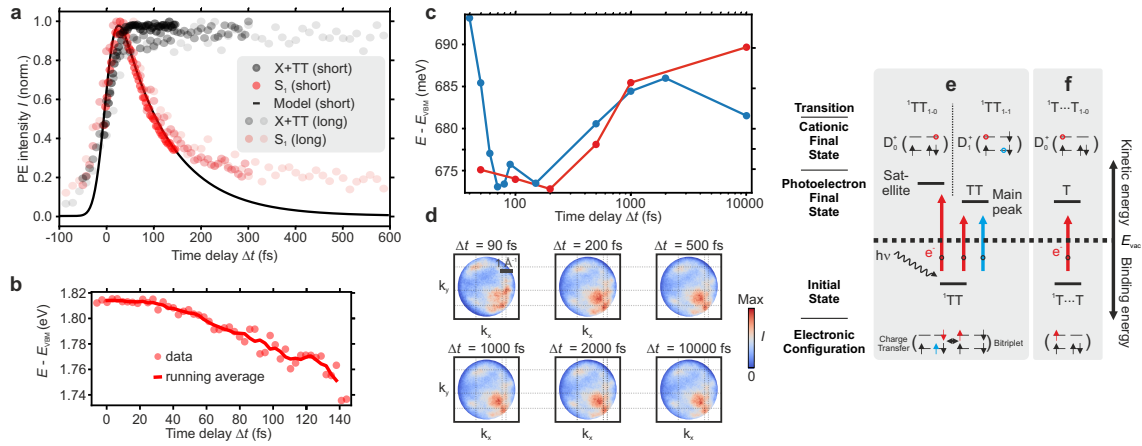


Figure 6.9. Evolution at longer delays. **a**, Dynamics of the singlet and the lower energy signal at longer delays, not orbital-projected. The short data set and model fit are the same as in Fig. 6.2e. The long data sets were acquired with a slightly longer instrument response function. **b**, Position of the higher energy signal. Time-dependence of the energetic position of the higher energy signal of the main high-statistics dataset. The energetic position was obtained by Gaussian fits to the momentum-integrated signal. **c**, Energetic position of the TT signal for two different data sets. The energies were obtained as in **b**. **d**, Momentum maps of the lower energy signal (integrated from 0.6 to 1.2 eV) at longer time delays. **e** and **f**, State diagram of the different initial states and the photoelectron and cationic final states after photoemission. **e**, Bitriplet exciton with charge-transfer character and **f**, separated, non-interacting bitriplet exciton. Transitions from the LUMO are shown in red, transitions from the HOMO in blue. Figure similarly published in [182].

population. This high-energy tail vanishes in the spectra at later times (> 1 ps); compare Fig. 8.4.

These observations can be explained by a mixture of charge-transfer states in the bitriplet exciton. If such states are present, a new photoemission transition is possible. An electron can be ejected from the LUMO of a CT state to create the ground state of the cation D_0^+ accounting for a satellite peak appearing at the energy of the bitriplet exciton $E_{\text{TT}} = 1.72$ eV (Fig. 6.9e). Additionally, the main transition that leaves the excited cation D_1^+ in the system should show a simultaneous HOMO and LUMO character. There are two pathways for this transition, one from the HOMO of a charge-transfer state and the other from a LUMO of the diabatic bitriplet state. As the bitriplet exciton ^1TT decays into the separated bitriplet exciton $^1\text{T}\cdots\text{T}$, the CT-character is lost and thereby the corresponding transitions. The energy of S relaxes because the signal at later times is not the main peak of the singlet exciton but rather the satellite of the bitriplet exciton, which is expected $E_S - E_{\text{TT}} = 90$ meV below. The upshift of the TT signal over longer time scales indicates a loss of stabilizing CT character.

To confirm the origin of S at later delays, it would be desirable to also see differences between the momentum maps right after excitation and after 300 fs. However, the weaker signal at these later delays makes a distinction based on the available data challenging. Furthermore, the expected difference lies in different widths of peaks in momentum space, arising from the different localization lengths of the singlet and bitriplet excitons. The corresponding signatures in the momentum maps are much more subtle than for states with different orbital characters (compare chapter 5).

6.4 Discussion

The results let us return to the questions regarding the fission mechanisms. Our observations confirm the theoretically predicted, but never experimentally verified, character of the singlet exciton in pentacene as being a 50/50-mixture of Frenkel and charge-transfer excitons [189]. Such a strong mixing between the diabatic Frenkel and charge-transfer states is only possible if their coupling is sufficiently strong and their energies almost degenerate.

The second signature of charge-transfer hybridization is the delocalization of the singlet exciton apparent in its momentum map. For a pure Frenkel exciton, electron and hole remain confined to the same molecule, and the size of the molecule limits the Bohr radius of the exciton. The triplet exciton in pentacene is known to be a pure Frenkel exciton. Its corresponding momentum map (Fig. 6.9d) looks dramatically different¹. The admixture of charge-transfer states reconciles the observed pronounced peaks in the momentum map of the singlet exciton with its excitonic character. In other words, exciton delocalization and exciton charge-transfer character describe the same phenomenon — the electrons and the hole in the singlet exciton have a significant probability of being found on different molecules.

Another critical point is the charge-transfer character of the bitriplet state. Two observations allow us to make a statement on the rough magnitude of the mixing. (1) The intensity of the high-energy signal at 500 fs, a signature of the charge-transfer character, is 20 % of the maximum of signal S. Because there are just as many bitriplet excitons as there are singlet excitons, the charge-transfer character in the bitriplet must be correspondingly small. (2) The energetic upshift of the TT signal by 10 meV, which is the biexciton binding energy E_{BX} that quantifies the energy difference between the pure bitriplet state ${}^1\text{T}\cdots\text{T}$ and the mixed and stabilized ${}^1\text{TT}$, is much smaller than the corresponding energy difference in the singlet exciton. That is quantified by the Davydov shift in pentacene, which amounts to 120 meV [192] and scales with the charge-transfer character of the singlet exciton. The charge-transfer character in the bitriplet exciton must hence be much smaller than in the singlet exciton, and we estimate its contribution to be less than 10 %. In other representatives of the acene series, this number could be significantly different. We predict an even more minor contribution in hexacene and a larger one in tetracene, in line with the energetic alignment of the diabatic states (see chapter 2.8).

Intriguingly, there is no apparent change in the momentum maps of the bitriplet and triplet excitons (Fig. 6.9d). We would expect to see a difference due to the delocalization of the state over two molecules inherent in the diabatic bitriplet state and the (minor) charge-transfer character. The effect of the latter should be insignificant because the charge-transfer character is small in the bitriplet exciton. However, the lack of a signature of the diabatic bitriplet state needs further consideration. It indicates that the electrons in the LUMOs of the bitriplet are coherently delocalized over a single molecule only.

A major controversy in the field has been the mechanism of the primary step, with contrasting views of a direct and coherent versus a charge-transfer mediated mechanism [53, 81]. With the decomposition of the signal into HOMO- and LUMO-projected DOS, it is clear that there is no direct population of the bitriplet exciton. In contrast, the lower energy signal immediately observed after excitation is a signature of the sizeable charge-transfer character of the singlet exciton. The bitriplet exciton is only generated by the decay of the singlet exciton. This observation rules out the coherent mechanism and supports the charge-transfer mediated mechanism.

¹Since we do not know the spin state of the electrons, it is impossible for trARPES to distinguish between the separated bitriplet exciton ${}^1\text{T}\cdots\text{T}$ and independent triplet excitons T_1 . For clarity, we just use the term triplet exciton.

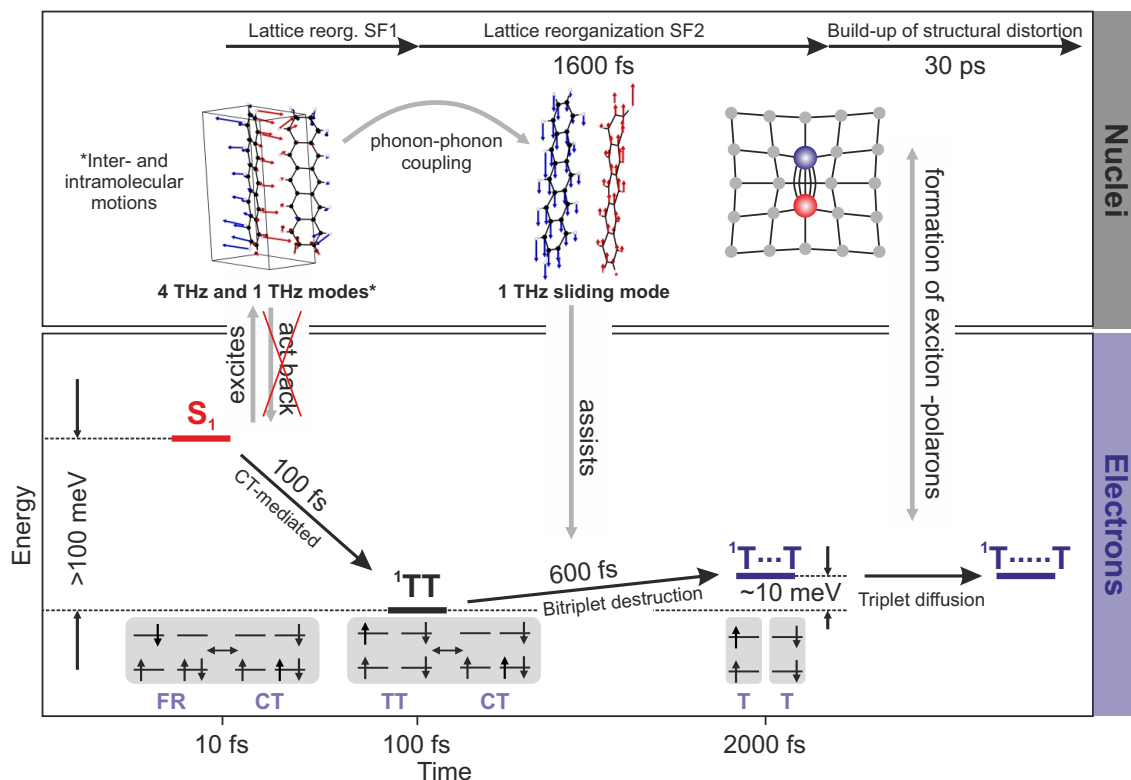


Figure 6.10. Overview of the nuclear and electronic dynamics in the first two steps of singlet exciton fission in crystalline pentacene. S_1 decays via a CT-mediated mechanism to the > 100 meV lower 1TT , accompanied by inter- and intramolecular vibrations that take up the excess energy. This dark state then loses its stabilizing CT character to form the dark $^1T \cdots T$ via triplet hopping. The observed 1 THz phonon might assist this process by significantly changing the electronic coupling between adjacent pentacene molecules. On later time scales, a structural distortion builds up in the lattice, flagging the formation of triplet exciton-polarons while the spin-correlated triplets diffuse further. Figure published in [183].

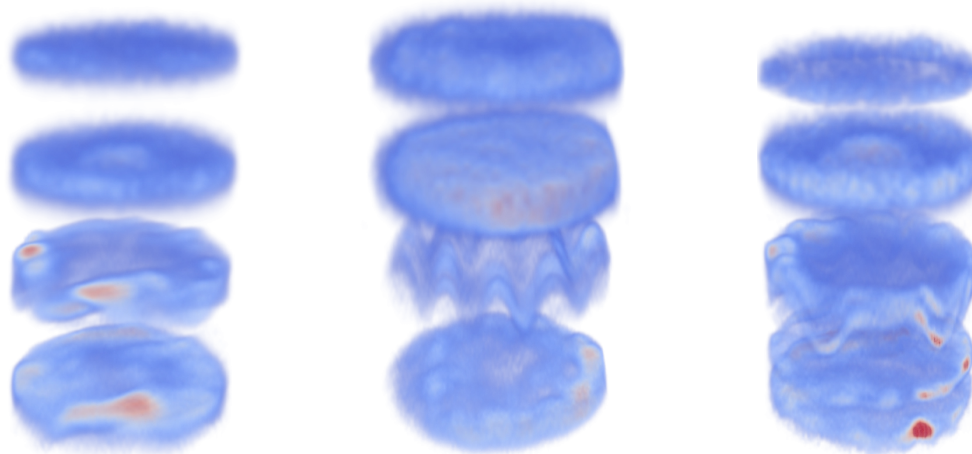
Apart from the electronic couplings, electron-phonon coupling may also play a role in the primary step. While it is evident that there will be some reaction of the nuclei to the perturbation of the system by the absorbed photon, it is the back action of the nuclei on the electrons that is subject to debate. There are currently two main lines of argumentation. The first emphasizes the role of specific strongly coupled modes that are thought to enable the primary step via a conical intersection mechanism [64, 65, 86, 193]. The argument is based on the consistent observation of nuclear coherences in different singlet exciton fission systems [64, 65, 86]. The nuclear coherences are commonly observed in optical spectroscopy and hence indicate a coupling between the nuclei and an optical transition. Through a back action of the nuclei to the electrons, these coherent modes are thought to enable singlet exciton fission. By contrast, the second line of argumentation views the observed vibrational coherence as a byproduct of the optical excitation and the electronic transition in the primary step [53, 194]. Crucially, there is no backaction of the nuclei on the electrons, and an incoherent vibrational bath is sufficient to explain the observations. The trARPES data do not provide evidence for the conical intersection mechanism in the form of oscillatory features on the singlet exciton population dynamics.¹

¹We note, however, that oscillations with a period smaller than the 43 fs FWHM of the instrument response function would not be visible in our data.

6.5 Conclusion

How, then, does singlet exciton fission play out in crystalline pentacene? The view supported by the work presented in this thesis and by femtosecond electron diffraction measurements carried out at the Fritz Haber Institute [195] is collected in Fig. 6.10. The singlet exciton transitions to the bitriplet exciton in a CT-mediated mechanism. In this step and the initial excitation of the singlet exciton, vibrational modes, especially around 1 and 4 THz are populated. Due to the lack of oscillatory features in the S_1 dynamics, we propose that the vibrational motion does not act back on the primary step. In the secondary step, the 600 fs conversion of 1TT to $^1T \cdots T$, a sliding mode of the pentacene molecules occurring around 1 THz might assist the destruction of the bitriplet exciton. The separated bitriplet exciton lies slightly higher (≈ 10 meV) than 1TT due to a loss of stabilizing CT character. On a time scale of 30 ps, a structural distortion builds up, most likely due to the formation of triplet exciton-polarons.

The next chapter discusses the singlet exciton fission dynamics of rubrene and tetracene single crystals in which the overall process is endothermic — in contrast to the exothermic case of pentacene.



7. Different pathways of endothermic singlet exciton fission

Following up on the investigation of exothermic singlet exciton fission in pentacene, we examine its endothermic counterpart in single crystals of rubrene and tetracene. Although the restricted excited states signal due to limitations set by the pump-induced space charge from a higher pump photon energy makes the experiments more challenging, we successfully observed the dynamics in both materials. In tetracene, the structural similarity of the electronic states to those in pentacene is immediately apparent. That provides us with the confidence to reinterpret the dynamics of the excited states — our results point to a ≈ 100 fs generation of the bitriplet exciton followed by a slower 6 ps dissociation into the separated bitriplet exciton. For rubrene crystals, we recapitulate that the coupling between diabatic charge transfer and bitriplet states is forbidden by symmetry and that the mechanism, therefore, skips the formation of the bitriplet exciton. Our results indicate that the separated bitriplet exciton is created directly from the singlet exciton within 1.85 ps. We conclude by matching our observations with literature results and by discussing the implications of such an ultrafast and endothermic process.

7.1 Introduction

Tetracene crystals were the first material in which singlet exciton fission was claimed to have been observed [60]. It was invoked to explain the observed low fluorescence yields in tetracene, and the explanation has withstood the test of time. Since these first works in the 1960s and 1970s, several new materials exhibiting singlet exciton fission have been found. On purely energetic considerations, the materials can be categorized into different classes. The first class encompasses materials in which the overall energetics, that is, the energy difference between the product triplet and the initial singlet excitons $\Delta E_{ST} = 2E_T - E_S$,¹ is negative and the process therefore exothermic. Pentacene, thoroughly discussed in the

¹The energy of the singlet exciton is taken from its photoluminescence peak, and not its absorption peak.

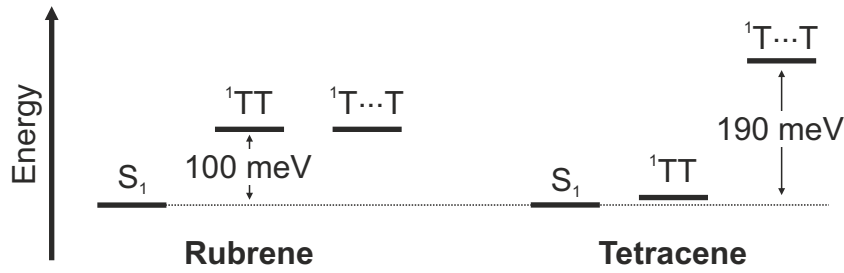
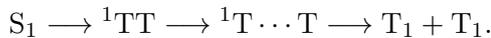


Figure 7.1. Energy diagram of the exciton states in rubrene and tetracene crystals. The energies are taken from table 7.1 and the bitriplet energy of tetracene from [82].

last chapter, is a prominent representative of this class. The second class includes materials in which the process is endothermic and $\Delta E_{ST} > 0$. In this chapter, trARPES studies of singlet exciton fission in two materials of this class will be discussed. These materials are tetracene and rubrene in their single-crystal form. Rubrene and tetracene share the tetracene core and are thus similar in their electronic structure in the gas phase. Due to the very different packing in the crystal, however, their properties in the solid state differ — as we have seen for their respective band structures. Nonetheless, singlet exciton fission is endothermic and ultrafast in both materials (see Table 7.1). It constitutes a major question in the field how a process that is considerably endothermic can occur on ultrafast time scales.

The reported time scales for the decay of the singlet exciton by transient absorption studies vary from < 50 fs in rubrene single crystals [85] to 100 ps in polycrystalline tetracene [75, 196], spanning over three orders of magnitude. These time scales must be taken with a grain of salt because of the challenging assignment of spectral features to the underlying states in transient absorption spectroscopy, especially because the relevant states in singlet exciton fission have overlapping spectroscopic features. Furthermore, measurements have been carried out on samples with different morphologies, i.e., on rather disordered thin films and morphologically well-defined single crystals, but frequently, conclusions have been drawn without referring to the lack of control over the morphology, albeit such differences can have a significant influence on the photophysics [197] and can even wholly suppress singlet exciton fission [198]. Such ambiguity calls for measurements that combine the propensity to assign signals to states and that work with single crystals. We thus study singlet exciton fission in rubrene and tetracene single crystals with trARPES.

The commonly accepted reaction scheme of singlet exciton fission is:



While the energies of the singlet and the triplet excitons are well known and account for the overall endothermicity, only recently have studies successfully obtained estimates of the energy of the intermediate 1TT [72, 82, 199]. In all studied systems, the estimated energy of 1TT lies below T_1 and ${}^1T \cdots T$, with the energy difference ranging between ≈ 0 meV in rubrene to 180 meV in tetracene. The reason for the lower energy of the bitriplet exciton is the admixture of $|CT\rangle$ states, leading to the large stabilization in tetracene. In rubrene, however, such an admixture is forbidden by the arrangement of neighboring molecules in the crystal, a point we will explore below.

A central question arises when comparing the two systems. How do the different energies of the bitriplet exciton affect the overall singlet exciton fission process? From Fig. 7.1, it is clear that the primary step is strongly endothermic in rubrene, whereas in tetracene, it is the secondary step. As shown in the case of pentacene, the dynamics of the excited states combined with the knowledge about their structure in momentum space allow a clear

Molecule	E_T	E_S (from PL)	E_S (from Abs.)	ΔE_{ST}
Pentacene	0.86 [82]	-	1.81 eV [192]	0.10 eV
Rubrene	1.15 [82]	2.22 [200]	2.32 [200]	-0.10 eV
Tetracene	1.25 [82]	2.31 [137]	2.33 [137]	-0.19 eV

Table 7.1. Energies of the lowest excitons in crystalline pentacene, rubrene, and tetracene from the literature. The energy of the triplet exciton E_T , the singlet exciton energy E_S from a photoluminescence and an absorption measurement, and the singlet exciton fission energy ΔE_{ST} are indicated.

assignment of the signal to states. In this chapter, it will be shown that such an approach can also be applied to rubrene and tetracene. There is, however, a major complication: the excited states signal is an order of magnitude weaker for these two systems compared to pentacene. For the former, higher energy photons are necessary to populate the excited states, and the increased pump-induced photoemission severely restricts the applicable fluence and, thus, the count rate in the excited states (see Table 7.2).

With the momentum maps, it is possible to distinguish between the singlet exciton fission pathways taken by rubrene and tetracene. They indicate that the primary step in tetracene is exceptionally rapid (< 200 fs) and the secondary step significantly slower (6 ps). By contrast, we observe no signatures of the bitriplet exciton in rubrene and suggest that the singlet exciton directly converts to the separated bitriplet exciton within 1.85 ps. Apart from these mechanistic insights, an overarching question arises from endothermic singlet exciton fission: Can we explain an energetically uphill process with a microscopic mechanism?

7.2 Singlet exciton fission in tetracene single crystals.

Ultrafast measurements on solid tetracene have been performed by several groups using transient absorption spectroscopy [73, 75, 196, 201–205]. Only a fraction of those were performed on tetracene single crystals [73, 201, 203–205]. These experiments were conducted with a time resolution ≈ 150 fs. They consistently report an ultrafast (~ 300 fs) appearance of an excited state absorption signal which has been interpreted as singlet exciton fission from higher-lying excitons or as relaxation within the singlet manifold. Furthermore, one study reported a ≈ 5 ps decay of the excited states absorption signal [203] that was also assigned to singlet exciton fission from higher-lying excitons. Throughout the transient absorption studies, it was claimed that singlet exciton fission occurs via a thermally activated process on a 50 to 100 ps time scale. In direct contradiction, two-photon photoemission spectroscopy was performed on vapor-grown tetracene films, revealing a 6 ps decay of the high-energy excited state signal, which was attributed to the conversion from S_1 to 1TT [67]. A quasi-instantaneous (< 20 fs) appearance of a lower-energy signal was interpreted as a signature of the bitriplet exciton coherently mixed into the photoexcited state.

Molecule	Pentacene	Rubrene	Tetracene
Incident fluence [$\mu\text{J cm}^{-2}$]	200	203	20
Photon energy [eV]	1.81	2.41	2.41
S_1 count rate [cts s^{-1}]	14	1.6	1.4

Table 7.2. Excitation parameters for the experiments with pentacene, rubrene, and tetracene. The S_1 count rate is the sum of all counts within the energy spread of the singlet exciton at the pump-probe delay where the signal in the singlet exciton is at its maximum.

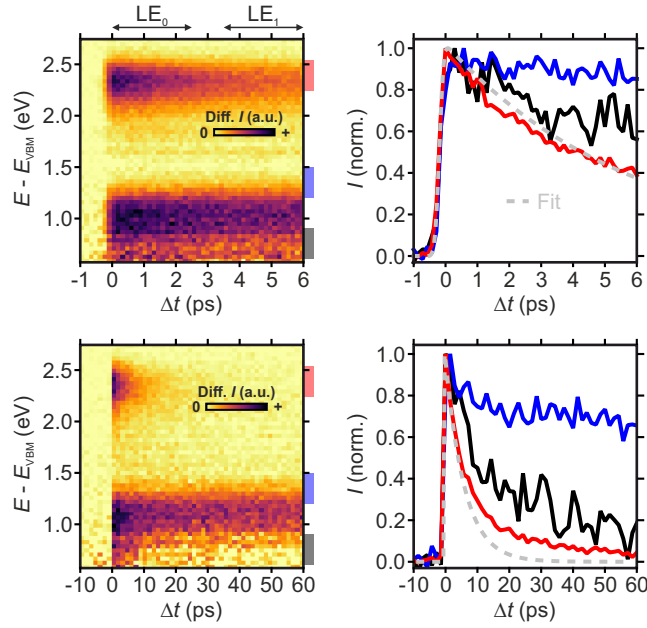


Figure 7.2. Excited states dynamics in tetracene. The left panels show the difference intensity $\text{Diff. } I$ (the PE intensity from which the pre-excitation PE intensity is subtracted) for tetracene excited with $h\nu = 2.4$ eV. The pump and probe pulses are incident at 60° to the surface normal; the pump is s- and the probe is p-polarized. The right panels show the energy-integrated dynamics of the signal; the energy intervals over which the PE intensity was integrated are indicated in the left panels. The fit is a convolution of a Gaussian pulse with $t_{\text{FWHM}} = 250$ fs and of an exponential decay with time constant $t_{\text{dec}} = 6$ ps.

The theoretical basis for singlet exciton fission in tetracene is much less established than in pentacene due to the lack of consensus on the basic time scales of singlet exciton fission reported by experiments. One theoretical study [206] proposed a vibronic mechanism to explain the instantaneous appearance of the lower-energy signal observed by Chan *et al.* in pentacene and tetracene [67]. From the experiments on pentacene, we know, however, that this signal is a satellite of the singlet exciton due to its $|CT\rangle$ character. Further theoretical studies are necessary to establish a better connection with experiments.

The understanding of endothermic singlet exciton fission is inconsistent, and the observations partially contradict each other. To address the outstanding controversy and unresolved questions, we performed trARPES on tetracene single crystals excited with 2.4 eV photons.

7.2.1 Experiment and Results

In the experiment, the pump pulse was s-polarized and incident at 60° to the surface normal. The electric field of the pump pulse was aligned with the \mathbf{a} -axis of the tetracene crystal along which the lowest bright singlet exciton is also polarized. After the photoexcitation, two signals simultaneously appear, a higher energy (HE) signal at $E - E_{\text{VBM}} = 2.32$ eV and a lower energy (LE) signal at $E - E_{\text{VBM}} = 1.02$ eV. (see upper row of Fig. 7.2). Within the time resolution of the experiment $t_{\text{FWHM}} = 250$ fs, there is no delay in the rise time of both signals. The HE signal decays with a time constant $t_{\text{dec}} \approx 6$ ps which is in agreement with the time constant reported in another time-resolved photoemission experiment [67]. Interestingly, the lower part of the LE signal (colored in black) shows different dynamics than the higher part (colored in blue) and degrades on a similar time scale as the HE signal. A data set taken over a longer time window up to 60 ps (see lower row of Fig. 7.2)

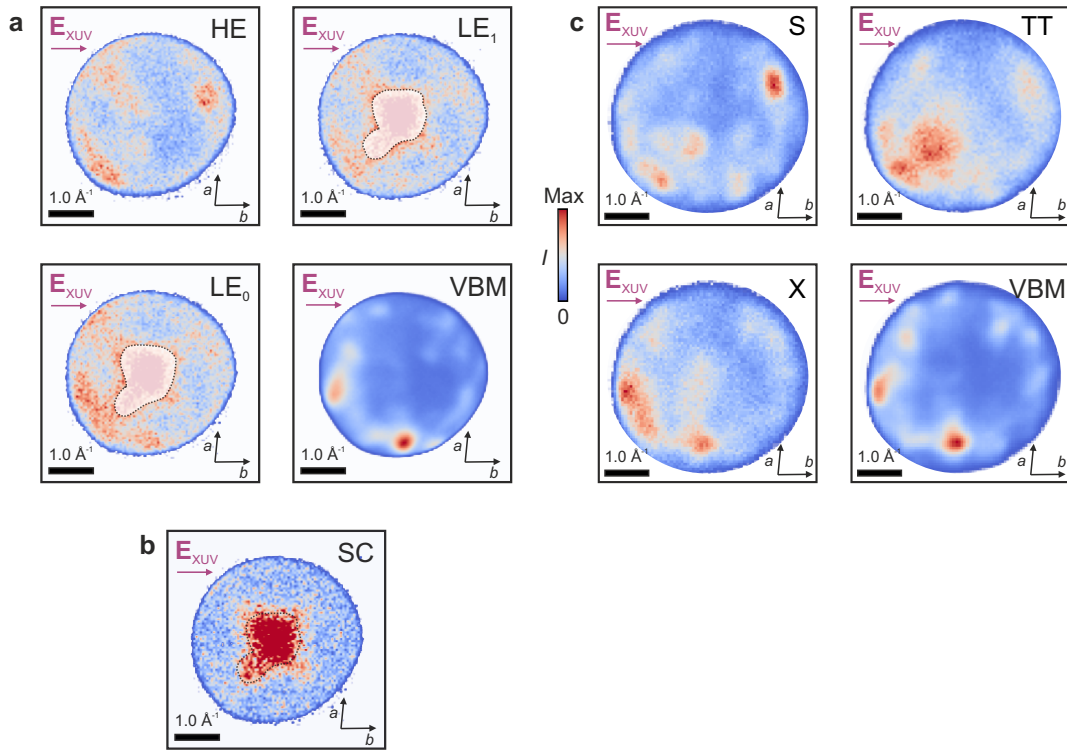


Figure 7.3. Momentum maps of the excited states in tetracene. **a**, The momentum map HE is the PE intensity of the higher-energy excited states signal integrated from 0 to 6 ps and from $E - E_{\text{VBM}} = 2.00$ to 2.60 eV. The momentum maps LE₀ and LE₁ result from integrating the lower-energy excited states signal over the time ranges indicated in Fig. 7.2 and from $E - E_{\text{VBM}} = 0.75$ to 1.35 eV. LE₀ is the early, and LE₁ is the late signal. The momentum map VBM is a constant energy cut through the PE intensity at $E - E_{\text{VBM}} = 0.00$ eV. The orientation of the crystal axes a and b and the XUV polarization are indicated. The signal within the dashed line in the LE momentum maps is an artifact that arises from XUV-induced space charge. **b**, Momentum map of the PE intensity arising from space charge. The signal was integrated from -1 to 0 ps and over the same energy range as the LE₀ and LE₁ momentum maps. **c**, Momentum maps of pentacene, reproduced for convenience from Fig. 6.2 in chapter 6. Note that the images are rotated by 90° here.

underlines this observation. The LE signal visibly shifts up in energy and is 70 meV higher at $E - E_{\text{VBM}} = 1.09$ eV after 60 ps. We must note here that this upshift coincides with the delay time at which the artefactual space charge interaction of pump- and probe-induced photoelectrons kicks in [207] and that this upshift has to be viewed with care. In addition to the fast ps-dynamics, the decay of the HE signal features biexponential dynamics over longer time scales with the second time constant $t_2 = 25$ ps. Over the same time window, the high-energy part of the LE signal decays with a time constant $t_3 = 190$ ps.

To address the nature of the observed signals, we show momentum maps for the VBM, the HE signal, the LE signal at early times, and the LE signal at later times in Fig. 7.3a. The first thing to notice is the similarity between the VBM momentum map of tetracene and that of pentacene - a point already discussed in chapter 5. The similarity is also visible in the momentum maps of the HE signal and momentum map S of pentacene. However, the momentum map of tetracene features peaks that are less pronounced and thus indicate a more localized real space character of the probed state. In analogy to pentacene, it is evident that the signal must come from a transition with LUMO character, and it is, hence, tempting to assign the momentum map to the singlet exciton. We refrain from doing so here but shift the explanation to a later section. The momentum map of the LE signal at

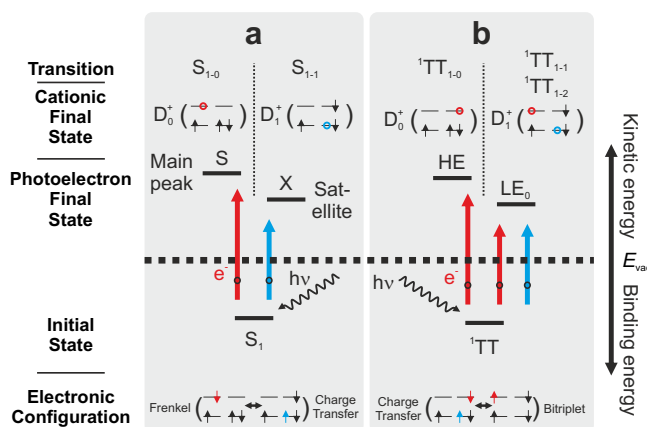


Figure 7.4. Photoemission transitions in tetracene. **a**, The two transitions of the singlet exciton, one with LUMO character (S_{1-0}) and the other with HOMO character (S_{1-1}). **b**, The three transitions of the bitriplet exciton, the highest-lying with LUMO character (${}^1\text{TT}_{1-0}$) and two isoenergetic transitions, one with LUMO (${}^1\text{TT}_{1-1}$) and the other with HOMO character (${}^1\text{TT}_{1-2}$). The two transitions ${}^1\text{TT}_{1-0}$ and ${}^1\text{TT}_{1-2}$ arise from the $|\text{CT}\rangle$ character of ${}^1\text{TT}$. Transitions with LUMO characters are shown in red and those with HOMO characters in blue.

early times ($\Delta t < 2.5$ ps), labeled LE_0 , shows a similarity with the HE momentum map and, notably, also with the VBM momentum map. It seems to be the sum of momentum maps with HOMO and LUMO characters. At later times ($\Delta t > 3$ ps), the momentum map of the LE signal appears more similar to the LE momentum map, and the HOMO-like signal faded. Note that the signal in the center of the LE momentum maps arises due to space charge, as shown by the momentum map of the space charge PE intensity in Fig. 7.3b.

7.2.2 Discussion

We propose two scenarios to explain the observations. (1) The observed dynamics are reminiscent of the dynamics in pentacene, i.e., the decay time scale $t_{\text{dec}} = 6$ ps quantifies SF1 and the HE momentum map can be assigned to the singlet exciton and the LE_0 momentum map to its satellite. (2) The decay of the HE signal corresponds to SF2 and the HE and LE_0 momentum maps; hence, both represent ${}^1\text{TT}$. In this scenario, the primary step is too fast to be observed with the time resolution of this experiment. Both scenarios will now be discussed in more detail.

If scenario (1) is correct, both the HE and LE signals at early times originate from the same state, the singlet exciton. By inspecting the possible PE transitions, we can infer that the HE signal should exhibit a LUMO character, while the LE signal should be only of HOMO character (see Fig. 7.4). Given the admixture of $|\text{CT}\rangle$ states, the ${}^1\text{TT}$ generated by SF1 should furthermore feature transitions that contribute both to the LE and the HE signal. The time scales of the primary step would then be $t_{\text{SF}} = 6$ ps for tetracene compared to $t_{\text{SF}} = 100$ fs for pentacene.

If on the other hand, scenario (2) is correct, the HE and LE signals at early times originate from the bitriplet exciton. The corresponding transitions indicate that the HE signal has LUMO character and the LE signal has both HOMO and LUMO character. Later, the LE signal is only due to the separated bitriplet exciton and thus of LUMO character. For this scenario to be correct, the primary step must be too rapid ($t_{\text{SF}} < 200$ fs) to be detected with the time resolution of the experiment. The time scale would then be comparable to SF1 in pentacene.

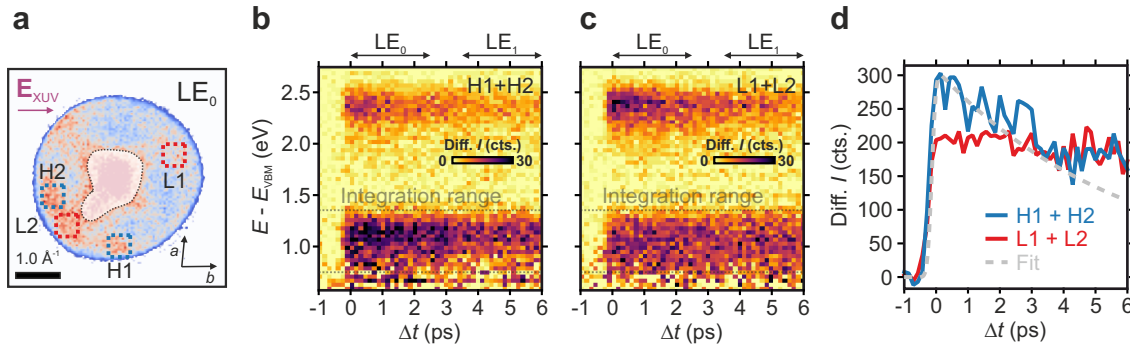


Figure 7.5. Dynamics of HOMO and LUMO features. **a**, Sections of momentum space characteristic of HOMO (H) and LUMO (L) orbital characters are indicated on the LE_0 momentum map. **b**, Differential PE intensity integrated over sections H1 and H2 and in **c** over L1 and L2. **d**, The corresponding differential PE intensity integrated over energy for the sum of the HOMO and LUMO features together with the same fit as in Fig. 7.2.

How do the scenarios fit to current knowledge? Several arguments are in contradiction to scenario (1). Firstly, the HE signal after $\Delta t = 30 \text{ ps}$ is dominated by the bitriplet exciton. Since the signal is relatively small, this suggests that ^1TT has limited $|\text{CT}\rangle$ character, similar or smaller than in pentacene – contradicting the expectation and measurements of the biexciton binding energy [72]. Most importantly, the momentum map LE_0 should be of dominant HOMO character, in apparent contradiction to the observation. Furthermore, the nearly two orders of magnitude difference in the time scale of SF1 in tetracene and pentacene needs explanation. Given the similar couplings in both systems, [53], this difference must come from the energetics. For pentacene, the energy difference between singlet and bitriplet exciton is $E_{\text{TT}} - E_{\text{S}} \approx -100 \text{ meV}$, whereas it is $E_{\text{TT}} - E_{\text{S}} \approx 100 \text{ meV}$ in tetracene. The uphill energetics in tetracene suggest that the rate should depend on temperature, calling for measurements that explicitly probe the temperature-dependence of the 6 ps time scale.

Scenario (2) can resolve the above discrepancies: it is consistent with a substantial $|\text{CT}\rangle$ character of the bitriplet exciton apparent in the strong HE signal. The simultaneous HOMO and LUMO characters in the momentum map LE_0 can then be readily explained as a result of the two possible ^1TT to D_1^+ transitions, one with HOMO and the other one with LUMO character (Fig. 7.4b). We need to emphasize again that this scenario implies that the singlet exciton is not directly observed because its conversion to the bitriplet exciton is too rapid.

Besides the two presented scenarios, there might be a third, intermediate one. If the singlet and bitriplet excitons are close in energy, there can be a dynamical equilibrium between them with the ratio of their populations governed by the respective energies. In this case, the observed LE and HE signals at early times would arise from both types of excitons featuring highly overlapping transitions.

To further examine the validity of the scenarios, the dynamics of different features in momentum space were investigated. In Fig. 7.5, the PE intensity was integrated over different sections of momentum space that are characteristic of either HOMO or LUMO orbital character. While the separation of the signal is not perfect, it does show clearly different dynamics for the two orbital characters. The resulting dynamics for the LE signal indicate that the HOMO character diminishes on a similar time scale as the HE signal and additionally that the LUMO character stays constant in the same time range. We must stress again: the LUMO character of the LE signal, which is not present if singlet excitons

dominate the excited state population, does not increase in the measured time window. This observation contrasts the primary step in pentacene and is evidence for scenario (2).

In conclusion, scenario (2) seems more plausible since it can explain the mixed character of the LE_0 momentum map and the lack of an increased LUMO orbital character in the LE_0 momentum map. We must thus reinterpret the dynamics of singlet exciton fission in tetracene single crystals, and deem the following scenario most likely. The primary step occurs within < 200 fs, a time scale that has been observed by transient absorption measurements in tetracene [197, 201, 205] and the related compound TIPS-tetracene [208]. Afterward, the bitriplet exciton formed in the primary step decays over 6 ps into the separated bitriplet exciton by triplet hopping. This process is accompanied by a loss of the stabilizing |CT⟩ character and is strongly endothermic — the biexciton binding energy is ≈ 180 meV in tetracene [72]. The 70 meV upshift of the LE signal might be evidence for the gain in energy during the secondary step. For this process to be spontaneous and rapid, there must be a gain in entropy in the secondary step as proposed by Chan *et al.* [67]. Indeed, the larger DOS for ${}^1T \cdots T$ compared to 1TT — in the former, the two triplets may be on any two molecules, whereas in the latter, they need to be nearest neighbors — leads to an increase in entropy. The entropy contribution to the Gibbs free energy has been estimated to be ~ 100 meV at room temperature and is therefore of a similar size as the biexciton binding energy [209].

To obtain a more precise time scale for the primary step, trARPES needs to be carried out with a time resolution $t_{FWHM} < 50$ fs. A decomposition based on the orbital character furthermore requires increased excited state count rates. Recalling the statistics of the pentacene projection, the total number of counts in the singlet exciton should be greater than ~ 150 kcts, which is slightly higher than in the current data sets (~ 100 kcts). The required number of counts should be even larger because the momentum maps of tetracene are more blurry, making the projection less stable.

7.3 Singlet exciton fission in rubrene single crystals

The coupling between singlet and bitriplet excitons, either in a mediated or direct mechanism, depends on two transfer integrals: the HOMO-HOMO transfer integral t_{HH} and the HOMO-LUMO transfer integral t_{HL} . In the low-symmetry crystals of tetracene and pentacene, both couplings are on the order of 100 meV [210], which is in sharp contrast to the situation in rubrene single crystals [85, 211]. Here, the high C_{2h} symmetry of neighboring pairs — the two molecules are stacked face-on with a displacement along the long axis — prohibits a coupling between HOMO and LUMO and hence $t_{HL} = 0$ meV (see Fig. 7.6). To allow the primary step, the coupling needs to be activated, which can be achieved by vibrational

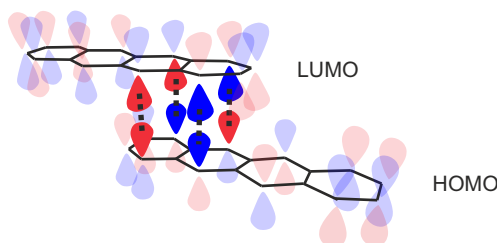


Figure 7.6. Symmetry restriction in rubrene. The HOMO and LUMO are shown for the two nearest neighbors in the crystal structure of rubrene. The highlighted orbital lobes overlap. Due to the different symmetries of the two orbitals along the short axis, the overlaps cancel each other. Adapted from [85].

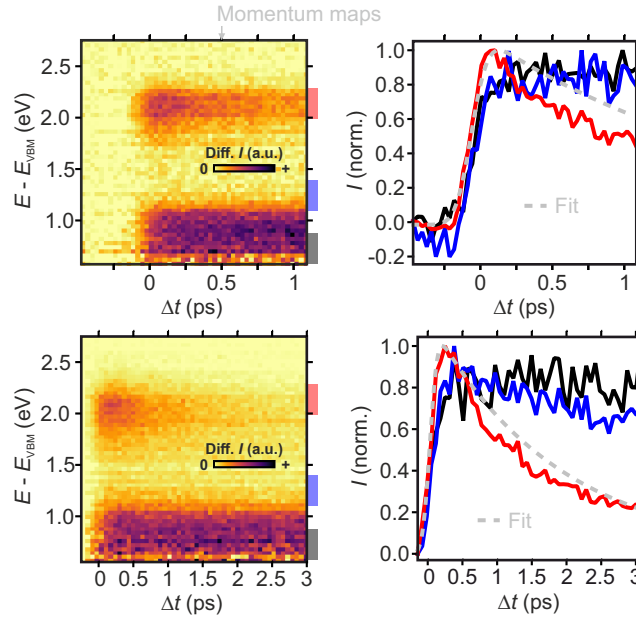
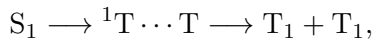


Figure 7.7. Excited states dynamics in rubrene. The left panels show Diff. I for rubrene excited with $h\nu = 2.4$ eV. The pump and probe pulses are incident at 60° to the surface normal; both pump and probe are p-polarized. The grey arrow indicates the time delay at which the momentum maps in Fig. 7.8 were acquired. The right panels show the energy-integrated dynamics of the signal; the energy intervals over which the PE intensity was integrated are indicated in the left panels. The fit is a convolution of a Gaussian pulse with $t_{\text{FWHM}} = 200$ fs and of an exponential decay with time constant $t_{\text{dec}} = 1.85$ ps.

modes that break the C_{2h} symmetry, e.g., by a displacement along the short axis. Due to the particular symmetry of the neighboring pairs in rubrene, singlet exciton fission may be amenable to a conical intersection mechanism [85]. The forbidden coupling has furthermore the immediate consequence that the $|\text{CT}\rangle$ character of the bitriplet exciton is negligible and that there should be little difference between ^1TT and $^1\text{T}\cdots\text{T}$, as confirmed by the lack of a ^1TT photoluminescence signature in rubrene single crystals [199]. We can then rewrite the singlet exciton fission reaction scheme to



which skips the formation of the bitriplet exciton. Writing the process in this way also highlights that the two triplets produced from the singlet exciton do not need to be nearest neighbors in rubrene. Since the singlet exciton in rubrene is delocalized over several molecules, the two triplets can be generated on all molecules over which the singlet exciton is delocalized — thus increasing the density of states.

7.3.1 Experiment and Results

In the experiment, rubrene single crystals were illuminated with $h\nu = 2.4$ eV photons with a polarization component along the surface normal, thus driving the out-of-plane polarized transition to the singlet exciton. Directly after photoexcitation, two excited states signals appear simultaneously (Fig. 7.7), as in tetracene and pentacene, a HE signal at $E - E_{\text{VBM}} = 2.14$ eV and a LE signal at 0.93 eV. Surprisingly, the HE signal is 80 meV lower than the well-known photoluminescence of the singlet exciton at 2.22 eV [200]. The subsequent decay of the HE signal can be roughly fit with a single exponential with the time

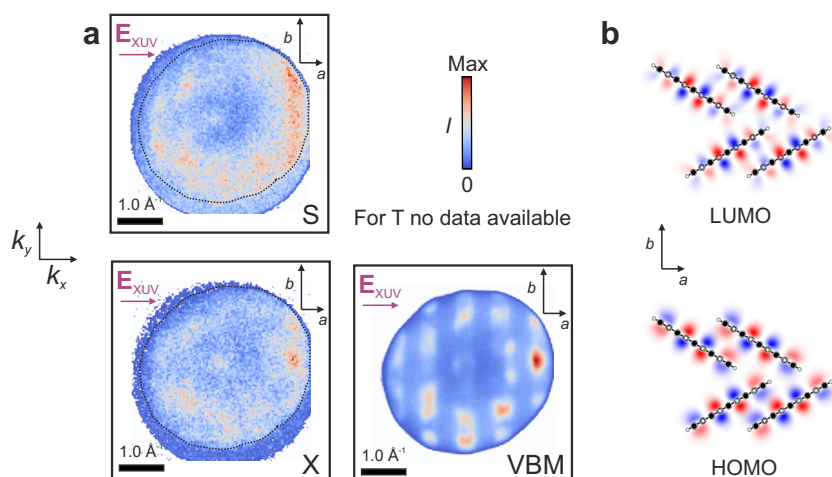


Figure 7.8. Momentum maps of the excited states in rubrene. **a**, The S and X momentum maps were acquired at a time delay $\Delta t = 500$ fs. S is the higher-energy signal (integrated from $E - E_{\text{VBM}} = 1.60$ to 2.40 eV), and X is the lower-energy excited states signal (integrated from $E - E_{\text{VBM}} = 0.95$ to 1.35 eV). The momentum map VBM is a constant energy cut through the PE intensity at $E - E_{\text{VBM}} = 0.00$ eV. The orientation of the crystal axes a and b and the XUV polarization are indicated. The signal outside the dashed line in the S and X momentum maps is an artifact. **b**, Visualization of HOMO and LUMO in the crystal geometry of rubrene in the ab -plane. The molecules are correspondingly viewed along their short axis.

constant $t_{\text{dec}} = 2$ ps. Over the first 3 ps, neither the energetic position nor the population of the LE signal change.

Momentum maps of the HE and LE signals were acquired at $\Delta t = 500$ fs and are shown in Fig. 7.8a. The total counts of the data sets acquired at later time delays (e.g., $\Delta t = 3$ ps) are insufficient to extract information from momentum maps. The HE signal in rubrene can only come from S_1 , and we thus label the corresponding momentum map as S. It features the same periodicity of the vertical stripes, spaced by the long reciprocal lattice vector \mathbf{a}_r , as the VBM momentum map, evidence for the delocalization of the singlet exciton. However, the features are less pronounced in S and point to a larger degree of localization than the VBM states. Additionally, there is a different overall modulation of the PE intensity in the two momentum maps stemming from the different orbital characters. In the S momentum map, the intensity is higher at large in-plane momenta along k_x than the VBM momentum map. Treating the PE process once again as a Fourier transform, we can relate this to the larger number of orbital nodes along the long axis in the LUMO compared to the HOMO, see Fig 7.8b. The LE signal at 500 fs is expected to be a mixture of S_{1-1} and T_{1-0} , but dominated by the singlet exciton contribution. The mixture is apparent in the LE momentum map, which is highly similar to the VBM momentum map due to the common HOMO character of the underlying transitions. It might be surprising that the energetic position of the LE signal does not change, although entirely different states lead to the signal. From naive energetic considerations, S_{1-1} is expected at $E_{\text{HE}} - E_{\text{T}} = 0.99$ eV and the position of T_{1-0} is not *a priori* clear. In analogy with pentacene, we roughly place it at $E_{\text{T}} - W/2 = 0.95$ eV, where W is the VB width. The different energetic positions of the two transitions might then be too close together to be resolved with our energy resolution.

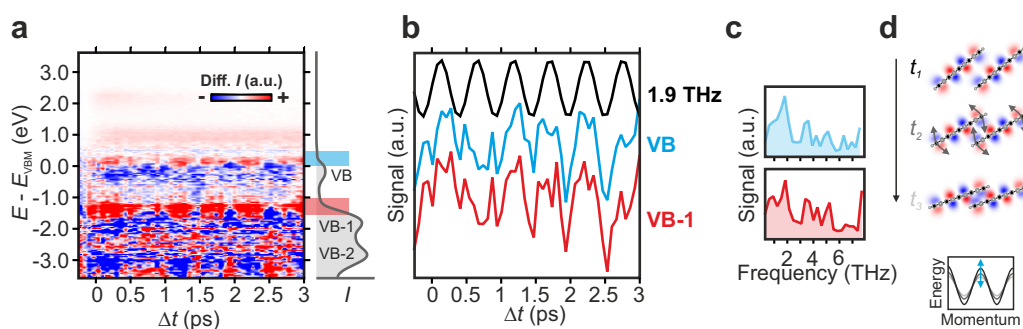


Figure 7.9. Dynamics of the valence states in rubrene. **a**, Momentum-integrated differential PE intensity in rubrene of valence and excited states after $h\nu = 2.4$ eV excitation. The grey line shows the static momentum-integrated PE intensity. **b**, Differential PE intensity of the VB and VB-1 integrated over the intervals shown in **a** together with a 1.9 THz oscillation. **c**, Fourier transform of the VB and VB-1 dynamics. **d**, Visualization of the movement of rubrene molecules at three different times due to the 2.2 THz phonon from ref. [85]. The change in orbital overlap leads to a modulation of the VB width.

7.3.2 Dynamics in the valence states

In the preceding discussions, we focussed on the dynamics of the excited states following photoexcitation. We also expect a response of the valence states to this perturbation. However, the change of the valence signal induced by the excitation lies buried in the large signal of the unperturbed states. It is thus challenging to extract, for example, the dynamics of the holes. Nonetheless, detailed information can be obtained from the valence state dynamics. We hence inspect the differential PE intensity of the valence states following the $h\nu = 2.4$ eV excitation over the first 3 ps, as shown in Fig. 7.9a. The signal at the center of the three visible bands is slightly depleted, and, strikingly, there is a periodic modulation of the signal at the upper band edges with the same frequency. This modulation is also apparent at the center of VB-2 with an inversed sign. In Fig. 7.9b, the signal integrated over a region in the upper edges of VB and VB-1 is shown, which emphasizes the periodicity of the modulation and indicates that the frequency of the modulation is 1.9 ± 0.2 THz. The Fourier transforms of these signals also peak at 1.9 ± 0.2 THz (see Fig. 7.9c). At such frequencies, we expect intermolecular vibrations, but how can they lead to the observed signal at the band edges?

Coherent oscillations with similar frequencies have been observed in rubrene employing transient absorption spectroscopy, Tao *et al.* observed it at 2.3 THz (ref. [212]) and Miyata *et al.* at 2.4 THz (ref. [85]). The latter authors matched the observed oscillation to a phonon at 2.2 THz through molecular mechanics simulations, a phonon that other groups have found [147, 149]. The displacement of this phonon is visualized in Fig. 7.9d. It strongly modulates the overlap between two HOMOs and, thereby, the HOMO transfer integral. The oscillation of the HOMO transfer integral translates into oscillation of the band width. This mechanism matches the observed periodic modulation in the PE data, which is most pronounced at the band edges — as expected for oscillations of the band width.

7.3.3 Discussion

The discussions of singlet exciton fission in rubrene in the literature have been highly controversial. Some authors claimed an ultrafast < 50 fs, coherent formation of the triplet excitons from S_1 (ref. [85, 213]), while others did only observe dynamics with a 2 ps time scale [199, 212, 214] in line with theoretical expectations [211]. The data presented here

does not support an ultrafast formation of the triplet excitons: in the momentum map at $\Delta t = 500$ fs we do not find the significant LUMO character expected if triplet excitons are present. Instead, the 1.85 ps singlet decay we observed agrees well with the reported slower time scale. Together with the lack of stable bitriplet excitons in rubrene due to the forbidden $|CT\rangle$ - $|TT\rangle$ coupling, this points to the following mechanism. Singlet excitons decay directly into the separated bitriplet exciton ${}^1T \cdots T$, where the electronic coupling could be either due to one-electron integrals (corresponding to the CT-mediated pathway) or due to two-electron integrals (corresponding to the direct pathway). The singlet exciton fission dynamics reported in the *ab initio* calculations by Tamura *et al.* are consistent with our observation, and these authors find that the direct pathway dominates in rubrene [211]. The forbidden coupling might be turned on either by the presence of thermal disorder, static disorder [199], or phonons populated by the initial excitation [85]. Furthermore, the optical transition triggers a reaction of the nuclei, which, amongst other unresolved movements, oscillate at 1.9 THz. It is very likely that this mode acts back on the singlet exciton fission dynamics since it strongly changes the exciton energies. Indeed, the deviation of the dynamics of the singlet exciton from an exponential decay could be a sign of the backaction. However, it is not possible to confirm that hypothesis at this point.

7.4 Conclusion

Despite the similarity between rubrene and tetracene molecules, singlet exciton fission plays out entirely differently in the single crystals of these two molecules. In tetracene, the formation of the bitriplet exciton is expected to be extremely fast due to the energetic proximity of singlet and bitriplet excitons and the well-established charge-transfer mediated coupling. Subsequently, the strongly bound bitriplet exciton dissociates into the separated bitriplet exciton on a time scale of 6 ps which we inferred from the early presence of a LUMO character in the LE momentum map. The loss of $|CT\rangle$ character accompanying the secondary step is revealed by the simultaneous reduction of HOMO character in the LE signal at $E - E_{\text{VBM}} \approx 1$ eV and the decay of the HE signal at 2.3 eV. On the same time scale, the upshift of the LE signal by 70 meV might present evidence for the gain in energy during the secondary step.

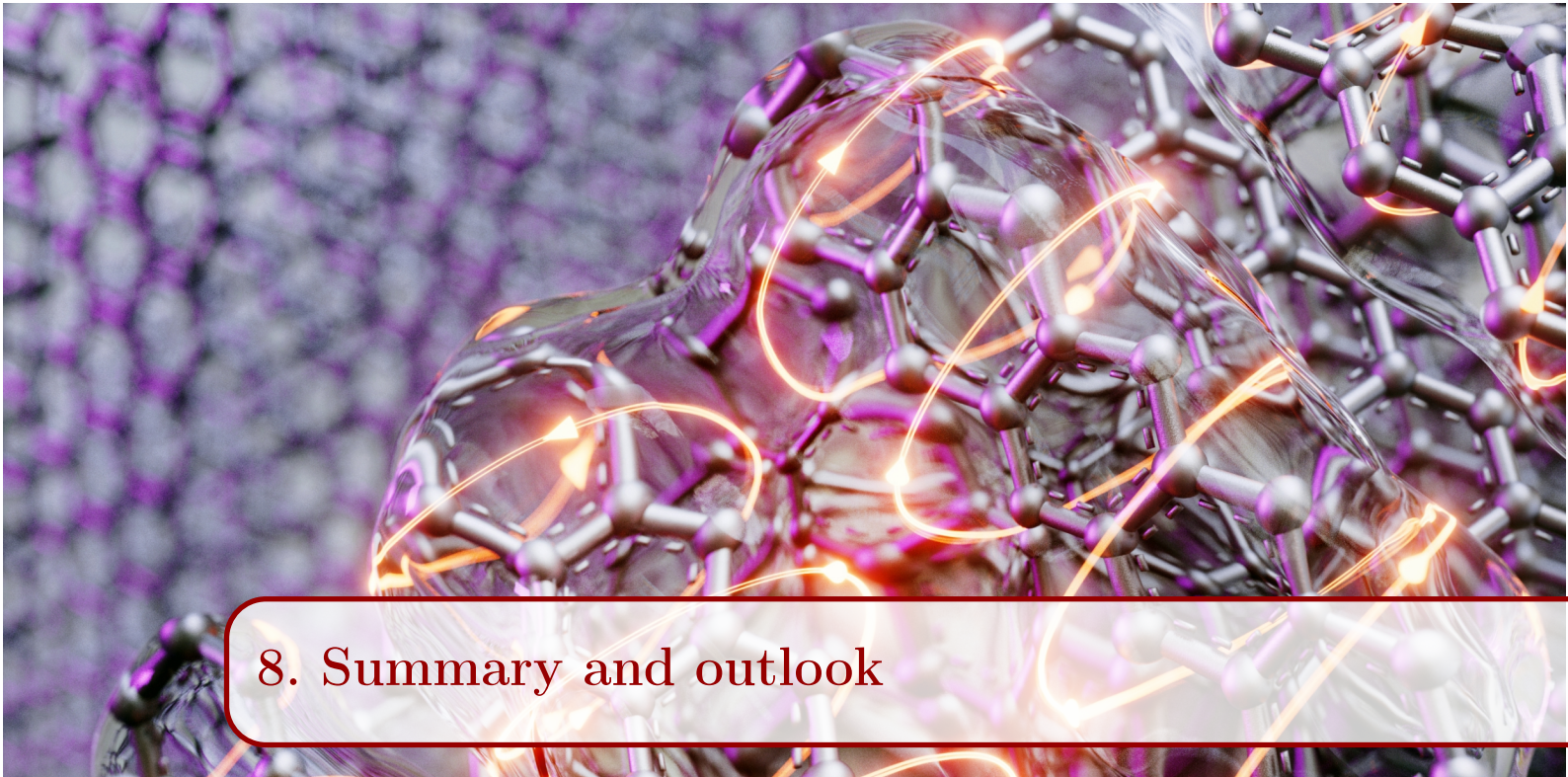
Because of the forbidden mixing of $|CT\rangle$ with $|TT\rangle$ states in rubrene single crystals, the bitriplet exciton 1TT is not stabilized with respect to the separated bitriplet exciton ${}^1T \cdots T$ — the two labels, essentially, represent the same state in rubrene. We observed a 1.85 ps decay of the singlet exciton, which correspondingly marks the transition to the separated bitriplet exciton. The decay of the singlet exciton is comparatively slow in rubrene because of the lack of $|CT\rangle$ - $|TT\rangle$ coupling in the equilibrium geometry. Only through the presence of disorder or phonons generated by the excitation can the transition to ${}^1T \cdots T$ occur. The momentum maps of the singlet exciton reveal that it has significant $|CT\rangle$ character — the PE intensity of the ratio of the main singlet exciton to the CT-induced satellite peak is similar to the ratio observed in pentacene. This observation aligns with theoretical expectations of a highly delocalized singlet exciton [215, 216]. In the dynamics of the valence states, we observe coherent oscillations with a frequency of 1.9 THz that are apparent at the band edges. These oscillations are consistent with the modulation of the band width of the valence states induced by a consistently reported phonon slightly above 2 THz. This phonon corresponds to a rotation of the tetracene core around the short molecular axis.

The interpretation of the presented results relies on the conclusions drawn from the experiments conducted on pentacene single crystals. As we have pointed out, however, the data sets for rubrene and tetracene do not feature the same signal quality in the excited states due to the intrinsically limited fluence for a higher photon energy. If this problem

can be solved, e.g., by repelling the pump-induced photoelectrons by a retarding field [217], an orbital-resolved analysis of the excited states is within reach for tetracene and rubrene. Furthermore, it is highly desirable to obtain momentum maps for all states involved in singlet exciton fission, especially those not reported here. These include the singlet exciton in tetracene and the separated bitriplet exciton in rubrene. Whereas the latter is accessible with the current experimental setup, for the former, the temporal width of the pump pulses at 2.4 eV would need to be reduced to < 50 fs.

The ultrafast and uphill conversion of singlet to triplet excitons presents a significant conceptual challenge. Temperature must play a role in this process, but experiments so far have been inconclusive [50, 75]. We furthermore believe that there must be a connection between the violent fluctuations of the electronic states discussed in chapter 4 and endothermic singlet exciton fission. It is conceivable that the dynamically disordered landscape of a molecular crystal provides sites wherein the energetics are more favorable than in the frozen and ordered crystal structure, thus allowing for rapid conversion. The crucial point is that the average value of the exciton energy is insufficient to understand the process, instead one has to analyze the distribution of exciton energies. To put it into the words of Anderson: *No real atom is an average atom, nor is an experiment ever done on an ensemble of samples. [...] this is the important, and deeply new, step taken here: the willingness to deal with distributions, not averages* [7]. Indeed, at the sizeable high-energy tail of the tetracene bitriplet exciton, the energetics for bitriplet separation are favorable (see Fig. 8.4). There is a high need for a joint effort of theory and experiment to explore the connection between excited state dynamics and (dynamic) disorder. Recent work on gallium nitride and the perovskites is pointing in the right direction and might prove fruitful for molecular semiconductors [218–221].

In conclusion, our studies of the dynamics of the excited states in these two systems indicate that the creation of triplet excitons as a result of singlet exciton fission can take different routes in the different crystal packings of tetracene units present in single crystals of rubrene and tetracene. The formation of the bitriplet exciton may be skipped, and triplet excitons generated directly from the singlet exciton. Furthermore, our findings emphasize the importance of obtaining information about the excited states in momentum space. Without knowledge about the structure of these states, the interpretation of the momentum-integrated dynamics of both rubrene and tetracene remains highly ambiguous.



8. Summary and outlook

In this work, time- and angle-resolved photoemission spectroscopy was used to study the fluctuating equilibrium and the exciton dynamics in molecular semiconductors. This chapter first summarizes the experimental results of the preceding chapters and is then followed by conclusions drawn at the end of this thesis and by ideas for future work in the field.

8.1 Summary

At equilibrium, we investigated the experimental band structures of five representative molecular semiconductors and revealed the relation to the crystal structure in chapter 4. The band structures could be reproduced with a tight-binding model that includes three distinct transfer integrals amongst nearest neighbors. From the understanding gained by the connection between the model and the crystal structure, it became clear that, apart from the relative position of the molecules dictated by the crystal structure, the π -topology of the molecular building blocks takes on a center-stage role in determining the electron-phonon coupling and the resilience to disorder in these systems. Both the coupling and the resilience are of fundamental importance for charge transport performance governed by dynamic disorder due to large fluctuations of the molecules around their equilibrium positions. We identified a path to engineer the π -topology and, thereby, to reduce the coupling of the inevitable fluctuations to the electrons, and to make the eigenstates resilient to localization in the presence of electronic disorder. To test the connection between electronic disorder and localization, tight-binding simulations were conducted with parameters directly extracted from the experiment. These simulations showed the presence of a tail of localized states at the upper edge of the bands. The width of this tail and the localization length of its states strongly depend on the relative values of the transfer integrals. Furthermore, we analyzed the nonlocal (Peierls) electron-phonon coupling for representative π -topologies and found a smaller coupling of the frontier orbitals of armchair-type such as picene compared to zigzag-type molecules such as pentacene. In the current model of charge transport in molecular semiconductors, i.e., transient localization theory, reduced electronic disorder due to small electron-phonon coupling, and an increased resilience to disorder are crucial for high

charge mobilities. These findings hence suggest that molecules with π -topologies similar to that of picene are promising materials for next-generation molecular semiconductors with high charge mobilities.

In chapter 5, we disentangled the different factors that make up the structure of momentum maps, i.e., constant-energy cuts through the three-dimensional photoemission intensity. The idealized view of momentum maps as Fourier transforms or momentum projections of (localized) Bloch orbitals in real space proved to be immensely fruitful for understanding the signatures arising from different crystal momenta, orbital characters, or localization lengths. Furthermore, the intuition granted by simple tight-binding models allowed us to reveal subtleties of the Bloch orbitals such as the character of the Wannier function. Finally, spatial signatures of localization in momentum maps of the tail states of rubrene's valence band were found.

With time- and angle-resolved photoemission spectroscopy, we examined exothermic singlet exciton fission in pentacene single crystals for chapter 6. Therein, the first momentum images of singlet and triplet excitons in a molecular semiconductor are shown. The understanding of momentum maps gained in the preceding chapter was instrumental in making sense of the intricate structure of the exciton images. These clearly showed that both types of excitons feature a similar orbital character and that the singlet exciton is considerably more delocalized than the triplet exciton. Crucially, we were able to identify an instantaneous signal accompanying the photoexcited singlet exciton as a satellite peak, and not, as was previously claimed, as the coherently populated bitriplet exciton. The satellite peak is a signature of the sizeable charge-transfer character present in the delocalized singlet exciton. The analysis was carried one step further by decomposing the exciton dynamics into signals from states with different orbital characters. This important advance allowed us to shed light on the underlying mechanism of singlet exciton fission. The observations are entirely consistent with a charge-transfer mediated mechanism, in which the considerable coupling between singlet and bitriplet exciton is mediated by a physical mixing of charge-transfer states into both types of excitons. No signatures of a mechanism governed by nuclear motion was found. Finally, we observed traces of the separation of the bitriplet exciton that point to a 600 fs time constant for this process and to a slight ≈ 10 meV stabilization of the bitriplet exciton ^1TT concerning the separated $^1\text{T}\cdots\text{T}$.

In the final chapter 7, different pathways of endothermic singlet exciton fission in rubrene and tetracene were discussed. The momentum maps of the excitons in tetracene are highly reminiscent of those in pentacene. The observed dynamics occur on a 6 ps time scale, apparently much slower than in pentacene. However, we found evidence that the bitriplet exciton appears quasi-instantaneously, that is, faster than the 200 fs time resolution of this experiment. The observed slower dynamics are then indicative of the separation of the bitriplet exciton which is accompanied by a loss of the stabilizing charge-transfer character. These findings are consistent with a sizeable binding energy (≈ 200 meV) of two triplets in tetracene. In line with the energetically uphill separation, the photoemission signal at the triplet energy rises by 70 meV on the same time scale as the loss of charge-transfer character. Compared to the dynamics in pentacene, the primary step in tetracene seems to happen just as rapidly, and it is the separation of the bitriplet exciton that is considerably slower. Due to the forbidden coupling between charge-transfer and bitriplet states in rubrene, we found evidence that singlet exciton fission takes a different path in rubrene. Instead of forming the bitriplet exciton ^1TT through the primary step, the separated bitriplet exciton $^1\text{T}\cdots\text{T}$ is directly populated from the singlet exciton within 1.85 ps. After optical excitation, a coherent phonon at 1.9 THz is visible as oscillations of the bandwidth that arise from the

strong electron-phonon coupling of this phonon. It strongly modulates the transfer integrals and is therefore also expected to have an impact on the singlet exciton fission dynamics.

8.2 Conclusions

Intriguingly, singlet exciton fission takes different paths amongst the three materials examined in this work. In both exo- and endothermic fission, the relative energy and the coupling of charge-transfer configurations are of paramount importance. This is exemplified by comparing tetracene and pentacene, and rubrene and tetracene. The crystal structures of the former are quasi-identical and hence also the coupling between the configurations. The difference lies, as discussed in the dimer model of chapter 2, in the relative energies of the electron configurations. The logic following from this model suggests a consistent understanding of singlet exciton fission in different systems. In tetracene, the charge-transfer configuration is energetically closest to the bitriplet configuration which enables a sizeable mixing and stabilizes the bitriplet exciton compared to the singlet exciton. By contrast, in pentacene, the Frenkel and charge-transfer configurations are closest and it is the singlet exciton that is stabilized compared to the bitriplet exciton. Thus, and that is the critical point, the mixing makes the primary step less *endothermic* in tetracene and less *exothermic* in pentacene. The energetics of the primary step cannot be understood without taking the physical mixing of charge-transfer configurations into account. Overall, the magnitudes of the energy differences between S_1 and 1TT are quite similar and the rates of the primary step should therefore also not differ significantly. It is the speed of the *secondary step*, the separation of the bitriplet exciton, that is dramatically different in the two materials with an order of magnitude higher rate in pentacene. Again, that arises from the relative energies of the charge-transfer configurations which stabilizes the bitriplet exciton in tetracene considerably more than in pentacene.

The comparison between rubrene and tetracene highlights the importance of the *coupling* of charge-transfer configurations. The forbidden coupling in rubrene slows down the singlet-bitriplet transition and makes the direct mechanism competitive with the charge-transfer mediated mechanism. Furthermore, in strong contrast to tetracene, the bitriplet exciton is not stabilized compared to free triplets. The following picture seems most appropriate for singlet exciton fission in rubrene: the delocalized and mobile singlet exciton first has to find a region in the dynamically disordered lattice where the coupling is allowed. There it undergoes fission directly to the separated bitriplet exciton. This process might be modulated by the backaction of the 1.9 THz coherent phonon triggered by the optical excitation.

The essential advance of this work on singlet exciton fission was to obtain state-resolved dynamics in molecular semiconductors. Instead of relying on ambiguous spectroscopic signals, time- and angle-resolved photoemission spectroscopy provides novel and fascinating insights into the character of the transient and highly correlated excitons. This additional information is crucial for interpreting the complex excited state dynamics in molecular semiconductors.

8.3 Outlook and future work

Coming back to the introduction and the discussion of how to achieve microscopy of orbitals, this work has shown that angle-resolved photoemission spectroscopy comes very close to this dream. Intricate features of the orbitals, and even of the many-body wave function, are directly visible in momentum maps. Future developments might lead to the possibility of transforming the momentum information to real space by reconstruction procedures [222,

223]. That would enable us to obtain transient snapshots of the orbitals during a wide variety of ultrafast transitions. Recent advances have been made in this direction [224].

Fluctuations

Thermal fluctuations of the molecules are an essential ingredient in the physics of molecular semiconductors. Their coupling to the electrons entails an interesting possibility: can we, by tuning the temperature and thereby the magnitude of the disorder, observe a transition from delocalized Bloch states to fully localized states in representative systems? Apart from the intellectual excitement of this endeavor, we would be rewarded with detailed information about the interplay between dynamic disorder and localization. A challenge of this experiment is to obtain data at low temperatures where sample charging presents an issue, which, however, might be overcome by working with thin samples. Future work should address the tail of localized states in greater detail. Some of the questions to be addressed are: Is it possible to extract a localization length for these states? How does the tail develop with temperature? And, most promisingly, do certain types of band structures exhibit less localization, i.e., can we observe that they are more resilient to disorder? To address these questions, the measurements should be carried out with an energy resolution <50 meV, thus promising to resolve the band tail.

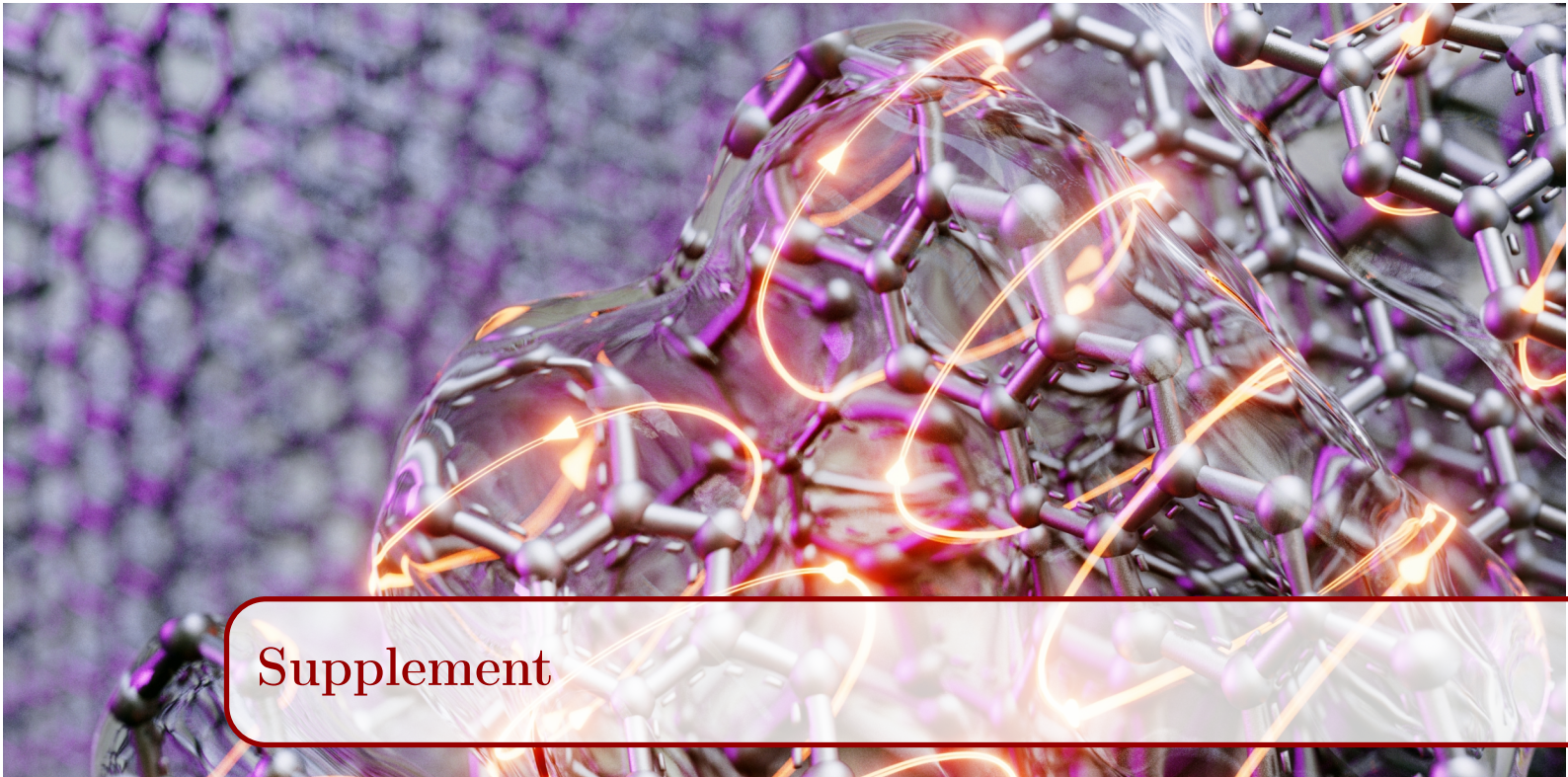
Exciton dynamics

While the amount of information in the photoemission data inspires confidence in the interpretation of the dynamics, uncertainties remain, especially for low excited state signals. It then becomes more important to match the observations with theoretical predictions. Some work has been done on photoemission spectra of the excitons in crystalline molecular semiconductors, but so far only for small model systems [225]. Advances in this direction and *ab initio* computations of momentum maps, already available for conventional semiconductors [226] and underway for molecular semiconductors [227], promise to greatly expand the knowledge about the excited states. Regarding experimental advances, it would be of great interest to obtain orbital-resolved dynamics for both tetracene and rubrene. These experiments, however, have to wait for techniques that suppress pump-induced space charge that inevitably arises when exciting with photon energies $h\nu > 2$ eV. Then, one should address the unresolved question of the temperature dependence of the endothermic steps in singlet exciton fission. An intriguing problem is the orbital-resolved observation of singlet exciton fission in hexacene. Due to energetics, the transition from the singlet exciton to a tritriplet state is allowed and might dominate [228], thus opening up the possibility of obtaining three excited electrons from a single photon.

Exploring the interplay of disorder and excitons

More broadly, our investigations touched on a hitherto mostly unexplored terrain — the combination of disorder and excited states. The most pressing question arising from our work is how endothermic singlet exciton fission can be explained. While several models exist to date, from thermal activation to entropy-driven, or disorder-induced, no mechanism has been proven. We think that dynamic disorder plays an essential role in providing "hot spots" in the fluctuating landscape of molecules, in which an endothermic process can become energetically favorable. Apart from the role of disorder in singlet exciton fission, it might prove important for organic photovoltaics. Currently, a big challenge in the field is to understand the mechanism of exciton dissociation. How can the strongly bound excitons in organic materials nonetheless efficiently separate into free charges? Here, the disorder might again enable dissociation by making sites with more favorable energetics available.

New insights are needed from both theory and experiment to better understand how the disorder affects the fate of excitons.



Supplement

Tight-binding model for ditetracene

Due to the four interacting tetracene cores, the tight-binding Hamiltonian of ditetracene is a 4x4-matrix. The relevant interaction terms are shown in Fig 8.2. With these additional transfer integrals, we can write the Hamiltonian as:

$$H = \begin{pmatrix} h_0 & h_{ud} & h_{AB} & h_d \\ h_{ud} & h_0 & h_d & h_{AB} \\ h_{AB} & h_d & h_0 & h_{ud} \\ h_d & h_{AB} & h_{ud} & h_0 \end{pmatrix},$$

with

$$h_0 = 2t_a \cos \mathbf{k} \cdot \mathbf{a}$$

$$h_{ud} = 2t_{ud}$$

$$h_{AB} = 2t_+ \cos \mathbf{k} \cdot \frac{\mathbf{a} + \mathbf{b}}{2} + 2t_- \cos \mathbf{k} \cdot \frac{\mathbf{a} - \mathbf{b}}{2}$$

$$h_d = 2t_{d+} \cos \mathbf{k} \cdot \frac{\mathbf{a} + \mathbf{b}}{2} + 2t_{d-} \cos \mathbf{k} \cdot \frac{\mathbf{a} - \mathbf{b}}{2}.$$

This Hamiltonian is diagonalized and the eigenvalues fitted to the measured band structure.

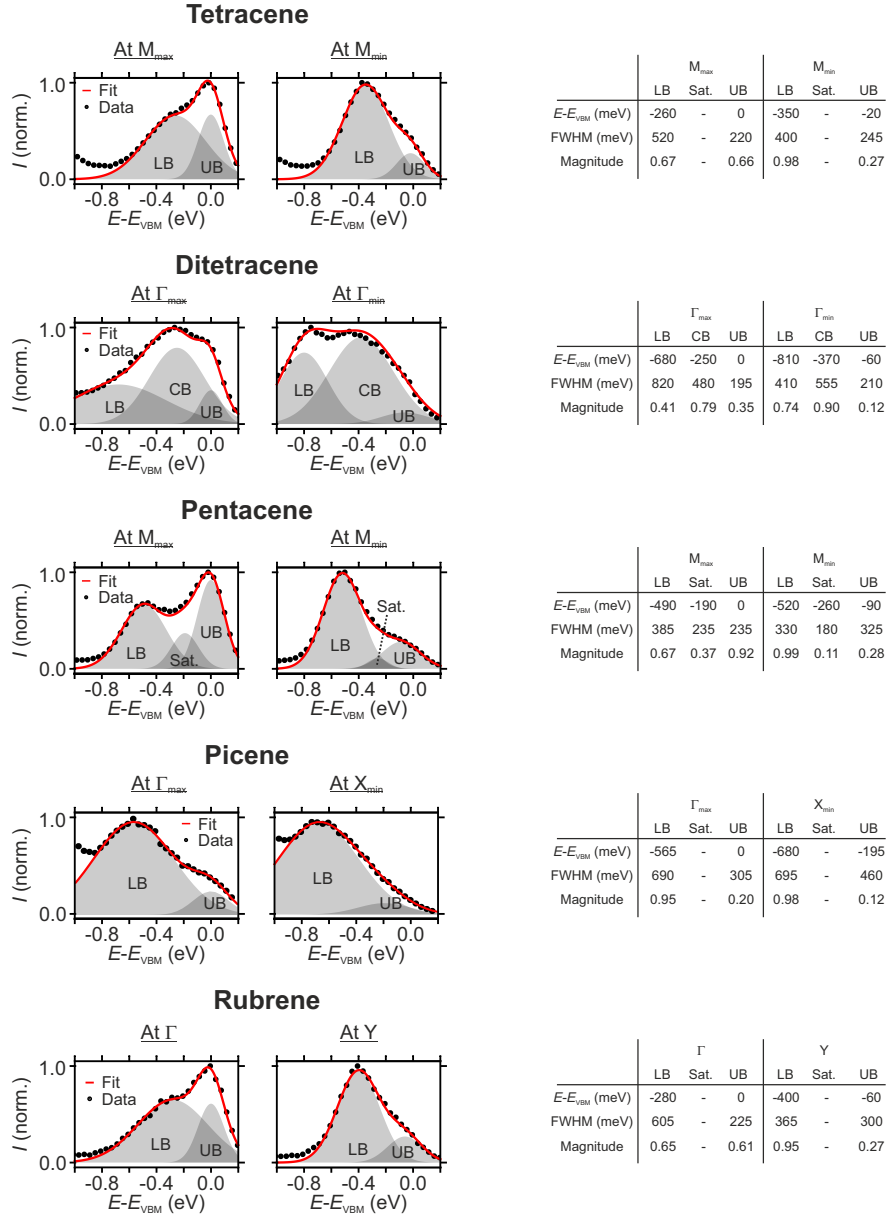


Figure 8.1. Energy distribution curves of the valence bands. Each row shows an EDC at the k -point with the maximum and at another point with the minimum band energy. Each EDC was fitted with Gaussian profiles, the parameters of which are shown to the right.

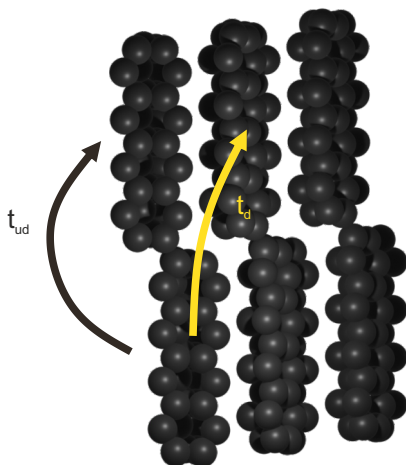


Figure 8.2. Additional transfer integrals in ditetracene. The transfer integral t_{ud} quantifies the intramolecular interaction between tetracene core in the upper and lower layer. The intermolecular interaction between tetracene cores in the upper and lower layer along $a + b$ and $a - b$ is quantified by the transfer integral t_d .

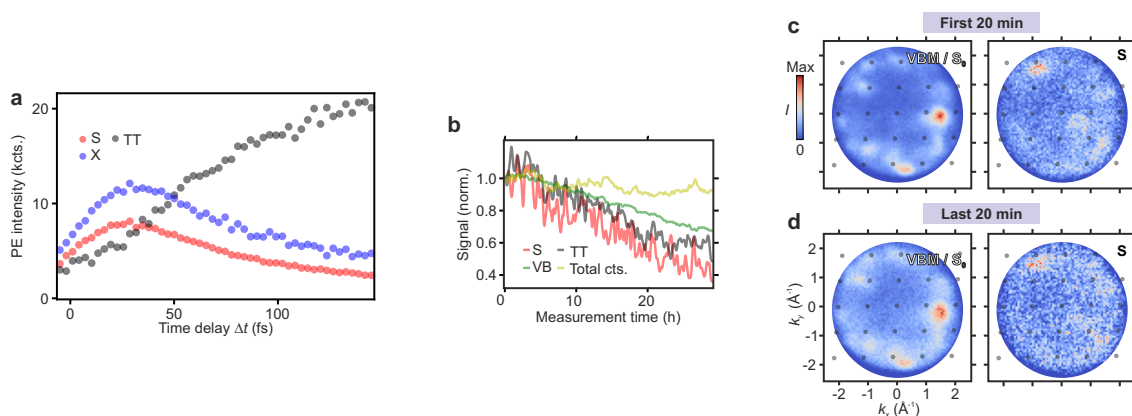


Figure 8.3. Non-normalized dynamics and sample degradation. **a**, Non-normalized dynamics of orbital-projected S, X and TT. **b**, Degradation of the signal of S, TT, and VBM throughout a measurement. For comparison, the total count rate, i.e., all measured electrons, is shown. **c**, Momentum maps of VBM and S of the first 20 minutes of measurement compared to **d**, the last 20 minutes of the same dataset as in **b**.

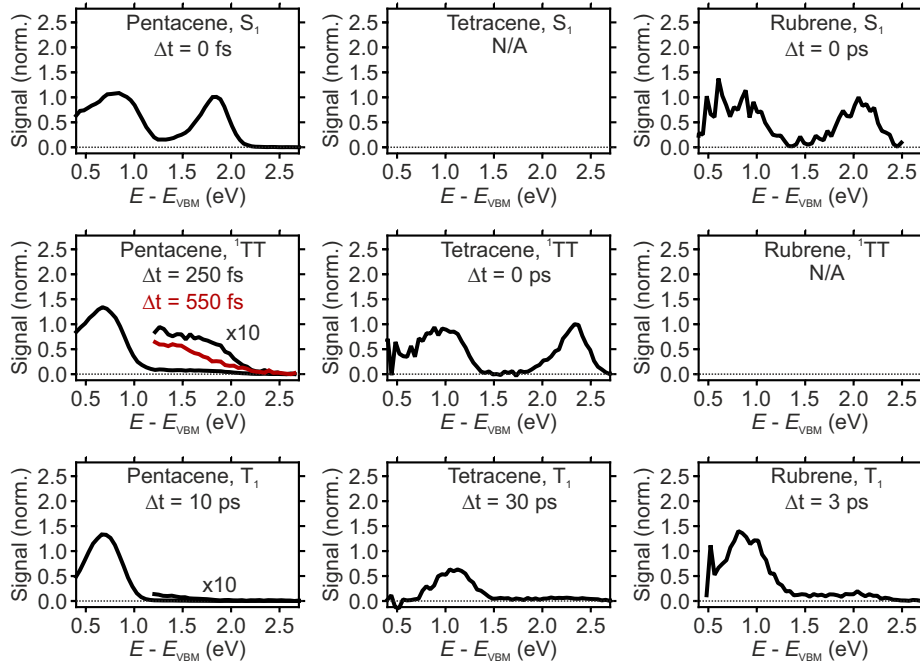


Figure 8.4. Intrinsic spectra of different exciton species. The upper row shows the Diff. PE intensity at zero time delay for pentacene, tetracene, and rubrene. The curves are normalized to the peak of the high-energy signal. The center row shows the Diff. PE intensity at a time delay at which the bitriplet exciton dominates the signal. The lower row shows the Diff. PE intensity at a time delay at which the signal from the triplet exciton dominates. The curves are normalized to the peak of high-energy signal and multiplied with the ratio $\frac{I_{\text{exp.}}}{I_{\text{inst.}}}$. Here, $I_{\text{exp.}}$ is the maximum PE intensity in the high-energy signal in the experiment with the pulse width t_{FWHM} and $I_{\text{inst.}}$ is the hypothetical maximum signal for a pulse with zero width, that is, it is the instantaneous response of the system. This procedure ensures that the signals represent the intrinsic spectra of the different excitonic species as closely as possible. The essential point is that the T_1 signal is relatively smaller in tetracene than in rubrene and pentacene, and that the ^1TT spectrum in pentacene has a high energy tail. Note that it is not possible not obtain a pure ^1TT spectrum for pentacene due to the similar time scales of SF1 and SF2. For some states, the intrinsic spectrum could not be obtained. The experimental conditions are described in chapters 6 and 7.



Data availability and code usage

Data availability

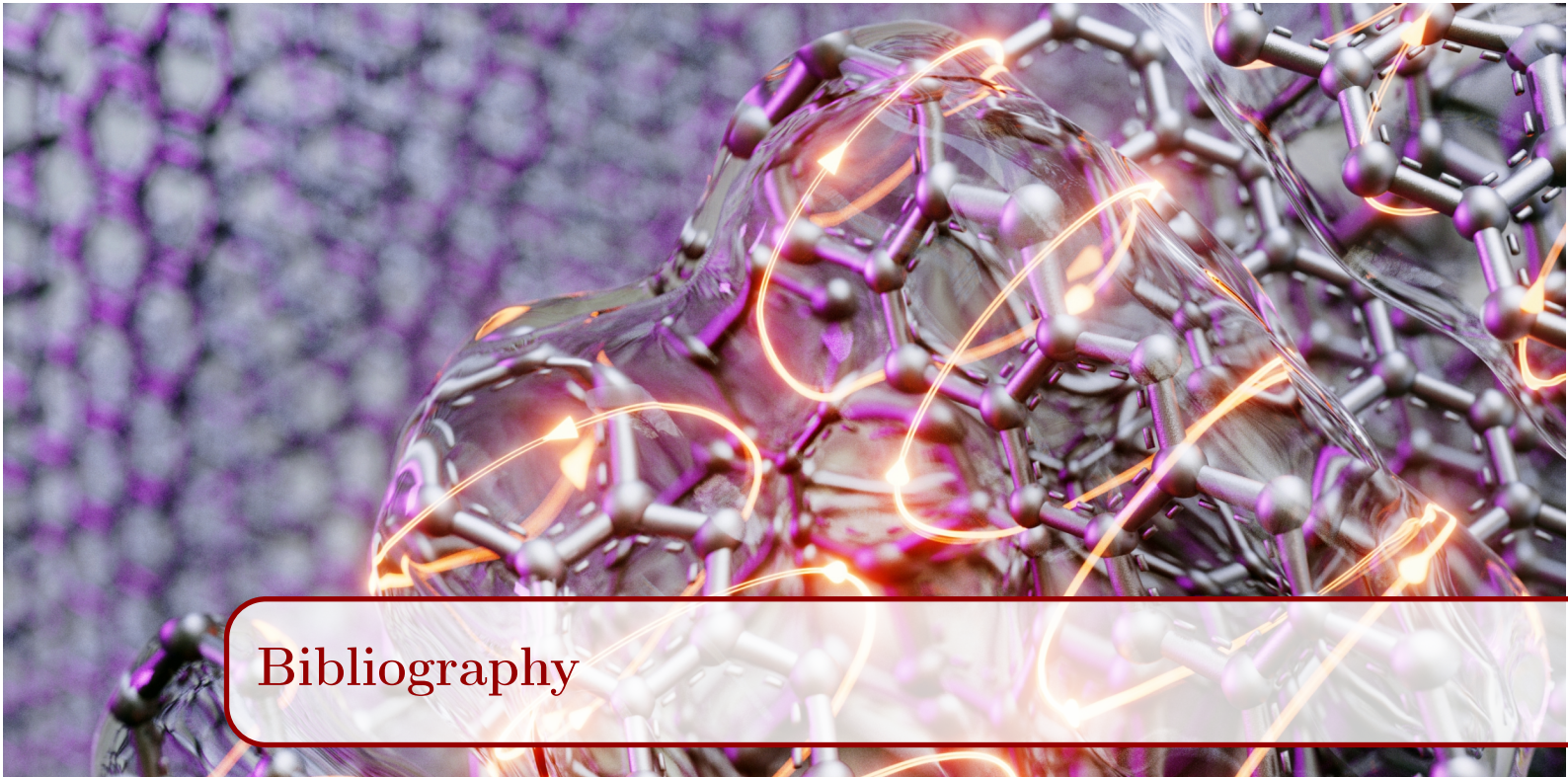
The data presented in chapter 4 will be made available in this [Zenodo repository](#) once the corresponding article has been published. These data sets include those analyzed in chapter 5.

The data presented in chapter 6 is openly available in this [Zenodo repository](#).

The data presented in chapter 7 will be made available in this [Zenodo repository](#) once a corresponding article has been published.

Code usage

The code used in this thesis to bin the single-event data coming from the time-of-flight momentum microscope detector was developed by R. Patrick Xian and can be found on this [Github project](#).



Bibliography

- ¹E. Schrödinger, “Nobel Lecture Physics 1933: The fundamental idea of wave mechanics”, *Reson.* **4**, 92–103 (1999).
- ²E. Schrödinger, “Quantisierung als Eigenwertproblem”, *Ann. Phys.* **384**, 361–376 (1926).
- ³R. S. Mulliken, “Nobel Lecture Chemistry 1966: Spectroscopy, Molecular Orbitals, and Chemical Bonding”, *Science* **157**, 13–24 (1967).
- ⁴K. Fukui, “Nobel Lecture Chemistry 1981: Role of Frontier Orbitals in Chemical Reactions”, *Science* **218**, 747–754 (1982).
- ⁵P. W. Anderson, “Absence of Diffusion in Certain Random Lattices”, *Phys. Rev.* **109**, 1492–1505 (1958).
- ⁶N. F. Mott and E. A. Davis, *Electronic processes in non-crystalline materials* (Clarendon Press, Oxford, 1979).
- ⁷P. W. Anderson, “Local moments and localized states”, *Rev. Mod. Phys.* **50**, 191–201 (1978).
- ⁸S. Fratini, D. Mayou, and S. Ciuchi, “The Transient Localization Scenario for Charge Transport in Crystalline Organic Materials”, *Adv. Funct. Mater.* **26**, 2292–2315 (2016).
- ⁹*Science Friday Picture of the Week: Milk Drop « Harold "Doc" Edgerton*, <https://edgerton-digital-collections.org/stories/picture-of-the-week>, [Online; accessed 9. Nov. 2023], 2015.
- ¹⁰M. A. Green, “Third generation photovoltaics: Ultra-high conversion efficiency at low cost”, *Prog. Photovoltaics Res. Appl.* **9**, 123–135 (2001).
- ¹¹M. C. Hanna and A. J. Nozik, “Solar conversion efficiency of photovoltaic and photoelectrolysis cells with carrier multiplication absorbers”, *J. Appl. Phys.* **100**, 074510 (2006).
- ¹²A. Pochettino, “Sul comportamento foto-elettrico dell’Antracene”, *Atti della reale accademia dei lincei. Rendiconti* **15**, 353–363 (1906).

- ¹³B. Lüssem, M. Riede, and K. Leo, “Doping of organic semiconductors”, *Phys. Status Solidi A* **210**, 9–43 (2013).
- ¹⁴A. Troisi, “Charge transport in high mobility molecular semiconductors: classical models and new theories”, *Chem. Soc. Rev.* **40**, 2347–2358 (2011).
- ¹⁵C. W. Tang and S. A. VanSlyke, “Organic electroluminescent diodes”, *Appl. Phys. Lett.* **51**, 913–915 (1987).
- ¹⁶M. B. Smith and J. Michl, “Singlet Fission”, *Chem. Rev.* **110**, 6891–6936 (2010).
- ¹⁷A. J. Stone, *The theory of intermolecular forces*, 32 (Oxford University Press, Oxford, 1996), 264 pp.
- ¹⁸A. Szabo and N. S. Ostlund, *Modern quantum chemistry: introduction to advanced electronic structure theory* (Dover Publications, Mineola, N.Y., 1996).
- ¹⁹O. V. Yazyev, “Emergence of magnetism in graphene materials and nanostructures”, *Rep. Prog. Phys.* **73**, 056501 (2010).
- ²⁰V. Coropceanu, J. Cornil, D. A. da Silva Filho, Y. Olivier, R. Silbey, and J.-L. Brédas, “Charge Transport in Organic Semiconductors”, *Chem. Rev.* **107**, 926–952 (2007).
- ²¹P. Brüesch, *Phonons: theory and experiments, vol. 1*, 34 (Springer-Verlag, Berlin, 1982), pp. 138–142.
- ²²A. Troisi and G. Orlandi, “Charge-Transport Regime of Crystalline Organic Semiconductors: Diffusion Limited by Thermal Off-Diagonal Electronic Disorder”, *Phys. Rev. Lett.* **96**, 086601 (2006).
- ²³T. C. Berkelbach, M. S. Hybertsen, and D. R. Reichman, “Microscopic theory of singlet exciton fission. I. General formulation”, *J. Chem. Phys.* **138**, 114102 (2013).
- ²⁴K. N. Houk, P. S. Lee, and M. Nendel, “Polyacene and Cyclacene Geometries and Electronic Structures: Bond Equalization, Vanishing Band Gaps, and Triplet Ground States Contrast with Polyacetylene”, *J. Org. Chem.* **66**, 5517–5521 (2001).
- ²⁵C. Cohen-Tannoudji, B. Diu, F. Laloë, S. R. Hemley, N. Ostrowsky, and D. Ostrowsky, *Quantum mechanics vol. II* (John Wiley & Sons, Ltd, New York, 1977).
- ²⁶J. I. Urgel, S. Mishra, H. Hayashi, J. Wilhelm, C. A. Pignedoli, M. Di Giovannantonio, R. Widmer, M. Yamashita, N. Hieda, P. Ruffieux, H. Yamada, and R. Fasel, “On-surface light-induced generation of higher acenes and elucidation of their open-shell character”, *Nat. Commun.* **10**, 1–9 (2019).
- ²⁷V. Coropceanu, M. Malagoli, D. A. da Silva Filho, N. E. Gruhn, T. G. Bill, and J. L. Brédas, “Hole- and Electron-Vibrational Couplings in Oligoacene Crystals: Intramolecular Contributions”, *Phys. Rev. Lett.* **89**, 275503 (2002).
- ²⁸R. P. Chatelain, V. R. Morrison, B. L. M. Klarenaar, and B. J. Siwick, “Coherent and Incoherent Electron-Phonon Coupling in Graphite Observed with Radio-Frequency Compressed Ultrafast Electron Diffraction”, *Phys. Rev. Lett.* **113**, 235502 (2014).
- ²⁹M. X. Na, A. K. Mills, F. Boschini, M. Michiardi, B. Nosarzewski, R. P. Day, E. Razzoli, A. Sheyerman, M. Schneider, G. Levy, S. Zhdanovich, T. P. Devereaux, A. F. Kemper, D. J. Jones, and A. Damascelli, “Direct determination of mode-projected electron-phonon coupling in the time domain”, *Science* **366**, 1231–1236 (2019).
- ³⁰A. Devos and M. Lannoo, “Electron-phonon coupling for aromatic molecular crystals: Possible consequences for their superconductivity”, *Phys. Rev. B* **58**, 8236–8239 (1998).

- ³¹M. Preuss and F. Bechstedt, “Vibrational spectra of ammonia, benzene, and benzene adsorbed on Si (001) by first principles calculations with periodic boundary conditions”, *Phys. Rev. B* **73**, 155413 (2006).
- ³²A. C. Ferrari, “Raman spectroscopy of graphene and graphite: Disorder, electron–phonon coupling, doping and nonadiabatic effects”, *Solid State Commun.* **143**, 47–57 (2007).
- ³³A. Jorio, L. G. Cançado, and L. M. Malard, “Vibrations in Graphene”, in *2D Materials: Properties and Devices* (Cambridge University Press, Cambridge, England, UK, 2017), pp. 71–89.
- ³⁴S. Fratini, M. Nikolka, A. Salleo, G. Schweicher, and H. Sirringhaus, “Charge transport in high-mobility conjugated polymers and molecular semiconductors”, *Nat. Mater.* **19**, 491–502 (2020).
- ³⁵D. Holmes, S. Kumaraswamy, A. J. Matzger, and K. P. C. Vollhardt, “On the Nature of Nonplanarity in the [N]Phenylenes”, *Chemistry – A European Journal* **5**, 3399–3412 (1999).
- ³⁶M. Schwoerer and H. C. Wolf, *Organic molecular solids* (John Wiley & Sons, Ltd, New York, 2006).
- ³⁷A. Troisi, “Prediction of the Absolute Charge Mobility of Molecular Semiconductors: the Case of Rubrene”, *Adv. Mater.* **19**, 2000–2004 (2007).
- ³⁸A. S. Eggeman, S. Illig, A. Troisi, H. Sirringhaus, and P. A. Midgley, “Measurement of molecular motion in organic semiconductors by thermal diffuse electron scattering”, *Nat. Mater.* **12**, 1045–1049 (2013).
- ³⁹N. W. Ashcroft and N. D. Mermin, *Solid state physics* (Holt, Rinehart and Winston, New York, 1976).
- ⁴⁰W. Demtröder, *Molecular physics: theoretical principles and experimental methods*, OCLC: ocm62946254 (Wiley-VCH, Weinheim, 2005).
- ⁴¹A. S. Davydov, *Quantum mechanics* (Pergamon Press, Oxford, 1976).
- ⁴²A. Troisi and G. Orlandi, “Band Structure of the Four Pentacene Polymorphs and Effect on the Hole Mobility at Low Temperature”, *J. Phys. Chem. B* **109**, 1849–1856 (2005).
- ⁴³S. Fratini, S. Ciuchi, D. Mayou, G. T. de Laissardière, and A. Troisi, “A map of high-mobility molecular semiconductors”, *Nat. Mater.* **16**, 998–1002 (2017).
- ⁴⁴S. Giannini and J. Blumberger, “Charge Transport in Organic Semiconductors: The Perspective from Nonadiabatic Molecular Dynamics”, *Acc. Chem. Res.* **55**, 819–830 (2022).
- ⁴⁵K. Marumoto, S.-i. Kuroda, T. Takenobu, and Y. Iwasa, “Spatial Extent of Wave Functions of Gate-Induced Hole Carriers in Pentacene Field-Effect Devices as Investigated by Electron Spin Resonance”, *Phys. Rev. Lett.* **97**, 256603 (2006).
- ⁴⁶H. Matsui, A. S. Mishchenko, and T. Hasegawa, “Distribution of Localized States from Fine Analysis of Electron Spin Resonance Spectra in Organic Transistors”, *Phys. Rev. Lett.* **104**, 056602 (2010).
- ⁴⁷J.-F. Chang, T. Sakanoue, Y. Olivier, T. Uemura, M.-B. Dufourg-Madec, S. G. Yeates, J. Cornil, J. Takeya, A. Troisi, and H. Sirringhaus, “Hall-Effect Measurements Probing the Degree of Charge-Carrier Delocalization in Solution-Processed Crystalline Molecular Semiconductors”, *Phys. Rev. Lett.* **107**, 066601 (2011).

- ⁴⁸P. A. Lee and T. V. Ramakrishnan, “Disordered electronic systems”, *Rev. Mod. Phys.* **57**, 287–337 (1985).
- ⁴⁹N. Karl, “Charge carrier transport in organic semiconductors”, *Synth. Met.* **133-134**, 649–657 (2003).
- ⁵⁰T. C. Berkelbach, “Electronic Structure and Dynamics of Singlet Fission in Organic Molecules and Crystals”, in *Advances in Chemical Physics* (John Wiley & Sons, Ltd, Hoboken, NJ, USA, 2017), pp. 1–38.
- ⁵¹T. C. Berkelbach, M. S. Hybertsen, and D. R. Reichman, “Theory of neutral and charged excitons in monolayer transition metal dichalcogenides”, *Phys. Rev. B* **88**, 045318 (2013).
- ⁵²P. Cudazzo, M. Gatti, and A. Rubio, “Excitons in molecular crystals from first-principles many-body perturbation theory: Picene versus pentacene”, *Phys. Rev. B* **86**, 195307 (2012).
- ⁵³T. C. Berkelbach, M. S. Hybertsen, and D. R. Reichman, “Microscopic theory of singlet exciton fission. II. Application to pentacene dimers and the role of superexchange”, *J. Chem. Phys.* **138**, 114103 (2013).
- ⁵⁴N. Hestand and F. C. Spano, “Expanded Theory of H- and J-Molecular Aggregates: The Effects of Vibronic Coupling and Intermolecular Charge Transfer”, *Chem. Rev.* **118**, 7069–7163 (2018).
- ⁵⁵H. Yamagata, J. Norton, E. Hontz, Y. Olivier, D. Beljonne, J. L. Brédas, R. J. Silbey, and F. C. Spano, “The nature of singlet excitons in oligoacene molecular crystals”, *J. Chem. Phys.* **134**, 204703 (2011).
- ⁵⁶M. Wolf, R. Brendel, J. H. Werner, and H. J. Queisser, “Solar cell efficiency and carrier multiplication in $\text{Si}_{1-x}\text{Ge}_x$ alloys”, *J. Appl. Phys.* **83**, 4213–4221 (1998).
- ⁵⁷M. C. Beard, J. M. Luther, O. E. Semonin, and A. J. Nozik, “Third Generation Photovoltaics based on Multiple Exciton Generation in Quantum Confined Semiconductors”, *Acc. Chem. Res.* **46**, 1252–1260 (2013).
- ⁵⁸R. E. Merrifield, “Diffusion and mutual annihilation of triplet excitons in organic crystals”, *Acc. Chem. Res.* **1**, 129–135 (1968).
- ⁵⁹R. C. Johnson and R. E. Merrifield, “Effects of Magnetic Fields on the Mutual Annihilation of Triplet Excitons in Anthracene Crystals”, *Phys. Rev. B* **1**, 896–902 (1970).
- ⁶⁰C. E. Swenberg and W. T. Stacy, “Bimolecular radiationless transitions in crystalline tetracene”, *Chem. Phys. Lett.* **2**, 327–328 (1968).
- ⁶¹G. D. Scholes, “Correlated Pair States Formed by Singlet Fission and Exciton–Exciton Annihilation”, *J. Phys. Chem. A* **119**, 12699–12705 (2015).
- ⁶²A. Chernikov, O. Yaffe, B. Kumar, Y. Zhong, C. Nuckolls, and T. F. Heinz, “Spectroscopic Study of Anisotropic Excitons in Single Crystal Hexacene”, *J. Phys. Chem. Lett.* **5**, 3632–3635 (2014).
- ⁶³R. Tempelaar and D. R. Reichman, “Vibronic exciton theory of singlet fission. III. How vibronic coupling and thermodynamics promote rapid triplet generation in pentacene crystals”, *J. Chem. Phys.* **148**, 244701 (2018).
- ⁶⁴A. J. Musser, M. Liebel, C. Schnedermann, T. Wende, T. B. Kehoe, A. Rao, and P. Kukura, “Evidence for conical intersection dynamics mediating ultrafast singlet exciton fission”, *Nat. Phys.* **11**, 352–357 (2015).

- ⁶⁵A. A. Bakulin, S. E. Morgan, T. B. Kehoe, M. W. B. Wilson, A. W. Chin, D. Zigmantas, D. Egorova, and A. Rao, “Real-time observation of multiexcitonic states in ultrafast singlet fission using coherent 2D electronic spectroscopy”, *Nat. Chem.* **8**, 16–23 (2016).
- ⁶⁶M. S. Schuurman and A. Stolow, “Dynamics at Conical Intersections”, *Annu. Rev. Phys. Chem.* **69**, 427–450 (2018).
- ⁶⁷W.-L. Chan, M. Ligges, and X.-Y. Zhu, “The energy barrier in singlet fission can be overcome through coherent coupling and entropic gain”, *Nat. Chem.* **4**, 840–845 (2012).
- ⁶⁸P. E. Teichen and J. D. Eaves, “Collective aspects of singlet fission in molecular crystals”, *J. Chem. Phys.* **143**, 044118 (2015).
- ⁶⁹D. Casanova, “Theoretical Modeling of Singlet Fission”, *Chem. Rev.* **118**, 7164–7207 (2018).
- ⁷⁰S. R. Yost, E. Hontz, S. Yeganeh, and T. Van Voorhis, “Triplet vs Singlet Energy Transfer in Organic Semiconductors: The Tortoise and the Hare”, *J. Phys. Chem. C* **116**, 17369–17377 (2012).
- ⁷¹K. Miyata, F. S. Conrad-Burton, F. L. Geyer, and X.-Y. Zhu, “Triplet Pair States in Singlet Fission”, *Chem. Rev.* **119**, 4261–4292 (2019).
- ⁷²A. J. Musser and J. Clark, “Triplet-Pair States in Organic Semiconductors”, *Annu. Rev. Phys. Chem.* **70**, 323–351 (2019).
- ⁷³V. K. Thorsmølle, R. D. Averitt, J. Demsar, D. L. Smith, S. Tretiak, R. L. Martin, X. Chi, B. K. Crone, A. P. Ramirez, and A. J. Taylor, “Morphology Effectively Controls Singlet-Triplet Exciton Relaxation and Charge Transport in Organic Semiconductors”, *Phys. Rev. Lett.* **102**, 017401 (2009).
- ⁷⁴J. J. Burdett, A. M. Müller, D. Gosztola, and C. J. Bardeen, “Excited state dynamics in solid and monomeric tetracene: The roles of superradiance and exciton fission”, *J. Chem. Phys.* **133**, 144506 (2010).
- ⁷⁵M. W. B. Wilson, A. Rao, K. Johnson, S. Gélinas, R. di Pietro, J. Clark, and R. H. Friend, “Temperature-Independent Singlet Exciton Fission in Tetracene”, *J. Am. Chem. Soc.* **135**, 16680–16688 (2013).
- ⁷⁶M. W. B. Wilson, A. Rao, J. Clark, R. S. S. Kumar, D. Brida, G. Cerullo, and R. H. Friend, “Ultrafast Dynamics of Exciton Fission in Polycrystalline Pentacene”, *J. Am. Chem. Soc.* **133**, 11830–11833 (2011).
- ⁷⁷A. Rao, M. W. B. Wilson, J. M. Hodgkiss, S. Albert-Seifried, H. Bässler, and R. H. Friend, “Exciton Fission and Charge Generation via Triplet Excitons in Pentacene/C60 Bilayers”, *J. Am. Chem. Soc.* **132**, 12698–12703 (2010).
- ⁷⁸H. Marciniak, M. Fiebig, M. Huth, S. Schiefer, B. Nickel, F. Selmaier, and S. Lochbrunner, “Ultrafast Exciton Relaxation in Microcrystalline Pentacene Films”, *Phys. Rev. Lett.* **99**, 176402 (2007).
- ⁷⁹C. Jundt, G. Klein, B. Sipp, J. Le Moigne, M. Joucla, and A. A. Villaeys, “Exciton dynamics in pentacene thin films studied by pump-probe spectroscopy”, *Chem. Phys. Lett.* **241**, 84–88 (1995).
- ⁸⁰R. D. Pensack, E. E. Ostroumov, A. J. Tilley, S. Mazza, C. Grieco, K. J. Thorley, J. B. Asbury, D. S. Seferos, J. E. Anthony, and G. D. Scholes, “Observation of Two Triplet-Pair Intermediates in Singlet Exciton Fission”, *J. Phys. Chem. Lett.* **7**, 2370–2375 (2016).

- ⁸¹W.-L. Chan, M. Ligges, A. Jailaubekov, L. Kaake, L. Miaja-Avila, and X.-Y. Zhu, “Observing the Multiexciton State in Singlet Fission and Ensuing Ultrafast Multielectron Transfer”, *Science* **334**, 1541–1545 (2011).
- ⁸²C. K. Yong, A. J. Musser, S. L. Bayliss, S. Lukman, H. Tamura, O. Bubnova, R. K. Hallani, A. Meneau, R. Resel, M. Maruyama, S. Hotta, L. M. Herz, D. Beljonne, J. E. Anthony, J. Clark, and H. Sirringhaus, “The entangled triplet pair state in acene and heteroacene materials”, *Nat. Commun.* **8**, 1–12 (2017).
- ⁸³D. G. Bossanyi, M. Matthiesen, S. Wang, J. A. Smith, R. C. Kilbride, J. D. Shipp, D. Chekulaev, E. Holland, J. E. Anthony, J. Zaumseil, A. J. Musser, and J. Clark, “Emissive spin-0 triplet-pairs are a direct product of triplet–triplet annihilation in pentacene single crystals and anthradithiophene films”, *Nat. Chem.* **13**, 163–171 (2021).
- ⁸⁴G. Orlandi and W. Siebrand, “Theory of vibronic intensity borrowing. Comparison of Herzberg-Teller and Born-Oppenheimer coupling”, *J. Chem. Phys.* **58**, 4513–4523 (1973).
- ⁸⁵K. Miyata, Y. Kurashige, K. Watanabe, T. Sugimoto, S. Takahashi, S. Tanaka, J. Takeya, T. Yanai, and Y. Matsumoto, “Coherent singlet fission activated by symmetry breaking”, *Nat. Chem.* **9**, 983–989 (2017).
- ⁸⁶H.-G. Duan, A. Jha, X. Li, V. Tiwari, H. Ye, P. K. Nayak, X.-L. Zhu, Z. Li, T. J. Martinez, M. Thorwart, and R. J. D. Miller, “Intermolecular vibrations mediate ultrafast singlet fission”, *Sci. Adv.* **6**, eabb0052 (2020).
- ⁸⁷H. Hertz, “Ueber einen Einfluss des ultravioletten Lichtes auf die elektrische Entladung”, *Ann. Phys.* **267**, 983–1000 (1887).
- ⁸⁸R. A. Millikan, “A Direct Determination of “ h .””, *Phys. Rev.* **4**, 73–75 (1914).
- ⁸⁹K. Siegbahn, “Electron spectroscopy for atoms, molecules, and condensed matter”, *Rev. Mod. Phys.* **54**, 709–728 (1982).
- ⁹⁰P. Thiry, D. Chandesris, J. Lecante, C. Guillot, R. Pinchaux, and Y. Pétroff, “ E vs \vec{k} and Inverse Lifetime of Cu(110)”, *Phys. Rev. Lett.* **43**, 82–85 (1979).
- ⁹¹T. Schmidt, S. Heun, J. Slezak, J. Diaz, K. C. Prince, G. Lilienkamp, and E. Bauer, “SPELEEM: Combining LEEM and Spectroscopic Imaging”, *Surf. Rev. Lett.* **05**, 1287–1296 (1998).
- ⁹²M. Kotsugi, W. Kuch, F. Offi, L. I. Chelaru, and J. Kirschner, “Microspectroscopic two-dimensional Fermi surface mapping using a photoelectron emission microscope”, *Rev. Sci. Instrum.* **74**, 2754–2758 (2003).
- ⁹³J. J. Thomson, “LVIII. On the masses of the ions in gases at low pressures”, *London, Edinburgh, and Dublin Philosophical Magazine and Journal of Science* **48**, 547–567 (1899).
- ⁹⁴A. Einstein, “Über einen die Erzeugung und Verwandlung des Lichtes betreffenden heuristischen Gesichtspunkt”, *Ann. Phys.* **322**, 132–148 (1905).
- ⁹⁵S. Hüfner, *Photoelectron Spectroscopy* (Springer, Berlin, Germany, 2003).
- ⁹⁶Z.-X. Shen, D. S. Dessau, B. O. Wells, D. M. King, W. E. Spicer, A. J. Arko, D. Marshall, L. W. Lombardo, A. Kapitulnik, P. Dickinson, S. Doniach, J. DiCarlo, T. Loeser, and C. H. Park, “Anomalously large gap anisotropy in the a-b plane of $\text{Bi}_2\text{Sr}_2\text{CaCu}_2\text{O}_{8+\delta}$ ”, *Phys. Rev. Lett.* **70**, 1553–1556 (1993).
- ⁹⁷S. Y. Zhou, G.-H. Gweon, J. Graf, A. V. Fedorov, C. D. Spataru, R. D. Diehl, Y. Kopelevich, D.-H. Lee, S. G. Louie, and A. Lanzara, “First direct observation of Dirac fermions in graphite”, *Nat. Phys.* **2**, 595–599 (2006).

- ⁹⁸A. Damascelli, Z. Hussain, and Z.-X. Shen, “Angle-resolved photoemission studies of the cuprate superconductors”, *Rev. Mod. Phys.* **75**, 473–541 (2003).
- ⁹⁹S. Moser, “An experimentalist’s guide to the matrix element in angle resolved photoemission”, *J. Electron Spectrosc. Relat. Phenom.* **214**, 29–52 (2017).
- ¹⁰⁰J. W. Gadzuk, “Angular distributions of electrons photoemitted from chemisorbed atoms”, *Solid State Commun.* **15**, 1011–1016 (1974).
- ¹⁰¹P. Puschnig, S. Berkebile, A. J. Fleming, G. Koller, K. Emtsev, T. Seyller, J. D. Riley, C. Ambrosch-Draxl, F. P. Netzer, and M. G. Ramsey, “Reconstruction of Molecular Orbital Densities from Photoemission Data”, *Science* **326**, 702–706 (2009).
- ¹⁰²W. D. Grobman, “Angle-resolved photoemission from molecules in the independent-atomic-center approximation”, *Phys. Rev. B* **17**, 4573–4585 (1978).
- ¹⁰³K. Siegbahn, *ESCA applied to free molecules* (North-Holland Publishing Company, Amsterdam, 1969).
- ¹⁰⁴R. Yen, J. M. Liu, N. Bloembergen, T. K. Yee, J. G. Fujimoto, and M. M. Salour, “Picosecond laser interaction with metallic zirconium”, *Appl. Phys. Lett.* **40**, 185–187 (1982).
- ¹⁰⁵H. Petek and S. Ogawa, “Femtosecond time-resolved two-photon photoemission studies of electron dynamics in metals”, *Prog. Surf. Sci.* **56**, 239–310 (1997).
- ¹⁰⁶M. Lewenstein, P. Balcou, M. Y. Ivanov, A. L’Huillier, and P. B. Corkum, “Theory of high-harmonic generation by low-frequency laser fields”, *Phys. Rev. A* **49**, 2117–2132 (1994).
- ¹⁰⁷D. Schmitt, J. P. Bange, W. Bennecke, A. Almutairi, G. Meneghini, K. Watanabe, T. Taniguchi, D. Steil, D. R. Luke, R. T. Weitz, S. Steil, G. S. M. Jansen, S. Brem, E. Malic, S. Hofmann, M. Reutzler, and S. Mathias, “Formation of moiré interlayer excitons in space and time”, *Nature* **608**, 499–503 (2022).
- ¹⁰⁸C. W. Nicholson, A. Lücke, W. G. Schmidt, M. Puppini, L. Rettig, R. Ernstorfer, and M. Wolf, “Beyond the molecular movie: Dynamics of bands and bonds during a photoinduced phase transition”, *Science* **362**, 821–825 (2018).
- ¹⁰⁹S. Beaulieu, S. Dong, N. Tancogne-Dejean, M. Dendzik, T. Pincelli, J. Maklar, R. P. Xian, M. A. Sentef, M. Wolf, A. Rubio, L. Rettig, and R. Ernstorfer, “Ultrafast dynamical Lifshitz transition”, *Sci. Adv.* **7**, eabd9275 (2021).
- ¹¹⁰J. Reimann, S. Schlauderer, C. P. Schmid, F. Langer, S. Baierl, K. A. Kokh, O. E. Tereshchenko, A. Kimura, C. Lange, J. GÜdde, U. Höfer, and R. Huber, “Subcycle observation of lightwave-driven Dirac currents in a topological surface band”, *Nature* **562**, 396–400 (2018).
- ¹¹¹P. Hein, S. Jauernik, H. Erk, L. Yang, Y. Qi, Y. Sun, C. Felser, and M. Bauer, “Mode-resolved reciprocal space mapping of electron-phonon interaction in the Weyl semimetal candidate *Td*-WTe₂”, *Nat. Commun.* **11**, 1–8 (2020).
- ¹¹²U. De Giovannini, H. Hübener, S. A. Sato, and A. Rubio, “Direct Measurement of Electron-Phonon Coupling with Time-Resolved ARPES”, *Phys. Rev. Lett.* **125**, 136401 (2020).
- ¹¹³H. Zhang, T. Pincelli, C. Jozwiak, T. Kondo, R. Ernstorfer, T. Sato, and S. Zhou, “Angle-resolved photoemission spectroscopy”, *Nat. Rev. Methods Primers* **2**, 1–22 (2022).

- ¹¹⁴J. Maklar, S. Dong, S. Beaulieu, T. Pincelli, M. Dendzik, Y. W. Windsor, R. P. Xian, M. Wolf, R. Ernstorfer, and L. Rettig, “A quantitative comparison of time-of-flight momentum microscopes and hemispherical analyzers for time- and angle-resolved photoemission spectroscopy experiments”, *Rev. Sci. Instrum.* **91**, 123112 (2020).
- ¹¹⁵E. J. Sie, T. Rohwer, C. Lee, and N. Gedik, “Time-resolved XUV ARPES with tunable 24–33 eV laser pulses at 30 meV resolution”, *Nat. Commun.* **10**, 1–11 (2019).
- ¹¹⁶B. Schönhense, K. Medjanik, O. Fedchenko, S. Chernov, M. Ellguth, D. Vasilyev, A. Oelsner, J. Viefhaus, D. Kutnyakhov, W. Wurth, H. J. Elmers, and G. Schönhense, “Multidimensional photoemission spectroscopy—the space-charge limit”, *New J. Phys.* **20**, 033004 (2018).
- ¹¹⁷G. Cerullo and S. De Silvestri, “Ultrafast optical parametric amplifiers”, *Rev. Sci. Instrum.* **74**, 1–18 (2003).
- ¹¹⁸M. Puppín, Y. Deng, O. Prochnow, J. Ahrens, T. Binhammer, U. Morgner, M. Krenz, M. Wolf, and R. Ernstorfer, “500 kHz OPCPA delivering tunable sub-20 fs pulses with 15 W average power based on an all-ytterbium laser”, *Opt. Express* **23**, 1491–1497 (2015).
- ¹¹⁹M. Puppín, Y. Deng, C. W. Nicholson, J. Feldl, N. B. M. Schröter, H. Vita, P. S. Kirchmann, C. Monney, L. Rettig, M. Wolf, and R. Ernstorfer, “Time- and angle-resolved photoemission spectroscopy of solids in the extreme ultraviolet at 500 kHz repetition rate”, *Rev. Sci. Instrum.* **90**, 023104 (2019).
- ¹²⁰R. P. Xian, Y. Acremann, S. Y. Agustsson, M. Dendzik, K. Bühlmann, D. Curcio, D. Kutnyakhov, F. Pressacco, M. Heber, S. Dong, T. Pincelli, J. Demsar, W. Wurth, P. Hofmann, M. Wolf, M. Scheidgen, L. Rettig, and R. Ernstorfer, “An open-source, end-to-end workflow for multidimensional photoemission spectroscopy”, *Sci. Data* **7**, 1–11 (2020).
- ¹²¹P. Drude, “Zur Elektronentheorie der Metalle”, *Ann. Phys.* **306**, 566–613 (1900).
- ¹²²F. Bloch, “Über die Quantenmechanik der Elektronen in Kristallgittern”, *Z. Phys.* **52**, 555–600 (1929).
- ¹²³E. A. Davis and N. F. Mott, “Conduction in non-crystalline systems V. Conductivity, optical absorption and photoconductivity in amorphous semiconductors”, *Philosophical Magazine: A Journal of Theoretical Experimental and Applied Physics* **22**, 0903–0922 (1970).
- ¹²⁴H. Bässler and A. Köhler, “Charge Transport in Organic Semiconductors”, in *Unimolecular and Supramolecular Electronics I* (Springer, Berlin, Germany, 2011), pp. 1–65.
- ¹²⁵J. Tsurumi, H. Matsui, T. Kubo, R. Häusermann, C. Mitsui, T. Okamoto, S. Watanabe, and J. Takeya, “Coexistence of ultra-long spin relaxation time and coherent charge transport in organic single-crystal semiconductors”, *Nat. Phys.* **13**, 994–998 (2017).
- ¹²⁶M. E. Gershenson, V. Podzorov, and A. F. Morpurgo, “Colloquium: Electronic transport in single-crystal organic transistors”, *Rev. Mod. Phys.* **78**, 973–989 (2006).
- ¹²⁷N. Koch, A. Vollmer, I. Salzmann, B. Nickel, H. Weiss, and J. P. Rabe, “Evidence for Temperature-Dependent Electron Band Dispersion in Pentacene”, *Phys. Rev. Lett.* **96**, 156803 (2006).
- ¹²⁸S.-i. Machida, Y. Nakayama, S. Duhm, Q. Xin, A. Funakoshi, N. Ogawa, S. Kera, N. Ueno, and H. Ishii, “Highest-Occupied-Molecular-Orbital Band Dispersion of Rubrene Single Crystals as Observed by Angle-Resolved Ultraviolet Photoelectron Spectroscopy”, *Phys. Rev. Lett.* **104**, 156401 (2010).

- ¹²⁹R. C. Hatch, D. L. Huber, and H. Höchst, “HOMO band structure and anisotropic effective hole mass in thin crystalline pentacene films”, *Phys. Rev. B* **80**, 081411 (2009).
- ¹³⁰G. H. Wannier, “Antiferromagnetism. The Triangular Ising Net”, *Phys. Rev.* **79**, 357–364 (1950).
- ¹³¹G. A. de Wijs, C. C. Mattheus, R. A. de Groot, and T. T. M. Palstra, “Anisotropy of the mobility of pentacene from frustration”, *Synth. Met.* **139**, 109–114 (2003).
- ¹³²Y. Nakayama, S. Kera, and N. Ueno, “Photoelectron spectroscopy on single crystals of organic semiconductors: experimental electronic band structure for optoelectronic properties”, *J. Mater. Chem. C* **8**, 9090–9132 (2020).
- ¹³³G. Koller, S. Berkebile, M. Oehzelt, P. Puschnig, C. Ambrosch-Draxl, F. P. Netzer, and M. G. Ramsey, “Intra- and Intermolecular Band Dispersion in an Organic Crystal”, *Science* **317**, 351–355 (2007).
- ¹³⁴S. Hammer, C. Zeiser, M. Deutsch, B. Engels, K. Broch, and J. Pflaum, “Spatial Anisotropy of Charge Transfer at Perfluoropentacene–Pentacene (001) Single-Crystal Interfaces and its Relevance for Thin Film Devices”, *ACS Appl. Mater. Interfaces* **12**, 53547–53556 (2020).
- ¹³⁵N. Sato, H. Inokuchi, B. M. Schmid, and N. Karl, “Ultraviolet photoemission spectra of organic single crystals”, *J. Chem. Phys.* **83**, 5413–5419 (1985).
- ¹³⁶O. D. Jurchescu, A. Meetsma, and T. T. M. Palstra, “Low-temperature structure of rubrene single crystals grown by vapor transport”, *Acta Crystallogr., Sect. B: Struct. Sci.* **62**, 330–334 (2006).
- ¹³⁷U. Müller, L. Roos, M. Frank, M. Deutsch, S. Hammer, M. Krumrein, A. Friedrich, T. B. Marder, B. Engels, A. Krueger, and J. Pflaum, “Role of Intermolecular Interactions in the Excited-State Photophysics of Tetracene and 2,2'-Ditetracene”, *J. Phys. Chem. C* **124**, 19435–19446 (2020).
- ¹³⁸C. C. Mattheus, G. A. de Wijs, R. A. de Groot, and T. T. M. Palstra, “Modeling the Polymorphism of Pentacene”, *J. Am. Chem. Soc.* **125**, 6323–6330 (2003).
- ¹³⁹B. Mahns, O. Kataeva, D. Islamov, S. Hampel, F. Steckel, C. Hess, M. Knupfer, B. Büchner, C. Himcinschi, T. Hahn, R. Renger, and J. Kortus, “Crystal Growth, Structure, and Transport Properties of the Charge-Transfer Salt Picene/2,3,5,6-Tetrafluoro-7,7,8,8-tetracyanoquinodimethane”, *Cryst. Growth Des.* **14**, 1338–1346 (2014).
- ¹⁴⁰R. A. Laudise, C. Kloc, P. G. Simpkins, and T. Siegrist, “Physical vapor growth of organic semiconductors”, *J. Cryst. Growth* **187**, 449–454 (1998).
- ¹⁴¹S. Ciuchi, R. C. Hatch, H. Höchst, C. Faber, X. Blase, and S. Fratini, “Molecular Fingerprints in the Electronic Properties of Crystalline Organic Semiconductors: From Experiment to Theory”, *Phys. Rev. Lett.* **108**, 256401 (2012).
- ¹⁴²T. C. Berkelbach, M. S. Hybertsen, and D. R. Reichman, “Microscopic theory of singlet exciton fission. III. Crystalline pentacene”, *J. Chem. Phys.* **141**, 10.1063/1.4892793 (2014).
- ¹⁴³S. Berkebile, P. Puschnig, G. Koller, M. Oehzelt, F. P. Netzer, C. Ambrosch-Draxl, and M. G. Ramsey, “Electronic band structure of pentacene: An experimental and theoretical study”, *Phys. Rev. B* **77**, 115312 (2008).
- ¹⁴⁴F. Bussolotti, J. Yang, T. Yamaguchi, K. Yonezawa, K. Sato, M. Matsunami, K. Tanaka, Y. Nakayama, H. Ishii, N. Ueno, and S. Kera, “Hole-phonon coupling effect on the band dispersion of organic molecular semiconductors”, *Nat. Commun.* **8**, 1–7 (2017).

- ¹⁴⁵R. C. Hatch, D. L. Huber, and H. Höchst, “Electron-Phonon Coupling in Crystalline Pentacene Films”, *Phys. Rev. Lett.* **104**, 047601 (2010).
- ¹⁴⁶H. Yoshida and N. Sato, “Crystallographic and electronic structures of three different polymorphs of pentacene”, *Phys. Rev. B* **77**, 235205 (2008).
- ¹⁴⁷A. Girlando, L. Grisanti, M. Masino, I. Bilotti, A. Brillante, R. G. Della Valle, and E. Venuti, “Peierls and Holstein carrier-phonon coupling in crystalline rubrene”, *Phys. Rev. B* **82**, 035208 (2010).
- ¹⁴⁸T. P. Nguyen, J. H. Shim, and J. Y. Lee, “Density Functional Theory Studies of Hole Mobility in Picene and Pentacene Crystals”, *J. Phys. Chem. C* **119**, 11301–11310 (2015).
- ¹⁴⁹G. Schweicher, G. D’Avino, M. T. Ruggiero, D. J. Harkin, K. Broch, D. Venkateshvaran, G. Liu, A. Richard, C. Ruzié, J. Armstrong, A. R. Kennedy, K. Shankland, K. Takimiya, Y. H. Geerts, J. A. Zeitler, S. Fratini, and H. Sirringhaus, “Chasing the “Killer” Phonon Mode for the Rational Design of Low-Disorder, High-Mobility Molecular Semiconductors”, *Adv. Mater.* **31**, 1902407 (2019).
- ¹⁵⁰R. Mitsuhashi, Y. Suzuki, Y. Yamanari, H. Mitamura, T. Kambe, N. Ikeda, H. Okamoto, A. Fujiwara, M. Yamaji, N. Kawasaki, Y. Maniwa, and Y. Kubozono, “Superconductivity in alkali-metal-doped picene”, *Nature* **464**, 76–79 (2010).
- ¹⁵¹A. Ruff, M. Sing, R. Claessen, H. Lee, M. Tomić, H. O. Jeschke, and R. Valenti, “Absence of Metallicity in K-doped Picene: Importance of Electronic Correlations”, *Phys. Rev. Lett.* **110**, 216403 (2013).
- ¹⁵²H. Okamoto, N. Kawasaki, Y. Kaji, Y. Kubozono, A. Fujiwara, and M. Yamaji, “Air-assisted High-performance Field-effect Transistor with Thin Films of Picene”, *J. Am. Chem. Soc.* **130**, 10470–10471 (2008).
- ¹⁵³S. Fanetti, M. Citroni, R. Bini, L. Malavasi, G. A. Artioli, and P. Postorino, “HOMO-LUMO transitions in solvated and crystalline picene”, *J. Chem. Phys.* **137**, 224506 (2012).
- ¹⁵⁴Q. Xin, S. Duhm, F. Bussolotti, K. Akaike, Y. Kubozono, H. Aoki, T. Kosugi, S. Kera, and N. Ueno, “Accessing Surface Brillouin Zone and Band Structure of Picene Single Crystals”, *Phys. Rev. Lett.* **108**, 226401 (2012).
- ¹⁵⁵T. Kosugi, T. Miyake, S. Ishibashi, R. Arita, and H. Aoki, “First-Principles Electronic Structure of Solid Picene”, *J. Phys. Soc. Jpn.* **78**, 113704 (2009).
- ¹⁵⁶A. De, R. Ghosh, S. Roychowdhury, and P. Roychowdhury, “Structural analysis of picene, C₂₂H₁₄”, *Acta Cryst. C* **41**, 907–909 (1985).
- ¹⁵⁷G. R. Desiraju and A. Gavezzotti, “Crystal structures of polynuclear aromatic hydrocarbons. Classification, rationalization and prediction from molecular structure”, *Acta Cryst. B* **45**, 473–482 (1989).
- ¹⁵⁸K. Nakada, M. Fujita, G. Dresselhaus, and M. S. Dresselhaus, “Edge state in graphene ribbons: Nanometer size effect and edge shape dependence”, *Phys. Rev. B* **54**, 17954–17961 (1996).
- ¹⁵⁹T. F. Harrelson, V. Dantanarayana, X. Xie, C. Koshnick, D. Nai, R. Fair, S. A. Nuñez, A. K. Thomas, T. L. Murrey, M. A. Hickner, J. K. Grey, J. E. Anthony, E. D. Gomez, A. Troisi, R. Faller, and A. J. Moulé, “Direct probe of the nuclear modes limiting charge mobility in molecular semiconductors”, *Mater. Horiz.* **6**, 182–191 (2019).
- ¹⁶⁰D. J. Thouless, “Electrons in disordered systems and the theory of localization”, *Phys. Rep.* **13**, 93–142 (1974).

- ¹⁶¹N. F. Mott and W. D. Twose, “The theory of impurity conduction”, *Adv. Phys.*, **107–163** (1961).
- ¹⁶²R. S. Sánchez-Carrera, P. Paramonov, G. M. Day, V. Coropceanu, and J.-L. Brédas, “Interaction of Charge Carriers with Lattice Vibrations in Oligoacene Crystals from Naphthalene to Pentacene”, *J. Am. Chem. Soc.* **132**, 14437–14446 (2010).
- ¹⁶³A. Girlando, M. Masino, I. Bilotti, A. Brillante, R. G. D. Valle, and E. Venuti, “Phonon dynamics and electron–phonon coupling in pristine picene”, *Phys. Chem. Chem. Phys.* **14**, 1694–1699 (2012).
- ¹⁶⁴S. Illig, A. S. Eggeman, A. Troisi, L. Jiang, C. Warwick, M. Nikolka, G. Schweicher, S. G. Yeates, Y. Henri Geerts, J. E. Anthony, and H. Sirringhaus, “Reducing dynamic disorder in small-molecule organic semiconductors by suppressing large-amplitude thermal motions”, *Nat. Commun.* **7**, 1–10 (2016).
- ¹⁶⁵S. Giannini, L. Di Virgilio, M. Bardini, J. Hausch, J. J. Geuchies, W. Zheng, M. Volpi, J. Elsner, K. Broch, Y. H. Geerts, F. Schreiber, G. Schweicher, H. I. Wang, J. Blumberger, M. Bonn, and D. Beljonne, “Transiently delocalized states enhance hole mobility in organic molecular semiconductors”, *Nat. Mater.*, 1–9 (2023).
- ¹⁶⁶A. Yamamoto, Y. Murata, C. Mitsui, H. Ishii, M. Yamagishi, M. Yano, H. Sato, A. Yamano, J. Takeya, and T. Okamoto, “Zigzag-Elongated Fused π -Electronic Core: A Molecular Design Strategy to Maximize Charge-Carrier Mobility”, *Adv. Sci.* **5**, 1700317 (2018).
- ¹⁶⁷T. Okamoto, C. P. Yu, C. Mitsui, M. Yamagishi, H. Ishii, and J. Takeya, “Bent-Shaped p-Type Small-Molecule Organic Semiconductors: A Molecular Design Strategy for Next-Generation Practical Applications”, *J. Am. Chem. Soc.* **142**, 9083–9096 (2020).
- ¹⁶⁸M. Mitani, S. Kumagai, C. P. Yu, A. Oi, M. Yamagishi, S. Nishinaga, H. Mori, Y. Nishihara, D. Hashizume, T. Kurosawa, H. Ishii, N. Kobayashi, J. Takeya, and T. Okamoto, “ π -Extended Zigzag-Shaped Diphenanthrene-Based p-Type Semiconductors Exhibiting Small Effective Masses”, *Adv. Electron. Mater.* **8**, 2200452 (2022).
- ¹⁶⁹M.-A. Stoeckel, Y. Olivier, M. Gobbi, D. Dudenko, V. Lemaury, M. Zbiri, A. A. Y. Guilbert, G. D’Avino, F. Liscio, A. Migliori, L. Ortolani, N. Demitri, X. Jin, Y.-G. Jeong, A. Liscio, M.-V. Nardi, L. Pasquali, L. Razzari, D. Beljonne, P. Samori, and E. Orgiu, “Analysis of External and Internal Disorder to Understand Band-Like Transport in n-Type Organic Semiconductors”, *Adv. Mater.* **33**, 2007870 (2021).
- ¹⁷⁰T. Okamoto, S. Kumagai, E. Fukuzaki, H. Ishii, G. Watanabe, N. Niitsu, T. Annaka, M. Yamagishi, Y. Tani, H. Sugiura, T. Watanabe, S. Watanabe, and J. Takeya, “Robust, high-performance n-type organic semiconductors”, *Sci. Adv.* **6**, eaaz0632 (2020).
- ¹⁷¹A. Landi and A. Troisi, “Rapid Evaluation of Dynamic Electronic Disorder in Molecular Semiconductors”, *J. Phys. Chem. C* **122**, 18336–18345 (2018).
- ¹⁷²N. Bohr, “Atomic Structure”, *Nature* **107**, 104–107 (1921).
- ¹⁷³Ø. Burrau, “Berechnung des Energiewertes des Wasserstoffmolekel-Ions (H_2^+) im Normalzustand”, *Naturwissenschaften* **15**, 16–17 (1927).
- ¹⁷⁴J. Itatani, J. Levesque, D. Zeidler, H. Niikura, H. Pépin, J. C. Kieffer, P. B. Corkum, and D. M. Villeneuve, “Tomographic imaging of molecular orbitals”, *Nature* **432**, 867–871 (2004).
- ¹⁷⁵J. Repp, G. Meyer, S. M. Stojković, A. Gourdon, and C. Joachim, “Molecules on Insulating Films: Scanning-Tunneling Microscopy Imaging of Individual Molecular Orbitals”, *Phys. Rev. Lett.* **94**, 026803 (2005).

- ¹⁷⁶F. Urbach, “The Long-Wavelength Edge of Photographic Sensitivity and of the Electronic Absorption of Solids”, *Phys. Rev.* **92**, 1324 (1953).
- ¹⁷⁷D. V. Lang, X. Chi, T. Siegrist, A. M. Sergent, and A. P. Ramirez, “Amorphouslike Density of Gap States in Single-Crystal Pentacene”, *Phys. Rev. Lett.* **93**, 086802 (2004).
- ¹⁷⁸W.-y. So, D. V. Lang, V. Y. Butko, X. Chi, J. C. Lashley, and A. P. Ramirez, “Dependence of mobility on density of gap states in organics by GAMEaS-gate modulated activation energy spectroscopy”, *J. Appl. Phys.* **104**, 054512 (2008).
- ¹⁷⁹X. Ren, M. J. Bruzek, D. A. Hanifi, A. Schulzetenberg, Y. Wu, C.-H. Kim, Z. Zhang, J. E. Johns, A. Salleo, S. Fratini, A. Troisi, C. J. Douglas, and C. D. Frisbie, “Negative Isotope Effect on Field-Effect Hole Transport in Fully Substituted ¹³C-Rubrene”, *Adv. Electron. Mater.* **3**, 1700018 (2017).
- ¹⁸⁰L. Tsetseris and S. T. Pantelides, “Large impurity effects in rubrene crystals: First-principles calculations”, *Phys. Rev. B* **78**, 115205 (2008).
- ¹⁸¹C. Krellner, S. Haas, C. Goldmann, K. P. Pernstich, D. J. Gundlach, and B. Batlogg, “Density of bulk trap states in organic semiconductor crystals: Discrete levels induced by oxygen in rubrene”, *Phys. Rev. B* **75**, 245115 (2007).
- ¹⁸²A. Neef, S. Beaulieu, S. Hammer, S. Dong, J. Maklar, T. Pincelli, R. P. Xian, M. Wolf, L. Rettig, J. Pflaum, and R. Ernstorfer, “Orbital-resolved observation of singlet fission”, *Nature* **616**, 275–279 (2023).
- ¹⁸³A. Neef, M. Rossi, M. Wolf, R. Ernstorfer, and H. Seiler, “On the Role of Nuclear Motion in Singlet Exciton Fission: The Case of Single-Crystal Pentacene”, *Phys. Status Solidi A* **n/a**, 2300304 (2023).
- ¹⁸⁴N. Geacintov, M. Pope, and F. Vogel, “Effect of Magnetic Field on the Fluorescence of Tetracene Crystals: Exciton Fission”, *Phys. Rev. Lett.* **22**, 593–596 (1969).
- ¹⁸⁵R. E. Merrifield, P. Avakian, and R. P. Groff, “Fission of singlet excitons into pairs of triplet excitons in tetracene crystals”, *Chem. Phys. Lett.* **3**, 155–157 (1969).
- ¹⁸⁶D. L. Dexter, “Two ideas on energy transfer phenomena: Ion-pair effects involving the OH stretching mode, and sensitization of photovoltaic cells”, *J. Lumin.* **18-19**, 779–784 (1979).
- ¹⁸⁷P. M. Zimmerman, F. Bell, D. Casanova, and M. Head-Gordon, “Mechanism for Singlet Fission in Pentacene and Tetracene: From Single Exciton to Two Triplets”, *J. Am. Chem. Soc.* **133**, 19944–19952 (2011).
- ¹⁸⁸S. Refaely-Abramson, F. H. da Jornada, S. G. Louie, and J. B. Neaton, “Origins of Singlet Fission in Solid Pentacene from an ab initio Green’s Function Approach”, *Phys. Rev. Lett.* **119**, 267401 (2017).
- ¹⁸⁹S. Sharifzadeh, P. Darancet, L. Kronik, and J. B. Neaton, “Low-Energy Charge-Transfer Excitons in Organic Solids from First-Principles: The Case of Pentacene”, *J. Phys. Chem. Lett.* **4**, 2197–2201 (2013).
- ¹⁹⁰J. Burgos, M. Pope, C. E. Swenberg, and R. R. Alfano, “Heterofission in pentacene-doped tetracene single crystals”, *Phys. Status Solidi B* **83**, 249–256 (1977).
- ¹⁹¹P. Puschnig, E.-M. Reinisch, T. Ules, G. Koller, S. Soubatch, M. Ostler, L. Romaner, F. S. Tautz, C. Ambrosch-Draxl, and M. G. Ramsey, “Orbital tomography: Deconvoluting photoemission spectra of organic molecules”, *Phys. Rev. B* **84**, 235427 (2011).

- ¹⁹²M. Dressel, B. Gompf, D. Faltermeier, A. K. Tripathi, J. Pflaum, and M. Schubert, “Kramers-Kronig-consistent optical functions of anisotropic crystals: generalized spectroscopic ellipsometry on pentacene”, *Opt. Express* **16**, 19770–19778 (2008).
- ¹⁹³P. M. Zimmerman, Z. Zhang, and C. B. Musgrave, “Singlet fission in pentacene through multi-exciton quantum states”, *Nat. Chem.* **2**, 648–652 (2010).
- ¹⁹⁴M. Andrzejak, T. Skóra, and P. Petelenz, “Is Vibrational Coherence a Byproduct of Singlet Exciton Fission?”, *J. Phys. Chem. C* **123**, 91–101 (2019).
- ¹⁹⁵H. Seiler, M. Krynski, D. Zahn, S. Hammer, Y. W. Windsor, T. Vasileiadis, J. Pflaum, R. Ernstorfer, M. Rossi, and H. Schwörer, “Nuclear dynamics of singlet exciton fission in pentacene single crystals”, *Sci. Adv.* **7**, eabg086 (2021).
- ¹⁹⁶J. J. Burdett, D. Gosztola, and C. J. Bardeen, “The dependence of singlet exciton relaxation on excitation density and temperature in polycrystalline tetracene thin films: Kinetic evidence for a dark intermediate state and implications for singlet fission”, *J. Chem. Phys.* **135**, 214508 (2011).
- ¹⁹⁷V. K. Thorsmølle, R. D. Averitt, J. Demsar, D. L. Smith, S. Tretiak, R. L. Martin, X. Chi, B. K. Crone, A. P. Ramirez, and A. J. Taylor, “Photoexcited carrier relaxation dynamics in pentacene probed by ultrafast optical spectroscopy: Influence of morphology on relaxation processes”, *Physica B* **404**, 3127–3130 (2009).
- ¹⁹⁸D. M. Finton, E. A. Wolf, V. S. Zoutenbier, K. A. Ward, and I. Biaggio, “Routes to singlet exciton fission in rubrene crystals and amorphous films”, *AIP Adv.* **9**, 095027 (2019).
- ¹⁹⁹D. G. Bossanyi, M. Matthiesen, R. Jayaprakash, S. Bhattacharya, J. Zaumseil, and J. Clark, “Singlet Fission is Incoherent in Pristine Orthorhombic Single Crystals of Rubrene: No Evidence of Triplet-Pair Emission”, *Faraday Discuss.*, Accepted (2023).
- ²⁰⁰P. Irkhin, A. Ryasnyanskiy, M. Koehler, and I. Biaggio, “Absorption and photoluminescence spectroscopy of rubrene single crystals”, *Phys. Rev. B* **86**, 085143 (2012).
- ²⁰¹S. V. Frolov, C. Kloc, J. H. Schön, and B. Batlogg, “Transient spectroscopy of tetracene single crystals”, *Chem. Phys. Lett.* **334**, 65–68 (2001).
- ²⁰²M. J. Y. Tayebjee, R. G. C. R. Clady, and T. W. Schmidt, “The exciton dynamics in tetracene thin films”, *Phys. Chem. Chem. Phys.* **15**, 14797–14805 (2013).
- ²⁰³Z. Birech, M. Schwörer, T. Schmeiler, J. Pflaum, and H. Schwörer, “Ultrafast dynamics of excitons in tetracene single crystals”, *J. Chem. Phys.* **140**, 144501 (2014).
- ²⁰⁴B. Zhang, C. Zhang, Y. Xu, R. Wang, B. He, Y. Liu, S. Zhang, X. Wang, and M. Xiao, “Polarization-dependent exciton dynamics in tetracene single crystals”, *J. Chem. Phys.* **141**, 244303 (2014).
- ²⁰⁵G. Wang, C. Zhang, Z. Liu, R. Wang, H. Ma, X. Wang, and M. Xiao, “Singlet Fission Dynamics in Tetracene Single Crystals Probed by Polarization-Dependent Two-Dimensional Electronic Spectroscopy”, *J. Phys. Chem. A* **124**, 10447–10456 (2020).
- ²⁰⁶A. F. Morrison and J. M. Herbert, “Evidence for Singlet Fission Driven by Vibronic Coherence in Crystalline Tetracene”, *J. Phys. Chem. Lett.* **8**, 1442–1448 (2017).

- ²⁰⁷D. Kutnyakhov, R. P. Xian, M. Dendzik, M. Heber, F. Pressacco, S. Y. Agustsson, L. Wenthaus, H. Meyer, S. Gieschen, G. Mercurio, A. Benz, K. Bühlman, S. Däster, R. Gort, D. Curcio, K. Volckaert, M. Bianchi, C. Sanders, J. A. Miwa, S. Ulstrup, A. Oelsner, C. Tusche, Y.-J. Chen, D. Vasilyev, K. Medjanik, G. Brenner, S. Dziarzhytski, H. Redlin, B. Manschwetus, S. Dong, J. Hauer, L. Rettig, F. Diekmann, K. Rossnagel, J. Demsar, H.-J. Elmers, P. Hofmann, R. Ernstorfer, G. Schönhense, Y. Acremann, and W. Wurth, “Time- and momentum-resolved photoemission studies using time-of-flight momentum microscopy at a free-electron laser”, *Rev. Sci. Instrum.* **91**, 013109 (2020).
- ²⁰⁸H. L. Stern, A. Cheminal, S. R. Yost, K. Broch, S. L. Bayliss, K. Chen, M. Tabachnyk, K. Thorley, N. Greenham, J. M. Hodgkiss, J. Anthony, M. Head-Gordon, A. J. Musser, A. Rao, and R. H. Friend, “Vibronically coherent ultrafast triplet-pair formation and subsequent thermally activated dissociation control efficient endothermic singlet fission”, *Nat. Chem.* **9**, 1205–1212 (2017).
- ²⁰⁹A. B. Kolomeisky, X. Feng, and A. I. Krylov, “A Simple Kinetic Model for Singlet Fission: A Role of Electronic and Entropic Contributions to Macroscopic Rates”, *J. Phys. Chem. C* **118**, 5188–5195 (2014).
- ²¹⁰C. Sutton, N. R. Tummala, D. Beljonne, and J.-L. Brédas, “Singlet Fission in Rubrene Derivatives: Impact of Molecular Packing”, *Chem. Mater.* **29**, 2777–2787 (2017).
- ²¹¹H. Tamura, M. Huix-Rotllant, I. Burghardt, Y. Olivier, and D. Beljonne, “First-Principles Quantum Dynamics of Singlet Fission: Coherent versus Thermally Activated Mechanisms Governed by Molecular π Stacking”, *Phys. Rev. Lett.* **115**, 107401 (2015).
- ²¹²S. Tao, N. Ohtani, R. Uchida, T. Miyamoto, Y. Matsui, H. Yada, H. Uemura, H. Matsuzaki, T. Uemura, J. Takeya, and H. Okamoto, “Relaxation Dynamics of Photoexcited Excitons in Rubrene Single Crystals Using Femtosecond Absorption Spectroscopy”, *Phys. Rev. Lett.* **109**, 097403 (2012).
- ²¹³I. Breen, R. Tempelaar, L. A. Bizimana, B. Kloss, D. R. Reichman, and D. B. Turner, “Triplet Separation Drives Singlet Fission after Femtosecond Correlated Triplet Pair Production in Rubrene”, *J. Am. Chem. Soc.* **139**, 11745–11751 (2017).
- ²¹⁴L. Ma, K. Zhang, C. Kloc, H. Sun, C. Soci, M. E. Michel-Beyerle, and G. G. Gurzadyan, “Fluorescence from rubrene single crystals: Interplay of singlet fission and energy trapping”, *Phys. Rev. B* **87**, 201203 (2013).
- ²¹⁵X. Wang, T. Garcia, S. Monaco, B. Schatschneider, and N. Marom, “Effect of crystal packing on the excitonic properties of rubrene polymorphs”, *CrystEngComm* **18**, 7353–7362 (2016).
- ²¹⁶T. Lettmann and M. Rohlfing, “Finite-momentum excitons in rubrene single crystals”, *Phys. Rev. B* **104**, 115427 (2021).
- ²¹⁷G. Schönhense, D. Kutnyakhov, F. Pressacco, M. Heber, N. Wind, S. Y. Agustsson, S. Babenkov, D. Vasilyev, O. Fedchenko, S. Chernov, L. Rettig, B. Schönhense, L. Wenthaus, G. Brenner, S. Dziarzhytski, S. Palutke, S. K. Mahatha, N. Schirmel, H. Redlin, B. Manschwetus, I. Hartl, Y. Matveyev, A. Gloskovskii, C. Schlueter, V. Shokeen, H. Duerr, T. K. Allison, M. Beye, K. Rossnagel, H. J. Elmers, and K. Medjanik, “Suppression of the vacuum space-charge effect in fs-photoemission by a retarding electrostatic front lens”, *Rev. Sci. Instrum.* **92**, 053703 (2021).
- ²¹⁸M. Filoche, M. Piccardo, Y.-R. Wu, C.-K. Li, C. Weisbuch, and S. Mayboroda, “Localization landscape theory of disorder in semiconductors. I. Theory and modeling”, *Phys. Rev. B* **95**, 144204 (2017).

- ²¹⁹J.-P. Banon, P. Pelletier, C. Weisbuch, S. Mayboroda, and M. Filoche, “Wigner-Weyl description of light absorption in disordered semiconductor alloys using the localization landscape theory”, *Phys. Rev. B* **105**, 125422 (2022).
- ²²⁰A. David and C. Weisbuch, “Excitons in a disordered medium: A numerical study in InGaN quantum wells”, *Phys. Rev. Res.* **4**, 043004 (2022).
- ²²¹Y. Liu, J.-P. Banon, K. Frohna, Y.-H. Chiang, G. Tumen-Ulzii, S. D. Stranks, M. Filoche, and R. H. Friend, “The Electronic Disorder Landscape of Mixed Halide Perovskites”, *ACS Energy Lett.* **8**, 250–258 (2023).
- ²²²W. S. Jung, C. S. Leem, C. Kim, S. R. Park, S. Y. Park, B. J. Kim, E. Rotenberg, and C. Kim, “Imaging the electron density in solids by using multi-Brillouin-zone angle resolved photoelectron spectroscopy”, *Phys. Rev. B* **82**, 235105 (2010).
- ²²³G. S. M. Jansen, M. Keunecke, M. Düvel, C. Möller, D. Schmitt, W. Bennecke, F. J. S. Kappert, D. Steil, D. R. Luke, S. Steil, and S. Mathias, “Efficient orbital imaging based on ultrafast momentum microscopy and sparsity-driven phase retrieval”, *New J. Phys.* **22**, 063012 (2020).
- ²²⁴R. Wallauer, M. Raths, K. Stallberg, L. Münster, D. Brandstetter, X. Yang, J. Güdde, P. Puschnig, S. Soubatch, C. Kumpf, F. C. Bocquet, F. S. Tautz, and U. Höfer, “Tracing orbital images on ultrafast time scales”, *Science* **371**, 1056–1059 (2021).
- ²²⁵A. M. Lewis and T. C. Berkelbach, “Ab Initio Linear and Pump–Probe Spectroscopy of Excitons in Molecular Crystals”, *J. Phys. Chem. Lett.* **11**, 2241–2246 (2020).
- ²²⁶J. Braun, J. Minár, and H. Ebert, “Correlation, temperature and disorder: Recent developments in the one-step description of angle-resolved photoemission”, *Phys. Rep.* **740**, 1–34 (2018).
- ²²⁷C. S. Kern, A. Windischbacher, and P. Puschnig, “Photoemission orbital tomography for excitons in organic molecules”, *Phys. Rev. B* **108**, 085132 (2023).
- ²²⁸E. Busby, T. C. Berkelbach, B. Kumar, A. Chernikov, Y. Zhong, H. Hlaing, X.-Y. Zhu, T. F. Heinz, M. S. Hybertsen, M. Y. Sfeir, D. R. Reichman, C. Nuckolls, and O. Yaffe, “Multiphonon Relaxation Slows Singlet Fission in Crystalline Hexacene”, *J. Am. Chem. Soc.* **136**, 10654–10660 (2014).